sustainability

MDPI

Article

Comparative Experimental Assessment of Photovoltaic Panel Stability Under Moderate Freeze–Thaw Thermal Cycling

Răzvan-Andrei Polcovnicu [1], Sebastian-Valeriu Hudișteanu [1,*], Nicolae Țăranu [1,2,3], Dragoș Ungureanu [1,2], Marius Alexa [1], Iuliana Hudișteanu [1], Nelu-Cristian Chereches [1], Florin-Emilian Țurcanu [1], Cătălin Onuțu [1] and Alexandru-Florin Mustiață [1]

[1] Faculty of Civil Engineering and Building Services, Technical University "Gheorghe Asachi" of Iasi, 67 Prof. D. Mangeron Blvd., 700050 Iasi, Romania; razvan-andrei.polcovnicu@student.tuiasi.ro (R.-A.P.); nicolae.taranu@academic.tuiasi.ro (N.Ț.); dragos.ungureanu@academic.tuiasi.ro (D.U.); marius.alexa@student.tuiasi.ro (M.A.); iuliana.hudisteanu@academic.tuiasi.ro (I.H.); nelu.chereches@academic.tuiasi.ro (N.-C.C.); florin-emilian.turcanu@academic.tuiasi.ro (F.-E.Ț.); catalin.onutu@academic.tuiasi.ro (C.O.); alexandru-florin.mustiata@student.tuiasi.ro (A.-F.M.)

[2] The Academy of Romanian Scientists, 3 Ilfov Street, Sector 5, 050663 Bucharest, Romania

[3] Technical Sciences Academy of Romania, 26 Dacia Blvd., 030167 Bucharest, Romania

* Correspondence: valeriu-sebastian.hudisteanu@academic.tuiasi.ro

Abstract

This study presents an experimental investigation on the electrical performance, durability, and sustainability of different types of photovoltaic panels subjected to controlled climatic conditions and simulated solar radiation. Four photovoltaic technologies were analyzed, including monocrystalline, polycrystalline, and two semi-flexible panels, to evaluate their behavior under thermal stress. The experimental methodology consisted of repeated freeze–thaw cycles conducted in a double climatic chamber, with temperatures varying between −18 °C and +5 °C. Each panel was subjected to up to 500 cycles designed to reproduce repeated freeze–thaw environmental conditions representative of moderate cold-climate operation. At predefined intervals, the electrical characteristics of the panels were assessed using a solar radiation simulator based on high-pressure mercury vapor lamps, ensuring controlled and repeatable irradiation conditions. The results indicate that all tested panels exhibited relatively stable open-circuit voltage and output current values throughout the investigated thermal cycling interval, with only minor fluctuations observed during the experimental measurements. No visible macroscopic structural degradation and no major variations in the monitored electrical parameters were identified during the investigated testing conditions. Semi-flexible panels demonstrated comparable behavior to rigid panels, highlighting their potential for applications requiring mechanical adaptability. From a sustainability perspective, the observed durability and performance stability contribute to extending the operational lifetime of photovoltaic systems, reducing maintenance needs and material replacement rates. The findings provide comparative experimental observations regarding the evolution of selected electrical parameters under repeated moderate freeze–thaw exposure conditions.

Keywords: photovoltaic panels; sustainability assessment; freeze–thaw cycles; climatic chamber testing; solar radiation simulator; electrical performance; thermal cycling

Check for updates

Academic Editors: Eva Schwenzfeier-Hellkamp, Fabian Schoden and Maria Malvoni

Received: 2 April 2026
Revised: 15 May 2026
Accepted: 22 May 2026
Published: 27 May 2026

Copyright: © 2026 by the authors. Licensee MDPI, Basel, Switzerland. This article is an open access article distributed under the terms and conditions of the Creative Commons Attribution (CC BY) license.

1. Introduction

The increasing demand for sustainable energy solutions has led to the rapid expansion of photovoltaic (PV) technologies worldwide [1]. Photovoltaic systems represent a key

component of the global transition toward renewable energy due to their scalability and environmental benefits [2–5]. However, their performance is strongly influenced by environmental conditions, particularly temperature variations, which can significantly affect efficiency [2–4,6–8] and long-term reliability.

Despite the technological advancements in photovoltaic systems [9], their performance remains highly dependent on external climatic factors such as temperature variations, humidity, and solar radiation intensity. In particular, extreme temperature fluctuations, including repeated freeze–thaw cycles, can induce mechanical stress and potential degradation in photovoltaic materials and electrical connections [10]. These effects may lead to performance losses over time, especially in regions characterized by harsh and variable climates. It is well established that elevated temperatures reduce the electrical efficiency of photovoltaic panels, while repeated thermal variations may induce mechanical stress and long-term degradation. Temperature-induced effects include changes in semiconductor properties, increased resistive losses, and potential structural damage in module components [6,7].

In cold and variable climates, photovoltaic panels are frequently exposed to freeze–thaw cycles and rapid temperature fluctuations, which may affect both structural integrity and electrical performance. Such environmental conditions have been identified as critical factors influencing the reliability of PV modules deployed in harsh climates [11–13].

Although numerous studies have investigated the influence of temperature and solar radiation on the performance of photovoltaic panels, limited research has focused on the combined effects of repeated thermal cycling and controlled solar radiation under laboratory conditions [10,14]. Furthermore, the behavior of emerging photovoltaic technologies, such as semi-flexible panels, under such stress conditions remains insufficiently documented. This lack of experimental data highlights the need for controlled investigations that simulate harsh environmental conditions and evaluate the long-term stability of different photovoltaic technologies.

However, limited experimental studies have comparatively investigated rigid and semi-flexible silicon photovoltaic panels under repeated moderate freeze–thaw cycling combined with controlled solar radiation exposure. In particular, the long-term electrical stability of semi-flexible photovoltaic technologies under realistic cyclic thermal conditions remains insufficiently documented. Therefore, the present study addresses this research gap through a comparative experimental assessment focused on electrical stability indicators during repeated thermal cycling.

In this context, the present study aims to experimentally evaluate the electrical performance and durability of multiple photovoltaic panel technologies subjected to controlled climatic stress and simulated solar radiation. The investigation includes monocrystalline, polycrystalline, and semi-flexible panels, tested under repeated freeze–thaw cycles in a double climatic chamber, followed by electrical characterization using a solar radiation simulator.

The main objective of this research is to assess the stability of key electrical parameters, such as open-circuit voltage and current intensity, and to identify potential performance variations induced by thermal stress. The results are intended to provide relevant insights for the design, selection, and implementation of photovoltaic systems in environments exposed to significant temperature fluctuations.

Although the photovoltaic panels analyzed in this study exhibit moderate efficiency levels compared to state-of-the-art technologies, they remain representative for small-scale, experimental, and cost-sensitive applications [15]. The objective of the present research is not to benchmark high-efficiency performance, but rather to investigate the durability and stability of different photovoltaic technologies under repeated thermal stress condi-

tions. This approach provides relevant insights into the behavior of photovoltaic systems operating in real environmental conditions.

The present investigation was limited to silicon-based photovoltaic technologies due to their dominant use in current commercial and building-integrated photovoltaic applications. Future studies may extend the experimental methodology to emerging photovoltaic technologies such as perovskite, organic, and dye-sensitized solar cells, whose degradation mechanisms under thermal cycling may differ substantially.

It should be emphasized that the present investigation was not conceived as a standardized photovoltaic qualification study according to IEC 61215 [16] procedures. Instead, the adopted methodology was designed as a comparative experimental assessment focused on the evolution of selected electrical stability indicators under repeated moderate freeze–thaw exposure conditions representative of practical outdoor operation.

Therefore, the selected thermal interval was intentionally limited to moderate freeze–thaw environmental conditions rather than the accelerated thermal stress conditions required within IEC 61215 qualification protocols. Consequently, the obtained results should be interpreted primarily as comparative observations regarding electrical stability trends under realistic cyclic exposure conditions and not as certification-oriented photovoltaic qualification data.

The specific objectives of this study are:

(i) To evaluate the evolution of open-circuit voltage and output current during repeated freeze–thaw cycling;

(ii) To compare the thermal stability of rigid and semi-flexible photovoltaic technologies;

(iii) To assess the implications of repeated thermal cycling on photovoltaic durability and sustainability.

2. Materials and Methods

2.1. Experimental Setup

The experimental investigation was conducted using a controlled laboratory setup designed to evaluate the behavior of photovoltaic panels under variable environmental conditions. The testing methodology involved two main stages: thermal cycling in a climatic chamber and electrical characterization under simulated solar radiation.

A double climatic chamber (Feutron Klimasimulation GmbH, Langenwetzendorf, Germany [17]—Figure 1) was used to reproduce controlled temperature and humidity conditions. The equipment allows the separation of two distinct thermal zones, enabling precise control of environmental parameters over a wide range. In the present investigation, one compartment of the double climatic chamber was used as the primary testing zone containing the photovoltaic panels, while the second compartment contributed to thermal regulation and stabilization during rapid freeze–thaw transitions. The temperature inside the chamber can be adjusted between −45 °C and +100 °C, while the relative humidity can be regulated within a range of 10% to 95%, depending on the selected operating mode.

Following the climatic testing phase, the photovoltaic panels were evaluated using a solar radiation simulation system. The simulator was designed to reproduce both the spectral characteristics of solar radiation relevant for photovoltaic conversion and the associated thermal effects. This combined approach ensured realistic testing conditions and allowed for accurate assessment of the electrical performance of the panels.

The experimental setup was designed to ensure repeatability, controlled testing conditions, and accurate measurement of the electrical parameters, providing a reliable basis for comparative analysis between different photovoltaic technologies [11,18].

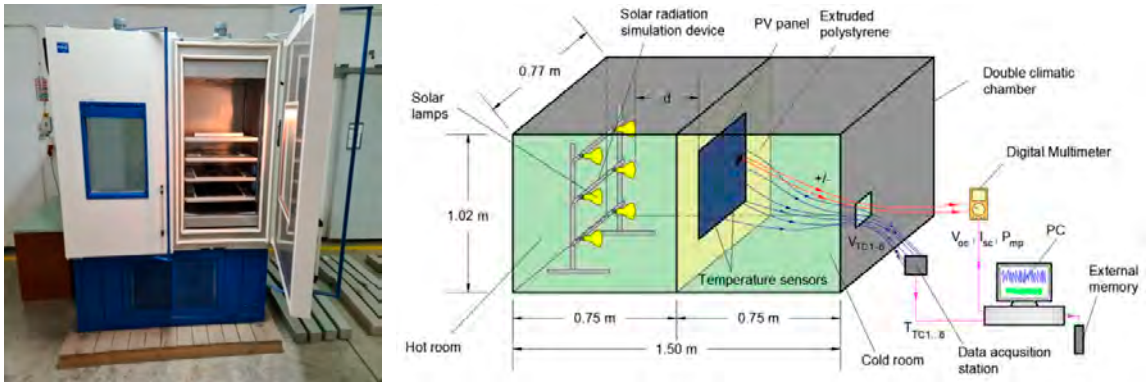


Figure 1. Double climatic chamber used for controlled freeze–thaw cycling of photovoltaic panels [19].

2.2. Photovoltaic Panels Description

Four photovoltaic panels with different technologies and characteristics were selected for the experimental investigation in order to enable a comparative analysis of their electrical performance under thermal stress conditions [13,14,18]. The analyzed panels included one monocrystalline panel, one polycrystalline panel, and two semi-flexible monocrystalline panels.

The selection of these panels was based on their different structural configurations and electrical characteristics, allowing the evaluation of both rigid and flexible photovoltaic technologies. Prior to testing, all panels were characterized according to their nominal electrical parameters provided by the manufacturer, including maximum power (P_{mp}), voltage at maximum power point (V_{mp}), current at maximum power point (I_{mp}), open-circuit voltage (V_{oc}), and short-circuit current (I_{sc}).

The monocrystalline panel had a nominal power of 24.8 W_p, while the polycrystalline panel was rated at 20 W_p. The semi-flexible panels exhibited higher nominal power, reaching 50 W_p, and were characterized by reduced thickness and increased mechanical adaptability. All panels were of comparable surface dimensions, ensuring consistency in testing conditions. The two semi-flexible photovoltaic panels had identical nominal characteristics and were included as replicated specimens in order to verify the repeatability and consistency of the experimental results obtained for flexible photovoltaic technology.

The present study was conceived as an exploratory comparative investigation focused on identifying general electrical stability trends under repeated thermal cycling conditions. Although a larger statistical sample population would improve the robustness of the analysis and reduce the influence of manufacturing variability, the experimental campaign was limited by equipment availability and the extended duration required for the climatic testing procedure.

A summary of the main electrical and geometrical characteristics of the analyzed photovoltaic panels is presented in Tables 1–3. These parameters served as a reference for evaluating the variations in electrical performance observed during and after the experimental testing procedures.

It should be noted that the electrical parameters presented in Tables 1–3 correspond to nominal manufacturer specifications, while the experimental values reported in the Results Section were obtained under the custom solar radiation simulator used in this study. Because the illumination source does not reproduce the standardized AM1.5G spectrum and the measurements were performed under simplified flash-testing conditions, differences between nominal and experimentally measured values are expected. Consequently, the present investigation focuses primarily on the relative stability and vari-

ation in electrical parameters during thermal cycling rather than on absolute photovoltaic performance benchmarking.

Table 1. Characteristics of the monocrystalline photovoltaic panel.

Monocrystalline Photovoltaic Panel	Specifications
	Maximum Power (P_{mp}): 24.8 W_p
	Voltage at Maximum Power (V_{mp}): 8 V
	Current at Maximum Power (I_{mp}): 3.1 A
	Open-Circuit Voltage (V_{oc}): 21.87 V
	Short-Circuit Current (I_{sc}): 3.7 A
	Dimensions ($L \times l \times g$): 500 mm × 350 mm × 15 mm

Table 2. Characteristics of the polycrystalline photovoltaic panel.

Polycrystalline Photovoltaic Panel	Specifications
	Maximum Power (P_{mp}): 20 W_p
	Voltage at Maximum Power (V_{mp}): 17.5 V
	Current at Maximum Power (I_{mp}): 1.15 A
	Open-Circuit Voltage (V_{oc}): 21 V
	Short-Circuit Current (I_{sc}): 1.36 A
	Dimensions ($L \times l \times g$): 500 mm × 350 mm × 15 mm

Table 3. Characteristics of the semi-flexible monocrystalline photovoltaic panel.

Semi-Flexible Monocrystalline Photovoltaic Panel	Specifications
	Maximum Power (P_{mp}): 50 W_p
	Voltage at Maximum Power (V_{mp}): 17.6 V
	Current at Maximum Power (I_{mp}): 2.84 A
	Open-Circuit Voltage (V_{oc}): 22 V
	Short-Circuit Current (I_{sc}): 3.38 A
	Dimensions ($L \times l \times g$): 560 mm × 530 mm × 3 mm

2.3. Climatic Chamber Testing Procedure

The climatic testing procedure was designed to evaluate the behavior of photovoltaic panels under repeated thermal stress conditions, simulating real environmental exposure in cold climates. The panels were subjected to controlled freeze–thaw cycles inside a double climatic chamber.

Each testing cycle consisted of a temperature variation from −18 °C to +5 °C and back to −18 °C, with a total duration of one hour per cycle. The temperature transitions between these limits were programmed to occur rapidly, in order to replicate abrupt environmental changes and induce thermal stress within the panel structure.

A total of 500 freeze–thaw cycles were applied to each photovoltaic panel, divided into five testing stages of 100 cycles each. After every 100 cycles, the panels were removed from the climatic chamber and subjected to electrical performance evaluation under simulated solar radiation.

The panels were positioned inside the chamber in a fixed configuration to ensure uniform exposure to thermal conditions (Figure 2). During the testing process, no mechanical constraints were applied that could influence the natural thermal expansion or contraction of the materials. The climatic chamber operates using forced-air circulation, ensuring thermal homogenization and minimizing temperature differences between panels positioned at different heights.



Figure 2. Configuration of the four photovoltaic panels in the climatic chamber.

The purpose of this testing procedure was to identify potential degradation effects, including structural damage or variations in electrical performance, induced by repeated temperature fluctuations. This approach allowed for a systematic assessment of the durability and stability of different photovoltaic technologies under controlled but realistic climatic stress conditions [20].

The selected temperature range was specifically chosen to simulate repeated freeze–thaw transitions frequently encountered in moderate continental climates, where photovoltaic systems are exposed to cyclic temperature variations around the freezing point. Unlike standardized IEC qualification tests intended for accelerated certification procedures, the present investigation focuses on comparative durability assessment under realistic environmental exposure conditions representative of practical outdoor operation.

In particular, the present study does not aim to reproduce the complete IEC 61215 thermal cycling protocol, which involves significantly broader temperature intervals (typically between −40 °C and +85 °C) and qualification-oriented degradation assessment criteria. The selected temperature interval was intentionally limited to moderate freeze–thaw conditions frequently encountered in continental outdoor environments in order to investigate comparative electrical stability trends under realistic cyclic exposure conditions.

The selected temperature range does not aim to replicate standardized photovoltaic qualification tests, such as those defined by IEC 61215, but rather to simulate realistic freeze–thaw conditions encountered in moderate cold climates. This approach allows the investigation of panel behavior under environmental conditions frequently observed in real-world applications.

2.4. Solar Radiation Simulation and Electrical Measurements

Following the climatic chamber testing, the photovoltaic panels were subjected to electrical characterization using a solar radiation simulation system [21]. The purpose of this stage was to evaluate the electrical response of the panels under controlled irradiation conditions, replicating the effects of natural solar exposure.

The solar simulator was based on 6 high-pressure mercury vapor lamps of 300 W each (OSRAM Ultra-Vitalux, OSRAM GmbH, Munich, Germany [22]—Table 4), capable of emitting radiation in both the visible and ultraviolet spectra. This configuration allowed not only the simulation of the photovoltaic conversion spectrum but also the reproduction of the associated thermal effects caused by solar radiation.

Table 4. Technical specifications of the OSRAM Ultra-Vitalux lamp.



Power = 300 W;
Socket type = E27;
Operating lifetime = 1000 h;
Emission spectrum = UVA + UVB;
Diameter = 127 mm;
Length = 185 mm.

The simulator consisted of six lamps arranged symmetrically in a structured configuration to ensure a uniform radiation distribution over the testing surface (Figure 3). In this figure, the blue color is used for the measured values of radiation, the black for numbering the points of measurements and red for isolines of radiation. Experimental observations indicated that a minimum distance of 15 cm between the radiation source and the photovoltaic panel was required to achieve acceptable uniformity of the incident flux. In the present study, a constant distance of 20 cm was adopted for all measurements to ensure consistency and repeatability.

It should be noted that the spectral distribution of the radiation source differs from the standard AM1.5G solar spectrum commonly used in photovoltaic testing. Therefore, the measurements obtained in this study are intended for comparative analysis between panels under consistent conditions rather than for absolute performance evaluation.

Electrical measurements were performed after each set of 100 freeze–thaw cycles. The measurements were not performed separately at the extreme temperatures of −18 °C and +5 °C during the thermal cycling process. Instead, the objective of the present study was to evaluate the cumulative effect of repeated freeze–thaw exposure on the overall electrical stability of the photovoltaic panels. Therefore, the reported results reflect comparative stability after thermal cycling rather than instantaneous temperature-dependent electrical behavior. The panels were tested individually, and the main parameters recorded were the open-circuit voltage (V_{oc}) and the output current (I). All photovoltaic panels were tested individually under identical positioning and illumination conditions in order to ensure comparable irradiation exposure. The measurements were conducted under rapid

illumination conditions (flash testing), allowing the capture of the instantaneous electrical response of the photovoltaic panels.

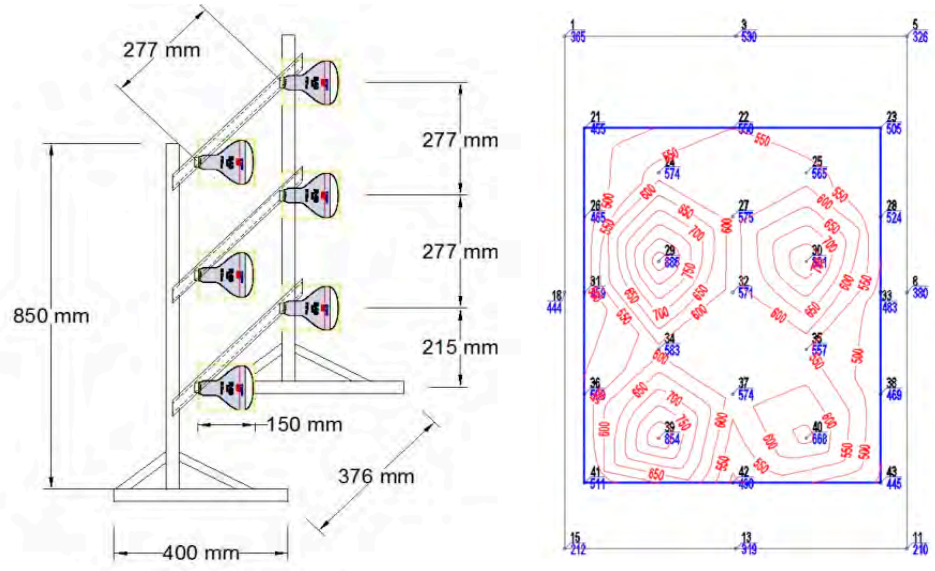


Figure 3. Schematic representation of the solar radiation simulator, lamp arrangement, and irradiation distribution used for photovoltaic testing [19].

Because the experimental setup was based on simplified flash-testing conditions and a custom solar radiation simulator, the investigation was limited to the evaluation of open-circuit voltage and output current stability. Full current–voltage (IV) curve acquisition, maximum power point tracking, fill factor determination, and precise power conversion efficiency measurements were beyond the scope of the present experimental configuration.

The authors acknowledge that maximum power output (P_{max}) represents one of the principal indicators used in standardized photovoltaic qualification procedures for evaluating degradation behavior. However, due to the limitations of the available experimental setup and the simplified flash-testing methodology adopted in the present investigation, the analysis was intentionally restricted to comparative monitoring of open-circuit voltage and output current stability.

Consequently, the present investigation does not provide a complete photovoltaic performance characterization according to standardized module qualification methodologies, where maximum power degradation represents the primary acceptance criterion. Instead, the study focuses on comparative monitoring of open-circuit voltage and output current stability as simplified indicators of electrical behavior during repeated thermal cycling.

Special attention was given to maintaining consistent testing conditions, including panel positioning, angle of incidence, and environmental factors, in order to minimize experimental errors. This methodology ensured reliable and comparable results for all tested photovoltaic technologies (Figure 4).

The lower measured electrical values observed for certain panels compared to nominal manufacturer specifications are primarily related to the non-standard irradiation spectrum, simplified flash-testing conditions, and the custom configuration of the solar radiation simulator used in this study. Consequently, the experimental results are intended primarily for comparative stability assessment under consistent laboratory conditions rather than for standardized photovoltaic performance certification.



Figure 4. (**a**) Solar radiation simulator; (**b**) photovoltaic panel positioning during flash testing; (**c**) electrical measurement configuration.

3. Results

The results presented in this section focus on the evolution of open-circuit voltage and output current as primary indicators of electrical stability during repeated thermal cycling. Although additional photovoltaic parameters such as fill factor (*FF*), maximum

power output (P_{max}), and complete IV curve characterization would provide a more comprehensive assessment of degradation phenomena, these measurements were not available within the limitations of the present experimental setup. Consequently, the investigation emphasizes comparative electrical stability trends rather than absolute photovoltaic performance evaluation.

The experimental investigation aimed to evaluate the electrical behavior of four photovoltaic panels subjected to repeated freeze–thaw cycles and controlled solar radiation simulation. Measurements were performed after each set of 100 thermal cycles, up to a total of 500 cycles. The analysis focuses on the evolution of open-circuit voltage and output current, as simplified comparative indicators of electrical stability during repeated thermal cycling.

Following the completion of the 500 freeze–thaw cycles, all photovoltaic panels were subjected to visual inspection in order to identify possible macroscopic defects such as delamination, discoloration, surface cracking, or connector degradation. No visible structural damage was observed for any of the tested panels. However, microscopic characterization methods capable of detecting internal microcracks or localized material degradation were not available within the scope of the present study.

3.1. Electrical Performance After Thermal Cycling

Table 5 presents the electrical parameters of the photovoltaic panels measured at each testing stage, including the initial state and subsequent measurements after every 100 freeze–thaw cycles.

Table 5. Electrical measurements of photovoltaic panels after successive freeze–thaw cycles.

Photovoltaic Panel Type	Test Number	Open-Circuit Voltage (V_{OC}) [V]	Output Current (I) [A]
Polycrystalline photovoltaic panel	0 (initial state)	9.73	2.98
	1	9.68	2.94
	2	9.77	2.93
	3	9.74	2.97
	4	9.69	3.01
	5	9.70	2.96
Monocrystalline photovoltaic panel	0 (initial state)	22.1	1.43
	1	22.4	1.40
	2	22.4	1,44
	3	22.2	1.40
	4	21.8	1.45
	5	22.3	1.41
Semi-flexible photovoltaic panel 1	0 (initial state)	20.84	2.84
	1	20.80	2.83
	2	20.79	2.84
	3	20.83	2.86
	4	20.82	2.85
	5	20.85	2.82

Table 5. *Cont.*

Photovoltaic Panel Type	Test Number	Open-Circuit Voltage (V_{OC}) [V]	Output Current (I) [A]
Semi-flexible photovoltaic panel 2	0 (initial state)	20.77	2.79
	1	20.78	2.81
	2	20.75	2.78
	3	20.74	2.77
	4	20.80	2.80
	5	20.78	2.83

All panels maintained electrical characteristics close to their initial values throughout the testing process [10]. Only limited variations in voltage and current were observed, indicating limited variations in the monitored electrical parameters during the investigated thermal cycling interval.

3.2. Evolution of Open-Circuit Voltage

Figure 5 shows the evolution of the open-circuit voltage as a function of the number of thermal cycles.

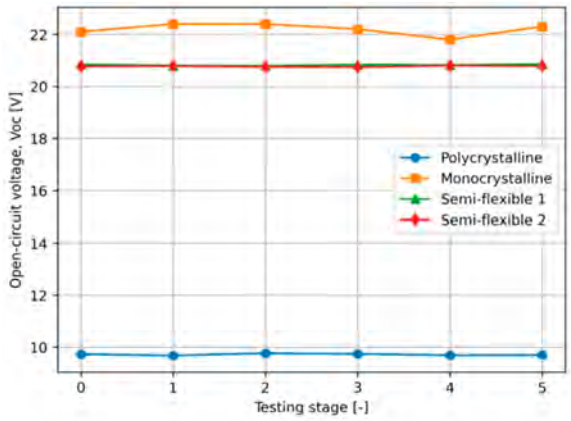


Figure 5. Evolution of open-circuit voltage for the analyzed photovoltaic panels as a function of testing stages.

All photovoltaic panels exhibit consistent voltage behavior, with only minor variations across the testing stages. The monocrystalline panel maintains the highest voltage values, while the polycrystalline panel shows slightly lower but stable values.

The semi-flexible panels display nearly constant voltage levels, confirming that their structural flexibility does not affect electrical stability under repeated freeze–thaw conditions.

3.3. Evolution of Output Current

Figure 6 illustrates the variation in the output current during the testing process.

The minor fluctuations observed in current measurements are attributed mainly to normal experimental variability associated with flash-testing conditions and small irradiation nonuniformities rather than to actual degradation effects.

The current remains stable for all tested panels, with only small fluctuations between successive measurements. The polycrystalline panel maintains values close to 3 A, while the monocrystalline panel remains around 1.4 A.

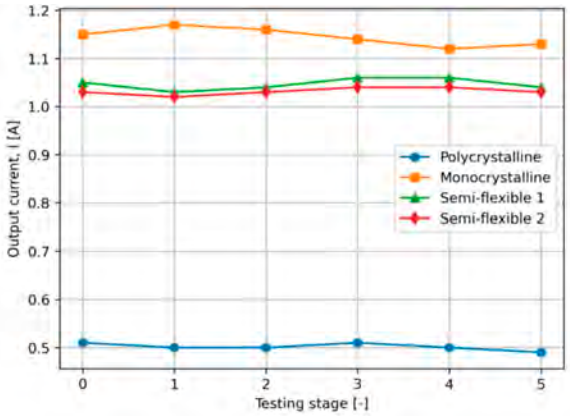


Figure 6. Evolution of output current for the analyzed photovoltaic panels during thermal cycling.

The semi-flexible panels exhibit a consistent current response, comparable to that of rigid panels. This behavior confirms that reduced thickness and flexibility do not negatively influence electrical performance.

3.4. Statistical Analysis of Electrical Parameters

Table 6 summarizes the statistical analysis of the measured electrical parameters, including mean values, standard deviations, and average percentage variations.

Table 6. Statistical analysis of electrical parameters (mean values, standard deviation, and percentage variation).

Panel Type	Mean V_{OC} [V]	V_{OC} Standard Deviation [V]	V_{OC} Mean Variation [%]	Mean *I* [A]	*I* Standard Deviation [A]	*I* Mean Variation [%]
Polycrystalline	9.718	0.031	−0.12	2.965	0.026	−0.50
Monocrystalline	22.200	0.208	+0.45	1.422	0.020	−0.58
Semi-flexible 1	20.822	0.021	−0.09	2.840	0.013	0.00
Semi-flexible 2	20.770	0.020	0.00	2.797	0.020	+0.24

The results confirm the high stability of all photovoltaic panels. The standard deviations for both voltage and current are very low, indicating consistent electrical behavior throughout the testing stages.

The average percentage variations remain below 1% for all parameters, demonstrating that repeated freeze–thaw cycles did not significantly affect the electrical performance of the panels [23–25].

4. Discussion

4.1. Influence of Thermal Cycling on Electrical Stability

The experimental results demonstrate that repeated freeze–thaw cycles between −18 °C and +5 °C did not significantly affect the electrical performance of the analyzed photovoltaic panels. Both the open-circuit voltage and output current remained stable throughout the 500 thermal cycles [10,13,14], as shown in Figures 5 and 6.

This behavior indicates a high level of structural integrity of the photovoltaic cells and their internal electrical connections. The absence of major variations in the monitored electrical parameters suggests that no severe electrical instability was detected within the limitations of the present experimental methodology. The observed electrical stability may also indicate that moderate freeze–thaw exposure primarily induces reversible thermo-

mechanical effects rather than permanent electrical degradation mechanisms within the investigated cycling interval.

Thermal cycling typically induces mechanical stress due to differences in thermal expansion coefficients between materials. However, the minimal variations observed in the measured parameters suggest that no critical damage, such as microcracks or delamination [26], occurred during the testing process [18,27].

From a sustainability perspective, the observed stability of the monitored electrical indicators may suggest favorable behavior under moderate cyclic thermal exposure conditions; however, no direct conclusions regarding long-term module lifetime, complete durability, or qualification-level reliability can be established without complete IV curve characterization and maximum power analysis.

The temperature interval selected in the present study was intended to reproduce repeated freeze–thaw transitions representative of moderate continental climatic conditions, particularly environments where photovoltaic systems frequently operate near the freezing point during winter periods. The objective was not to replicate IEC accelerated qualification protocols, but rather to evaluate comparative electrical stability under realistic cyclic thermal exposure conditions.

More extreme temperatures, such as −40 °C, may generate additional thermomechanical stress and potentially accelerate degradation mechanisms, including microcrack formation, encapsulant degradation, and interconnection fatigue. These aspects will be investigated in future studies.

A detailed comparison of photovoltaic behavior at the individual temperature limits of −18 °C and +5 °C could provide additional insight into the temperature dependence of electrical parameters such as voltage and current. Such investigations require real-time electrical characterization directly during thermal exposure and represent an important direction for future research.

4.2. Comparison Between Photovoltaic Technologies

A comparative analysis of the tested photovoltaic technologies highlights slight differences in electrical behavior, while confirming overall stability for all panel types.

The monocrystalline panel exhibited the highest open-circuit voltage values, consistent with its higher efficiency and material quality [15]. The polycrystalline panel showed lower voltage values but maintained a similarly stable trend, demonstrating reliable performance under thermal stress conditions.

The differences between the two technologies are mainly related to their intrinsic material structure [2,10]. Monocrystalline panels generally offer higher efficiency, while polycrystalline panels provide a more cost-effective solution with slightly lower performance but comparable stability.

In the context of sustainability, these results suggest that both technologies can offer long-term reliability, allowing system designers to balance efficiency, cost, and environmental impact. While monocrystalline panels maximize energy yield, polycrystalline panels may represent a viable option for cost-effective and sustainable large-scale deployments.

4.3. Behavior of Semi-Flexible Photovoltaic Panels

One of the most relevant findings of this study is the behavior of semi-flexible photovoltaic panels under repeated thermal cycling.

The semi-flexible panels analyzed in this study had a thickness of approximately 3 mm, compared to 15 mm for the rigid photovoltaic panels, highlighting the significant structural differences between the analyzed technologies.

Despite their reduced thickness and increased mechanical flexibility, the semi-flexible panels demonstrated electrical stability comparable to that of conventional rigid panels. This behavior may be associated with the polymer-based flexible substrate and the reduced structural rigidity of the panels, which can partially accommodate thermomechanical stress generated during repeated temperature cycling. In addition, the moderate thermal interval used in the present study may have limited the development of severe mechanical defects such as microcracks or interconnection fatigue. The variations in both voltage and current remained minimal, as shown in Figures 5 and 6.

This result is particularly significant, as flexible photovoltaic technologies are generally considered more vulnerable to mechanical and thermal stress [14,27]. The limited variations observed in the monitored electrical parameters suggest that the investigated semi-flexible panels maintained comparable electrical behavior to rigid panels within the investigated moderate thermal cycling interval. This result further suggests that modern semi-flexible photovoltaic technologies may achieve durability levels comparable to conventional rigid silicon modules when exposed to moderate cyclic thermal stress conditions [11,28].

These findings support the use of semi-flexible panels in applications where mechanical adaptability is required, such as installation on curved surfaces or mobile systems.

From a sustainability standpoint, the ability to integrate semi-flexible panels into non-standard or previously unsuitable surfaces expands the usable area for photovoltaic deployment, contributing to increased renewable energy generation without additional land use. This aspect is particularly relevant for building-integrated and resource-efficient energy solutions.

4.4. Practical Implications for Photovoltaic Applications

The results obtained in this study have direct implications for the design and implementation of photovoltaic systems in regions characterized by significant temperature variations.

The demonstrated stability of all tested panels under repeated freeze–thaw cycles confirms their suitability for use in cold climates and environments with dynamic thermal conditions. This is particularly relevant for applications in mountainous regions or areas with harsh winters.

Furthermore, the comparable performance of semi-flexible panels expands the range of possible applications, enabling the integration of photovoltaic systems in non-conventional configurations.

The experimental methodology used in this study, combining climatic chamber testing with solar radiation simulation, also proves to be an effective approach for evaluating the long-term reliability of photovoltaic technologies under controlled conditions.

In addition, these findings support sustainability-oriented design strategies by enabling more accurate prediction of long-term performance and durability. This contributes to optimizing system sizing, reducing overdesign, and minimizing lifecycle costs and environmental impact.

A limitation of the present study is the absence of full IV curve characterization, maximum power point tracking, and fill factor evaluation, which could provide a more comprehensive assessment of internal photovoltaic degradation mechanisms induced by thermal cycling. In the present work, the analysis was intentionally limited to the stability of open-circuit voltage and output current under consistent comparative testing conditions.

Additionally, the solar radiation simulator used does not fully reproduce the standardized AM1.5G spectrum, and microscopic imaging techniques for detecting internal defects such as microcracks were not available. Another limitation of the present investigation is the relatively small number of tested photovoltaic specimens for each technology. Conse-

quently, the results should be interpreted primarily as indicative comparative trends rather than statistically generalized performance laws.

Future investigations will address these aspects through calibrated solar simulations, complete IV characterization, microscopic structural analysis, and larger sample populations in order to improve statistical significance and evaluate the influence of manufacturing variability on long-term thermal degradation behavior.

The authors acknowledge that the evaluation of maximum power output (P_{max}), fill factor, and complete IV curve evolution would provide a more comprehensive assessment of photovoltaic degradation mechanisms during thermal cycling. Such measurements are commonly required within standardized qualification frameworks such as IEC 61215. However, the objective of the present study was intentionally limited to a comparative exploratory investigation of electrical stability trends under repeated moderate freeze–thaw exposure conditions using the available experimental infrastructure.

Therefore, the reported results should not be interpreted as evidence of full compliance with standardized photovoltaic qualification requirements, but rather as comparative experimental observations regarding the stability of selected electrical parameters under the investigated testing conditions.

5. Conclusions

This study presented an experimental investigation of the electrical performance, durability, and sustainability of four photovoltaic panels subjected to repeated freeze–thaw cycles and controlled solar radiation simulation.

The experimental results indicated relatively limited variations in the monitored electrical parameters during the investigated thermal cycling procedure. Variations in open-circuit voltage and output current were minimal and remained within a very narrow range, even after 500 thermal cycles, within the investigated moderate freeze–thaw exposure interval.

The monocrystalline panel exhibited the highest voltage values, consistent with its superior efficiency, while the polycrystalline panel showed slightly lower values but comparable stability. The semi-flexible photovoltaic panels demonstrated electrical behavior like that of conventional rigid panels, confirming that their structural flexibility does not negatively affect performance under repeated temperature variations.

A key outcome of this study is the absence of significant degradation in electrical parameters and the lack of visible macroscopic defects after thermal cycling, suggesting a high level of structural integrity of the tested photovoltaic panels under the investigated conditions. These observations provide comparative experimental information regarding the evolution of selected electrical indicators under repeated moderate thermal cycling conditions. From a sustainability perspective, this durability contributes to extending the operational lifetime of photovoltaic systems, reducing maintenance requirements and limiting material replacement, thereby supporting more resource-efficient energy systems.

From a practical standpoint, the monitored electrical behavior suggests that the investigated photovoltaic technologies maintained comparable responses during the selected experimental procedure. Semi-flexible panels represent a viable solution for applications requiring adaptability to non-standard surfaces without compromising electrical performance, further supporting sustainable design flexibility in photovoltaic integration.

Furthermore, the experimental approach combining climatic chamber testing with solar radiation simulation proved to be an effective and reliable method for assessing durability and performance under controlled yet realistic conditions, contributing to improved sustainability-oriented evaluation methodologies.

It is important to note that the results of this study are primarily intended for comparative analysis under controlled experimental conditions, rather than for absolute performance benchmarking according to standardized photovoltaic testing protocols.

The present investigation should therefore be interpreted primarily as a comparative experimental durability study focused on electrical stability indicators under repeated freeze–thaw exposure conditions.

Because of the limited number of tested specimens, the reported results should be interpreted as exploratory comparative findings intended to identify general durability trends rather than statistically representative degradation behavior for the analyzed photovoltaic technologies.

The selected thermal cycling interval specifically targeted realistic freeze–thaw exposure conditions rather than standardized accelerated qualification testing, allowing the investigation of photovoltaic stability under representative environmental operating scenarios.

The authors recognize that standardized photovoltaic qualification procedures, such as IEC 61215, require broader thermal intervals and degradation assessment based primarily on maximum power evolution obtained from complete IV curve characterization. Consequently, the findings of the present study should not be interpreted as certification-oriented validation results, but rather as exploratory comparative observations obtained under moderate freeze–thaw cycling conditions.

Future work will focus on extending the experimental methodology toward qualification-oriented testing procedures based on IEC 61215 recommendations, including broader temperature intervals, calibrated AM1.5G solar simulation, complete IV characterization, maximum power degradation analysis, and microscopic structural evaluation of thermo-mechanical defects.

Future research should focus on extending the number of thermal cycles, analyzing long-term degradation mechanisms, and investigating the combined effects of additional environmental factors such as humidity, mechanical stress, and prolonged UV exposure, to further enhance the sustainability and resilience of photovoltaic systems.

Author Contributions: Conceptualization, R.-A.P., N.Ț. and S.-V.H.; methodology, R.-A.P., N.Ț. and D.U.; software, R.-A.P., N.-C.C. and M.A.; validation, S.-V.H., D.U. and I.H.; formal analysis, R.-A.P., C.O., M.A., F.-E.Ț. and I.H.; investigation, R.-A.P., C.O. and A.-F.M.; resources, N.Ț., N.-C.C. and S.-V.H.; data curation, S.-V.H., C.O., M.A., N.-C.C., F.-E.Ț. and I.H.; writing—original draft preparation, R.-A.P., N.Ț. and S.-V.H.; writing—review and editing, R.-A.P., N.Ț., S.-V.H. and I.H.; visualization, R.-A.P., D.U. and A.-F.M.; supervision, N.Ț.; project administration, R.-A.P. and N.Ț.; funding acquisition, N.Ț. and S.-V.H. All authors have read and agreed to the published version of the manuscript.

Funding: This research received no external funding.

Institutional Review Board Statement: Not applicable.

Informed Consent Statement: Not applicable.

Data Availability Statement: The original contributions presented in this study are included in the article. Further inquiries can be directed to the corresponding author.

Conflicts of Interest: The authors declare no conflicts of interest.

References

1. Haegel, N.M.; Atwater, H., Jr.; Barnes, T.; Breyer, C.; Burrell, A.; Chiang, Y.M.; Bett, A.W. Terawatt-scale photovoltaics. *Science* **2019**, *364*, 836–838. [CrossRef] [PubMed]
2. Skoplaki, E.; Palyvos, J.A. On the temperature dependence of photovoltaic module electrical performance: A review of efficiency/power correlations. *Sol. Energy* **2009**, *83*, 614–624. [CrossRef]
3. Dubey, S.; Sarvaiya, J.N.; Seshadri, B. Temperature dependent photovoltaic (PV) efficiency and its effect on PV production in the world—A review. *Energy Procedia* **2013**, *33*, 311–321. [CrossRef]
4. Cuce, E.; Cuce, P.M.; Bali, T. An experimental analysis of illumination intensity and temperature dependency of photovoltaic cell parameters. *Appl. Energy* **2013**, *111*, 374–382. [CrossRef]
5. IEA PVPS. *Trends in Photovoltaic Applications*; IEA PVPS: Paris, France, 2023.
6. Mattei, M.; Notton, G.; Cristofari, C.; Muselli, M.; Poggi, P. Calculation of the polycrystalline PV module temperature using a simple method of energy balance. *Renew. Energy* **2006**, *31*, 553–567. [CrossRef]
7. Faiman, D. Assessing the outdoor operating temperature of photovoltaic modules. *Prog. Photovolt. Res. Appl.* **2008**, *16*, 307–315. [CrossRef]
8. Makrides, G.; Zinsser, B.; Georghiou, G.E.; Schubert, M.; Werner, J.H. Temperature behaviour of different photovoltaic systems installed in Cyprus and Germany. *Sol. Energy Mater. Sol. Cells* **2009**, *93*, 1095–1099. [CrossRef]
9. Fraunhofer ISE. Photovoltaics Report. 2024. Available online: https://www.ise.fraunhofer.de/en/publications/studies/photovoltaics-report.html (accessed on 1 May 2026).
10. Jordan, D.C.; Kurtz, S.R. Photovoltaic degradation rates—An analytical review. *Prog. Photovolt. Res. Appl.* **2013**, *21*, 12–29. [CrossRef]
11. Osterwald, C.R.; McMahon, T.J. History of accelerated and qualification testing of terrestrial photovoltaic modules. *Prog. Photovolt. Res. Appl.* **2009**, *17*, 11–33. [CrossRef]
12. Kontges, M.; Kurtz, S.; Packard, C.; Jahn, U.; Berger, K.; Kato, K.; Friesen, T.; Liu, H. *Review of Failures of Photovoltaic Modules*; Report IEA-PVPS T13-01:2014; IEA International Energy Agency: Paris, France, 2014.
13. Wohlgemuth, J.H.; Kurtz, S.; Whitfield, K.; TamizhMani, G.; Koehl, M.; Miller, D.; Joyce, J.; Zgonena, T. Evaluation of high-temperature exposure of photovoltaic modules. *Prog. Photovolt. Res. Appl.* **2011**, *19*, 954–965.
14. Nyarko, F.K.A.; Takyi, G.; Amalu, E.H.; Adaramola, M.S. Generating temperature cycle profile from in-situ climatic condition for accurate prediction of thermo-mechanical degradation of c-Si photovoltaic module. *Eng. Sci. Technol.* **2019**, *22*, 502–514. [CrossRef]
15. NREL. *Best Research-Cell Efficiency Chart*; NREL: Golden, CO, USA, 2024.
16. *IEC 61215-1:2021*; Terrestrial Photovoltaic (PV) Modules—Design Qualification and Type Approval—Part 1: Test Requirements. iTeh Standard: Jerusalem, Israel, 2021.
17. Hudisteanu, S.V.; Pruteanu, M.; Mateescu, T.D.; Vasilache, M. Experimental investigation of temperature effects on the parameters of photovoltaic panels. *Environ. Eng. Manag. J.* **2017**, *16*, 1643–1648. [CrossRef]
18. Herrmann, W.; Wiesmeier, S.; Wirth, H. PV module degradation caused by thermomechanical stress. In *Reliability of Photovoltaic Cells, Modules, Components, and Systems III*; SPIE: Bellingham, WA, USA, 2010. [CrossRef]
19. Hudișteanu, V.-S.; Chereches, N.-C.; Țurcanu, F.-E.; Hudișteanu, I.; Romila, C. Impact of Temperature on the Efficiency of Monocrystalline and Polycrystalline Photovoltaic Panels: A Comprehensive Experimental Analysis for Sustainable Energy Solutions. *Sustainability* **2024**, *16*, 10566. [CrossRef]
20. Hacke, P.; Spataru, S.; Terwilliger, K.; Perrin, G.; Glick, S.; Kurtz, S.; Wohlgemuth, J. Accelerated testing and modeling of PV module degradation. *IEEE J. Photovolt.* **2021**, *11*, 123–130.
21. Hudisteanu, S.V.; Chereches, C.N.; Turcanu, F.E.; Taranu, N.; Verdes, M.; Ancas, A.D.; Hudisteanu, I.; Ungureanu, D.; Polcovnicu, R.A. Solar radiation simulation device for investigation of thermal and photovoltaic panels. *Int. J. Mod. Manuf. Technol.* **2022**, *14*, 76–85. [CrossRef]
22. Available online: https://www.osram.com/appsj/pdc/pdf.do?cid=GPS01_265609&vid=MP_APAC_JP_eCat&lid=EN&mpid=ZMP_60829 (accessed on 1 May 2026).
23. *ASTM E927-19*; Standard Specification for Solar Simulation for Photovoltaic Testing. ASTM International: West Conshohocken, PA, USA, 2015.
24. *IEC 60904-9:2020*; Photovoltaic Devices—Solar Simulator Performance Requirements. IEC: Geneva, Switzerland, 2020.
25. Emery, K. *Solar Simulators and Their Calibration*; National Renewable Energy Laboratory (NREL): Golden, CO, USA, 2002.
26. Dhimish, M.; Holmes, V. Microcracks in photovoltaic modules: A review. *Renew. Sustain. Energy Rev.* **2020**, *132*, 110069.

27. Paggi, M.; Corrado, M.; Rodriguez, M.A. A multi-physics and multi-scale numerical approach to microcracking and power-loss in photovoltaic modules. *Compos. Struct.* **2013**, *95*, 630–638. [CrossRef]
28. Ndiaye, A.; Charki, A.; Kobi, A.; Kébé, C.M.F.; Ndiaye, P.A.; Sambou, V. Degradation evaluation of crystalline-silicon photovoltaic modules after long-term outdoor exposure. *Sol. Energy* **2013**, *96*, 142–148.

Disclaimer/Publisher's Note: The statements, opinions and data contained in all publications are solely those of the individual author(s) and contributor(s) and not of MDPI and/or the editor(s). MDPI and/or the editor(s) disclaim responsibility for any injury to people or property resulting from any ideas, methods, instructions or products referred to in the content.

sustainability

MDPI

Article

Technical and Economic Analysis of Sustainable Photovoltaic Systems for Street Lighting

Valeriu-Sebastian Hudișteanu *, Ionuț Nica, Marina Verdeș, Iuliana Hudișteanu, Nelu-Cristian Chereches, Florin-Emilian Țurcanu, Iulian Gherasim and Catalin-Daniel Galatanu

Faculty of Civil Engineering and Building Services, Gheorghe Asachi Technical University of Iasi, 700050 Iasi, Romania; ionut.i.nica@gmail.com (I.N.); marina.verdes@academic.tuiasi.ro (M.V.); iuliana.hudisteanu@academic.tuiasi.ro (I.H.); nelu.chereches@academic.tuiasi.ro (N.-C.C.); florin-emilian.turcanu@academic.tuiasi.ro (F.-E.Ț.); iulian.gherasim@academic.tuiasi.ro (I.G.); catalin-daniel.galatanu@academic.tuiasi.ro (C.-D.G.)

* Correspondence: valeriu-sebastian.hudisteanu@academic.tuiasi.ro

Abstract

This paper presents an analysis of the feasibility and sustainability of using local photovoltaic systems, ON-GRID central photovoltaic systems, and HYBRID systems for street lighting. By generating electricity from renewable sources (photovoltaic panels), solar energy contributes to environmental protection by avoiding the use of fossil fuels and nuclear fission energy, while also aligning with the European Union's Energy Strategy commitments for the medium term (until 2030) and long term (toward 2050). The implementation of local/central photovoltaic systems for street lighting largely depends on the existing power supply infrastructure, the solar potential of the site, and a clear understanding of potential electricity and cost savings. This study compares local and central photovoltaic systems for street lighting to analyze their technical performance and economic feasibility. The main sustainable objective that this work aims to achieve is Sustainable Development Goal 7. The optimal solution for photovoltaic systems in street lighting was determined through this analysis. The estimated cost for implementing an ON-GRID photovoltaic power plant with a capacity of 153.90 kWp is approximately EUR 773,977.22, with a discounted Payback Time of about 9.33 years. The implementation of this solution results in an annual reduction in greenhouse gas emissions by approximately 58.52 tons of CO_2.

Keywords: photovoltaic systems; public lighting; economic viability; economic efficiency; sustainable development

check for updates

Academic Editor: Idiano D'Adamo

Received: 10 July 2025
Revised: 30 July 2025
Accepted: 31 July 2025
Published: 8 August 2025

Citation: Hudișteanu, V.-S.; Nica, I.; Verdeș, M.; Hudișteanu, I.; Chereches, N.-C.; Țurcanu, F.-E.; Gherasim, I.; Galatanu, C.-D. Technical and Economic Analysis of Sustainable Photovoltaic Systems for Street Lighting. *Sustainability* **2025**, *17*, 7179. https://doi.org/10.3390/su17167179

Copyright: © 2025 by the authors. Licensee MDPI, Basel, Switzerland. This article is an open access article distributed under the terms and conditions of the Creative Commons Attribution (CC BY) license (https://creativecommons.org/licenses/by/4.0/).

1. Introduction

In recent decades, air pollution has become the greatest environmental health threat and a major cause of diseases [1]. Clean energy and energy efficiency are key components of the European Union's Sustainable Energy Strategy for the medium term (until 2030) and long term (toward 2050) in order to reduce energy consumption and air pollutants [2,3]. Renewable energy sources have experienced continuous growth and have proven to be a suitable solution for humanity [4]. The world's smart cities frequently use energy from renewable sources [4,5]. The smart grid concept is also an integral part of a smart city. Smart grids are capable of integrating distributed energy sources [4]. Also, sustainable development in the energy sector represents an important mission in terms of energy efficiency and low GHG emissions [1,3,6].

Romania has various renewable energy resources, including biomass, hydropower, geothermal potential, wind energy, solar energy, and photovoltaics [7]. These resources are distributed throughout the country [8] and can be further exploited as technology advances and becomes more cost-effective. In 2024, the electricity production structure was as follows: 32.16% hydro, 19.16% nuclear, 15.43% wind, 15.11% natural gas, 13.45% coal, 3.01% photovoltaic, 0.83% biomass, and 0.01% fuel oil [9], while the average CO_2 emissions from electricity production were close to the European level, around 172 g CO_2/kWh [9]. The installed capacity of photovoltaic power plants in Romania is approximately 2000 MWp [7].

In the context of the need to implement energy efficiency measures in all areas with real energy-saving potential, public lighting becomes an important element of the energy efficiency process [10]. The lighting sources used for public lighting have become increasingly efficient and necessary in order to achieve sustainable systems [11,12]. Nowadays, the recommendation is to fully use public lighting based on LED sources [13,14].

The main sustainable objective that this work aims to achieve is Sustainable Development Goal 7 (SDG 7)—ensure access to affordable, reliable, sustainable, and modern energy for all [15]. A growing number of scientific studies have investigated how PV-powered LED public lighting systems contribute to this objective [16–20], especially in reducing urban energy demand and enhancing access in off-grid areas [21].

The types of electricity supply for public lighting have evolved over time, from the electrical grid to those completely autonomous [22]. Also, a multitude of energy sources are used, such as conventional or renewable ones. Among the renewable energy sources used to power public lighting systems, both centralized and local, can be mentioned: photovoltaic systems [23], wind power plants [24], micro-hydropower plants [25], or biomass [13].

Contemporary solar street lighting systems combine high-efficiency photovoltaic panels with advanced lithium battery storage [26], smart LED lighting assemblies [27,28], and sophisticated control systems that optimize energy consumption based on environmental conditions and usage patterns [29]. These systems have proven especially beneficial in remote areas, humanitarian settings, and regions with unreliable grid electricity, offering autonomous lighting solutions that improve safety, security, and quality of life. Recent technological advancements have led to the development of more efficient and durable photovoltaic panels, high-performance LED lighting with intelligent controls [30], and sophisticated battery storage systems [26] that offer enhanced safety and longevity. Due to the degradation models [31,32] of the batteries by high operating temperatures, their capacity fades after 10 years of operation, and they need to be replaced.

Considering the versatility of photovoltaic systems, which can be integrated both as local [33,34] and central sources of electricity supply [30,35], these are the most widespread alternative solutions to power public lighting. Over the past decade, the photovoltaic public lighting sector has seen significant growth due to a rising awareness of sustainability [36], energy efficiency, and the necessity for resilient infrastructure in both developed and developing regions. Solar-powered street lighting exemplifies the integration of various technological fields, including photovoltaic engineering, LED lighting technology, energy storage systems [26], and intelligent control mechanisms [37].

Strong evidence supports the expanded implementation of photovoltaic public lighting systems as key to sustainable infrastructure development, the renewable energy transition, and climate change mitigation. With appropriate planning, community involvement, and technical design, these systems offer reliable, cost-effective, and environmentally responsible lighting solutions for a wide range of applications and locations [38].

The environmental benefits of solar street lighting are significant, including substantial reductions in carbon emissions, resource conservation, and ecosystem protection, often

justifying the implementation costs even when direct economic returns are minimal. Economic analyses show that solar solutions are becoming more cost-effective, especially in areas with high electricity prices and abundant solar resources [39].

Challenges remain, particularly regarding upfront capital costs, technical capacity building, and regulatory frameworks. However, innovative financing solutions, standardization efforts, and supportive policy development are effectively mitigating these barriers [38]. The literature presents studies on the use of electricity generated by photovoltaic systems, covering both autonomous solutions [33] and ON-GRID or HYBRID variants [35]. Most studies focus on each solution separately, and very few of them present technical–economic and comparative environmental impact components [39].

The most important thing is that a technical–economic analysis is not universally valid, because some costs are strongly dependent on the local context and particularities: the price of electricity and the price of assembly labor [39]. Moreover, in the literature consulted, details are not available regarding how various costs are taken into account.

In the present study, we explored the economic and environmental impact of using autonomous, ON-GRID, and HYBRID photovoltaic systems for public lighting to determine the optimal energy supply solution for implementation. The optimal use of photovoltaic systems was determined by comparing the three photovoltaic systems in terms of technical feasibility, compliance with road and pedestrian lighting requirements (regulated by NP 062-2002 [40], SR-EN 13201-2015 [41], and SR-EN 13201-2016 [42–45]), photovoltaic system performance, economic viability, economic efficiency, and environmental protection. This study was conducted numerically using Dialux Evo, and the results were processed analytically. The results are concluded in compliance with lighting requirements M4, M5, and M6 [41–46].

2. Materials and Methods

This study analyzes the use of local/central photovoltaic systems (Figure 1) for street lighting for a total of 726 lighting fixtures across three types of roads: 7200 m of national road, 2300 m of communal road, and 25,000 m of local roads. The analysis focuses on a functional public lighting system installed near roadways and pedestrian paths, utilizing LED lighting fixtures.

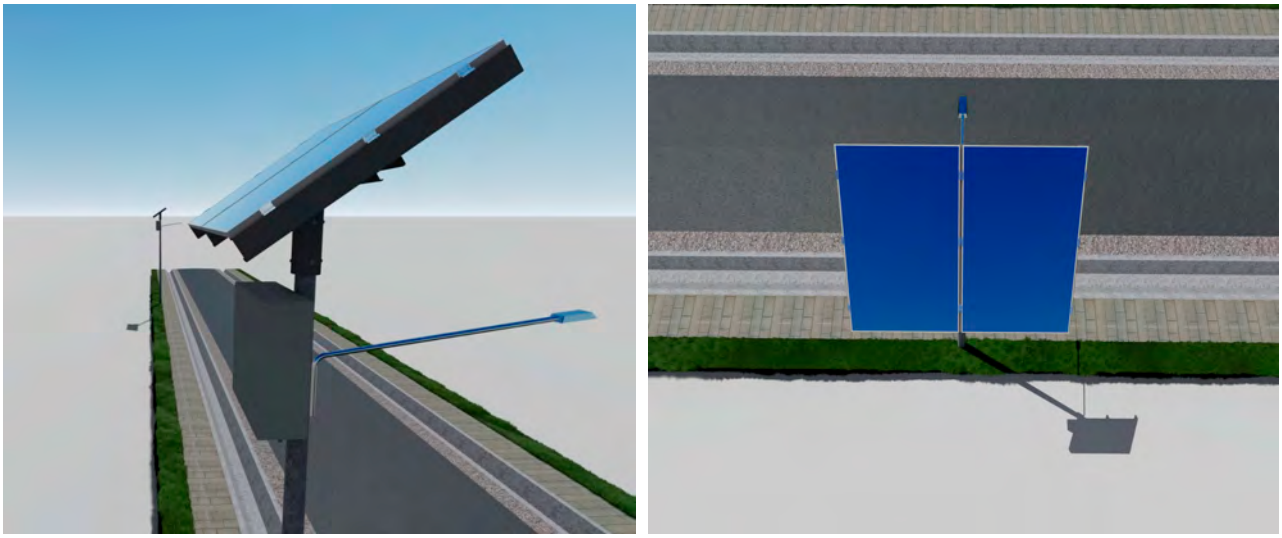


Figure 1. Three-dimensional analysis—aesthetic design for street lighting fixture, monocrystalline photovoltaic panels, battery box, and charge regulator mounted on the existing electric line poles.

2.1. Public Lighting

2.1.1. Technical Standards

For the design of the public lighting system, the following standards are currently used as the basis: SR EN 13201-1 [41]; SR EN 13201-2 [42]; SR EN 13201-3 [43]; SR EN 13201-4 [44]; and SR EN 13201-5 [45].

2.1.2. The Components of the Public Lighting System

The main components of the public lighting system are public lighting poles, electrical lines for powering the public lighting fixtures, lighting system ignition points, distribution boxes, lighting fixtures, motion detection sensors, modern communication networks for public lighting systems, and the remote management platform associated with a public lighting system [46].

2.1.3. Analysis of the Existing Situation

In preparing the analysis, the existing infrastructure of the electricity supply system was identified, along with the solar potential of the site, a clear understanding of the potential electricity savings and costs to be achieved through the implementation of photovoltaic systems for powering street lighting, as well as the quantitative determination of the reduction in greenhouse gas emissions resulting from this implementation.

The lighting fixtures will be mounted on the electrical poles of the 0.40 kV distribution line at a height of 8 to 10 m using brackets made from galvanized steel flat bars and notch clamps [27,47].

As a result of the energy balance of the analyzed lighting system with an installed power of 45.76 kW, Table 1, and an energy consumption of 177.44 MWh/year, Table 2, the consumption is based on the installed power of the lighting system and the schedule for switching on and off public lighting with monthly adjustment, as presented in Table 3.

Table 1. Installed power of lighting fixtures.

Road Class	Power of the Lighting Fixture [W]	Number of Lighting Fixtures	Installed Power [kW]
Technical class II (national road—M4)	100	180	18.00
Technical class IV (communal road—M5)	60	46	2.76
Technical class IV (local road—M6)	50	500	25.00
		TOTAL	**45.76**

Table 2. Estimation of the energy consumption of the analyzed public lighting system.

Estimation of the Energy Consumption of the Analyzed Public Lighting System.			
Month	**Operating Hours**	**Installed Power [kW]**	**Monthly Energy Consumption [kWh]**
January	432.45	45.76	19,788.91
February	346.36	45.76	15,849.43
March	343.17	45.76	15,703.46
April	279.00	45.76	12,767.04
May	268.15	45.76	12,270.54
June	219.00	45.76	10,021.44
July	244.28	45.76	11,178.25

Table 2. *Cont.*

Estimation of the Energy Consumption of the Analyzed Public Lighting System.			
Month	**Operating Hours**	**Installed Power [kW]**	**Monthly Energy Consumption [kWh]**
August	279.00	45.76	12,767.04
September	321.00	45.76	14,688.96
October	358.67	45.76	16,412.74
November	397.50	45.76	18,189.60
December	389.05	45.76	17,802.93

Table 3. Schedule for switching on and off public lighting, with monthly adjustment [48].

Schedule for Switching On and Off Public Lighting, with Monthly Adjustment (Considering the Average Values)				
No. Crt.	**Month**	**Period**	**Zone 1**	
			Switch-On Time	**Switch-Off Time**
0	**1**	**2**	**3**	**4**
1	January	1–31	17:22	7:17
2	February	1–28	18:00	6:37
3	March	1–31	18:40	5:47
4	April	1–30	19:17	4:47
5	May	1–31	19:52	4:17
6	June	1–30	20:22	3:52
7	July	1–31	20:12	4:00
8	August	1–31	19:37	4:37
9	September	1–30	18:52	5:22
10	October	1–31	18:00	5:57
11	November	1–30	17:10	6:35
12	December	1–31	18:52	7:07

This energy consumption estimate was made to facilitate the calculation of greenhouse gas (GHG) emissions (CO_2).

2.1.4. Selection of Lighting Classes

The present study is focused on evaluating the ecological, energy, and economic impact of street lighting for three types of roads: national, communal, and local. The selection of the lighting class for the national road was carried out in accordance with standardized photometric and traffic-based criteria. Table 4 presents the classification process based on traffic intensity, road geometry, and safety needs, as defined by European Norm EN 13201. The information regarding the real situation of the systems is as follows:

Table 4. Selection of the lighting class for the national road [32].

Parameter	**Options**	**Evaluation Index VWS**	**Selected Criterion**		
			National Road	**Communal Road**	**Local Road**
Velocity	Very high ($V \geq 100$ km/h)	2	0	−1	−1
	High ($70 < V < 100$ km/h)	1			
	Moderate ($40 < V < 70$ km/h)	0			
	Low ($V \leq 40$ km/h)	−1			

Table 4. *Cont.*

Parameter	Options	Evaluation Index VWS	Selected Criterion		
			National Road	Communal Road	Local Road
Traffic volume	High	1	0	0	−1
	Moderate	0			
	Low	−1			
Traffic composition	Mixed, with a high percentage of non-motorized vehicles	2	1	1	1
	Mixt	1			
	Only motorized vehicles	0			
Separation of traffic directions	No	1	1	1	1
	Yes	0			
Intersection density	High (>3/km)	1	1	1	1
	Moderate (≤3/km)	0			
Parked vehicles	Yes	1	0	0	0
	No	0			
Ambient lighting	High	1	−1	−1	−1
	Moderate	0			
	Low	−1			
Navigation load	Poor	1	0	0	0
	Good	0			
	Very good	−1			
Sum of weighted values (VWS)			**2**	**1**	**0**
The lighting class number is calculated as follows: M = 6 — VWS					
Resulting lighting class			**M4**	**M5**	**M6**

The analyzed **national road (NR)** has the following characteristics:

- Design speed for roads of technical class II: 50 km/h [49];
- Importance category: C [49];
- Road platform width: 7.00 m [49];
- Average distance between poles: 40.00 m;
- Maximum height for lighting fixture installation: 10.00 m;
- Number of lanes: 2;
- Distance from the curb: 3.00 ÷ 6.00 m;
- Pole placement: unilateral;
- Average reflection coefficient: 0.07—(corresponding to asphalt road R3).

The analyzed **communal road** (**CR**) has the following characteristics:

- Design speed for roads of technical class IV: 40 km/h [49];
- Importance category: C [49];
- Road platform width: 5.50 m [49];
- Average distance between poles: 50.00 m;
- Maximum height for lighting fixture installation: 10.00 m;
- Number of lanes: 2;
- Distance from the curb: 1.00 ÷ 3.00 m;
- Pole placement: unilateral;
- Average reflection coefficient: 0.07—(corresponding to asphalt road R3).

The analyzed **local road (LR)** has the following characteristics:

- Design speed for roads of technical class IV: 30 km/h [49];

- Importance category: C [49];
- Road platform: 5.50 m wide [49];
- Average distance between poles: 50.00 m;
- Maximum height of the lighting fixture installation: 10.00 m;
- Number of traffic lanes: 2;
- Distance from the curb: 1.00 to 2.00 m;
- Placement of poles: unilateral;
- Average reflection coefficient: 0.07—(corresponding to asphalt road R3).

3. Results and Discussion

3.1. Calculation Summary

The dimensioning of the street lighting system was carried out using a specialized calculation program DIALux evo [50], adhering to the provisions of the standards "NP-062 Standard for the design of road and pedestrian lighting systems" [40] and "SR-EN 13201-3 Public Lighting—Part 3: Calculation of performance" [43]. The input data for the **national road** lighting analysis is presented in Table 5, while the results are presented numerically in Table 5 and graphically in Figures 2–4. Table 5 summarizes the classification of the lighting system as M4 for the national road, based on factors such as traffic intensity, design speed, and environmental conditions.

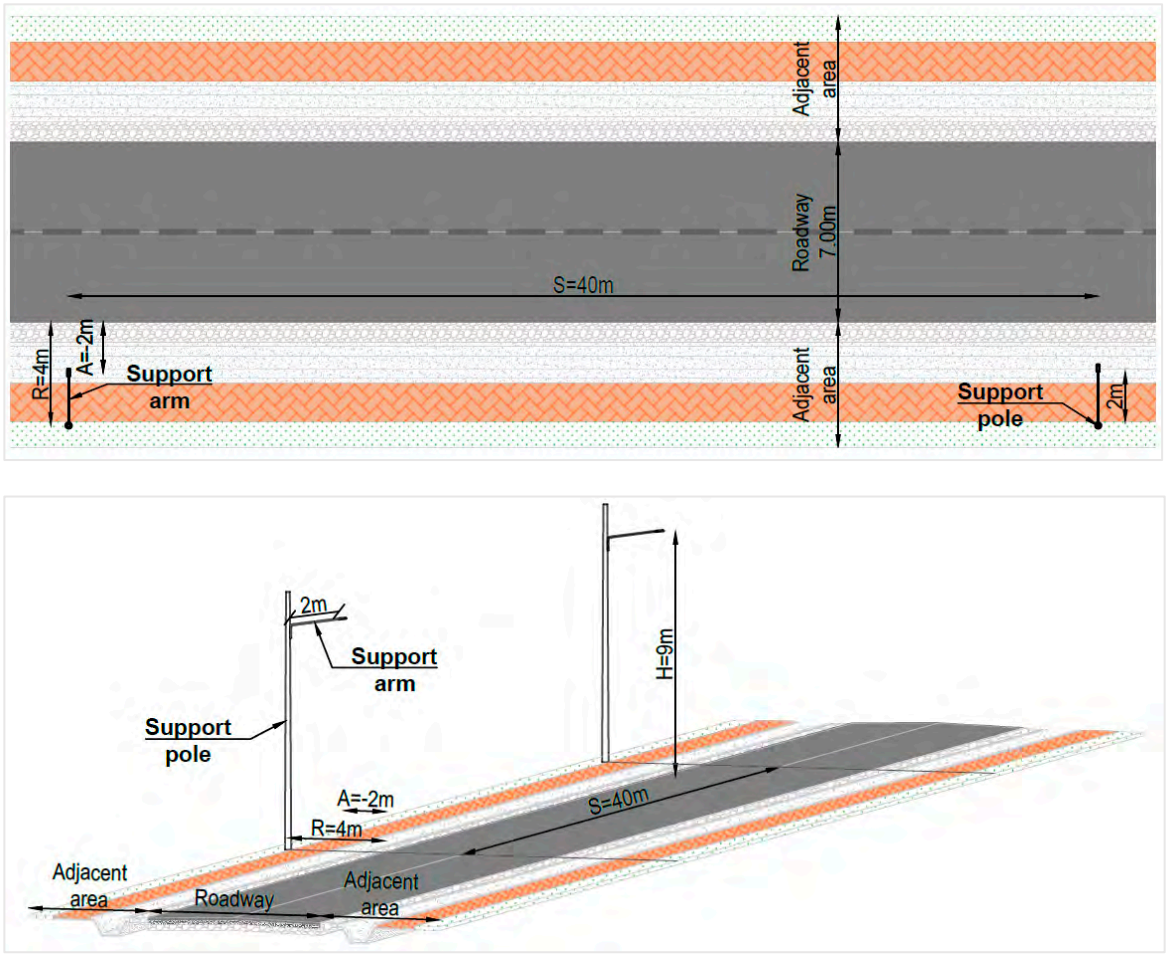


Figure 2. Geometric characteristics of the lighting system in the national road area.

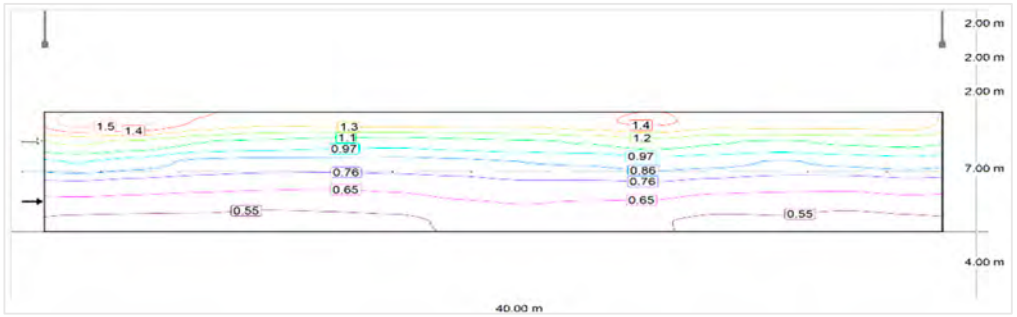


Figure 3. Road luminance [cd/m^2] (iso-luminance curves), M4.

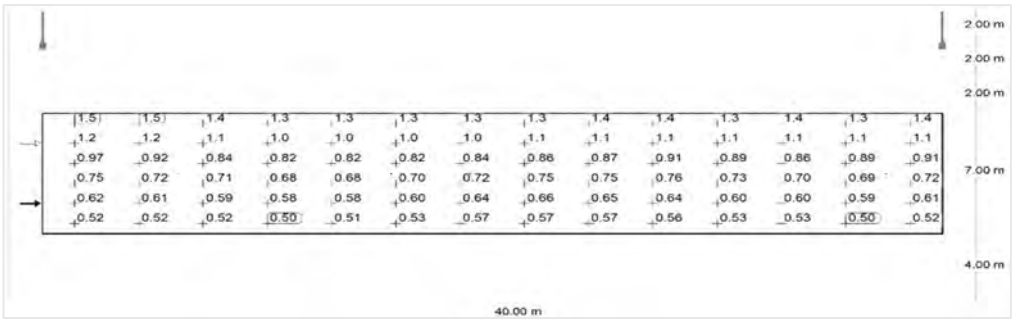


Figure 4. Road luminance [cd/m^2] (value grid), M4.

Table 5. National road—lighting system class M4.

National Road—Lighting System Class M4	
Characteristics	
Distance between poles	40.00 m
Height of the light point	9.00 m
Bracket extension of the light point	4.00 m
Overhang (advancement) (A)	−2.00 m
Bracket tilt	15°
Bracket length	2.00 m

To validate the lighting design for class M4, performance parameters were computed and are detailed in Table 6.

Table 6. Parameters calculated for NR—M4.

Parameter	Calculated	Nominal
L_m	0.76 cd/m^2	≥0.75 cd/m^2
U_o	0.58	≥0.40
U_I	0.81	≥0.60
TI	15%	≥15%
R_{EI}	0.68	≥0.30

The input data for the M5 **(communal road)** lighting analysis is presented in Table 7, while the results are presented numerically in Table 8 and graphically in Figures 5–7.

Table 7. Communal road—lighting system class M5.

Communal Road—Lighting System Class M5	
Parameter	
Distance between poles	50.00 m
Height of the light point	8.00 m
Clearance (*R*)	1.50 m
Bracket extension of the light point	−0.50 m
Bracket tilt	15°
Bracket length	1.00 m

Table 8. Parameters calculated for CR—M5.

Parameter	Calculated	Nominal
L_m	0.51 cd/m^2	≥0.50 cd/m^2
U_o	0.44	≥0.35
U_I	0.47	≥0.40
TI	15%	≤15%
R_{EI}	0.79	≥0.30

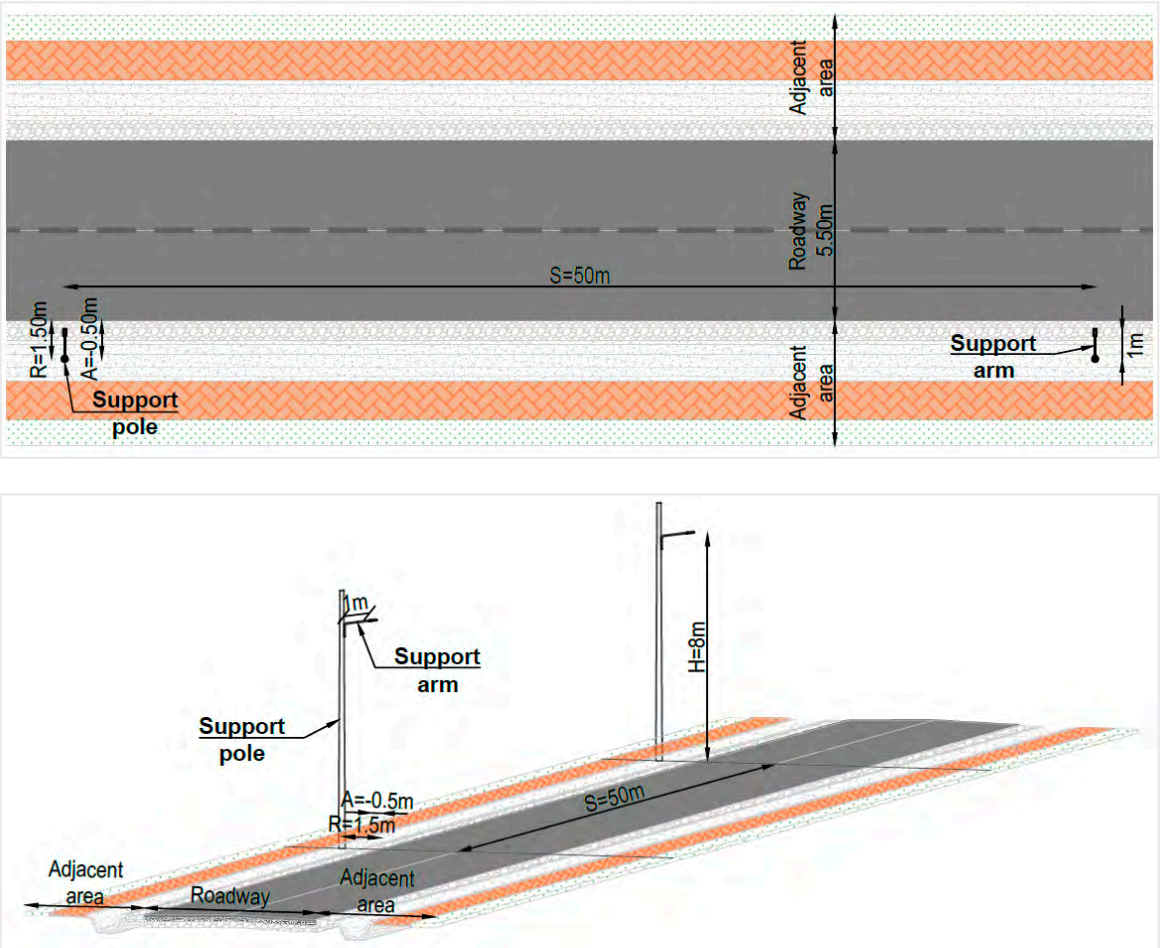


Figure 5. Geometric characteristics of the lighting system in the communal road area.

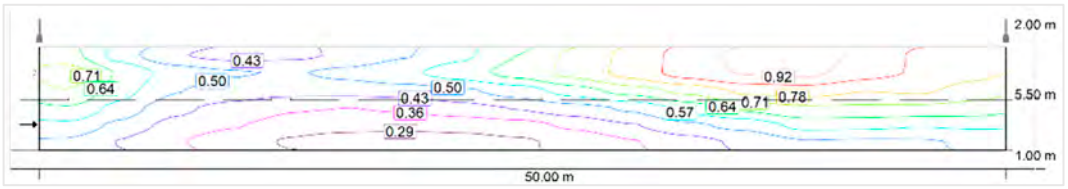


Figure 6. Horizontal luminance [cd/m^2] (iso-luminance curves), M5.

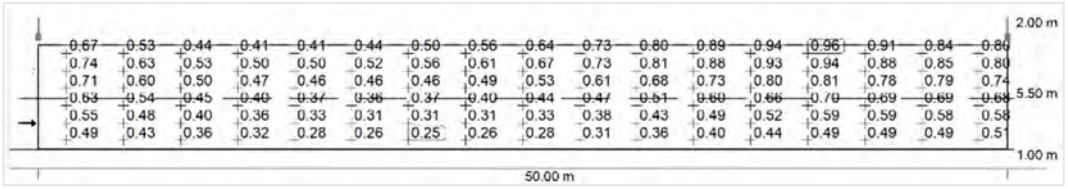


Figure 7. Horizontal luminance [cd/m^2] (value grid), M5.

For evaluating the **local road** lighting, the following input data was used, Table 9, while the results are presented numerically in Table 10 and graphically in Figures 8–10.

Table 9. Local road—lighting system class M6.

Local Road—Lighting System Class M6	
Parameter	
Distance between poles	50.00 m
Height of the light point	8.00 m
Clearance (R)	0.80 m
Bracket extension of the light point	0.20 m
Bracket tilt	15°
Bracket length	1.00 m

Table 10. Parameters calculated for LR—M6.

Parameter	Calculated	Nominal
L_m	0.44 cd/m^2	≥0.30 cd/m^2
U_o	0.44	≥0.35
U_l	0.45	≥0.40
TI	12%	≥20%
R_{EI}	0.72	≥0.30

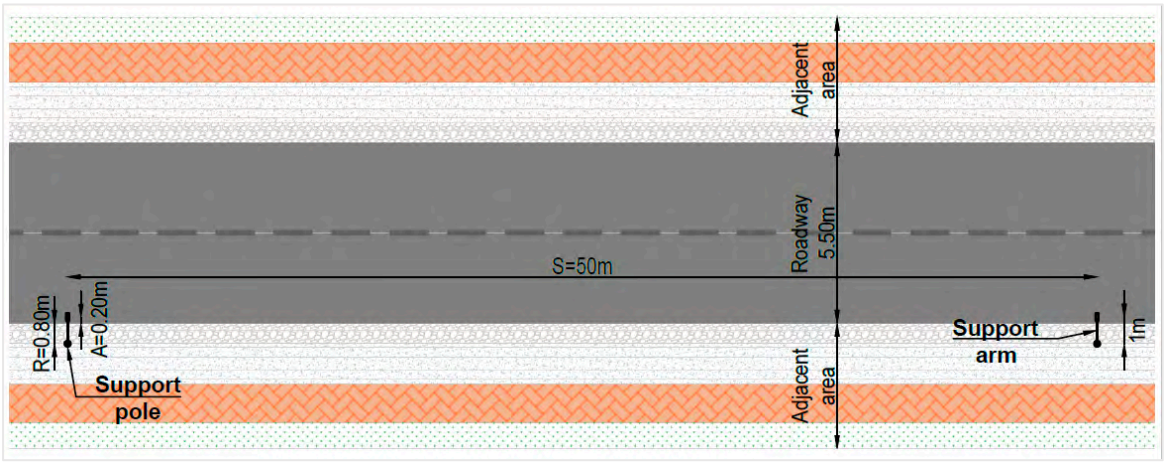


Figure 8. *Cont.*

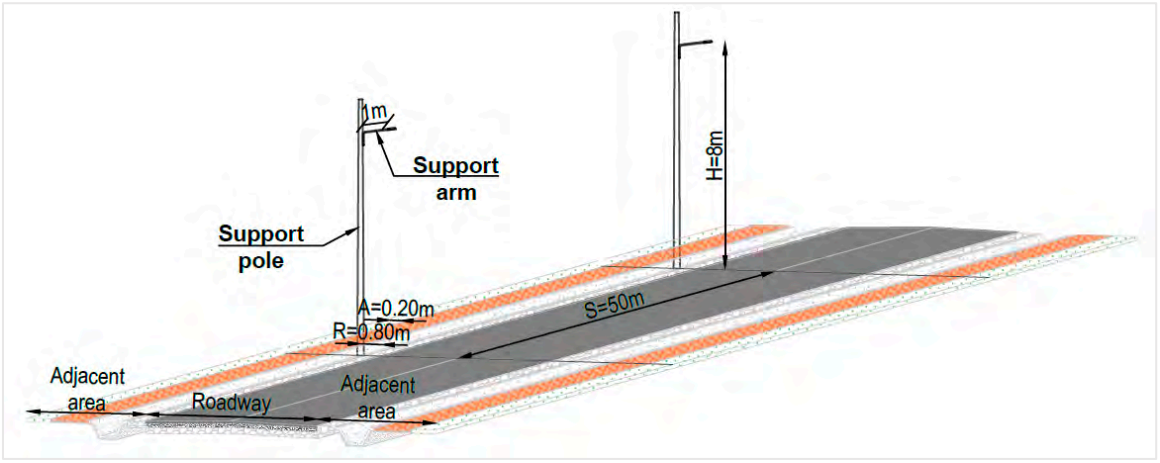


Figure 8. Geometric characteristics of the lighting system in the local road area.

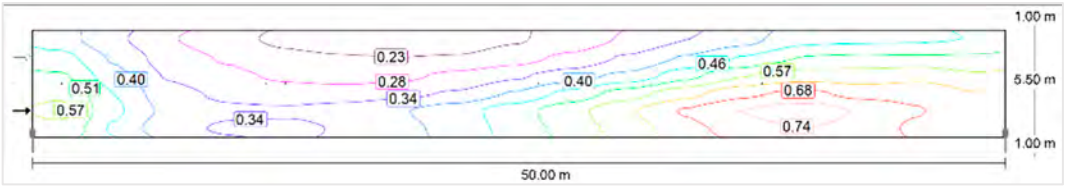


Figure 9. Horizontal luminance [cd/m^2] (iso-luminance curves), M6.

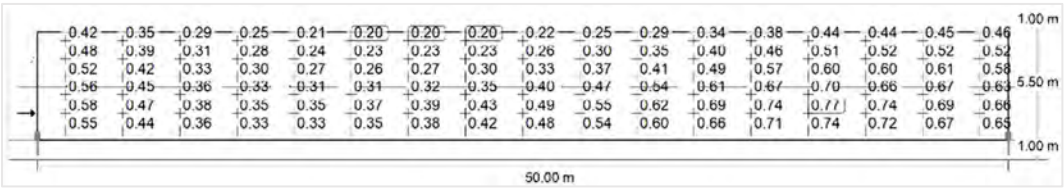


Figure 10. Horizontal luminance [cd/m^2] (value grid), M6.

The 3D analysis presented in Figure 11 regarding the night frontal view and Figure 12 regarding the aerial view demonstrates the integration of the street lighting system within the transverse profile of the road, ensuring proper alignment of the poles and uniform light distribution in accordance with the requirements of the road lighting class [51].

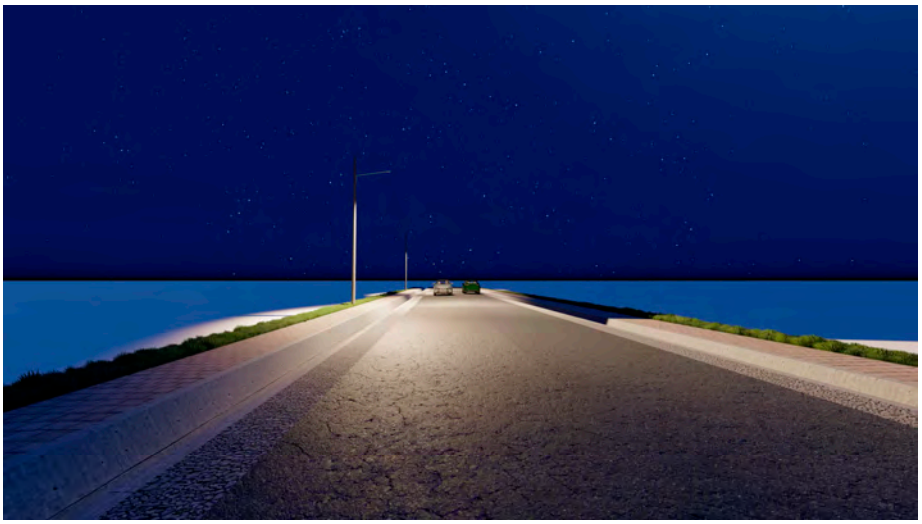


Figure 11. Three-dimensional analysis—night frontal view of the street lighting system.

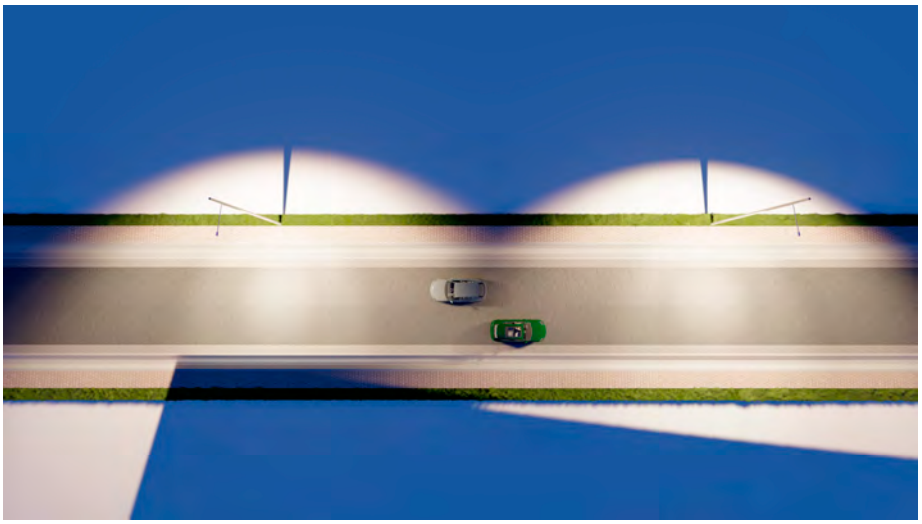


Figure 12. Three-dimensional analysis—aerial view of the street lighting system.

Daytime perspective view (Figure 13) illustrates the integration of the street lighting system into the geometric configuration of the road, with the placement of lighting poles on the sidewalks, ensuring safety zone compliance and conformity with road lighting regulations.



Figure 13. Three-dimensional qualitative analysis—daytime perspective view.

3.2. Analysis of Local Photovoltaic System for Street Lighting

Autonomous photovoltaic lighting fixtures can be installed on the electric poles of the 0.40 kV distribution line by replacing the existing lighting devices with a complete independent lighting system consisting of a monocrystalline photovoltaic panel, programmable charge controller, batteries, LED luminares, and auxiliary materials [17,52].

The panels used in this study are high-quality monocrystalline photovoltaic modules with a robust anodized aluminum frame to prevent the accumulation of ice and water [53]. Their efficiency, quality-to-price ratio, and compact construction characteristics recommend these modules as an integral part of an autonomous lighting system [53].

The photovoltaic module is mounted at the top of the pole at an optimal angle (less than 15°) to maximize incident solar radiation, and the batteries are placed in a box attached to the existing pole. During installation, the module is oriented toward the south, ensuring it receives solar radiation throughout the day without shading. The electrical energy

generated by the photovoltaic modules will charge the batteries during the day. This system operates from dusk until dawn.

To determine the performance of photovoltaic systems that are not connected to the electrical grid but instead rely on storing electrical energy in batteries to provide power when the sun is not shining, the OFF-GRID photovoltaic systems performance calculation tool (PVGIS) developed by the European Union [54] was used. This application utilizes information about the daily variation in electrical energy consumption to simulate the flow of energy to users and from the batteries.

Before choosing this autonomy, the battery discharge patterns were simulated using historical meteorological data (low irradiance winter days), and the 3 days of storage were used in the following calculation, which ensures >90% lighting reliability during the entire year. The installed photovoltaic power and the storage capacity of the solar battery for the studied case are reported in Table 11 and also in Appendix A.

Table 11. Components of the autonomous photovoltaic pole—**national road**.

Component	Parameter	Value	Quantity
Monocrystalline photovoltaic panel [33]	Nominal electrical power	550 W	2 pieces
	Nominal current	13.20 A	
	Short-circuit current	14.00 A	
	Nominal voltage	41.70 V	
	Open circuit voltage	49.60 V	
	Dimensions	2.261 × 1134 × 30 mm	
Solar regulator [34]	Maximum voltage	100 V	1 piece
	Maximum charging current	15.00 A	
	Low-voltage disconnect	22.00 V	
	Reconnect	25.20 V	
	Boost charging voltage	28.80 V	
	Overvoltage protection	Yes	
	Reverse polarity protection	Yes	
	Degree of protection	IP32	
	Size	133.50 × 70 × 35 mm	
	Weight	165 g	
Gel solar battery [35]	Nominal voltage	12 V	2 pieces
	Capacity	150 Ah	
	Dimensions ($L \times l \times h$)	485 × 172 × 240 mm	
	Weight	44 kg	
LED street lighting fixture [36]	Power	100 W	1 piece
	Nominal voltage	24 V	
	Degree of protection	IP65	
	LED type	multiled	
Auxiliary materials [20,37]	Battery box IP65, connectivity, protections, conductors, metal support, brackets, and OL-Zn collars		

In terms of energy production, battery performance, and discharge state, the results are detailed in the following images—Figures 14–16 and in Appendix A.

During the present study, load was considered as a constant value without considering the dynamic impact of factors such as seasonal variations in nighttime lighting duration and power changes due to appliance aging on the load.

Analyzing the data from Figures 9, 12 and 15, the installation of two photovoltaic panels with total powers of 1100 Wp, 600 Wp, and 500 Wp generates an average production deficit of 425.96 Wh, 269.27 Wh, and 224.39 Wh, respectively, while the average uncaptured energy is 2963.16 Wh, 1613.40 Wh, and 1344.50 Wh.

From Figures 10, 13 and 16, it is evident that in the months of January, February, November, and December, the power supply for public lighting at night cannot be guaranteed every day, as there are periods when the batteries do not charge completely. This situation is also confirmed by the data from Figures 9, 12 and 15, which indicate that during

the same time of the year, the electricity production is insufficient to ensure the operation of the system.

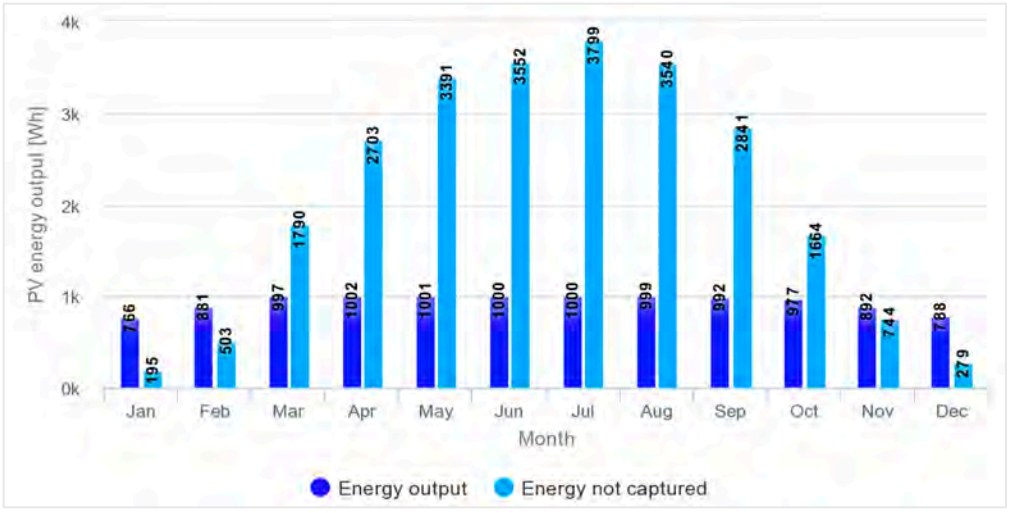


Figure 14. Estimation of energy production for the photovoltaic system OFF-GRID—NR.

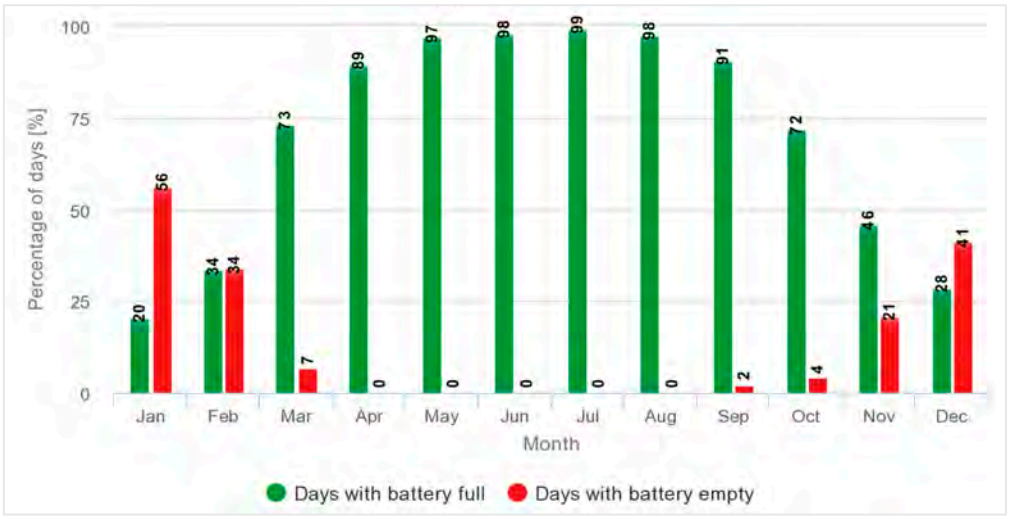


Figure 15. Battery performance for the photovoltaic system OFF-GRID—NR.

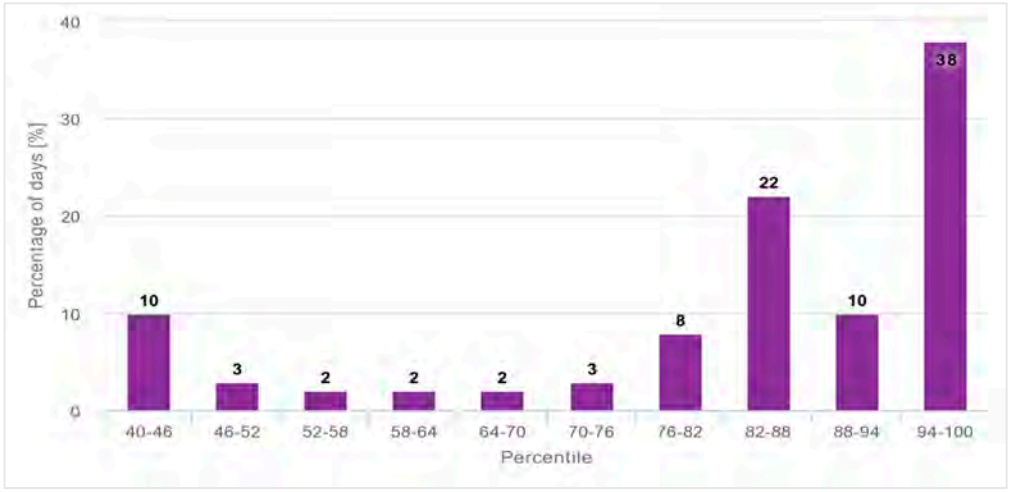


Figure 16. Battery charge percentage at the end of the day—NR.

Analyzing the data from Figures 11, 14 and 16, the results show that the batteries are fully charged in 70.57%, 67.53%, and 67.53% of the days in a year, while in 13.69%, 13.12%, and 13.12% of the days they are discharged. Under these conditions, public lighting cannot be ensured for approximately 50, 48, and 48 days per year, which limits the use of the system only to well-justified cases, considering its importance for road and pedestrian safety.

The energy storage systems, with capacities of 3600 Wh, 2880 Wh, and 2400 Wh, have been sized to ensure the operation of public lighting during the winter season for approximately 1.5 days, with a discharge cutoff limit of 40% for the batteries.

3.3. Analysis of Central ON-GRID Photovoltaic System for Street Lighting

Currently, the technology used in this energy context is traditional [55]. Therefore, an analysis was conducted on the establishment of a photovoltaic power plant designed to cover the electricity consumption of street lighting. The change in production technology is justified from three essential perspectives: technical, economic, and environmental impact. It is proposed to analyze a photovoltaic power plant installed on non-productive agricultural land, located on the outskirts of a locality.

The determination of the performance of the studied photovoltaic system was carried out by monitoring the average and annual energy productions, without energy storage in batteries. The calculation takes into account solar radiation, air temperature, wind speed, and the type of PV module. The user can choose how the modules are mounted, either on a standalone support or integrated into a building surface. By simulating in PVGIS, the optimal tilt and orientation that maximizes annual energy production were also calculated.

For this case, the PV solar system includes the following main components:

- Photovoltaic modules: composed of 144 monocrystalline photovoltaic cells and have a nominal unit power of 450 Wp. In the installation, 342 photovoltaic modules will be mounted to cover the electricity consumption of the analyzed public lighting;
- Power inverter: three-phase unidirectional with a nominal unit power of 60.00 kW (alternating current). Three-phase unidirectional power inverters will be installed in the system—three pieces;
- Mounting structure for photovoltaic modules: metal parts made of OL, sized and designed for the specific conditions of the project;
- Electrical panel: within the photovoltaic solar system, it provides switching devices and protective and/or measuring devices specific to photovoltaic systems. An electrical panel for the power plant will be installed in the system (TPV);
- Junction box for the PV arrays: a housing in which all the PV strings are electrically connected and where protection devices are located. In the installation, 22 junction boxes for the PV arrays will be mounted;
- The electrical cable networks within the photovoltaic solar include the energy cables laid in metal conduits up to the connection of the photovoltaic electrical installation to the distribution network of the national energy system;
- Grounding system: conductors and components used to establish equipotential bonds between the metallic elements associated with the photovoltaic solar installation and the conductors and components connecting to the grounding electrode of the metallic elements related to the photovoltaic solar system;
- Low-voltage electrical installation: data cables and equipment associated with the remote monitoring of the installed power inverters and the control and monitoring system of the installed power inverter.

The proposed photovoltaic power plant has a capacity of 153.90 [kWp] with an annual electricity production of 177,334.56 [kWh]—Figure 17, covering almost entirely the electricity consumption of the analyzed lighting system.



Figure 17. The monthly energy production from the fixed-tilt photovoltaic system.

3.4. Analysis of Using Central HYBRID Photovoltaic Systems for Street Lighting

The photovoltaic system described in Section 3.3 will be studied next as a HYBRID system, as follows:

- Replacing the three ON-GRID inverters with three HYBRID inverters with the same technical specifications;
- Implementing an energy storage system composed of 50 B-BOX systems, each including one cabinet and two lithium iron phosphate (LiFePO4) batteries with a battery management system (BMS) for use with an external inverter or charger;
- Extending the electrical network to connect public lamps to the solar energy source.

Thus, the possibility of using a HYBRID central photovoltaic system that includes photovoltaic panels, batteries, and HYBRID inverters is being analyzed. The photovoltaic system converts solar energy into electrical energy, which can be stored in a set of batteries for use at night or in low-light conditions.

Once energy consumption exceeds the capacity of the batteries, the system automatically switches to the power supply from the grid, which serves as a backup source for supplying street lighting.

The calculation uses information about the daily variation in electricity consumption to simulate the flow of energy to users and into the batteries [45]. The batteries were sized to store the electrical energy necessary for the operation of the lighting device for an average period of one day.

Figure 18 highlights the dependence of the photovoltaic system on the electrical grid power supply, illustrating the automatic switching of the system when the batteries reach a discharge limit of 40% during certain times of the year.

Figure 19 shows that the batteries are fully charged in 42.14% of the days of the year, while in 57.86% of the days, they do not reach maximum capacity. The storage system, with a capacity of 690,000 Wh, ensures the operation of public lighting for approximately one day, with a discharge limit of 40%. Although it does not fully cover nighttime consumption, the use of stored energy helps reduce dependence on conventional energy sources.

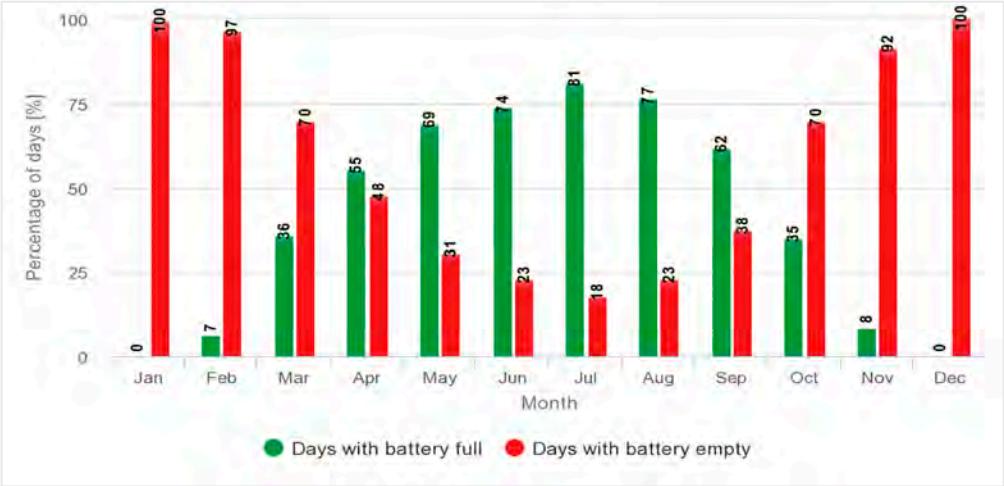


Figure 18. Battery performance for the photovoltaic system.

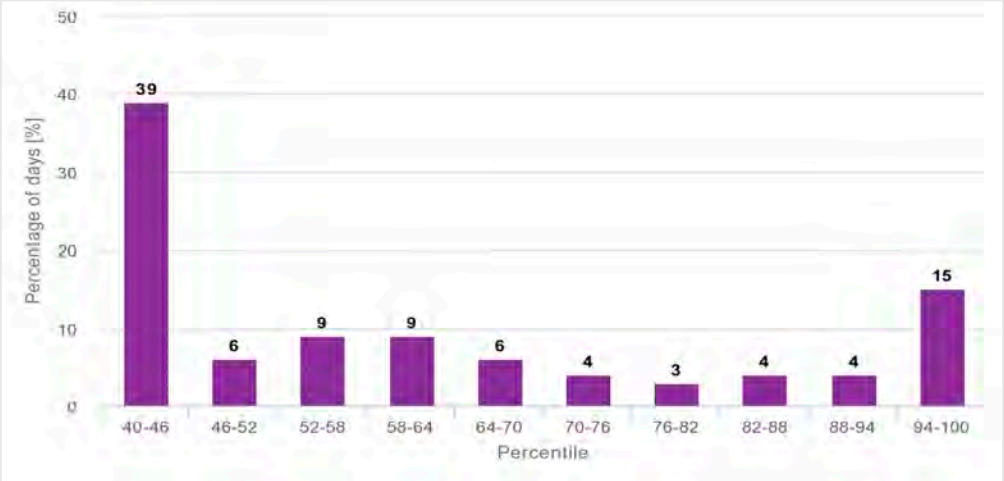


Figure 19. The battery charging percentage at the end of the day.

3.5. Analysis of Local Photovoltaic System for Street Lighting

3.5.1. Economic Viability Analysis

The estimated value of the project for a total of 726 autonomous photovoltaic poles is presented below in Table 12. The average total price per autonomous photovoltaic pole was estimated at EUR 1750.92, including VAT.

Table 12. Implementation costs of the investment—**local photovoltaic system**.

Description	Euro (Including VAT)	Pieces	Total Euro (Including VAT)
Obj. 1 Remove existing lighting fixtures	**25.85**	**726**	**18,763.42**
1.1. Remove existing lighting fixtures	25.85	726	18,763.42
Obj. 2 Autonomous photovoltaic pole—NR (M4)	**1854.41**	**180**	**333,793.64**
2.1. Equipment	1150.50	180	207,089.17
2.1.1. Monocrystalline photovoltaic panel 550 W	157.79	360	56,803.54
2.1.2. Charge controllers 100 V 15 A	73.34	180	13,201.93
2.1.3. Solar battery 12 V 150 Ah	331.27	360	118,999.04
2.1.4. LED lighting fixture 24 V 100 W	100.47	180	18,084.65
2.2. Street photovoltaic pole	487.77	180	87,798.03
2.3. Installation of machinery/equipment	216.15	180	38,906.45

Table 12. *Cont.*

Description	Euro (Including VAT)	Pieces	Total Euro (Including VAT)
Obj. 3 Autonomous photovoltaic pole—CR (M5)	**1453.80**	**46**	**66,874.69**
3.1. Equipment	752.46	46	34,613.41
3.1.1. Monocrystalline photovoltaic panel 300 W	110.07	92	10,126.16
3.1.2. Charge controllers 100 V 15 A	73.34	46	3373.83
3.1.3. Solar battery 12 V 120 Ah	247.56	72	17,824.51
3.1.4. LED lighting fixture 24 V 60 W	71.50	46	3288.91
3.2. Street photovoltaic pole	485.18	46	22,318.52
3.3. Installation of machinery/equipment	216.15	46	9942.76
Obj. 4 Autonomous photovoltaic pole—LR (M6)	**1352.20**	**500**	**676,098.15**
4.1. Equipment	650.87	500	325,432.06
4.1.1. Monocrystalline photovoltaic panel 250 W	110.32	1000	110,319.80
4.1.2. Charge controllers 75 V 10 A	73.34	500	36,672.04
4.1.3. Solar battery 12 V 100 Ah	158.65	1000	158,646.74
4.1.4 LED lighting fixture 24 V 60 W	39.59	500	19,793.48
4.2. Street photovoltaic pole	485.18	500	242,592.63
4.3. Installation of machinery/equipment	216.15	500	108,073.46
TOTAL	**1750.92**	**726**	**1,271,170.15**
TOTAL C + I	**777.22**	**726**	**564,263.86**

3.5.2. Calculation of Economic Efficiency

The electricity savings over a 20-year period were determined, and a comparison between expenses and revenues was made, taking into account system maintenance and the necessary battery replacements every 7 years [55]. The weighted average electricity price for the year 2024 in Romania was 0.26 Euro/kWh [56]. The recommended energy efficiency measures are relevant to the beneficiary's activity if they can be quantified in monetary terms or energy savings. In this regard, considering the mathematical model for assessing the economic efficiency of the proposed solution, the energy savings for the energy efficiency measures were estimated. During the present analysis, the soft costs that may distort investment comparison were neglected, considering the large scale of the systems and study interval.

The Payback Time (PBT) of the investment was calculated for the energy efficiency measures that require investments for their implementation, along with a series of indicators highlighting the feasibility of the proposed measures (Table 13), namely the investment payback period, the net present value, and the internal rate of return. For all proposed solutions, an inflation rate of 5% was considered, corresponding to an emerging country (Romania), with a solution lifespan of 20 years. Since the investment values are known, Figure 20 presents the cumulative cash flow over the considered 20-year period.

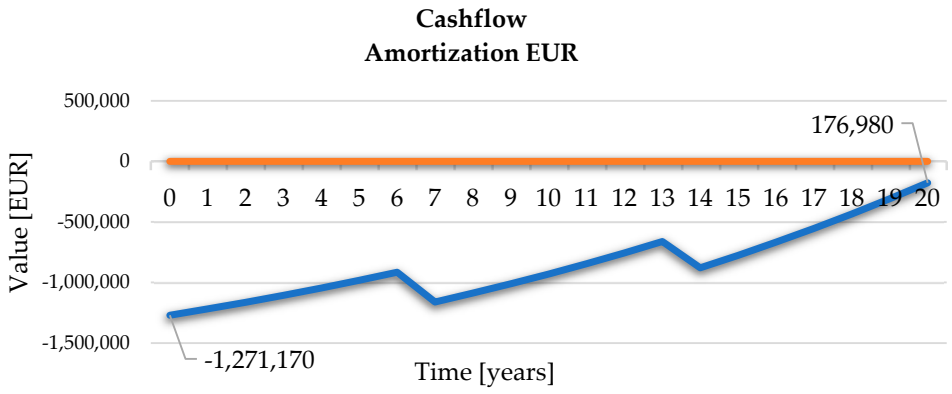


Figure 20. Cumulative cash flow for the considered 20-year period—**local photovoltaic system**.

Table 13. Feasibility indicators of the proposed measures.

Description	Unit	Value
Total investment value	EUR	1,271,170.15
Maintenance costs	EUR	729,290.55
The value of the economy per year	EUR	91,173.99
Net Present Income (NPI)	EUR	−176,980.80
Discount rate	%	5
Lifespan of the solution	YEARS	20
Payback Time (PBT)	YEARS	13.94
Discounted Payback Time (DPBT)	YEARS	21.94
Internal rate of return (IRR)	%	−13.92

3.5.3. Quantitative and Percentage Reduction in Resulting Greenhouse Gas Emissions

CO_2 emissions were calculated using the emission factor from annex VI of Regulation (EU) No. 601/2012 [48] on the monitoring and reporting of greenhouse gas emissions in accordance with Directive 2003/87/EC [46] of the European Parliament and of the Council (based on the fuel used), which is multiplied by the amount of energy savings proposed to be achieved annually through the project until the end of the project's sustainability period (measured in MWh). For saved electricity, the emission factor used is 0.33 tons CO_2/MWh [46].

Based on the data presented above, greenhouse gas emissions for energy production in power plants within the National Electricity System (SEN) are calculated, as the energy produced from renewable sources has a very low impact on the three types of fuel. In this context, the value of greenhouse gas emissions for the first year after the implementation of the project involving the installation of a 475.60 kWp photovoltaic panel system is calculated. During the present study, the GHG emissions calculation method does not account for the carbon footprint of photovoltaic equipment over its entire lifecycle.

GHG for the energy saved (177.40 MWh/year) will be

$$\mathbf{GHG_r = 177.40\ MWh \times 0.33\ t_{CO_2}/MWh = 58.54\ t_{CO_2}}$$

$$\mathbf{GHG_{PV} = 177.40\ MWh \times 0.33\ t_{CO_2}/MWh = 58.54\ t_{CO_2}}$$

The GHG_1 value of 0.00 t_{CO_2} after the implementation of the project:

$$\mathbf{GHG_1 = GHG_r - GHG_{PV} = 58.54\ t_{CO_2} - 58.54\ t_{CO_2} = 0.00\ t_{CO_2}}$$

The percentage value of GHG after the implementation of the project will be

$$\mathbf{GHG_{CO_2} = \frac{(GHG_r - GHG_1)}{GHG_r} \times 100 = \frac{(58.54 - 0.00)}{58.54} \times 100 = 100\%}$$

3.6. Analysis of Using Grid-Connected Central Photovoltaic System for Street Lighting

3.6.1. Economic Viability Analysis

The estimated value of the investment for the construction of the photovoltaic power plant is EUR 773,977.22 including VAT—Table 14.

Construction and installation (C + I) represents the set of execution works necessary for the realization of an investment objective, including both the actual construction works (structures, foundations, finishes, etc.) and the assembly works for the related equipment and installations. The value of C + I, expressed in euros and included in the general estimate, reflects the costs associated with these works, according to the categories of expenses specified in the relevant chapters and subsections of the general estimate.

Table 14. Implementation costs of the investment—grid-connected central photovoltaic system.

Description	Total Euro (Including VAT)
Obj. 1 Utilities	**87,076.34**
1.1. Electric connection	79,719.02
1.2. Telecommunications—data voice	7357.32
Obj. 2 Land development	**79,695.46**
2.1. Removal of the topsoil layer (2.448 m^2)	7965.32
2.2. Fencing (203.00 m, with a 4.00 m vehicle access gate and a 1.00 m pedestrian access gate)	30,164.68
2.3. Foundations for lighting poles	4920.10
2.4. Container platforms for personnel and transformer station	16,058.21
2.5. Access road made of stone (40.00 m)	20,587.14
Obj. 3 Photovoltaic power plant 153,90 kWp	**373,524.51**
3.1. Foundations for metal supports	58,907.70
3.2. Supports for photovoltaic panels	122,241.18
3.3. Wiring and accessories	101,313.45
3.4. Grounding	21,204.10
3.5. Junction boxes for PV (22 pieces)	32,711.14
3.6. Photovoltaic power plant panel board	14,479.95
3.7. Earthworks	16,217.02
3.8. Lighting poles (6 pieces)	4641.87
3.9. Transport	1808.09
Obj. 4 Video surveillance subsystem	**14,747.55**
4.1. Earthworks	6105.62
4.2. Trenches and cables	3110.25
4.3. Equipment	4232.23
4.4. Transport	1299.46
Obj. 5 Installation of machines/equipment	**150,156.38**
5.1. Equipment	129,768.38
5.1.1. Monocrystalline photovoltaic panel 450 W (342 pieces)	103,015.46
5.1.2. 60 kW three-phase grid-connected inverter (3 pieces)	21,422.51
5.1.3. UPS 3000 VA 2U RACK	2377.98
5.1.4. Outdoor video surveillance camera (12 pieces)	1017.56
5.1.5. NVR 32 CH	703.30
5.1.6. Street lighting fixture LED 80 W	1231.57
5.2. Installation of machinery/equipment	20,388.01
TOTAL	**773,977.22**
TOTAL C + I	**611,300.46**

3.6.2. Calculation of Economic Efficiency

The calculation of economic efficiency was performed similarly to Section 3.5.2.

The feasibility indicators for the investment in energy efficiency measures that involve investments in their implementation, as well as a series of indicators that highlight the feasibility of the proposed measures, are presented in Table 15. To emphasize the payback period of the investment, the cumulative cash flow for the 20 years considered is indicated in Figure 21.

Table 15. Feasibility indicators of the proposed measures.

Description	Unit	Value
Total investment value	EUR	773,977.22
Maintenance costs	EUR	75,943.55
Annual savings value	EUR	91,140.36
Net Present Income (NPI)	EUR	972,886.48
Discount rate	%	5
Lifespan of the solution	YEARS	20
Payback Time (PBT)	YEARS	8.49
Discounted Payback Time (DPBT)	YEARS	9.33
Internal rate of return (IRR)	%	125.70

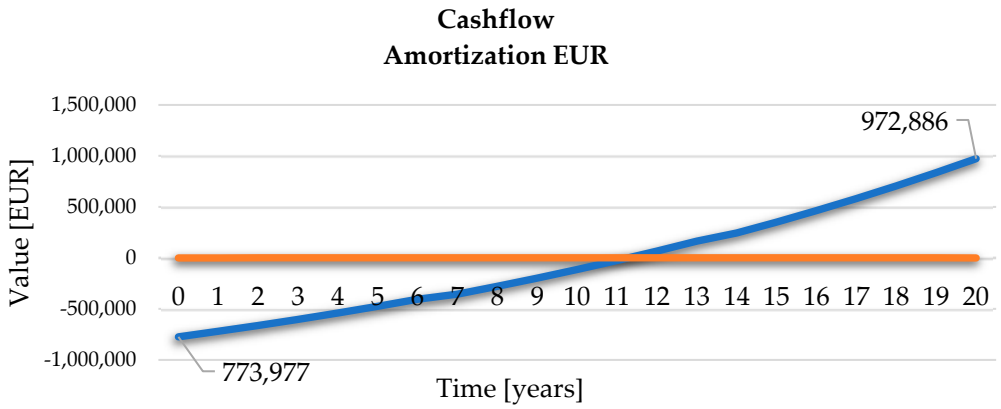


Figure 21. Cumulative cash flow for the 20 years considered—**grid-connected photovoltaic system**.

3.6.3. Quantitative and Percentage Reduction in Resulting Greenhouse Gas Emissions

The calculation for the reduction in greenhouse gases was performed similarly to Section 3.5.3. In this context, the value of greenhouse gas emissions for the first year after the implementation of the project involving the installation of a 153.90 kWp photovoltaic panel system is calculated.

GHG for the energy saved (177.33 MWh/year) will be

$$\mathbf{GHG_r = 177.40\ MWh \times 0.33\ t_{CO_2}/MWh = 58.54\ t_{CO_2}}$$

$$\mathbf{GHG_{PV} = 177.33\ MWh \times 0.33\ t_{CO_2}/MWh = 58.52\ t_{CO_2}}$$

The value of GHG1 is 0.02 t_{CO_2} after the implementation of the project:

$$\mathbf{GHG_1 = GHG_r - GHG_{PV} = 58.54\ t_{CO_2} - 58.52\ t_{CO_2} = 0.02\ t_{CO_2}}$$

The percentage value of GHG after the implementation of the project will be

$$\mathbf{GHG_{CO_2} = \frac{(GHG_r - GHG_1)}{GHG_r} \times 100 = \frac{(58.54 - 0.02)}{58.54} \times 100 = 99.97\%}$$

3.7. Analysis of HYBRID Central Photovoltaic System for Street Lighting

3.7.1. Economic Viability Analysis

The estimated value of the project for the construction of the photovoltaic power plant is EUR 1,574,660.16 including VAT are presented in Table 16.

Table 16. Implementation costs of the investment—HYBRID central photovoltaic system.

Description	Total Euro (Including VAT)
Obj. 1 Utilities—similar to grid-connected PV system	**87,076.34**
Obj. 2 Land development—similar to grid-connected PV system	**79,695.46**
Obj. 3 Photovoltaic power plant 153.90 kWp	**422,934.97**
3.1.–3.9. **Similar to grid-connected PV system**	373,524.51
3.10. Concrete platforms and containers (energy storage system)	49,410.46
Obj. 4 Video surveillance subsystem	**14,747.55**
Obj. 5 Installation of machines/equipment	**586,878.97**
5.1. Equipment	530,978.10
5.1.1. Monocrystalline photovoltaic panel 450 W (342 pieces)	103,015.46
5.1.2. 60 kW three-phase grid-connected inverter (3 pieces)	56,923.80

Table 16. *Cont.*

Description	Total Euro (Including VAT)
5.1.3. UPS 3000 VA 2U RACK	2377.98
5.1.4. Outdoor video surveillance camera (12 pieces)	1017.56
5.1.5. NVR 32 CH	703.30
5.1.6. Street lighting fixture LED 80 W	1231.57
5.1.7. Lithium-ion battery storage system B-BOX 13.80 kW (50 pieces)	365,708.44
5.2. Installation of machinery/equipment	55,900.87
TOTAL	**1,574,660.16**
TOTAL C + I	**938,978.40**

3.7.2. Calculation of Economic Efficiency

The investment feasibility indicators for energy efficiency measures that involve investments in their implementation, as well as a series of indicators highlighting the feasibility of the proposed measures, are presented in Table 17. Additionally, to emphasize the payback period of the investment, Figure 22 illustrates the cumulative cash flow for the considered 20-year period.

Table 17. Feasibility indicators of the proposed measures.

Description	Unit	Value
Total investment value	EUR	1,574,660.16
Maintenance costs	EUR	949,388.73
Annual savings value	EUR	91,140.36
Net Present Income (NPI)	EUR	−701,241.65
Discount rate	%	5
Lifespan of the solution	YEARS	20
Payback Time (PBT)	YEARS	17.28
Discounted Payback Time (DPBT)	YEARS	27.69
Internal rate of return (IRR)	%	−44.53

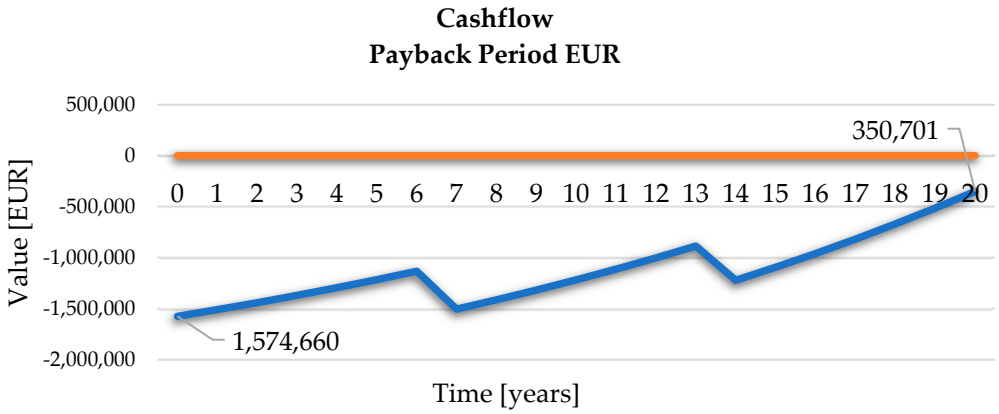


Figure 22. Cumulative cash flow for the 20 years considered—**HYBRID photovoltaic system**.

3.7.3. Quantitative and Percentage Reduction in Greenhouse Gas Emissions

The calculation for the reduction in greenhouse gases was performed similarly to Section 3.5.3. In this context, the value of greenhouse gas emissions for the first year after the implementation of the project, which involves the installation of a photovoltaic system of 153.90 kWp, is calculated.

GHG for the saved energy (177.33 MWh/year) will be

$$\mathbf{GHG_r = 177.40\ MWh \times 0.33\ t_{CO_2}/MWh = 58.54\ t_{CO_2}}$$

$$\mathbf{GHG_{PV} = 177.33\ MWh \times 0.33\ t_{CO_2}/MWh = 58.52\ t_{CO_2}}$$

The value of GHG1 is 0.02 t_{CO_2} after the implementation of the project:

$$\mathbf{GHG_1 = GHG_r - GHG_{PV} = 58.54\ t_{CO_2} - 58.52\ t_{CO_2} = 0.02\ t_{CO_2}}$$

The percentage value of GHG after the implementation of the project will be

$$\mathbf{GHG_{CO_2} = \frac{(GHG_r - GHG_1)}{GHG_r} \times 100 = \frac{(58.54 - 0.02)}{58.54} \times 100 = 99.97\%}$$

3.8. Discussion

As observed in Figure 23, the use of HYBRID photovoltaic systems for street lighting represents the least economically viable option, while the use of ON-GRID photovoltaic systems represents the most economically viable option. The economic feasibility of using autonomous photovoltaic poles is similar to that of HYBRID photovoltaic systems in the analysis conducted, but it represents the most viable option for street lighting in areas where there is no electricity network or where the existing network is very old or damaged.

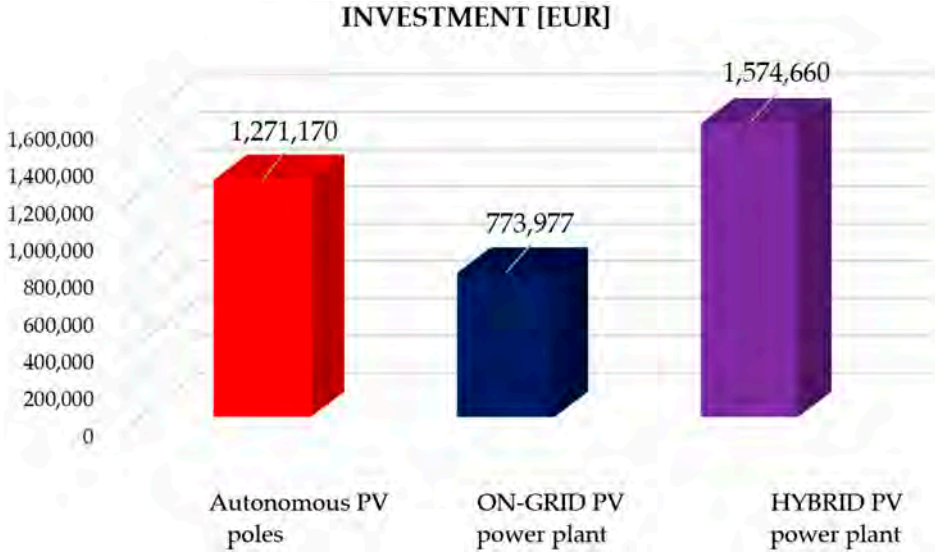


Figure 23. Comparative chart of analyzed scenarios: investment value.

The HYBRID photovoltaic power plant incurs the highest maintenance costs over the entire analysis period, including the annual washing of the photovoltaic panels and the replacement of inverters and storage systems every 7 years.

The ON-GRID photovoltaic power plant has the lowest maintenance costs throughout the analysis period, as this system does not store electrical energy. Maintenance expenses are limited to the annual washing of the photovoltaic panels and replacement of inverters every 7 years, as shown in Figure 24.

The longest payback period is for the HYBRID photovoltaic power plant, at 27.69 years, followed by autonomous photovoltaic poles with a payback period of 21.94 years. The advantage of these solutions is the storage of electrical energy in batteries to provide power for street lighting during the night, while the drawbacks are the high costs for investment and long payback periods.

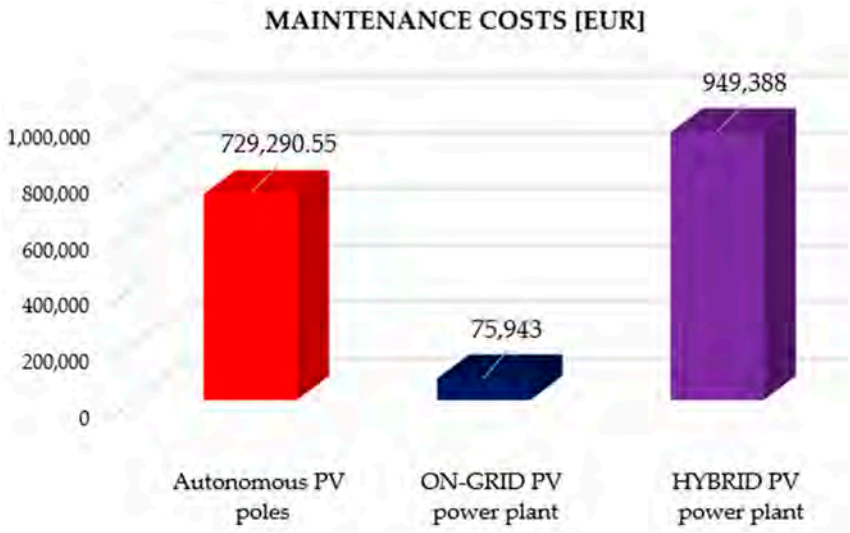


Figure 24. Comparative chart of analyzed scenarios: maintenance costs.

The ON-GRID photovoltaic power plant has the shortest payback period of 9.33 years, due to the lower costs associated with its implementation—Figure 25. However, its disadvantage lies in its dependence on the electricity grid and government programs regarding the share of renewable energy sources in the national energy system.

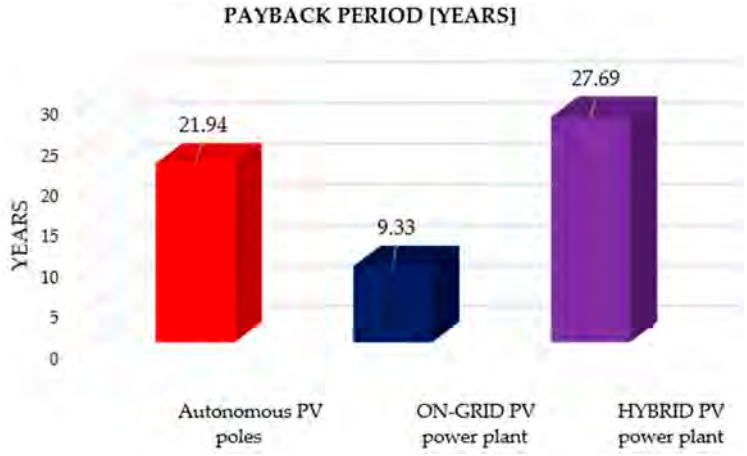


Figure 25. Comparative chart of analyzed scenarios: payback period.

By comparing expenses and revenues, taking into account the system maintenance over a 20-year period, the ON-GRID photovoltaic power plant generates a significantly higher net present value than the other analyzed systems. Figure 26 shows that the autonomous photovoltaic poles and the HYBRID photovoltaic power plant do not recoup their investment within the analysis period.

The internal rate of return indicates the efficiency of the analyzed scenarios. Figure 27 shows that the ON-GRID photovoltaic power plant represents a feasible solution, while the autonomous photovoltaic poles and the HYBRID photovoltaic power plant are not economically viable for the analyzed objective.

From a technical perspective, the deployment of photovoltaic panels requires an estimated surface area of approximately 2500 m^2. To optimize land use and minimize ecological impact, it is recommended that the PV system be installed preferentially on artificialized surfaces such as industrial rooftops, parking areas, or—where these are unavailable—on non-productive agricultural land. Furthermore, the proximity of a medium-voltage electrical network is a critical requirement for the proposed site. Such proximity ensures minimal costs associated with injecting electricity into the distribution grid. National grid

data provided by Transelectrica [8] indicate that the available connection capacity in the targeted region, identified as Zone J, is 1000 MW, thereby confirming the feasibility of integrating the PV system within existing infrastructure. In alignment with the European Union's climate and energy policy, the project also supports broader objectives by promoting energy consumption reduction measures at both enterprise and public utility levels, including street lighting. These policies incentivize the adoption of renewable energy sources through mechanisms such as quantitative compensation and financial settlement schemes for prosumers.

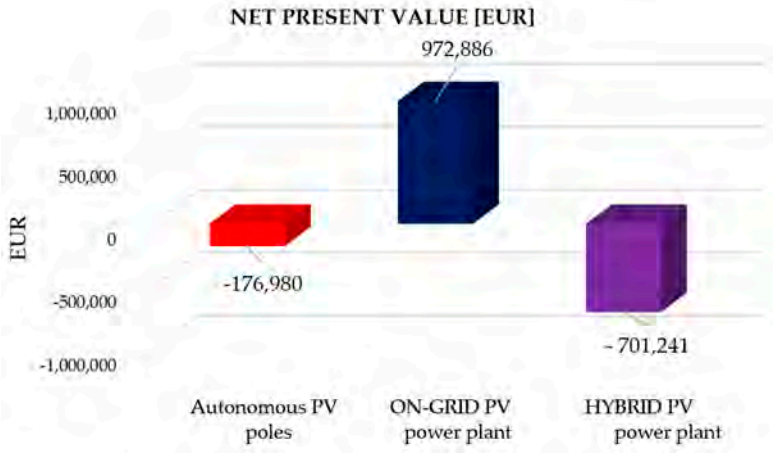


Figure 26. Comparative chart of analyzed scenarios: net present value.

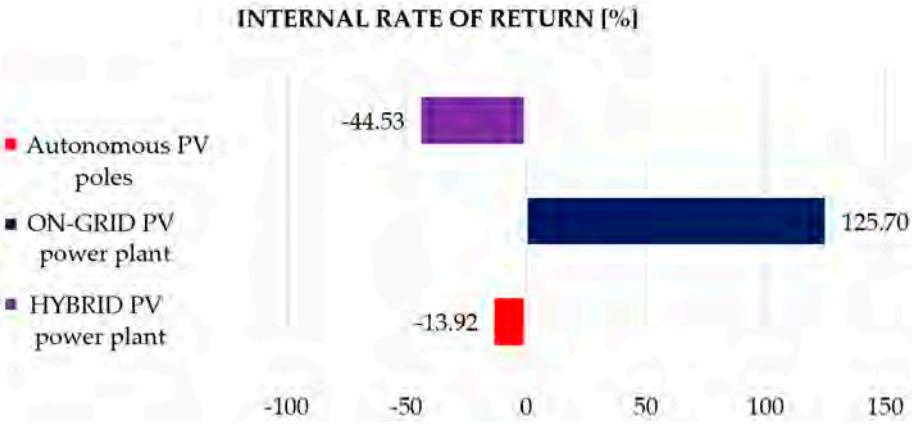


Figure 27. Comparative chart of analyzed scenarios: internal rate of return.

The adoption of PV-LED public lighting not only accelerates SDG 7 but also intersects with SDG 11 (Sustainable Cities), SDG 13 (Climate Action), and SDG 3 (Good Health and Well-Being), making it one of the most catalytic infrastructure upgrades of the coming decade.

The disadvantage of this system is its dependence on the national energy system. The electricity produced during the day is injected into the grid, and at night, through EU prosumer policy facilities, represented by quantitative compensation and financial settlement, electricity is consumed from the public electricity supply grid for street lighting. The electricity consumed from the national energy system at night is produced from the following sources: hydro, coal, nuclear, hydrocarbons, wind, and biomass [7]. From this data, we can observe that a portion of the energy is produced by burning fossil and nuclear fission fuels.

This means that by implementing this system, there is no contribution to environmental protection at night by not using fossil and nuclear fission fuels.

However, this disadvantage will be eliminated through EU policy [7]. Thus, Romania, through the National Energy Strategy 2018–2030, commits to constructing two new nuclear units and maintaining an increasing trend in production capacities from intermittent renewable sources. Also, the construction of a large-capacity pumped storage power plant is mandatory for the stability of the power system.

Economic sensitivity

Considering the long analysis period of photovoltaic systems, a sensitivity analysis of economic parameters was conducted. Therefore, the following variations in costs were considered:

- A ±20% variation in electricity price;
- A ±10% variation in annual maintenance costs.

The results highlight the influence of these parameters on the amortization. However, the main results in terms of economic efficiency remain the same, while Case 3 is close to breakeven, but still a loss. In Table 18, the following scenarios were analyzed: favorable scenario (+20% energy and −10% maintenance) and unfavorable scenario (−20% energy and +10% maintenance).

Table 18. Economic sensitivity to fluctuations in electricity pricing and maintenance costs.

Scenario	Case 1	Case 2	Case 3
Favorable scenario	2,502,428	8,873,577	−327,061
Unfavorable scenario	−773,708	4,298,485	−3,163,473

Therefore, Case 2 is the most robust to variations (positive and negative), Case 1 has high sensitivity and the risk of going into loss, and Case 3 remains economically inefficient even in the favorable scenario.

SWOT Analysis

In order to outline potential directions for the future development of similar research, a SWOT analysis was carried out on the solutions proposed in this study—Table 19. This structured assessment highlights the strengths, weaknesses, opportunities, and threats associated with the implementation of these solutions.

Table 19. SWOT analysis of the studied cases.

Aspect	Autonomous PV Poles	ON-GRID PV Power Plant	HYBRID PV System (PV + Battery + Grid Backup)
Strengths	- Full energy independence - Modular and easy to deploy - No grid connection required	- Lower cost per kWh at scale - Economically efficient for large deployments - Easier to monitor and maintain	- Combines autonomy and efficiency - Provides backup during grid outages - High resilience and flexibility
Weaknesses	- Limited storage capacity - Sensitive to adverse weather - Higher unit cost	- Fully dependent on grid availability - Requires centralized space - Potential distribution losses	- Higher upfront cost (PV + battery) - More complex to manage - Needs dual maintenance
Opportunities	- Suitable for remote/off-grid areas - Can be integrated into smart city projects - Easy to scale gradually	- Surplus energy can be fed into the grid - Eligible for support schemes (e.g., feed-in tariff, net metering) - Ideal for urban municipalities	- Suitable for unstable grid regions - Can participate in demand–response programs - Scalable and future-proof
Threats	- Battery aging and degradation - Blackout risk in poor solar conditions - Legal risk in case of failures	- Vulnerable to energy price fluctuations - Regulatory risk regarding grid injection - May face grid capacity limits	- Higher long-term costs (battery replacement) - Risk of over-engineering for small applications - More points of failure

Based on the SWOT analysis, a logic flow was developed to guide decision making regarding the optimal photovoltaic lighting system. This flow considers factors such as grid availability, reliability requirements, budget constraints, sustainability goals, and available space. The main implications reveal that OFF-GRID systems are suitable only for remote or low-priority areas due to limited reliability, ON-GRID solutions offer the best economic efficiency but rely on grid stability, while HYBRID systems provide the highest resilience

and CO_2 reduction potential, albeit at a higher cost. This structured approach supports strategic planning for sustainable public lighting infrastructure.

4. Conclusions

The implementation of an ON-GRID photovoltaic (PV) power plant specifically designed to meet the electricity demands of street lighting emerges as the optimal solution for integrating photovoltaic systems into public infrastructure. This transition in electricity generation technology is substantiated by a multidimensional analysis encompassing technical, economic, and environmental criteria.

From an economic standpoint, the analysis clearly identifies the ON-GRID PV scenario as the most cost-effective option. As illustrated in Figure 28, this solution demonstrates superior financial viability. Notably, the internal rate of return (IRR) associated with this scenario reaches 125.7%, reflecting the high economic efficiency and attractiveness of the investment.

energy systems.

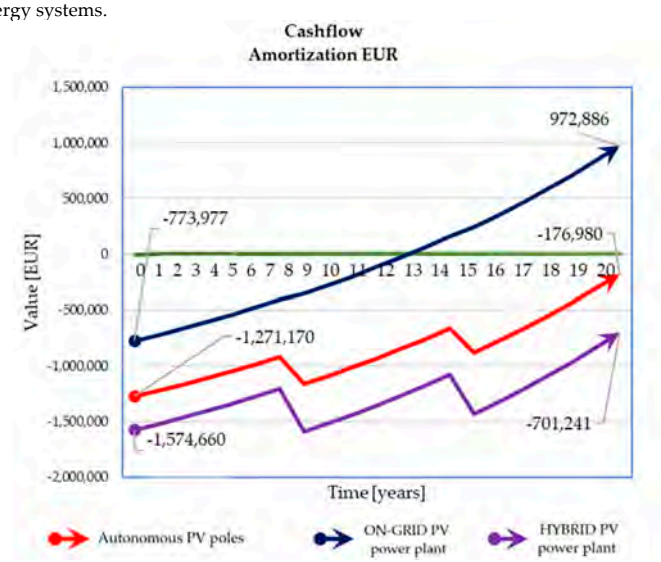


Figure 28. Comparative graph of analyzed scenarios: cash flow.

In terms of environmental impact, the current level of greenhouse gas emissions associated with electricity consumption from the grid is quantified at 58.52 metric tons of CO_2 (tCO_2), as shown in Figure 29. The implementation of the ON-GRID photovoltaic project results in a complete offset of this emission volume, achieving a reduction of 58.52 tCO_2. This translates to an emissions mitigation rate of 99.97%, thereby underlining the project's significant contribution to environmental sustainability and climate change mitigation.

The proposed ON-GRID photovoltaic solution for street lighting not only satisfies technical feasibility and economic efficiency criteria but also delivers substantial environmental benefits, positioning it as a robust and sustainable choice for modern urban energy systems.

In terms of achieving Sustainable Development Goal (SDG) 7, the present analysis makes an important contribution by studying the share of renewables in the energy mix, efficient LED luminaires, autonomous and modular energy solutions, and financial savings for municipalities. These findings highlight that PV-powered public lighting can significantly support SDG 7 by promoting clean energy access, improving energy efficiency, and enabling resilient infrastructure, especially in urban expansion zones and remote communities.

The analysis presented and the available details regarding costs allow comparisons with the situation in other geographical areas, different in terms of available solar radiation but also in terms of implementation costs.

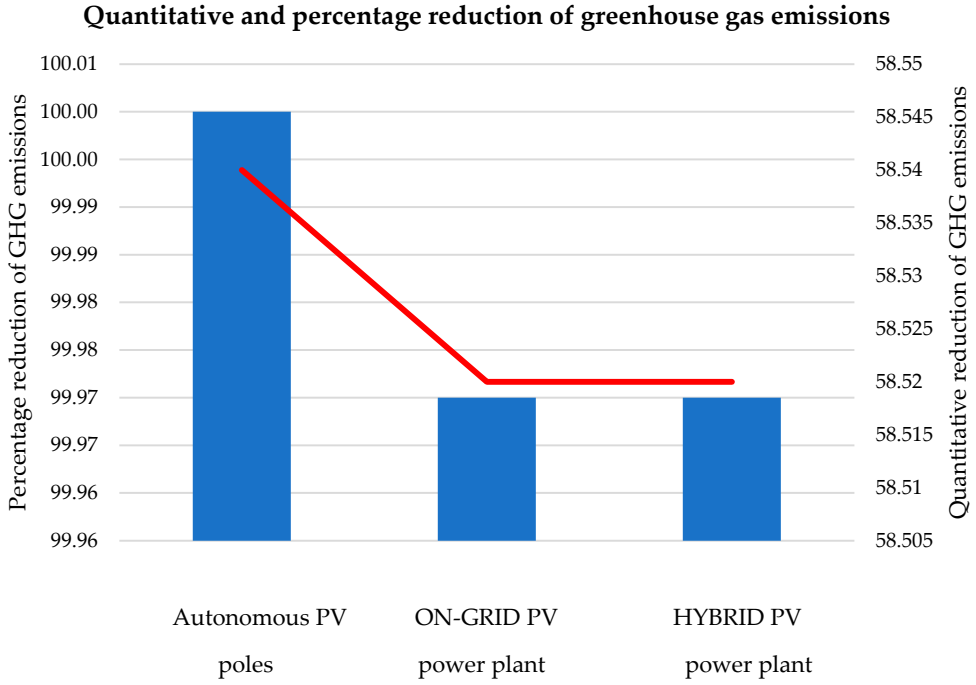


Figure 29. Comparative graph of analyzed scenarios: quantitative and percentage reduction in GHG emissions.

Further development

Building upon the results and limitations outlined in this study, several opportunities for future research and practical improvements were identified. These directions aim to enhance the applicability, accuracy, and scalability of the current work, while also addressing unresolved challenges and exploring new dimensions of the topic.

Based on opportunities, the role of a large-capacity pumped storage power plant in electricity could be a good solution to store the surplus energy produced during the day by photovoltaic and wind systems. At night, electricity is produced by high-head pumped storage hydroelectric plants, which pump water from a lower storage lake to an upper storage lake, consuming the surplus electricity produced during the day from renewable energy sources.

The technical evolution of Romania's energy sector must introduce the sixth dimension of the energy system—(6) electricity storage, alongside (1) energy sources, (2) production, (3) transmission, (4) distribution, and (5) consumption. In future studies, a broader, more global perspective could be adopted to analyze the adaptability and scalability of the proposed solutions under varying climatic and solar resource conditions.

It is not justified to implement small storage capacities for consumers but rather to implement large storage capacities that exhibit high economic efficiency, high efficiency, and contribute to the flexibility of the energy system. Electricity storage capacity is of particular importance, similar to the natural gas market. In terms of battery behavior, future studies could analyze the passive or active battery thermal management to ensure stability and an extended period of operation. Therefore, the smart lighting concept would permit solving the issues with batteries not fully loaded, coupled with an occupancy system.

The incorporation of detailed control algorithms and decision-making models for source switching and load prioritization, particularly for public lighting applications,

together with battery management are immediate directions that will be conducted in future research. Also, the carbon intensity of nighttime electricity consumption, accounting for the evolving national energy mix over time, would generate more accurate results in terms of long-term impact.

Author Contributions: Conceptualization, V.-S.H., I.N. and N.-C.C.; methodology, V.-S.H., C.-D.G. and N.-C.C.; software, V.-S.H. and I.N.; validation, V.-S.H., C.-D.G. and I.G.; formal analysis, V.-S.H. and I.H.; investigation, V.-S.H., I.N., F.-E.Ț., M.V. and I.H.; resources, V.-S.H. and I.N.; data curation, V.-S.H., F.-E.Ț., C.-D.G., I.G. and I.H.; writing—original draft preparation, V.-S.H., M.V. and I.N.; writing—review and editing, V.-S.H., N.-C.C., C.-D.G. and I.H.; visualization, V.-S.H. and I.N.; supervision, V.-S.H. and C.-D.G.; project administration, V.-S.H.; funding acquisition, V.-S.H. and M.V. All authors have read and agreed to the published version of the manuscript.

Funding: This research received no external funding.

Institutional Review Board Statement: Not applicable.

Informed Consent Statement: Not applicable.

Data Availability Statement: Data are contained within the article.

Conflicts of Interest: The authors declare no conflicts of interest.

Nomenclature

Acronyms

PNIESC	The Project of the National Integrated Plan in the Field of Energy and Climate Change
EU	European Union
LEA	Overhead Power Line
VWS	Visual Weighted Score
PV	Photovoltaic
PVGIS	Photovoltaic Geographical Information System
BMS	Building Management System
UNI	Updated Net Income
PBT	Payback Time
DPBT	Discounted Payback Time
GHG	Greenhouse Gas
IRR	Internal Rate of Return
UPS	Uninterruptible Power Supply
NVR	Network Video Recorder

Parameters

L_m	Average luminance [cd/m^2]
U_o	General luminance uniformity coefficient
U_l	Longitudinal luminance uniformity coefficient
TI	Threshold increment
R_{EI}	Lighting efficiency ratio
S	Distance between poles [m]
H	Mounting height [m]
R	Clearance [m]
A	Overhang (advancement) [m]

Appendix A

The annex contains additional information regarding the structure of autonomous systems for powering the lighting system for CR case—Table A1 and Figures A1–A3 and LR case—Table A2 and Figures A4–A6.

Table A1. The components of the autonomous photovoltaic pole—**communal road**.

Component	Parameter	Value	Quantity
Monocrystalline photovoltaic panel [55]	Nominal electrical power Nominal current Short-circuit current Nominal voltage Open circuit voltage Dimensions	300 W 9.17 A 9.78 A 32.70 V 39.80 V 1.640 × 990 × 30 mm	2 pieces
Solar regulator [56]	Maximum voltage Maximum charging current Low-voltage disconnect Reconnect Boost charging voltage Overvoltage protection Reverse polarity protection Degree of protection Size Weight	100 V 15.00 A 22.00 V 25.20 V 28.80 V Yes Yes IP32 133.50 × 70 × 35 mm 165 g	1 piece
Gel solar battery [57]	Nominal voltage Capacity Dimensions ($L \times l \times h$) Weight	12 V 120 Ah 410 × 175 × 227 mm 33.50 kg	2 pieces
LED street lighting fixture [58]	Power Nominal voltage Degree of protection LED type	60 W 24 V IP65 multiled	1 piece
Auxiliary materials [47,59–63]	Battery box IP65, connectivity, protections, conductors, metal support, brackets, and OL-Zn collars	-	-

Table A2. The components of the autonomous photovoltaic pole—**local road**.

Component	Parameter	Value	Quantity
Monocrystalline photovoltaic panel [55]	Nominal electrical power Nominal current Short-circuit current Nominal voltage Open circuit voltage Dimensions	250 W 9.33 A 9.87 A 26.80 V 32.84 V 1.350 × 880 × 35 mm	2 pieces
Solar regulator [56]	Maximum voltage Maximum charging current Low-voltage disconnect Reconnect Boost charging voltage Overvoltage protection Reverse polarity protection Degree of protection Size Weight	75 V 10.00 A 22.00 V 25.20 V 28.80 V Yes Yes IP32 133.50 × 70 × 35 mm 165 g	1 piece
Gel solar battery [57]	Nominal voltage Capacity Dimensions ($L \times l \times h$) Weight	12 V 100 Ah 330 × 171 × 224 mm 27.50 kg	2 pieces
LED street lighting fixture [58]	Power Nominal voltage Degree of protection LED type	50 W 24 V IP65 multiled	1 piece
Auxiliary materials [47,59–63]	Battery box IP65, connectivity, protections, conductors, metal support, brackets, and OL-Zn collars	-	-

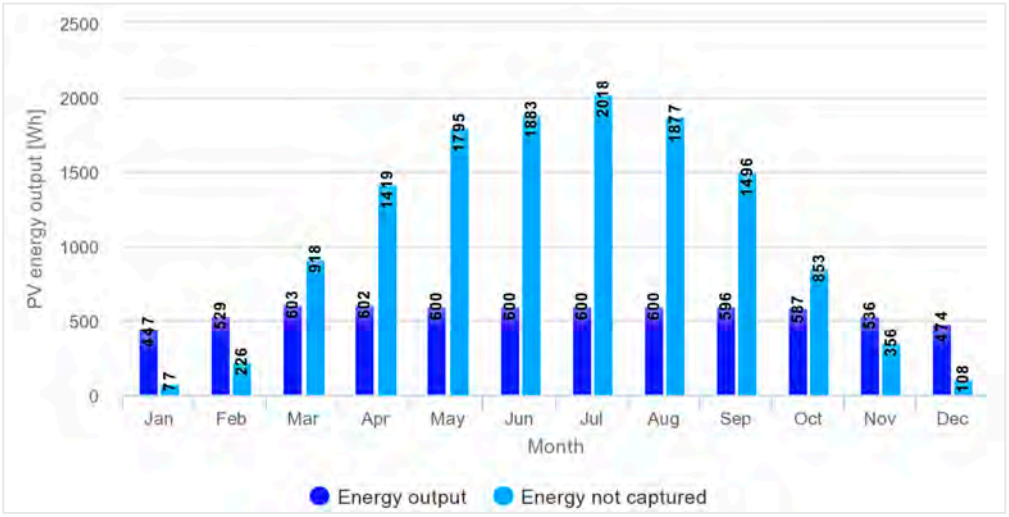


Figure A1. Estimation of energy production for the OFF-GRID photovoltaic system—CR.

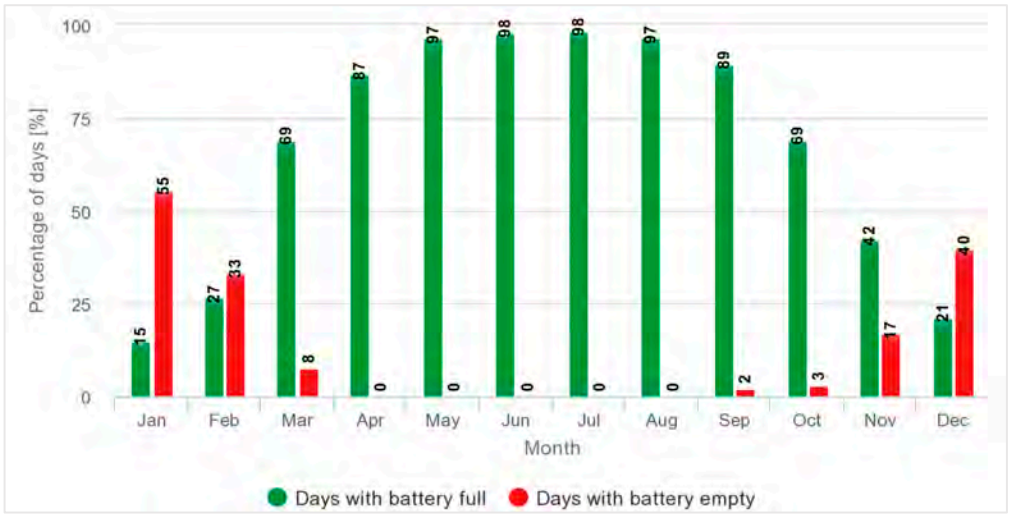


Figure A2. Battery performance for the OFF-GRID photovoltaic system—CR.

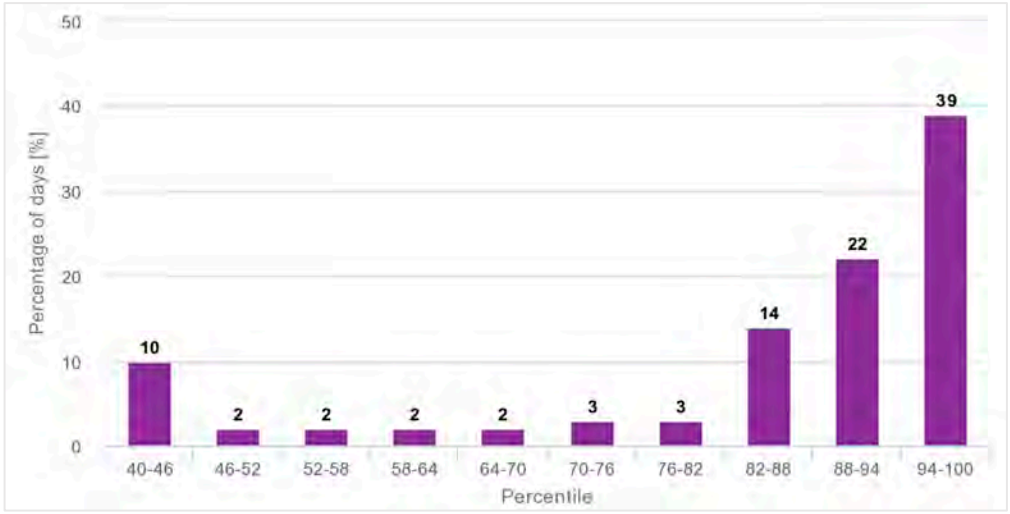


Figure A3. The battery charging percentage at the end of the day—CR.

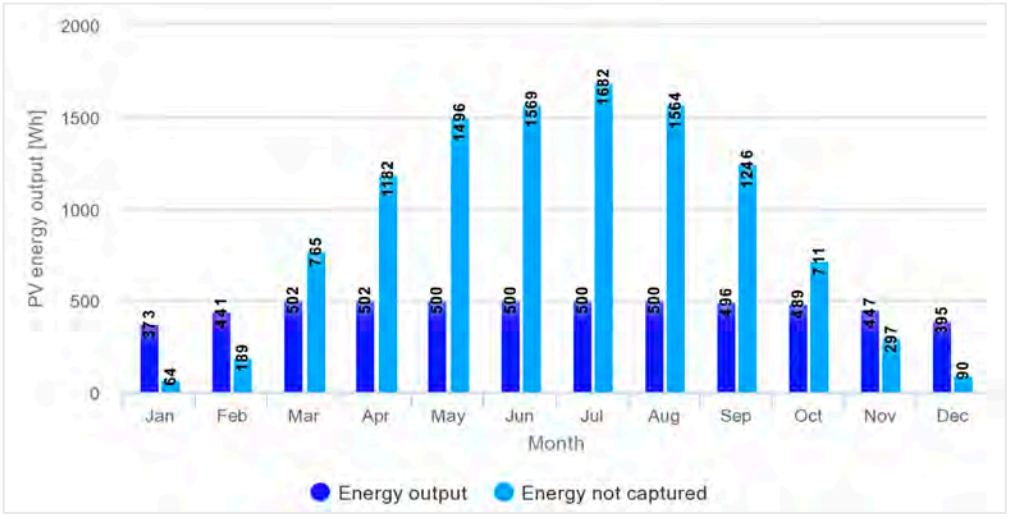


Figure A4. Estimation of energy production for the OFF-GRID photovoltaic system—LR.

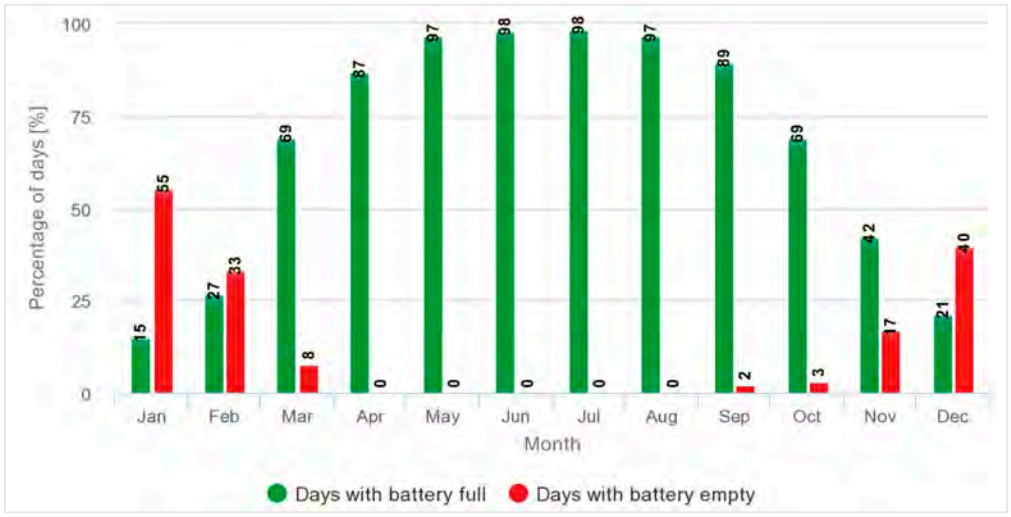


Figure A5. Battery performance for the OFF-GRID photovoltaic system—LR.

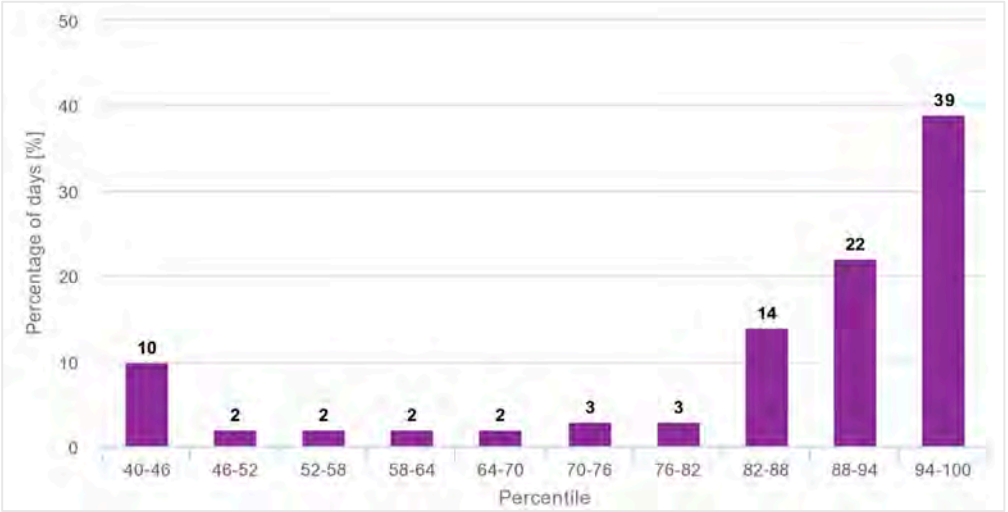


Figure A6. The battery charging percentage at the end of the day—LR.

References

1. Cumo, F.; Pennacchia, E.; Sferra, A.S. Sustainability in Public Lighting: The Methodology for Identifying Environmentally Optimal Solutions in Replacement Planning—A Case Study. *Energies* **2025**, *18*, 535. [CrossRef]
2. European Commission. Available online: https://climate.ec.europa.eu (accessed on 23 June 2025).
3. UNDP. *Sustainable Street Lighting, A Guide to Efficient Public Street Lighting for Lebanon*; UNDP-CEDRO Publication: New York, NY, USA, 2015.
4. Alboteanu, L.; Manolea, G. Photovoltaic Panels—Solutions for a Smart City (Panourile Fotovoltaice—Soluții pentru un oraș inteligent). *AGIR Bull.* **2017**, *1*, 69–75.
5. Belloni, E.; Massaccesi, A.; Moscatiello, C.; Martirano, L. Implementation of a New Solar-Powered Street Lighting System: Optimization and Technical-Economic Analysis Using Artificial Intelligence. *IEEE Access* **2024**, *12*, 46657–46667. [CrossRef]
6. Omar, A.; Almaeeni, S.; Attia, H.; Takruri, M.; Altunaiji, A.; Sanduleanu, M.; Shubair, R.; Ashhab, M.S.; al Ali, M.; al Hebsi, G. Smart City: Recent Advances in Intelligent Street Lighting Systems Based on IoT. *J. Sens.* **2022**, *2022*, 5249187. [CrossRef]
7. Ministry of Energy. *Romania's Energy Strategy 2016–2030, with a View to 2050*; Romania Ministry of Energy: Bucharest, Romania, 2016.
8. Available online: https://www.transelectrica.ro/en/web/tel/home (accessed on 23 June 2025).
9. National Energy Regulatory Authority. *Report on the Results of the Electricity Market Monitoring in December 2023*; National Energy Regulatory Authority: Ljubljana, Slovenia, 2023.
10. Sustainable Street Lighting, Brighter Cities, Brighter Future. The Conoler Series. Available online: www.econoler.com (accessed on 23 June 2025).
11. Velásquez, C.; Espín, F.; Castro, M.Á.; Rodríguez, F. Energy Efficiency in Public Lighting Systems Friendly to the Environment and Protected Areas. *Sustainability* **2024**, *16*, 5113. [CrossRef]
12. Lv, Z.; Guo, H.; Zhang, L.; Liang, D.; Zhu, Q.; Liu, X.; Zhou, H.; Liu, Y.; Gou, Y.; Dou, X.; et al. Urban public lighting classification method and analysis of energy and environmental effects based on SDGSAT-1 glimmer imager data. *Appl. Energy* **2024**, *355*, 122355. [CrossRef]
13. Molina-Moreno, V.; Utrilla, P.N.C.; Cortés-García, F.J.; Peña-García, A. The use of led technology and biomass to power public lighting in a local context: The case of baeza (Spain). *Energies* **2018**, *11*, 1783. [CrossRef]
14. Meflah, A.; Chekired, F.; Drir, N.; Canale, L. Accurate Method for Solar Power Generation Estimation for Different PV (Photovoltaic Panels) Technologies. *Resources* **2024**, *13*, 166. [CrossRef]
15. Available online: https://sdgs.un.org/goals/goal7 (accessed on 23 June 2025).
16. Sorooshian, S. The sustainable development goals of the United Nations: A comparative midterm research review. *J. Clean. Prod.* **2024**, *453*, 142272. [CrossRef]
17. Tavares, P.; Ingi, D.; Araújo, L.; Pinho, P.; Bhusal, P. Reviewing the Role of Outdoor Lighting in Achieving Sustainable Development Goals. *Sustainability* **2021**, *13*, 12657. [CrossRef]
18. Valetti, L.; Piccablotto, G.; Taraglio, R.; Pellegrino, A. Long-Term Monitoring Campaign of LED Street Lighting Systems: Focus on Photometric Performances, Maintenance and Energy Savings. *Sustainability* **2023**, *15*, 16910. [CrossRef]
19. Jettanasen, C.; Ngaopitakkul, A. Characteristics and Effects of Conducted Emission from Grid-Connected and Stand-Alone Micro-Inverters in a Nano-Grid Road Lighting System. *Sustainability* **2019**, *11*, 5690. [CrossRef]
20. Pardo-Bosch, F.; Blanco, A.; Sesé, E.; Ezcurra, F.; Pujadas, P. Sustainable strategy for the implementation of energy efficient smart public lighting in urban areas: Case study in San Sebastian. *Sustain. Cities Soc.* **2022**, *76*, 103454. [CrossRef]
21. Bian, J.; Yang, J.J. Smart Street Lighting Powered by Renewable Energy: A Multi-Criteria, Data-Driven Decision Framework. *Sustainability* **2025**, *17*, 5874. [CrossRef]
22. Canale, L.; Hamady, M. History of Artificial Lighting, from Fire to LED [History]. *IEEE Ind. Appl. Mag.* **2025**, *31*, 10–25. [CrossRef]
23. Faustino, R.; Lameirinhas, R.A.M.; Bernardo, C.P.C.V.; Torres, J.P.N.; Santos, M. Study of the application of solar cells in public lighting. *Int. J. Innov. Res. Sci. Stud.* **2025**, *8*, 543–559. [CrossRef]
24. Allery, T.A.; Martino, A.; Begay, S. Solar Street Lighting: Using Renewable Energy for Safety for the Turtle Mountain Band of Chippewa. 2018. Available online: https://www.energy.gov/sites/prod/files/2018/11/f57/Allery-2018-solar-street-lighting.pdf (accessed on 23 June 2025).
25. Ocana-Miguel, A.; Gago-Calderon, A.; Andres-Diaz, J.R. Experimental Outdoor Public Lighting Installation Powered by a Hydraulic Turbine Installed in the Municipal Water Supply Network. *Water* **2022**, *14*, 710. [CrossRef]
26. Slimene, M.B.; Arbi Khlifi, M. Modelling and study of energy storage devices for photovoltaic lighting. *Energy Explor. Exploit.* **2020**, *38*, 1932–1945. [CrossRef]
27. Zerari, H.; Messikh, L.; Kouzou, A.; Ouchtati, S. Smart energy management and monitoring system for public lighting system based on photovoltaic and storage systems. *Electroteh. Electron. Autom. (EEA)* **2021**, *69*, 5–10. [CrossRef]

28. Baburajan, S.; Amin, F.; Zarooni, A.; Osman, A. Solar-powered LED Street Lighting System Case Study-American University of Sharjah, UAE. *Saudi J. Eng. Technol.* **2017**, *2*, 49–56. [CrossRef]
29. Simanjuntak, I.U.V.; Dani, A.W.; Salamah, K.S.; Silalahi, L.M. Analysis of solar power public street lighting optimization with Pvsyst software in a residential complex area. *Int. J. Electron. Telecommun.* **2024**, *70*, 743–749. [CrossRef]
30. Junisbekov, M.; Grigoryev, D.; Tolganbayeva, M.; Turgynbekov, Y.; Omirbekova, Z. Design, Simulation, and Analysis of a Solar-Powered Street Lighting Control System for Power Consumption Prediction. *Preprints* **2024**, 2024120003. [CrossRef]
31. Wang, Q.; Jiang, B.; Li, B.; Yan, Y. A critical review of thermal management models and solutions of lithium-ion batteries for the development of pure electric vehicles. *Renew. Sustain. Energy Rev.* **2016**, *64*, 106–128. [CrossRef]
32. Kalkan, O.; Celen, A.; Bakirci, K. Experimental and numerical investigation of the LiFePO4 battery cooling by natural convection. *J. Energy Storage* **2021**, *40*, 102796. [CrossRef]
33. Orejon-Sanchez, R.D.; Andres-Diaz, J.R.; Gago-Calderon, A. Autonomous photovoltaic led urban street lighting: Technical, economic, and social viability analysis based on a case study. *Sustainability* **2021**, *13*, 11746. [CrossRef]
34. Pratama, S.G.; Namyra Alissa, R.A.D.; Nafis, R.F.; Arrayyan, A.Z.; Putra, K.T. Implementation and Feasibility Study of Solar-powered Streetlighting Systems in Rural Community Area. *E3S Web Conf.* **2023**, *425*, 05007. [CrossRef]
35. M'hamed, R.; Boussemaha, B.; Mouaadh, Y.; Youcef, H.; Mohammed, D. Low cost of smart unilateral street lighting system with photovoltaic power plant using particle swarm optimization. *Stud. Eng. Exact Sci.* **2024**, *5*, e11658. [CrossRef]
36. Liu, G. Sustainable feasibility of solar photovoltaic powered street lighting systems. *Int. J. Electr. Power Energy Syst.* **2014**, *56*, 168–174. [CrossRef]
37. Sadeghian, O.; Mohammadi-Ivatloo, B.; Oshnoei, A.; Aghaei, J. Unveiling the potential of renewable energy and battery utilization in real-world public lighting systems: A review. Renew. Sustain. *Energy Rev.* **2024**, *192*, 114241. [CrossRef]
38. Vargas-Salgado, C.; Montagud-Montalvá, C.; Alfonso-Solar, D.; Izquierdo-De-Andrés, L. Toward Carbon Neutrality: A Methodological Approach for Assessing and Mitigating Urban Emissions at the Neighborhood Level, Applied to Benicalap, Valencia. *Sustainability* **2025**, *17*, 5150. [CrossRef]
39. Duman, A.C.; Güler, Ö. Techno-economic analysis of off-grid photovoltaic LED road lighting systems: A case study for northern, central and southern regions of Turkey. *Build. Environ.* **2019**, *156*, 89–98. [CrossRef]
40. *NP 062-2002*; Norm for the Design of Road and Pedestrian Lighting Systems. MDPLA: Bucharest, Romania, 2002.
41. *EN 13201-1*; 2015 Public Lighting—Part 1. Selection of Lighting Classes. CEN: Brussels, Belgium, 2016.
42. *EN 13201-2*; 2016 Public Lighting—Part 2: Performance Requirements. CEN: Brussels, Belgium, 2016.
43. *EN 13201-3*; 2016 Public Lighting—Part 3: Calculation of Performance. CEN: Brussels, Belgium, 2016.
44. *EN 13201-4*; 2016 Public Lighting—Part 4: Methods for Measuring Photometric Performance. CEN: Brussels, Belgium, 2016.
45. *EN 13201-5*; 2016 Public Lighting—Part 5: Energy Performance Indicators. CEN: Brussels, Belgium, 2016.
46. European Union. *Directive 2003/87/EC of the European Parliament and of the Council of 13 October 2003 Establishing a Scheme for Greenhouse Gas Emission Allowance Trading Within the Community and Amending Council Directive 96/61/EC*; EU: Brussels, Belgium, 2003.
47. Ciobanu, I. Increasing Energy Efficiency in Modern PUBLIC Lighting Systems (Creșterea Eficienței Energetice în Sistemele de Iluminat Public Moderne). Ph.D. Thesis, Polytechnic University of Bucharest, Bucharest, Romania, 2022.
48. Available online: www.ro-electrice.ro (accessed on 23 June 2025).
49. *PE 136-1988*; Republican Regulation for the Rational Use of Electricity in Artificial Lighting and Domestic Uses. Ministry of Development, Public Works and Administration: Bucharest, Romania, 1988.
50. DIALux Evo. Lighting Design Software for Individual Rooms, Entire Buildings, Streets, Outdoor Areas and Emergency Lighting. Available online: https://www.dialux.com/en-GB/download (accessed on 23 June 2025).
51. ORDER No. 49 of January 27, 1998: Technical Norms Regarding the Design, Construction and Modernization of Roads. Available online: https://legislatie.just.ro/Public/DetaliiDocument/15882 (accessed on 23 June 2025).
52. Shahzad, K.; Čuček, L.; Sagir, M.; Ali, N.; Rashid, M.I.; Nazir, R.; Nizami, A.S.; Al-Turaif, H.A.; Ismail, I.M.I. An ecological feasibility study for developing sustainable street lighting system. *J. Clean. Prod.* **2018**, *175*, 683–695. [CrossRef]
53. Available online: www.energyprod.ro (accessed on 23 June 2025).
54. Photovoltaic Geographial Information System (PVGIS). Available online: https://re.jrc.ec.europa.eu (accessed on 23 June 2025).
55. Aitio, A.; Howey, D.A. Predicting battery end of life from solar off-grid system field data using machine learning. *Joule* **2021**, *5*, 3204–3220. [CrossRef]
56. Available online: www.depozitsolar.ro (accessed on 23 June 2025).
57. Skandali, C.; Zerefos, S.; Tsangrassoulis, A.; Peña-García, A.; Triantafyllidis, G.A.; Zissis, G.; Doulos, L.T. Reviewing the parameters that affect sustainability and energy efficient concepts in road and urban lighting design. *J. Clean. Prod.* **2025**, *490*, 144607. [CrossRef]

58. GEO 27-2022 Regarding the Measures Applicable to Final Customers in the Electricity and Natural Gas Market, as Well as for Amending and Supplementing Certain Normative Acts in the Energy Field. Available online: https://www.correggionet.eu/wp-content/uploads/2022/03/GEO-272022_EN.pdf (accessed on 23 June 2025).
59. Available online: www.generatoare-solare.ro (accessed on 23 June 2025).
60. European Comission. Commission Regulation (EU) No 601/2012 of 21 June 2012 on the monitoring and reporting of greenhouse gas emissions pursuant to Directive 2003/87/EC of the European Parliament and of the Council. *Off. J. Eur. Union* **2012**, *181*, 30–104.
61. Available online: www.e-acumulatori.ro (accessed on 23 June 2025).
62. Available online: www.electric14.ro (accessed on 23 June 2025).
63. Available online: www.schrack.ro (accessed on 23 June 2025).

Disclaimer/Publisher's Note: The statements, opinions and data contained in all publications are solely those of the individual author(s) and contributor(s) and not of MDPI and/or the editor(s). MDPI and/or the editor(s) disclaim responsibility for any injury to people or property resulting from any ideas, methods, instructions or products referred to in the content.

sustainability

MDPI

Article

Experimental Investigation of Wind Effect on Roof Configurations with Photovoltaic Panel Systems for Sustainable Building Design

Răzvan-Andrei Polcovnicu [1], Sebastian-Valeriu Hudișteanu [1,*], Nicolae Ţăranu [1,2,3], Dragoș Ungureanu [1,2], Marius Alexa [1], Iuliana Hudișteanu [1], Cătălin Onuțu [1] and Alexandru-Florin Mustiață [1]

[1] Faculty of Civil Engineering and Building Services, Technical University "Gheorghe Asachi" of Iasi, 67 Prof. D. Mangeron, 700050 Iasi, Romania; razvan-andrei.polcovnicu@student.tuiasi.ro (R.-A.P.); nicolae.taranu@academic.tuiasi.ro (N.Ţ.); dragos.ungureanu@academic.tuiasi.ro (D.U.); marius.alexa@student.tuiasi.ro (M.A.); iuliana.hudisteanu@academic.tuiasi.ro (I.H.); catalin.onutu@academic.tuiasi.ro (C.O.); alexandru-florin.mustiata@student.tuiasi.ro (A.-F.M.)
[2] The Academy of Romanian Scientists, 3 Ilfov Street, Sector 5, 050663 Bucharest, Romania
[3] Technical Sciences Academy of Romania, 26 Dacia Blvd., 030167 Bucharest, Romania
* Correspondence: valeriu-sebastian.hudisteanu@academic.tuiasi.ro

Abstract: This study investigates the aerodynamic behavior of roof structures under wind-induced forces, focusing on buildings equipped with photovoltaic panels. Experimental data were obtained through wind tunnel testing of three 1:100 scale models, each representing a distinct roof geometry: gabled, hipped, and multi-pitched. Measurements of dynamic pressure and pressure coefficients were conducted for various wind incidence angles, ranging from 0° to ±150°. The results highlight the impact of roof geometry and PV panel placement on the pressure distribution, with notable variations due to flow separation and vortex formation around the panels. Gabled roofs exhibited pronounced pressure gradients, while hipped roofs showed more uniform distributions. Multi-pitched roofs demonstrated the most complex aerodynamic behavior due to their variable slopes. These findings enhance the understanding of wind-structure interactions for buildings with roof photovoltaic panels, contributing to the development of more resilient and energy-efficient structures. The research supports sustainable construction practices by improving wind load predictions and informing design decisions that promote the safe integration of renewable energy systems into the built environment.

Keywords: wind-structure interaction; photovoltaic panels; sustainable building design; renewable energy integration; roof aerodynamics; wind loads

check for updates

Academic Editor: Yuanda Cheng

Received: 16 April 2025
Revised: 16 May 2025
Accepted: 20 May 2025
Published: 21 May 2025

Citation: Polcovnicu, R.-A.; Hudișteanu, S.-V.; Țăranu, N.; Ungureanu, D.; Alexa, M.; Hudișteanu, I.; Onuțu, C.; Mustiață, A.-F. Experimental Investigation of Wind Effect on Roof Configurations with Photovoltaic Panel Systems for Sustainable Building Design. *Sustainability* **2025**, *17*, 4739. https://doi.org/10.3390/su17104739

Copyright: © 2025 by the authors. Licensee MDPI, Basel, Switzerland. This article is an open access article distributed under the terms and conditions of the Creative Commons Attribution (CC BY) license (https://creativecommons.org/licenses/by/4.0/).

1. Introduction

The integration of rooftop photovoltaic (PV) panel systems has become increasingly prevalent as the global energy sector shifts toward renewable sources. Rooftops of existing and newly constructed buildings provide a practical platform for implementing solar energy systems, optimizing otherwise underutilized surfaces. For pitched roofs, especially on existing structures, stand-off mounting methods are widely used, where PV modules are installed above the roof surface using structural supports [1,2]. However, these systems introduce significant aerodynamic complexity, which remains insufficiently explored in current literature.

Recent studies have shown that rooftop-mounted PV panels are highly susceptible to wind-induced loads, particularly uplift and suction forces, which can threaten their

structural integrity during high wind events [3–5]. Experimental and numerical investigations emphasize that the presence of PV panels modifies the boundary layer flow, promotes vortex formation, and alters pressure distributions, especially near panel edges and roof eaves [6–8]. Wind tunnel studies [9–12] have demonstrated that peak pressure coefficients on tilted PV panels can significantly exceed those on bare roofs, raising critical design concerns.

Previous studies [6,10] identified substantial pressure variations caused by rooftop PV installations, particularly at roof edges and panel corners. Our results confirm these observations by showing that peak uplift forces tend to occur near the rear edges of panels on pitched and complex roofs. Moreover, the experimental data reinforce conclusions drawn by Aly and Rone [9], who reported that tilted panel installations intensify aerodynamic loading due to flow separation. Despite the growing number of studies in this domain [13], comprehensive comparative analyses between various roof geometries under consistent experimental conditions remain scarce. This gap hinders the development of standardized design solutions for PV systems on complex rooftops.

Understanding the wind behavior around rooftop PV systems is essential for their safe and reliable deployment. Wind loads not only impact structural safety but also influence panel lifespan, energy performance, and long-term maintenance costs. Current design standards, such as Eurocode 1 and ASCE 7-22, provide general guidance for wind actions on structures but often lack detailed prescriptions for roof-mounted PV arrays, especially on non-flat or irregular roofs [14].

Furthermore, lightweight building structures—frequently used in residential and modular construction—are particularly vulnerable to wind uplift when PV systems are installed. This underscores the importance of accurately quantifying pressure coefficients for varied roof geometries to improve resilience under extreme wind events [15].

This study contributes to sustainable construction practices by providing experimental data that improve the safety, resilience, and performance of rooftop PV systems. The results are relevant for engineers and designers aiming to create buildings that are both energy-efficient and structurally robust, aligning with the goals of climate-resilient and sustainable urban development.

The novelty of this research lies in the experimental investigation of three distinct roof geometries—gable, hip, and multi-pitched—each equipped with PV panel systems, tested under consistent wind tunnel conditions. By capturing pressure distributions at various wind incidence angles, the study offers new insights into complex wind-structure interactions specific to PV-equipped sloped roofs.

The main objective of this work is to analyze and compare dynamic pressure coefficients on different pitched roof configurations with PV systems, thereby improving wind load estimation and informing safer, more efficient rooftop solar designs.

2. Theoretical Background and Basis for Calculations

2.1. Fundamental Equations for Wind Pressure Analysis

Dynamic pressure represents the kinetic energy per unit volume of wind and is essential for understanding the forces exerted on a surface. It plays a crucial role in structural engineering by estimating the wind loads acting on building components such as roofs, facades, and walls [16].

$$p_d = 0.5\ \rho\ v^2 \quad (1)$$

where p_d represents the dynamic pressure [Pa], ρ denotes the air density [kg/m^3] (Air density can be considered 1225 kg/m^3 in standard conditions), and v is the wind velocity [m/s].

To account for variations in pressure distribution across different roof geometries, dynamic pressure coefficients are employed. These dimensionless coefficients express the ratio of actual wind pressure on a surface to the reference dynamic pressure [17]:

$$c_v = \frac{p}{p_d} \tag{2}$$

where c_v characterizes the dynamic pressure coefficient, p is the wind pressure on a given surface [Pa], and p_d represents the reference dynamic pressure [Pa].

Pressure coefficients provide a fundamental means of assessing wind-induced loads and are highly sensitive to factors such as roof geometry, surface roughness, and orientation relative to wind direction [18].

2.2. Aerodynamic Principles of Wind-Structure Interaction

A deeper understanding of wind-structure interactions, particularly for roofs with externally mounted PV panels, requires consideration of key aerodynamic principles. One of the most fundamental is Bernoulli's principle, which states that within a steady, incompressible flow, an increase in wind velocity results in a decrease in pressure. This principle helps explain how variations in wind speed across a roof surface generate pressure differentials [7].

When wind encounters obstacles such as roofs or photovoltaic panels, the airflow tends to separate from the surface, creating turbulence and vortices [19]. These phenomena cause significant pressure variations, especially in the wake regions behind the panels, which can influence both structural integrity and performance [18].

Additionally, the boundary layer, defined as the thin region of air near the roof surface where viscous effects are significant, is affected by the presence of PV panels. These panels alter the characteristics of the boundary layer, increasing turbulence and modifying wind speed and pressure distribution on the surface [9].

The turbulence and wake effects caused by PV installations are further intensified by increased surface roughness. Panel tilt angle, orientation, and arrangement influence wake dynamics, generating non-uniform aerodynamic behavior across the roof and contributing to complex and asymmetric pressure distributions [10].

2.3. Effect of Roof Geometry on Wind Pressure Distribution

Roof geometry significantly influences how dynamic pressure is distributed on a building's surface. Traditional aerodynamic models typically classify roofs as either flat or pitched, with pressure coefficients obtained through experimental data. However, the introduction of photovoltaic panels complicates these models by introducing additional airflow disturbances that affect the aerodynamic response.

For flat roofs, wind tends to impact the surface perpendicularly, resulting in a relatively uniform pressure field. However, the addition of PV panels alters this behavior by creating localized flow disturbances. These disruptions lead to pressure variations, particularly on the leeward side of the panels, where turbulence develops and suction forces may increase [6,20].

In the case of pitched roofs, both the angle of inclination and the wind direction play major roles in determining how pressure is distributed along the windward and leeward faces. The installation of PV panels on such roofs further complicates airflow behavior by enhancing turbulence and modifying the existing pressure patterns. Variables such as panel tilt, spacing, and alignment relative to the roof slope can either amplify or mitigate these aerodynamic effects [10].

Understanding these effects is very important, especially for lightweight roofs, which are more prone to failure under unbalanced uplift forces.

2.4. Empirical Models and Experimental Data

Empirical models estimate dynamic pressure coefficients based on wind tunnel experiments and real-world data. These models incorporate variables such as roof geometry, wind direction, and surface roughness to approximate wind forces. However, existing models primarily focus on standard roof designs and often overlook complexities introduced by PV panels [21].

Wind tunnel experiments remain essential in refining empirical models. By simulating different wind conditions and measuring resulting pressures on various roof and PV configurations, researchers improve pressure coefficient accuracy. These studies enhance structural load predictions, leading to more reliable design methodologies [10,22,23]. Despite these advancements, empirical models still lack calibration for PV-equipped pitched roofs, creating uncertainty in load estimation.

2.5. Implications for Structural Design

The theoretical aspects discussed have significant implications for designing buildings with externally mounted PV panels. The aerodynamic alterations introduced by PV systems require new design standards that account for these changes. Accurate wind pressure prediction is essential for ensuring roof structural integrity while optimizing energy performance [24].

A thorough understanding of wind behavior around PV-equipped roofs enables engineers to develop more resilient structures that withstand wind forces while maintaining long-term sustainability. The presence of PV panels on building roofs presents both challenges and opportunities, requiring an advanced theoretical framework based on fluid dynamics, aerodynamic drag, and empirical data to inform future research and design advancements [25,26].

However, both Eurocode 1 [14] and ASCE 7-22 [27] provide only general guidance for wind loads on building surfaces and lack specific criteria for pitched roofs with elevated PV systems. This absence leads to uncertainty in design, especially when accounting for complex geometries and varying panel tilt angles. Recent critiques in the literature also highlight that the conservative simplifications used in current codes may result in either underestimation or overestimation of actual uplift forces [9,21]. This reinforces the need for wind tunnel data under controlled conditions to supplement existing code provisions.

3. Experimental Setup and Measurement Methodology

The experiments conducted in this study to determine the dynamic pressure coefficients and dynamic pressures on rigid roof models with photovoltaic panel systems were carried out in the Building Aerodynamics Laboratory, part of the Department of Civil and Industrial Construction at the Faculty of Civil Engineering and Installations, "Gheorghe Asachi" Technical University of Iași (Figure 1). To perform the experiment and evaluate the predefined parameters, including measuring the velocities and average pressures necessary to determine the mean pressure coefficients on the studied models, the following specialized equipment, shown in Figure 2, was used: an anemometer, TESTO 435 digital anemometer, hot-wire anemometric probes from TSI Incorporated, headquartered in Shoreview, Minnesota, differential micromanometer, Pitot tube, pressure taps and connecting tubes, and an alcohol manometer.



Figure 1. The wind tunnel at the Building Aerodynamics Laboratory, "Gheorghe Asachi" Technical University of Iași.



(**a**) (**b**) (**c**)

Figure 2. Instruments used for measurements in the wind tunnel: (**a**) pressure sensor plate and connecting tubes; (**b**) Pitot tube; (**c**) digital anemometer.

The measurement of fluctuating pressures on rigid models, which allows for the determination of mean values, peak pressure coefficients, and standard deviations, was conducted using the specialized experimental equipment illustrated in Figure 2. To capture and store the data obtained during testing, a combination of software tools was employed. LABVIEW and LABWINDOWS were used for data acquisition and processing, generating files with the .DAT extension compatible with DOS-WINDOWS operating systems. Subsequently, dedicated programs were utilized to convert these files into binary format (.BIN) and to perform corrections and statistical analysis on the recorded data. All instruments and procedures were selected based on international wind engineering best practices and in line with recommendations from EN 1991-1-4 [14] and relevant aerodynamic testing protocols [28].

3.1. Local Pressure Measurement Protocol

The pressure measurement approach followed established methods commonly used in wind tunnel testing of architectural models [14,28]. Where applicable, standard relationships and calibration steps were applied to ensure reproducibility and accuracy. In the aerodynamic tunnel, static and total pressures are measured using a Pitot tube, which is securely positioned in the direction of airflow. This setup enables the accurate determination of the reference wind velocity, a key parameter in the evaluation of dynamic pressure. The appropriate height for taking pressure and velocity measurements is selected based on the

geometric proportions of the model being tested, ensuring that the Pitot tube is aligned with the model's effective reference height.

Once positioned, the Pitot tube provides direct readings for both the total pressure (p_{t0}) and the static pressure (p_{s0}) at the reference point. With these values, the dynamic pressure (p_{d0}) is calculated as the difference between total and static pressure, as expressed by the following relation [14]:

$$p_{d0} = p_{t0} - p_{s0} \tag{3}$$

The pressures on the surface of the models were measured using pressure transducers, positioned according to the principle of systems that collect data from multiple pressure ports. The pressure changes applied to both sides of the transducer membrane are detected electrically, using capacitive or inductive methods, or through micro-comparators. The transducers used in the aerodynamic tunnel on models are connected via a system of tubes to the pressure ports.

The process of installing and measuring local pressures on the wind-exposed surface of the model begins with the mounting of the pressure transducer. This device is affixed to the model's surface, oriented perpendicularly to the direction of wind flow to accurately capture pressure fluctuations. The installation height is selected based on the mean velocity profile corresponding to the simulated atmospheric boundary layer, ensuring consistent reference conditions across all measurements. The transducer placed at this position provides reference data essential for interpreting the pressure distribution.

Following installation, the terminals of the pressure transducers are connected to the terminal block of the data acquisition board, as illustrated in Figure 3. This setup allows for the synchronized signal transmission from the pressure taps to the recording system, enabling precise tracking of aerodynamic effects during testing.

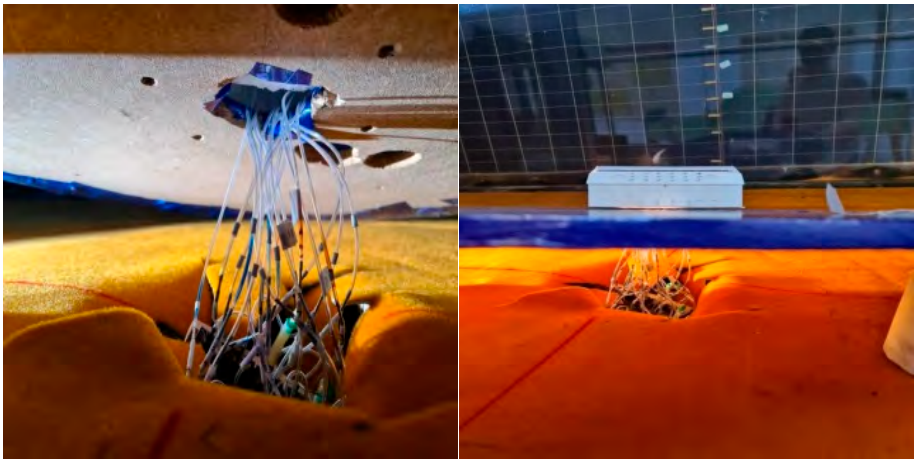


Figure 3. Recording circuit: data acquisition board—pressure transducers—model.

The data acquisition board is connected to a computer system to facilitate the digital recording of measured values. The recording and monitoring process is managed using LABVIEW Signal Express software, which enables real-time data visualization, storage, and subsequent processing.

Local pressure measurements obtained at various points on the surface of the model—denoted as point i—are used to compute the corresponding local aerodynamic coefficients. These are expressed through the following relation [9]:

$$c_{p_i} = \frac{p_i - p_s}{p_t - p_s} \tag{4}$$

where c_{p_i} represents the dynamic pressure coefficient at point i, p_i is the measured dynamic pressure at point i on the tested model [Pa], p_s is the static pressure [Pa], and p_t is the reference total pressure measured in the airflow region [Pa].

This dimensionless coefficient provides a normalized measure of wind-induced pressure relative to the reference dynamic conditions, offering a basis for comparing aerodynamic behavior across different roof geometries.

To ensure the accuracy of the recorded data, two preliminary correction procedures were conducted before initiating the actual measurements. The first correction involved measuring the pressure using a Pitot tube positioned at the reference height, upstream of the model. This step provided initial values for total pressure (p_{t1}) and static pressure (p_{s1}), establishing a baseline for the airflow conditions within the tunnel.

In the second step, the total pressure was measured again at the same reference height, but this time at the precise location where the model would be placed, while the model itself was absent. This measurement yielded a second pair of values, namely p_{t0} for total pressure and p_{s0} for static pressure, representing the undisturbed airflow conditions at the intended test location. These values served as calibration references to correct for any spatial variability in pressure within the wind tunnel.

These correction steps are crucial to compensate for potential variations in the measurement environment and to ensure the accuracy and reliability of the data obtained during the experiment.

Although, in theory, static pressure should remain constant, in practice, small differences are observed in the wind tunnel along the airflow direction. To correct these discrepancies and ensure data coherence, correction factors are determined in accordance with the specifications provided. This is done by applying relations (5) and (6) [21]:

$$\Delta c_{ps} = \frac{p_{s1} - p_{s0}}{p_{t0} - p_{s0}} \tag{5}$$

where Δc_{ps} represents the differential correction for static pressure, p_{s1} is the static pressure measured at a point in the wind tunnel [Pa], p_{s0} is the reference static pressure [Pa], and p_{t0} is the reference total pressure [Pa] [21].

$$\gamma = \frac{p_{t0} - p_{s0}}{p_{t1} - p_{s1}} \tag{6}$$

where γ is the correction factor, p_{t1} represents the total pressure measured at a point in the tunnel [Pa], p_{s1} is the static pressure measured at the same point [Pa].

The corrections can be integrated directly into the aerodynamic coefficients according to the relation (7) [29]:

$$c_{pi} = \frac{1}{\gamma} \cdot \frac{p_i - p_{s1}}{p_{t1} - p_{s1}} + \Delta c_{ps} \tag{7}$$

where c_{pi} is the corrected pressure coefficient, p_i represents the pressure measured at the point of interest [Pa], and Δc_{ps} is the differential correction of the static pressure.

Before beginning the actual test sequence, each sensor's signal output was individually verified using a manual air pump. This verification ensured that all sensors and pressure transducers responded correctly to sudden variations in pressure, confirming their operational sensitivity and the absence of signal lag or faults in the system.

Following this verification step, the Pitot tube was securely mounted in its designated position within the wind tunnel and connected to the pressure transducers. With the system fully assembled, instantaneous pressure values generated by the wind at a specific point k on the model's surface were recorded over a given time interval t. These measurements enabled the calculation of local aerodynamic coefficients at each point, based on the cor-

responding reference pressure values. The reference pressure was determined using the established reference wind speed, in accordance with applicable aerodynamic standards.

The aerodynamic coefficients obtained through this process are statistical in nature, representing time-averaged quantities that characterize the wind's interaction with the model surface. These values are essential for evaluating pressure distributions and aerodynamic loads across the roof configurations tested. These procedures were followed uniformly for all tested configurations to ensure consistency and allow comparative analysis across the roof geometries.

The mean value of the pressure coefficient at a given point k on the surface of the model was determined using the time-averaged pressure measured during the test interval. This average value, denoted as $\overline{c}_{p_k}$, is calculated according to Equation (8), which relates the mean pressure to the dynamic pressure derived from the reference wind speed [10]:

$$\overline{c}_{p_k} = \frac{\overline{p}_k}{\frac{1}{2} \cdot \rho \cdot \overline{u}_{ref}^2} \tag{8}$$

where $\overline{c}_{p_k}$ represents the mean pressure coefficient, $\overline{p}_k$ is the mean pressure at point k [Pa], ρ defines the air density [kg/m^3], and $\overline{u}_{ref}$ characterizes the reference average wind speed [m/s].

The standard deviation of the pressure coefficient, also referred to as the root mean square of the pressure fluctuations, is calculated using Equation (9). This parameter quantifies the magnitude of pressure variation around the mean value at point k, providing insight into the unsteady aerodynamic behavior at that location [10]:

$$\left(c'_p\right)_k = \frac{\sqrt{\overline{(p_k(t) - \overline{p}_k)^2}}}{\frac{1}{2}\rho \cdot \overline{u}_{ref}^2} \tag{9}$$

where $\left(c'_p\right)_k$ is the standard deviation of the pressure coefficient, $p_k(t)$ expresses the instantaneous pressure measured at point k at time t [Pa], and $\overline{p}_k$ characterizes the mean pressure at point k [Pa].

The experimental procedure began with the careful positioning of the model on the rotating platform inside the wind tunnel. Initially, the model was oriented perpendicularly to the airflow to ensure uniform exposure across its surface. Once the setup was verified, the access door of the wind tunnel was closed and securely fastened to eliminate any external disturbances during the test.

Before activating the motor, an initial set of pressure readings was taken at each pressure tap while the wind speed was set to zero. This baseline measurement established a reference point for subsequent dynamic comparisons. Following this step, the electric motor was gradually powered up, and the airflow velocity was increased in controlled increments—typically between 1 and 2 m/s—until the predetermined test speed was reached.

Once steady-state conditions were achieved, the data acquisition system was activated, and pressure values at all ports were recorded at a high sampling frequency. The first complete set of fluctuating pressure data was captured over a defined interval, generally lasting 30 s, and stored for later analysis and interpretation.

Subsequently, the model was repositioned on the rotating platform to simulate different wind incidence angles. For each new orientation, a fresh series of pressure measurements was recorded, allowing the researchers to evaluate variations in pressure distribution due to changes in wind direction.

Following the completion of the testing sequence, the motor speed was gradually reduced until the wind tunnel came to a complete stop, thereby marking the end of the experiment.

3.2. Data Acquisition and Processing Procedure

The data collected from the pressure taps were statistically processed using established signal analysis techniques adapted from Bendat and Piersol [23], ensuring accurate calculation of mean values and dynamic pressure coefficients. To process the data obtained from the laboratory tests conducted in the wind tunnel, a structured methodology was applied, involving several distinct stages. The total number of pressure taps installed on the three roof models—M_1, M_2, and M_3—was denoted by k, ranging from 1 to 19, including the Pitot tube channel.

At time zero, with the wind tunnel motor turned off and wind speed set to zero, the signal was collected from all pressure taps and the Pitot tube. For each pressure tap k, the signal was recorded over a time interval T of 30 s, resulting in 30,000 samples denoted as $u^i_{k1}, \ldots, u^i_{k30,000}$. Later, at a time t_i, with the wind speed increased to a predefined testing level, the signal from each pressure tap on the models was recorded again over the same 30 s interval, generating a new set of 30,000 samples: u_{km}, where $k = 1 \ldots 30{,}000$ and $m = 1 \ldots 30{,}000$.

To correct the raw data, the mean offset for each pressure tap was first calculated using Equation (10) [28]:

$$\overline{u}^o_k = \frac{\left(\overline{u}^1_k + \ldots + \overline{u}^{30,000}_k\right)}{30,000} \tag{10}$$

Subsequently, the corrected signal values were obtained by subtracting this mean offset from the corresponding measurement taken during motor operation at the test speed, as shown in Equation (11) [28]:

$$u^{cor}_{km} = u_{km} - \overline{u}^o_k \tag{11}$$

Once the corrected signal values were established, statistical analysis was performed to derive the relevant parameters. The first step involved calculating the arithmetic mean of the measured values for each pressure tap using the following expression [28]:

$$\overline{X} = \frac{\sum_{i=1}^{n} x_i}{n} \tag{12}$$

where $\overline{X}$ is the arithmetic mean, x_i denotes the individual measured values, and n represents the total number of values.

Next, the sample standard deviation (mean square deviation) was computed to quantify the variability of the pressure data. This was done according to Equation (13) [28]:

$$s = \pm\sqrt{\frac{\sum_{i=1}^{n}\left(x_i - \overline{X}\right)^2}{(n-1)}} \tag{13}$$

The standard error of the mean, which estimates the uncertainty in the sample mean, was then determined using Equation (14) [28]:

$$s_r = \pm\frac{s}{\sqrt{n}} \tag{14}$$

To evaluate the relative variability of the dataset, the coefficient of variation was calculated, as defined by Equation (15) [28]:

$$V = \frac{s}{\overline{X}} \times 100 \tag{15}$$

A small value of V indicates low variability and a consistent dataset, while a large V points to greater dispersion in the measured data.

The test precision index, used to express the precision of repeated measurements as a percentage, was computed using Equation (16) [28]:

$$p = \frac{2s_r}{\overline{X}} \times 100 \tag{16}$$

Finally, after applying all the above computations, the corrected final value of the measured parameter at each tap and for each test configuration was determined using the following relation [28]:

$$x = \overline{X} - s_r \tag{17}$$

3.3. Scaling and Dimensional Analysis

To ensure that the results obtained in the wind tunnel can be meaningfully applied to real-life buildings, the principle of similarity was respected in terms of geometry (1:100 scale) and flow behavior (using dimensionless parameters such as pressure coefficients). Although it was not feasible to match the Reynolds number exactly due to laboratory limitations, the flow regime remained within an acceptable range to preserve key aerodynamic features like separation and vortex formation.

Importantly, pressure coefficients, being non-dimensional quantities, allow direct extrapolation to full-scale conditions. This means that while absolute pressure values differ at full scale, the aerodynamic trends and relative distributions remain valid.

Nonetheless, it must be acknowledged that certain aspects of natural wind, such as large-scale turbulence, gust effects, and transient flow features, are not fully replicated in a wind tunnel. These limitations imply that further validation, for example through full-scale testing or CFD simulations, would strengthen the generalizability of the findings. While absolute values may differ at full scale, the use of non-dimensional pressure coefficients ensures the transferability of aerodynamic behavior trends across scales, making the experimental findings applicable for practical design scenarios.

4. Results and Discussion: Aerodynamic Behavior of PV-Equipped Roof Configurations

The experimental program was carried out in the Wind Engineering Laboratory at the Faculty of Civil Engineering and Building Services, using three scaled roof models (1:100) representing different architectural geometries. A wind tunnel with a turbulent boundary layer was used to replicate realistic wind conditions. Each model was tested under 12 different wind incidence angles ranging from -150° to $+180^\circ$, at a reference wind speed of 7.95 m/s. Each test lasted 30 s, during which 30,000 data samples were collected at a frequency of 1000 Hz. A total of 36 tests were conducted—12 per model—ensuring consistent boundary conditions and measurement protocols.

The following sections detail the objectives, instrumentation, setup procedures, and analysis of the aerodynamic response of each roof configuration equipped with photovoltaic panels.

4.1. Research Objectives

The primary goal of this study is to quantify and compare wind-induced dynamic pressure coefficients on different sloped roof types equipped with PV systems, based on wind tunnel testing. For each model, dynamic pressure measurements were taken at various wind incidence angles, including 0°, 30°, 60°, 90°, 120°, 150°, 180°, -30°, -60°, -90°, -120°, and -150° relative to the main wind direction. These measurements allowed for the determination of pressure coefficients specific to each incidence angle, thus contributing to the understanding of the aerodynamic behavior of the roofs. A detailed

analysis of the collected data revealed how the airflow interacts with the varied geometry of the roofs, highlighting differences in pressure distribution depending on the structure and the roof type.

The objective was to determine the dynamic pressure coefficients and dynamic pressures at different roof types, measured under the established experimental conditions. Furthermore, the aim was to establish correlations between the experimental results and values determined according to current standards. This comparison was crucial for validating the experimental methodologies used and providing a solid foundation for assessing the aerodynamic behavior of the roofs.

These data are important in the design process as they allow the identification of critical areas with high pressure and the optimization of roof design to ensure greater resistance to wind forces. Thus, risks associated with extreme weather phenomena can be significantly reduced. By understanding and utilizing dynamic pressure coefficients, designers and engineers can develop innovative and efficient solutions for protecting buildings against wind effects. This not only improves structural resistance but also contributes to creating optimal conditions for comfort and safety inside buildings, ensuring their durability and functionality in the face of severe weather events.

In order to gain a deeper understanding of the behavior of roofs with installed photovoltaic panel systems, additional calculations were performed based on the data obtained from the wind tunnel tests. These calculations aimed to determine the dynamic pressure exerted on the roof under various wind conditions. By analyzing these results, the goal was to obtain a complete and detailed picture of how wind interacts with the roof and the photovoltaic panel system, providing crucial information for optimizing their design and performance in variable wind conditions.

Dynamic pressure (p_d) represents the kinetic energy per unit volume of a moving fluid and is measured in pressure units. The calculation formula is [24]:

$$p_d = 0.5\ \rho\ v^2\ c_v \tag{18}$$

where p_d is the dynamic pressure [Pa], ρ denotes the air density [kg/m^3] (air density can be considered 1.225 kg/m^3 under standard conditions), v characterizes the wind speed [m/s], and c_v represents the dynamic pressure coefficient.

4.2. Experimental Program Overview

The experiment was conducted in a wind tunnel with a turbulent boundary layer, using 1:100 scale models for different types of buildings. The tests included M_1—a house with a gable roof, M_2—a house with a hip roof, and M_3—an institutional building with a multi-section roof, including sections with variable slopes (Figures 4–6). Measurements were taken to determine the reference wind speed, as well as dynamic, static, and total pressures, both at the reference point and at the roof level of each model.

Several preparatory steps were undertaken for the experiment. First, the positions of the 18 sensors were marked on the roof, arranged in three rows of six columns each, and centered in the area where the photovoltaic panel system was to be installed. An additional reference pressure point, the 19th sensor, was placed below the eaves.

Following this, holes were drilled to allow for the installation of the connecting tubes between the roof surface and the sensor plate. The tubes were then inserted into the designated positions in accordance with the experimental setup. Finally, the tubes were secured by gluing and their upper ends were carefully adjusted to align precisely with the roof level. The upper limit of the tubes was fixed at the roof level of the models, while each tube mounted on the acquisition plate had a length of 25 cm. This length facilitated handling the models while adjusting their positions for measurements in different wind directions.



Figure 4. House with a gable roof model at scale 1:100 (M_1).



Figure 5. House with a hip roof model at the scale of 1:100 (M_2).



Figure 6. Institutional building with a multi-section roof model at the scale 1 to 100 (M_3).

For each model, dynamic pressure measurements were taken at multiple wind incidence angles, including 0°, 30°, 60°, 90°, 120°, 150°, 180°, −30°, −60°, −90°, −120°, and −150° relative to the main wind direction. Additionally, sensor number 0 was connected to both the acquisition plate and the Pitot tube to enable simultaneous data recording.

Following the model fabrication and instrumentation according to the aforementioned steps, the next phase involved preparing the models for the experiment, which included

verifying sensor functionality. Each sensor was tested individually using an air blower to check the integrity of the tubing. This test ensured that there were no air leaks in the system and that each sensor's signal was within the appropriate range. This guaranteed the correct operation of the sensors and the measurement system before commencing the actual experiments.

During the experiment, a wind speed of 8 m/s was used for measurements. Each model underwent 12 test runs, totaling 36 tests for all three models. Each test lasted 30 s, with 30,000 values recorded per measurement. In all cases, the same parameters regarding model positioning in the tunnel and wind direction were maintained to ensure consistent experimental conditions throughout the tests.

To provide a clearer overview of the experimental parameters used in the wind tunnel tests, the main characteristics of the program are summarized in Table 1.

Table 1. Summary of the main experimental conditions and testing parameters applied to the three scaled roof models in the wind tunnel setup.

Parameter	Description
Test facility	Wind tunnel with turbulent boundary layer, Technical University of Iași
Scale of physical models	1:100
Roof types tested	M_1—Gable, M_2—Hip, M_3—Multi-section
Number of sensors per model	18 pressure sensors + 1 reference sensor
Wind incidence angles	0°, ±30°, ±60°, ±90°, ±120°, ±150°, 180° (12 angles total)
Reference wind speed	7.95 m/s
Duration per test	30 s
Number of samples per test	30,000
Total number of tests	36 (12 per model)
Data acquisition frequency	1000 Hz
Software used	LABVIEW and custom processing scripts

4.3. Results: Gable Roof (Model M_1)

The average values of the dynamic pressure coefficient and the corresponding dynamic pressure (Table 2) represent essential parameters in evaluating the distribution of wind-induced forces on the roof surface. These values are determined based on data collected from pressure taps mounted on the roof surface, allowing for a detailed analysis of both local and global variations in wind-induced pressure. The interpretation of dynamic pressure coefficients provides an accurate understanding of how air currents interact with the structure, highlighting areas of high or low pressure—fundamental aspects for optimizing the aerodynamic performance of the roof and ensuring the stability of the photovoltaic system installed on it.

During the wind action testing on the gable roof with photovoltaic panels, relevant data were obtained for various wind incidence angles relative to the horizontal plane. The reference wind velocity used in these experiments was 7.95 m/s, and for each incidence angle, the average values of the dynamic pressure coefficient (Figure 7) and dynamic pressure (Figure 8) were determined. These results are essential for evaluating the structural behavior of the roof under wind influence and identifying potential risk areas.

The aerodynamic response of the gable roof (Model M_1) showed significant variations in dynamic pressure coefficients depending on the wind incidence angle. The highest positive values occurred at 0° and –30°, with dynamic pressure coefficients of 0.378 and 0.384, respectively, corresponding to dynamic pressures of 14.63 Pa and 14.86 Pa. These indicate strong frontal compression forces acting directly on the photovoltaic panels.

Table 2. Average values of the dynamic pressure coefficient and corresponding dynamic pressure for the gable roof model (M_1) at 7.95 m/s reference wind speed, across 12 wind incidence angles.

Reference Wind Speed (v_{ref}) [m/s]	Angle of Incidence of Reference Wind Speed [°]	Average Dynamic Pressure Coefficient (c_v)	Dynamic Pressure (p_d) [Pa]
7.95	0°	0.378	14.63
	30°	0.302	11.69
	60°	0.245	9.48
	90°	0.177	6.85
	120°	−0.132	−5.11
	150°	−0.169	−6.54
	180°	−0.204	−7.89
	−30°	0.384	14.86
	−60°	0.311	12.04
	−90°	0.228	8.82
	−120°	−0.145	−5.61
	−150°	−0.189	−7.32

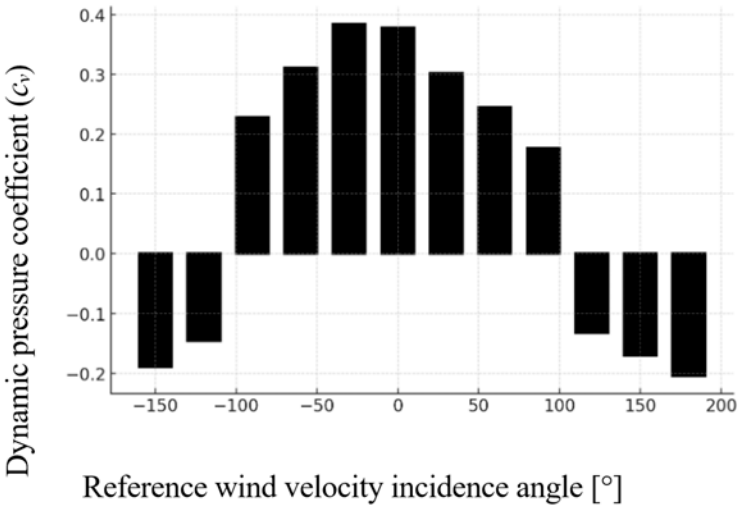


Figure 7. Graph showing the variation of dynamic pressure coefficient for the gable roof model (M_1) as a function of wind incidence angle, highlighting zones of compression and suction.

As the wind angle shifted from frontal to oblique and reverse directions, a progressive decrease in both dynamic pressure and pressure coefficients was observed. At 60° and 90°, the pressure values dropped to 9.48 Pa and 6.85 Pa, respectively. Beyond 120°, the pressure coefficients became negative, indicating suction effects, with the most significant uplift observed at 150° (–0.189) and 180° (–0.204), equating to –7.32 Pa and –7.89 Pa.

This pattern demonstrates a clear aerodynamic transition from compression to uplift, associated with flow separation and vortex formation at higher wind angles. These suction forces are critical, as they generate upward loads that may compromise the structural integrity of the PV mounting system, particularly near panel edges and rear fixings. This observation aligns with [10], who reported elevated suction forces behind PV panels at oblique wind angles on gabled roofs.

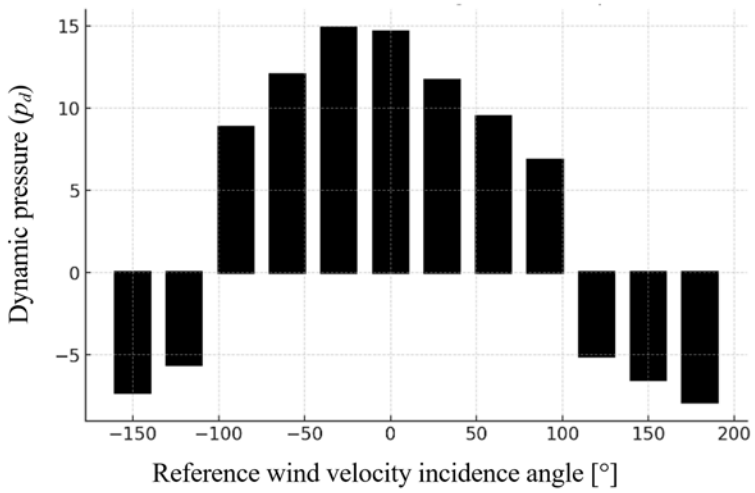


Figure 8. Corresponding dynamic pressure values for the gable roof model (M_1), indicating higher pressure loads at 0° and −30° angles.

The variation in aerodynamic behavior across the incidence angles highlights the sensitivity of gable roofs to wind direction, especially in the context of elevated PV installations. Wind exposure from the rear can generate significant uplift forces, which must be carefully considered during the design and anchorage of PV systems.

In summary, the gable roof configuration exhibited the highest-pressure differentials among the three models tested, confirming its vulnerability to wind-induced uplift. Reinforcement of panel anchoring at rear and edge zones is recommended to enhance structural resilience.

4.4. Results: Hip Roof (Model M_2)

The values determined for the dynamic pressure coefficient and dynamic pressure, presented in Table 3, represent essential factors in the analysis of the distribution of aerodynamic forces generated by the wind on the roof. These data are obtained from measurements taken at the pressure taps, optimally placed on its surface, allowing for a detailed assessment of the local and global variations of the pressure exerted by the airflow. Investigating these parameters provides a clear perspective on the areas subjected to significant aerodynamic influences, playing an important role in optimizing the structural configuration and ensuring the stability of the photovoltaic system installed on the roof.

The interpretation of the data in Table 2 provides a detailed perspective on how the wind's angle of incidence influences the distribution of dynamic pressure on the surface of the roof equipped with photovoltaic panels. The values of the dynamic pressure coefficient (Figure 9) and dynamic pressure (Figure 10) vary significantly depending on the wind direction, indicating both compression and suction zones, phenomena with major implications for the stability of the structure.

The hip roof (Model M_2) demonstrated a more uniform aerodynamic response compared to the gable roof. The maximum dynamic pressure coefficient was observed at −30° (c_v = 0.564) and 0° (c_v = 0.555), corresponding to dynamic pressures of 21.83 Pa and 21.54 Pa, respectively. These indicate strong frontal wind loading on the PV panels mounted on the upper portion of the roof.

As the wind incidence angle increased, the aerodynamic response gradually diminished. At 60° and 90°, the dynamic pressure coefficients decreased to 0.360 and 0.260, indicating a reduced compression effect. Like model M_1, suction forces began to appear beyond 120°, with c_v values becoming negative. At 150° and 180°, significant suction was recorded (−0.278 and −0.300), with dynamic pressures of −10.75 Pa and −11.61 Pa, respectively.

Table 3. Summary of the dynamic pressure coefficients and pressures measured for the hip roof model (M_2) under controlled wind tunnel conditions, showing variation by incidence angle.

Reference Wind Speed (v_{ref}) [m/s]	Angle of Incidence of Reference Wind Speed [°]	Average Dynamic Pressure Coefficient (c_v)	Dynamic Pressure (p_d) [Pa]
7.95	0°	0.555	21,536
	30°	0.444	17,190
	60°	0.360	13,926
	90°	0.260	10,055
	120°	−0.194	−7511
	150°	−0.248	−9617
	180°	−0.300	−11,611
	−30°	0.564	21,827
	−60°	0.457	17,095
	−90°	0.335	12,964
	−120°	−0.213	−8252
	−150°	−0.278	−10,752

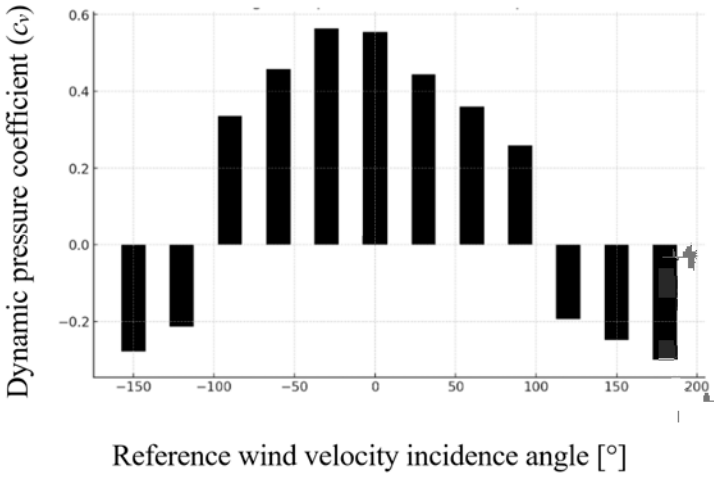


Figure 9. Dynamic pressure coefficient distribution for the hip roof model (M_2), revealing more uniform aerodynamic behavior than the gable roof.

The more gradual decline in pressure and the smoother transition from compression to suction suggest improved aerodynamic stability. This behavior can be attributed to the hip roof's sloped geometry on all sides, which facilitates flow deflection and reduces vortex intensity. These findings are consistent with the results of Kopp and Morrison [5], who emphasized the stabilizing effect of hipped roof forms under turbulent wind conditions.

While the hip roof still exhibits areas of suction at higher wind angles, the magnitude of these uplift forces is lower than in the gable configuration. This implies a reduced risk of panel detachment, although anchorage design should still consider rear and lateral suction zones.

Overall, the hip roof configuration showed a balanced aerodynamic profile with lower peak suctions, confirming its relative resilience to wind-induced loading on rooftop PV systems.

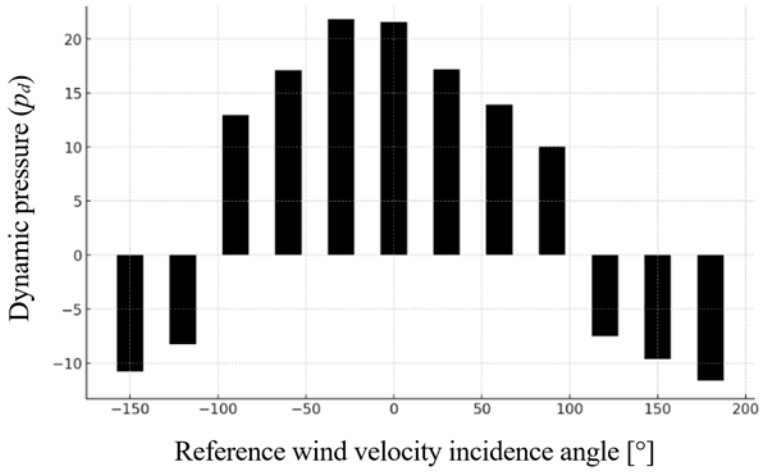


Figure 10. Dynamic pressure values across wind incidence angles for the hip roof model (M_2), with peak values at frontal wind directions and suction observed at rear angles.

4.5. Results: Multi-Section Roof (Model M_3)

The values of the dynamic pressure coefficient and dynamic pressure, presented in Table 4, represent fundamental information for understanding how wind influences the distribution of aerodynamic forces on the roof. These data are extracted from measurements made using pressure taps placed across the entire roof surface, allowing for a detailed evaluation of pressure fluctuations across different areas. The analysis of these parameters helps identify regions subjected to significant aerodynamic loads, which is essential for improving the structural design and ensuring the stability of the photovoltaic system mounted on the roof.

Table 4. Experimental results for the multi-section institutional roof model (M_3), highlighting both positive and negative pressure effects across varying wind directions.

Reference Wind Speed (v_{ref}) [m/s]	Angle of Incidence of Reference Wind Speed [°]	Average Dynamic Pressure Coefficient (c_v)	Dynamic Pressure (p_d) [Pa]
7.95	0°	0.510	19,809
	30°	0.409	15,830
	60°	0.331	12,822
	90°	0.239	9257
	120°	−0.179	−6910
	150°	−0.229	−8859
	180°	−0.276	−10,682
	−30°	0.520	20,094
	−60°	0.421	15,730
	−90°	0.309	11,933
	−120°	−0.196	−7593
	−150°	−0.256	−9892

Following the analysis of the results, a significant distribution of the dynamic pressure coefficient (Figure 11) and dynamic pressure (Figure 12) can be observed depending on the wind incidence angle, with maximum and minimum values indicating the variability of the aerodynamic forces applied to the roof.

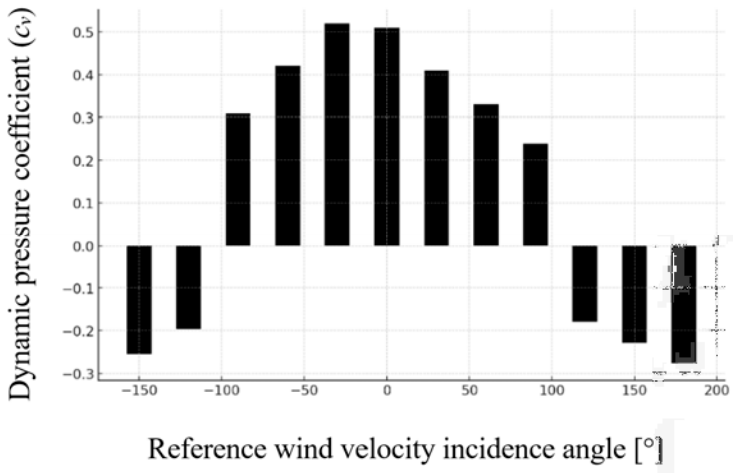


Figure 11. Coefficient of dynamic pressure variation for the multi-section roof model (M_3), showing irregular behavior due to complex geometry.

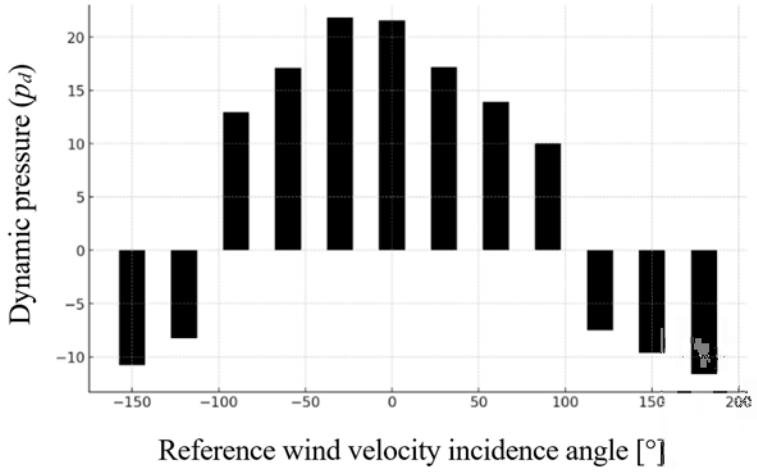


Figure 12. Recorded dynamic pressure values for the multi-section roof model (M_3), reflecting both peak compressive and uplift forces.

The multi-section roof (Model M_3) displayed a complex aerodynamic behavior, influenced by the variation in roof slopes and junctions between segments. The highest dynamic pressure coefficient was recorded at –30° (c_v = 0.626), corresponding to a dynamic pressure of 24.23 Pa, followed closely by 0° (c_v = 0.587, p_d = 22.72 Pa). These values indicate strong frontal wind loading, especially in zones where PV panels are aligned with roof ridges.

Between 30° and 90°, dynamic pressure coefficients decreased significantly, reaching a minimum of 0.197 at 90°, equivalent to a dynamic pressure of 7.63 Pa. As with the previous models, suction effects emerged beyond 120°, with negative pressure coefficients recorded at 150° and 180° (c_v = –0.257 and –0.284, p_d = –9.94 Pa and –10.98 Pa, respectively).

Due to its complex geometry, the multi-section roof produced asymmetric flow patterns and non-uniform pressure distributions. This was particularly evident at oblique wind angles (60–120°), where pressure zones shifted unevenly across the roof surface, affecting PV panels mounted on different slopes in distinct ways. These effects mirror those reported in experimental studies on irregular roof shapes, where multiple flow separations and reattachments occur simultaneously [7,21].

The variability in wind-induced pressures across different sections of the roof highlights the challenge of designing uniform anchoring systems for PV modules. Specific zones may experience significantly higher uplift or compression depending on panel orientation relative to wind direction.

In conclusion, the multi-section roof exhibited the most spatially complex pressure behavior, with localized zones of high suction and compression. Customized PV mounting strategies are necessary for such geometries, especially in areas near slope transitions and ridgelines.

5. Conclusions

This study experimentally examined the aerodynamic behavior of photovoltaic (PV) panel systems installed on three different roof configurations—gable, hip, and multi-section—by conducting wind tunnel tests on 1:100 scale models exposed to varying wind incidence angles. The results revealed significant differences in pressure distribution based on roof geometry and wind direction, with gable roofs showing high frontal pressure peaks, hip roofs demonstrating more uniform loading, and multi-segment roofs presenting complex aerodynamic patterns with alternating suction and compression zones.

The presence of negative pressure coefficients at high incidence angles underscores the critical need to account for uplift forces when designing and installing rooftop PV systems. These insights contribute valuable experimental evidence that supports safer and more efficient structural integration of solar technologies, particularly in wind-exposed regions.

Practically, the results suggest that mounting systems for PV panels on gable and multi-pitched roofs should be reinforced especially at edges and corners, where uplift forces are highest. Designers should consider the dominant wind directions in their regions and integrate safety margins for both suction and compression effects when dimensioning supports.

While the results are consistent and statistically reliable, several limitations should be acknowledged. The wind tunnel setup cannot fully replicate real atmospheric turbulence, especially large-scale eddies and gusts. Moreover, the simplifications of model geometry and fixed panel angles may limit the generalizability to irregular installations. Future work should include CFD simulations and full-scale field testing to validate and refine these findings under natural wind conditions.

Beyond the immediate design implications, the findings of this study lay the groundwork for further investigations aimed at enhancing predictive accuracy and structural resilience. Future research should build on this dataset to develop validated numerical simulations, such as CFD models, capable of extrapolating the observed aerodynamic phenomena to full-scale conditions. Additionally, extended studies could explore the long-term behavior of PV mounting systems under fluctuating wind loads and help inform updates to design standards for complex roof geometries.

In this context, the current work serves not only as a contribution to experimental wind engineering but also as a reference point for ongoing research efforts focused on integrating renewable energy systems safely and sustainably into the built environment.

Given the increasing emphasis on sustainable development in civil engineering, this study offers practical guidance for enhancing the reliability of solar energy systems in diverse architectural contexts. By improving the understanding of wind effects on PV-equipped roofs, the research supports informed decisions in both design and policy, contributing to the broader objectives of environmental responsibility, energy efficiency, and resilience in the built environment.

Author Contributions: Conceptualization, R.-A.P., N.Ţ. and S.-V.H.; methodology, R.-A.P., N.Ţ. and D.U.; software, R.-A.P. and M.A.; validation, S.-V.H., D.U. and I.H.; formal analysis, R.-A.P., C.O., M.A. and I.H.; investigation, R.-A.P., C.O. and A.-F.M.; resources, N.Ţ.; data curation, S.-V.H., C.O., M.A. and I.H.; writing—original draft preparation, R.-A.P., N.Ţ. and S.-V.H.; writing—review and editing, R.-A.P., N.Ţ., S.-V.H. and I.H.; visualization, R.-A.P., D.U. and A.-F.M.; supervision, N.Ţ.; project administration, R.-A.P. and N.Ţ.; funding acquisition, N.Ţ. All authors have read and agreed to the published version of the manuscript.

Funding: This research received no external funding.

Institutional Review Board Statement: Not applicable.

Informed Consent Statement: Not applicable.

Data Availability Statement: The data presented in this study are available on request from the corresponding author.

Conflicts of Interest: The authors declare no conflicts of interest.

References

1. Polcovnicu, R.A.; Ţăranu, N.; Ungureanu, D.; Sbîrlea, C.; Cozmanciuc, R. Building Integrated Photovoltaics Systems: State-of-the-Art Review. *Bull. Inst. Politeh. Iași. Archit. Sect.* **2021**, *67*, 71. [CrossRef]
2. Polcovnicu, R.A.; Ţăranu, N.; Ungureanu, D.; Zghibarcea, Ș.V.; Hudișteanu, V.S. Modern Manufacturing Technology for Modular Photovoltaic Panels: State-of-the-Art and Future Trends. In *IOP Conference Series: Materials Science and Engineering*; IOP Publishing: Bristol, UK, 2020; p. 1182.
3. Eslami Majd, A.; Adebayo, D.S.; Tchuenbou-Magaia, F.; Willetts, J.; Nwosu, D.; Matthews, Z.; Ekere, N.N. Wind Flow and Its Interaction with a Mobile Solar PV System Mounted on a Trailer. *Sustainability* **2024**, *16*, 2038. [CrossRef]
4. Jackson, A.; Donaldson, G.; Gómez-Amo, J. Impact of Extreme Weather Conditions on the Performance of Utility-Scale PV Systems. *Sustainability* **2023**, *15*, 731.
5. Tu, Z.; Zheng, G.; Yao, J.; Shen, G.; Lou, W. Computational Investigation of Wind Loads on Tilted Roof-Mounted Solar Array. *Sustainability* **2022**, *14*, 15653. [CrossRef]
6. Kopp, G.A.; Morrison, M.J. Wind Effects on Rooftop-Mounted Solar Photovoltaic Systems. *J. Struct. Eng.* **2018**, *144*, 04018001.
7. Khadimallah, M.A.; Abdelbaky, M.; Bouafia, Y. Numerical Modeling of Wind Loads on Solar PV Arrays in Built Environments. *J. Wind Eng. Ind. Aerodyn.* **2024**, *200*, 104985.
8. Ke, Y.; Shen, G.; Yang, X.; Xie, J. Effects of Surface-Attached Vertical Ribs on Wind Loads and Wind-Induced Responses of High-Rise Buildings. *Sustainability* **2022**, *14*, 11394. [CrossRef]
9. Aly, A.M.; Rone, E. Wind Loads on a Low-Rise Gable Roof with and without Solar Panels and Comparison to Design Standards. *Sustain. Resil. Infrastruct.* **2024**, *9*, 589–609. [CrossRef]
10. Hudisteanu, S.V.; Popovici, C.G. Experimental investigation of the wind direction influence on the cooling of photovoltaic panels integrated in double skin facades. *E3S Web Conf.* **2019**, *111*, 03045. [CrossRef]
11. Wang, L.; Shi, F.; Wang, Z.; Liang, S. Blockage Effects in Wind Tunnel Tests for Tall Buildings with Surrounding Buildings. *Appl. Sci.* **2022**, *12*, 7087. [CrossRef]
12. Peng, H.Y.; Liang, H.; Dai, S.F.; Liu, H.J. Wind load analysis for rooftop solar photovoltaic panels in the presence of building interference: A wind tunnel study. *J. Build. Eng.* **2025**, *100*, 111702. [CrossRef]
13. Hudișteanu, S.V.; Ţurcanu, F.E.; Chereches, N.-C.; Popovici, C.-G.; Verdeș, M.; Ancaș, D.-A.; Hudișteanu, I. Effect of Wind Direction and Velocity on PV Panels Cooling with Perforated Heat Sinks. *Appl. Sci.* **2022**, *12*, 9665. [CrossRef]
14. *EN 1991-1-4:2005+A1:2010*; Eurocode 1: Actions on Structures—Part 1–4: General Actions—Wind Actions. CEN: Brussels, Belgium, 2010.
15. Zhang, J.; Lou, Y. Study of Wind Load Influencing Factors of Flexibly Supported Photovoltaic Panels. *Buildings* **2024**, *14*, 1677. [CrossRef]
16. Geurts, C.; van Bentum, C. *Wind Loading on Buildings: Eurocode and Experimental Approach*; CISM International Centre for Mechanical Sciences; Springer: Vienna, Austria, 2007; Volume 493. [CrossRef]
17. Yao, J.; Tu, Z.; Wang, D.; Shen, G.; Lou, W. Experimental Investigation of Wind Loads on Roof-Mounted Solar Arrays. *Sustainability* **2022**, *14*, 8477. [CrossRef]
18. Wang, W.; Zhu, Y.; Shu, Z.; Li, Y. A Review on Aerodynamic Characteristics and Wind-Induced Response of Flexible Support Photovoltaic System. *Atmosphere* **2023**, *14*, 731. [CrossRef]
19. Nezamisavojbolaghi, M.; Davodian, E.; Bouich, A.; Tlemçani, M.; Mesbahi, O.; Janeiro, F.M. The Impact of Dust Deposition on PV Panels' Efficiency and Mitigation Solutions: Review Article. *Energies* **2023**, *16*, 8022. [CrossRef]
20. Wang, J.; Liu, M.; Yang, Q.; Hui, Y.; Nie, S. Extreme Wind Loading on Flat-Roof-Mounted Solar Arrays with Consideration of Wind Directionality. *Buildings* **2024**, *14*, 221. [CrossRef]
21. Hu, J.; Wang, X.; Yang, H.; Huang, B. Experimental Study on Rooftop Flow Field of Building Based on the Operation of Vertical-Axis Wind Turbines. *J. Renew. Sustain. Energy* **2024**, *16*, 053301. [CrossRef]
22. Shen, G.; Yu, S.; Lou, W. Experimental Investigation of the Parapet Effect on the Wind Load of Roof-Mounted Solar Arrays. *Sustainability* **2023**, *15*, 5052. [CrossRef]

23. Kopp, G.A.; Banks, D. Use of Wind Tunnel Measurements in Wind Load Design of Solar Panels. *J. Wind Eng. Ind. Aerodyn.* **2013**, *123*, 232–240.
24. Li, S.; Xiao, F.; Li, S.; Hui, Y.; Yang, Q.; Li, B.; Chen, Y.; Zhou, S.; Liu, M. Wind Loads on Solar Panels Mounted on Facade of High-Rise Residential Building. *Int. J. Struct. Stab. Dyn.* **2024**, *24*, 2240019. [CrossRef]
25. ASME. Numerical Simulation of Wind Load on Roof-Mounted Solar Panels. In Proceedings of the ASME International Conference, Boston, MA, USA, 30 June–2 July 2014.
26. ICRAES-2020. Wind Pressure Distribution on PV Panels Mounted on Saw-Type Roofs. In Proceedings of the International Conference on Recent Advances in Engineering & Science, New York, NY, USA, 17 November 2020.
27. *ASCE/SEI 7-22*; Minimum Design Loads and Associated Criteria for Buildings and Other Structures. American Society of Civil Engineers: Reston, VA, USA, 2022.
28. Bendat, J.S.; Piersol, A.G. *Random Data: Analysis and Measurement Procedures*, 4th ed.; Wiley: Hoboken, NJ, USA, 2010.
29. Spanelis, A.; Georgiou, D. Assessment of Aerodynamic Wake Effects on PV-Mounted Rooftops. *Resources* **2023**, *12*, 90.

Disclaimer/Publisher's Note: The statements, opinions and data contained in all publications are solely those of the individual author(s) and contributor(s) and not of MDPI and/or the editor(s). MDPI and/or the editor(s) disclaim responsibility for any injury to people or property resulting from any ideas, methods, instructions or products referred to in the content.

Energy Conversion and Management: X 25 (2025) 100842

Contents lists available at ScienceDirect

Energy Conversion and Management: X

journal homepage: www.sciencedirect.com/journal/energy-conversion-and-management-x

Experimental analysis of innovative perforated heat sinks for enhanced photovoltaic efficiency

Sebastian-Valeriu Hudișteanu *, Nelu-Cristian Cherecheș, Florin-Emilian Țurcanu, Iuliana Hudișteanu, Marina Verdeș, Ana-Diana Ancaș

Faculty of Civil Engineering and Building Services, Gheorghe Asachi Technical University of Iasi, Iași 700050, Romania

ARTICLE INFO

Keywords:
Heat sinks
Photovoltaics
Solar energy
Passive cooling
Wind effect
PV temperature

ABSTRACT

One of the main challenges in photovoltaic panel operation is the significant increase in operating temperature, which leads to a notable decrease in conversion efficiency. Addressing this issue, the present study focuses on the investigation of air-cooling solutions for photovoltaic (PV) panels integrated into an operational system. The proposed cooling solutions for the photovoltaic panels include four different types of heat sinks with fins. The experimental setup was placed on a roof terrace, exposing the panels to real-world weather and functional conditions. Each cooling solution, designed with variable characteristics, aimed to efficiently dissipate heat generated by the PV panels, particularly during warmer seasons. Each cooling solution tested in this research improves the efficiency of photovoltaic panels and ensures uniform temperature distribution across the panel surface. The advantage of the air-cooling solutions (heat sinks with fins) is their ability to provide passive cooling of the photovoltaic panels without additional energy or mass consumption. These passive cooling solutions are advantageous as they lower PV temperatures without requiring additional energy input, thus aligning with sustainable design principles by enhancing energy output while minimizing the system's carbon footprint. The originality of the work consists in outdoor testing of the patented idea of perforating the heat sink to improve air circulation. The results demonstrated notable efficiency improvements across all models, ranging from 5.28% to 5.92%, with slight advantages induced by perforated fin heat sinks (5.82% to 5.92%) compared to non-perforated ones (5.28% to 5.69%). Additionally, perforated designs achieved approximately 5% material savings, offering superior efficiency gains at a reduced cost. The research involved both theoretical analysis and experimental approach.

Introduction

The current global energy context is characterized by the energy consumption of humanity which has reached impressive values in recent years, while the world's energy production still has an important percentage of conventional sources [1]. In the current year (2024) it was "celebrated" the well-known Overshoot Day on August 1st. This means that humanity has already used up all the restorable resources of Earth for an entire year. From August 2nd we have started consuming more resources than the planet can regenerate [2]. Therefore, by the end of the year 2024, the energy consumption will reach about 1.71xEarth. It is a global emergency and every small step in reducing this tendency will become decisive in achieving this task.

Photovoltaic conversion has important advantages, considering that the energy source is renewable and free, and the processes of electricity production do not have a negative impact on the environment (CO_2 or NOx emissions, waste, noise etc.). The generation of electricity is done without the use of moving parts, so the costs of maintenance are reduced. The energy produced is consumed locally, which results in reduced power losses.

The Building Integrated Photovoltaics (BIPV) concept consists in placing PV panels on the roof or facades of buildings. This integration is justified if there are analyzed the main advantages of the local production and consumption of electricity, which imply reduced energy losses and the possibility of complex use of electricity and heat [3].

Photovoltaic systems typically operate in a functional context where, over long periods (years of operation), there is often a mismatch between the months of **maximum energy production** and the months when **maximum efficiency** is achieved [4]**.** It is necessary to **overcome these technological and conceptual barriers** that are currently assumed by default. For example, during intermediate seasons like

* Corresponding author.
E-mail address: valeriu-sebastian.hudisteanu@academic.tuiasi.ro (S.-V. Hudișteanu).

https://doi.org/10.1016/j.ecmx.2024.100842
Received 30 October 2024; Received in revised form 11 December 2024; Accepted 15 December 2024
Available online 17 December 2024
2590-1745/© 2024 The Authors. Published by Elsevier Ltd. This is an open access article under the CC BY license (http://creativecommons.org/licenses/by/4.0/).

Nomenclature

P_{mp}	Maximum power point (Wp)
V_{mp}	Voltage at the maximum power point (V)
I_{mp}	Current at the maximum power point (A)
V_{oc}	Open circuit voltage (V)
I_{sc}	Short-circuit current (A)
η	Efficiency of conversion in STC (%)
β	Temperature Coefficient of a PV Cell Efficiency (%/°C)
T_{STC}	Operating temperature in standard test conditions (T_{STC} = 25 °C);
ΔT	Temperature difference between T_{STC} and T (°C);
η_T	PV panel efficiency for temperature T (%);
t_{NOCT}	Nominal Operating Cell Temperature (°C)
L, l, h	Dimensions of PV panel Length (mm), Width (mm), Height (mm)
t_{cell}	Operating temperature of the PV cell (°C)
G	Solar irradiance (W/m^2)
K_{Cu}	Conductivity of copper (W/m·K)
a	Accuracy of measurement device
u	Uncertainty of measurement device
h	Heat transfer coefficient
Re	Reynolds number
Pr	Prandtl number
PV	Photovoltaic
BIPV	Building Integrated Photovoltaics
PVT	Photovoltaic Thermal
BIPVT	Building Integrated Photovoltaic Thermal
STC	Standard test conditions
AM	Air mass
AM1.5	Air mass in standard test conditions
Cool-PV-ANPHF	**A**ir cooled heat sink **N**on-**P**erforated **H**orizontal **F**ins
Cool-PV-ANPHF30	**A**ir cooled heat sink **30** mm **P**erforated **H**orizontal **F**ins
Cool-PV-ANPVF	**A**ir cooled heat sink **N**on-**P**erforated **V**ertical **F**ins
Cool-PV-ANPVF30	**A**ir cooled heat sink **30** mm **P**erforated **V**ertical **F**ins

March-May 2023, as well as October-November 2023, the maximum hourly power produced by the PV systems in Romania (**879–906 MW**) exceeded the maximum hourly values from June-August 2023 (**864 MW**) [5]. Knowing that the intensity of solar radiation between June and August has the highest values of the year, it turns out that the most important cause of not reaching the production potential was the **uncontrolled increase of the operating temperatures of the PV panels** during the summer [6].

There are solutions for improving the global efficiency of PV panels, like bifacial technology, N-type cells [7] or solar tracking systems [8], but in terms of temperature effect, the most recommended solutions are to realize an efficient cooling [9–17]. In literature there are complementary PV panels cooling solutions that are recommended to achieve high productivity [18–20]. The interest regarding the PV panels cooling is supported by the high amount of research in literature on improving the conversion efficiency by decreasing the temperature of the photovoltaic panels [6,21,22] and on using the extracted thermal energy [23]. The integration of photovoltaic panels in buildings is another topic of interest, both from an energetic and architectural point of view, known as BIPV (Building Integrated Photovoltaics) [24].

One of the main problems concerning the operation of photovoltaic panels is the significant increase of their operating temperature, which causes an important drop in conversion efficiency [13,25,26]. The decrease of efficiency and of the produced power related to the increase of the temperature have values between −0,46…-0,50 %/°C and −0,47…-0,50 %/°C, respectively [22].

As the power of a photovoltaic cell is influenced by the temperature and radiation levels, the standard test conditions (STC) parameters were defined [6]: t_{cell} = 25 °C, G = 1000 W/m^2, AM1.5. In STC the PV panels produce the Watt-peak power [W_p], but a real concern is that in regular operation, at 1000 W/m^2, the photovoltaic panels can reach temperatures of 80…90 °C [3], leading to a significant decrease of the efficiency.

Experimental tests on monocrystalline or polycrystalline photovoltaic panels, that show the decrease of efficiency as the operating temperature increases and the necessity of cooling solutions are current concerns in the literature [17,20,27–29].

Most of the studies on the cooling of photovoltaic panels are also focused on the usage of the thermal energy extracted because of this process [27,30–33], so that the recovery time of the investment is less than of the stand-alone photovoltaic systems [34,35].

The simultaneous conversion of solar energy into electric and thermal energy using photovoltaic-thermal panels is known in the literature as PVT (Photovoltaic-Thermal System) [27,30–33]. A particular feature of this solution is the BIPVT concept, which implies the integration of photovoltaic panels into buildings [36,37]. The generation of two of the most used types of energy is performed under the conditions in which the operation of each of the two systems is beneficial to the other, with priority to the production of electricity and ensuring the efficiency of photovoltaic conversion. Already commercialized solutions of PVT are known (hybrid photovoltaic solar panels, passive cooling solutions with polymeric films, ventilated cooling systems – [38]), but comparisons and quantifiable data regarding the effect of these solutions compared to the basic variants under similar conditions are not available. Most of them provide only global information under laboratory standard operating conditions [39].

There are at least two main directions for cooling PV panels: passive and active. Though there are a lot of many other technologies, materials and solutions used (such as: PCM [20,40–42], nanofluids [43,44,45 46,47], heat pipes [18,41], radiative cooling [1], thermoelectric devices [1,45,48]), the most widespread thermal agents for extracting the heat from the PV panels are still water [28,31,49] and air [19,25,50,51,52]. The most used agent for active cooling is water – in different systems and configurations [31,53,54]. From passive cooling technologies, the most widespread are air cooling [3,22,50,55].

Although water cooling has some clear advantages over air cooling, there are many situations where air cooling is preferred because it has no moving parts, requires simple maintenance, and has a relatively low initial investment cost compared to water cooling solutions [55,56]. The air cooling is ideal for areas where thermal energy is not required or where water or other thermal agents cannot be used [22]. Also, air cooling is recommended for locations where bifacial PV panels cannot be used [7].

Different technologies to improve the efficiency of photovoltaic panels by passive cooling using air are studied in the literature [57]. Initial studies on the cooling of photovoltaic (PV) panels using air and heat sinks compared the characteristic values of photovoltaic cells under different conditions through experimental tests [22,58,59]. Many studies have the same approach by comparing in laboratory conditions the basic case with heat absorption and dissipation system on the backside area. In these studies [60,61] the system consists of a network of fins made of aluminum or copper, being thermally coupled to the photovoltaic cell. An increase in the heat extracted from the photovoltaic cell and a decrease in its temperature, with values between 5 °C and 9 °C is recorded. Over the years, this research direction has been followed and improved both from the point of view of the materials used, but also of the geometric configurations [62–64].



Fig. 1. Location of the operational photovoltaic system [69].

Recent studies from literature have some inconveniences such as: focusing only on the small-scale photovoltaic cell, active cooling by forced convection or using controlled laboratory conditions. The non-uniformity of the distribution of the temperatures across photovoltaic panels is also an important factor which affects their global efficiency [19,26,65,66].

The main objective of the present study was to realize real outdoor experimental tests of the innovative technologies of air-cooling photovoltaic (PV) panels to improve their conversion efficiency. The **monocrystalline silicon photovoltaic panels** analyzed will be referred hereinafter as **photovoltaic (PV) panels**. The basic concept of the analysis was the designing and testing of PV panels cooling technologies. The innovative passive air cooling has assumed the use of **heat sinks with perforated/non-perforated fins** and natural ventilation. Considering the sensitivity of PV panels to high operating temperatures, the implementation of the proposed cooling technologies will enhance the electric energy generation of photovoltaic systems throughout the entire year. Compared to the studies mentioned above, the originality of the work consists in outdoor testing of the patented idea of perforating the heat sink to improve air circulation [67].

The novelty of the present study is that the cooling effect was analyzed and extended to a larger scale on an operating photovoltaic system. The types of heat sinks proposed in this paper have more advantages than the technologies found in existing studies, such as the use of copper as the heat sink material and optimized fins with perforations [3,22,68].

Experimental setup

The experimental research was realized on a real operational PV system placed on the terrace roof of the Department of Building Services Engineering at the Faculty of Civil Engineering and Building Services, "Gheorghe Asachi" Technical University of Iasi, Romania (47.15 N, 27.59 E – [69]) – Fig. 1. The purpose of the experimental tests was to implement the established models for cooling photovoltaic panels and to verify their operational parameters. Additionally, the increase in efficiency was graphically and numerically quantified. The experimental program involved testing the influence of various climatic parameters for four heat sink configurations.

The operational photovoltaic system has the following characteristics – Fig. 2:

– Installed power = 2.56 kWp;

– Number of panels = 8 monocrystalline photovoltaic panels of 320 Wp each (Number of cells: 60, Minimum efficiency: 19 %, Panel dimensions: 1690 x 996 x 35 mm, Panel weight: 18.5 kg, MC4 connectors, advantageous position of the IP67 junction box – in order to have maximum space for heat sink positioning) – Fig. 2;

– Single-phase hybrid inverter compatible with the photovoltaic system (Minimum efficiency: 96.7 %, Maximum input voltage: 600 V, Minimum voltage: 100 V, Number of MPPT: 2; Maximum input current per MPPT: 12.5 A, Maximum short-circuit current: 18 A);

– DC and AC cables, connectors, and panels.

The positioning of the photovoltaic panels at the optimum angle of 35° was established numerically [22]. Table 1 presents the electrical and functional characteristics of the Si-based photovoltaic panels used in the system.

The experimental stand composed of a total of 8 identical photovoltaic panels was grouped into **2 subsystems**, for which the cooling technologies were implemented, as follows:

Subsystem 1 – Consists in 4 **pilot photovoltaic panels**, with standard mounting (without additional devices to improve cooling). This subsystem represents the **base case** for comparing the tested cooling technologies, operating under the same conditions. **Four** pilot photovoltaic panels were installed into the subsystem. The measurements for the PV panels which are part of Subsystem 1 are averaged during the study, to exclude errors or particularities.

Subsystem 2 – Consists of 4 photovoltaic panels cooled using **heat sinks with perforated and non-perforated fins** placed on the back of

Table 1
General specifications of the selected PV panel – AE Solar AE320HM6-60 [70].

AE Solar AE320HM6-60 PV Panel	
P_{mp}	320 Wp
V_{mp}	33.40 V
I_{mp}	9.59 A
V_{oc}	40.90 V
I_{sc}	10.15 A
η	19.22 %
β	−0.37 %/°C
t_{NOCT}	47 °C
Dimensions ($L \times l \times h$)	1665 mm × 996 mm × 35 mm



Fig. 2. The photovoltaic system (2.56 kWp) – 8 Photovoltaic panels of 320 Wp each.

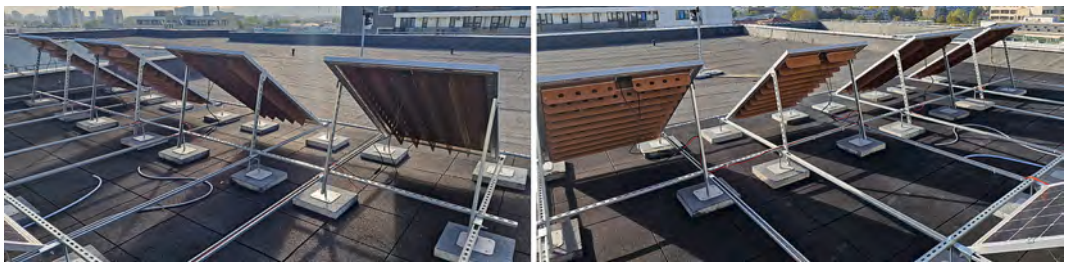


Fig. 3. Subsystem 2 – Photovoltaic panels with heat sinks.

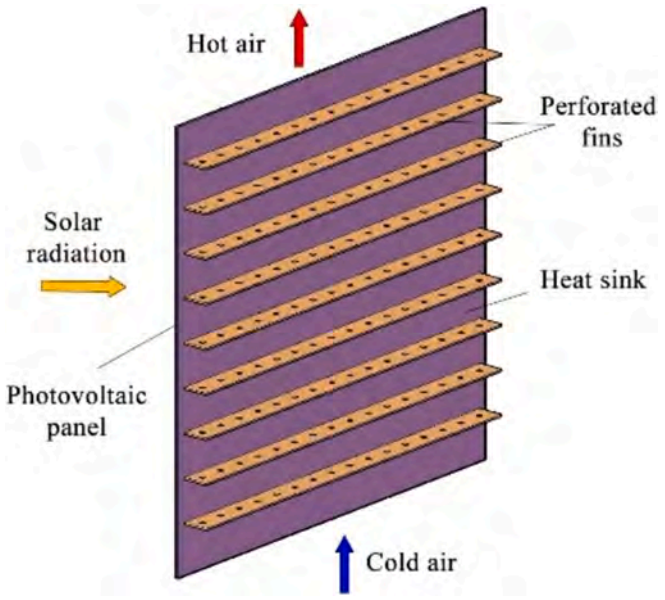


Fig. 4. Heat sink with perforated fins for cooling PV panels – principle of operation.

PV panels and fixed using thermal paste and adhesive. This subsystem is used to analyze the effect of the innovative heat sinks with perforated fins, in order to determine the additional energy produced as a result of lower operating temperature. A total of **four** photovoltaic panels were installed with attached heat sinks made of copper, two of them with perforated fins and two without perforations – Fig. 3.

The **heat sinks** attached to photovoltaic panels for cooling, Fig. 4, consist of a metal plate with **perforated or non-perforated fins**. The dimensions of the heat sink plate were considered at maximum technical to cover as much as possible of the panel surface. The geometrical dimensions of the fins and perforations were chosen following the numerical optimization studies carried out before the experimental implementation [3,22,68,71].

The copper fins (K_{Cu} = 400 W/m·K) were placed in two configurations (horizontal and vertical) at distance of **10 cm**, having holes arranged in one row and staggered from one to another. The role of the designed holes on the fins is both **quantitative** (by **reducing the amount of material** necessary for device construction) and **qualitative** (by **amplifying the turbulence and heat transfer** in the immediate vicinity of PV panel) [3,55,72,73].

The photovoltaic panels were equipped with copper sheet heat sinks, as shown in Fig. 5. The contact between the back surface of the photovoltaic panel and the heat sink plate was ensured by using thermally conductive silicone paste.

Fig. 6 presents the experimental stand used for testing the technologies for efficiency improvement of PV panels by cooling.

Monitoring of the external climatic parameters was carried out using the Vantage Pro2 Plus weather station [74], positioned on the roof of the building, near the experimental stand – Fig. 7.

The experimental stand was designed to facilitate both separate and simultaneous measurements for all proposed air-cooling solution models. The arrangement of photovoltaic panels, cooling solutions and the weather station is illustrated in Fig. 7. The interior equipment of the experimental stand is situated in the technical space, located in the immediate vicinity of the photovoltaic system. In this space, measurement and control equipment have been placed, as well as the internal components of the electrical installation of the photovoltaic system (cables, inverter, equipment and electrical panels) – Fig. 8.

To verify the performance of the proposed heat sinks, an experimental research program was performed on a full-scale physical model integrated into a functional photovoltaic system. The testing program considered the variation of the climatic parameters (ambient air temperature, solar radiation, wind direction and wind speed). The functional photovoltaic system consists of 8 photovoltaic panels, with 4 of them equipped with the proposed real-scale air-cooling solutions. The 4 constructive variants are presented in Tables 2–5. Based on the initial numerical analysis [22], the experimental study focused on two main configurations: longitudinal (vertical, aligned with the length of the PV panel) and transverse (horizontal, aligned with the width of the PV panel). The distance between the fins was set to 150 mm, with a height of 100 mm for each fin.

The approximate lengths of the fins were 1520 mm for the longitudinal configuration and 860 mm for the transverse configuration. There

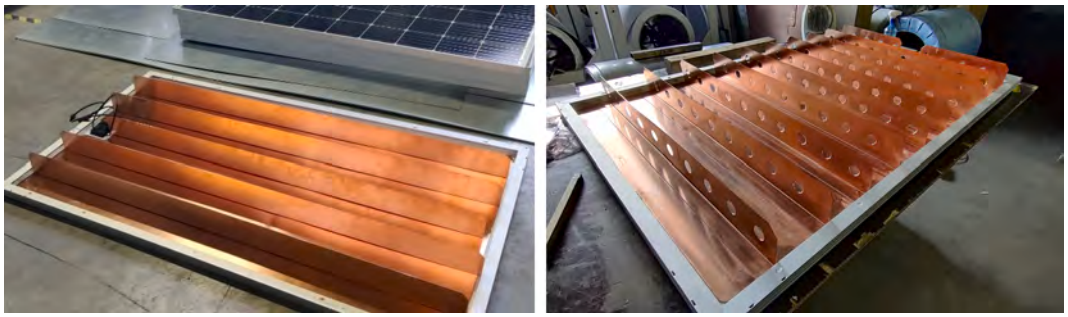


Fig. 5. Mounting heat sinks on the back of the photovoltaic panel.

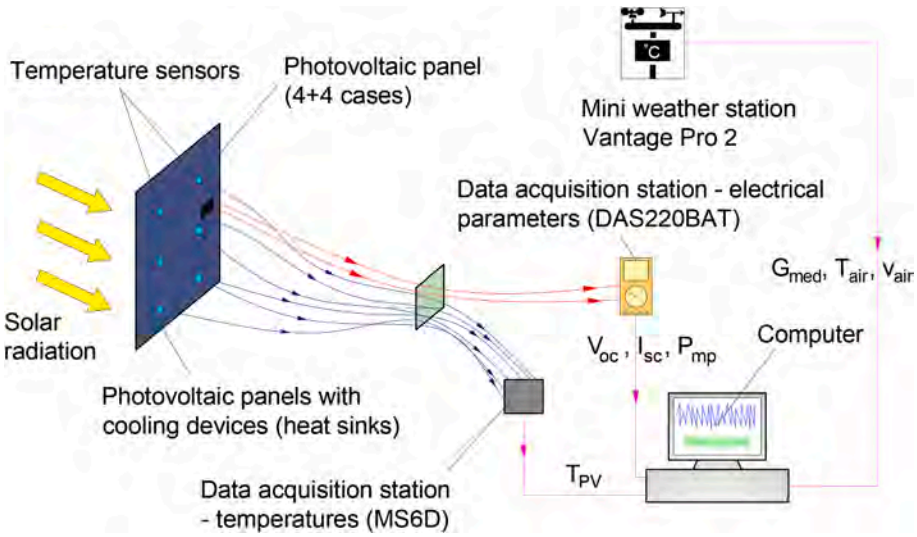


Fig. 6. Experimental stand for testing the cooling of PV panels.



Fig. 7. The experimental stand with the arrangement of photovoltaic panels, cooling solutions, and the weather station near the photovoltaic system.



Fig. 8. Arrangement of the technical space.

were 11 fins in the horizontal arrangement and 5 in the vertical arrangement. The perforations were circular, with a diameter of 30 mm. The distance between the centers of the perforations on the fins was 100 mm, staggered by 50 mm between successive fins. The role of the offset between the rows of perforations is to generate local turbulence, to remove any stagnant air and to ensure a more balanced circulation of air currents for uniform cooling of the photovoltaic panel surfaces.

The arrangement of the PV panels is shown in Fig. 9. The minimum distance of 1 m was imposed between two panels, to assure good air circulation and cooling effect.

Table 2
Heat sink for cooling photovoltaic panels with horizontal fins (***Cool-PV-ANPHF***).

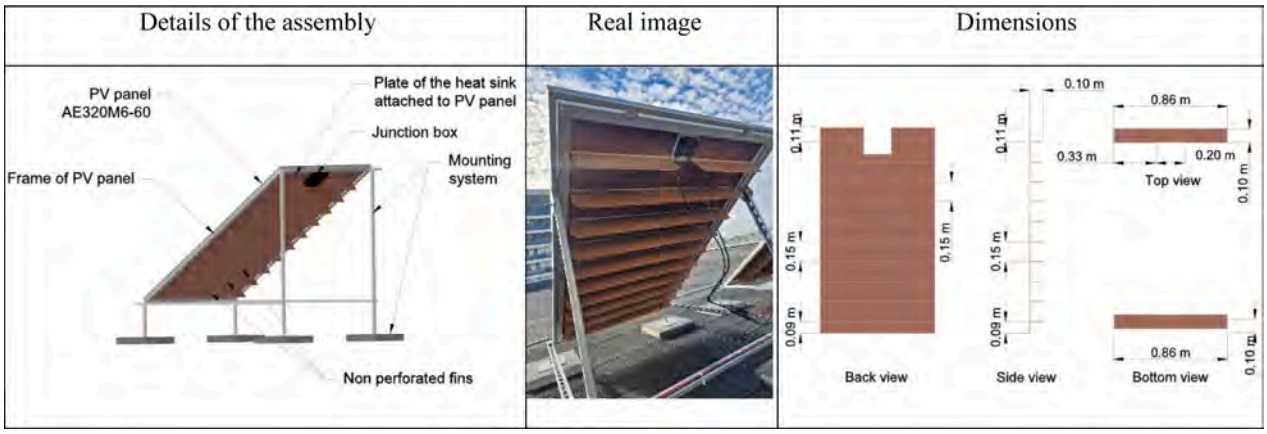


Table 3
Heat sink for cooling photovoltaic panels with perforated horizontal fins (***Cool-PV-APHF30***).

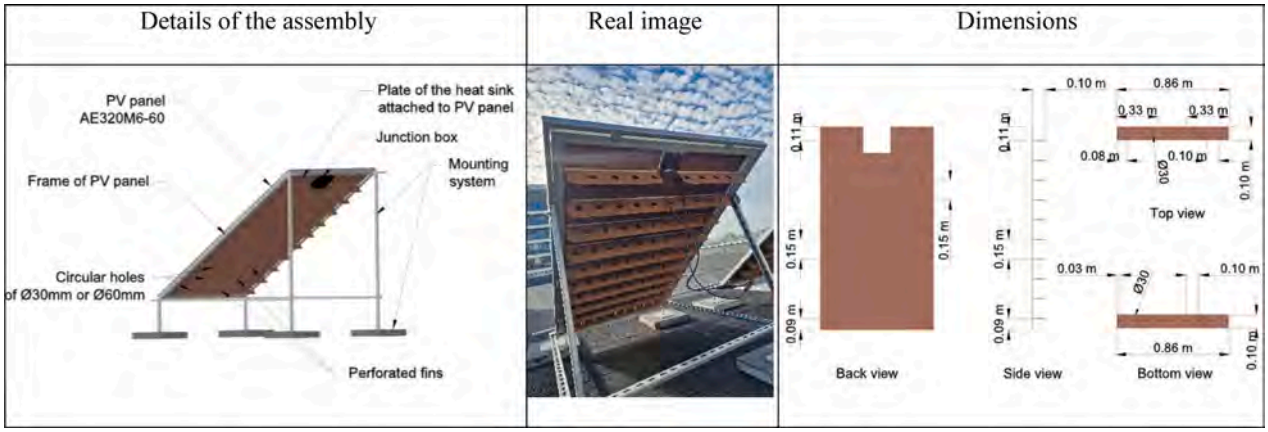
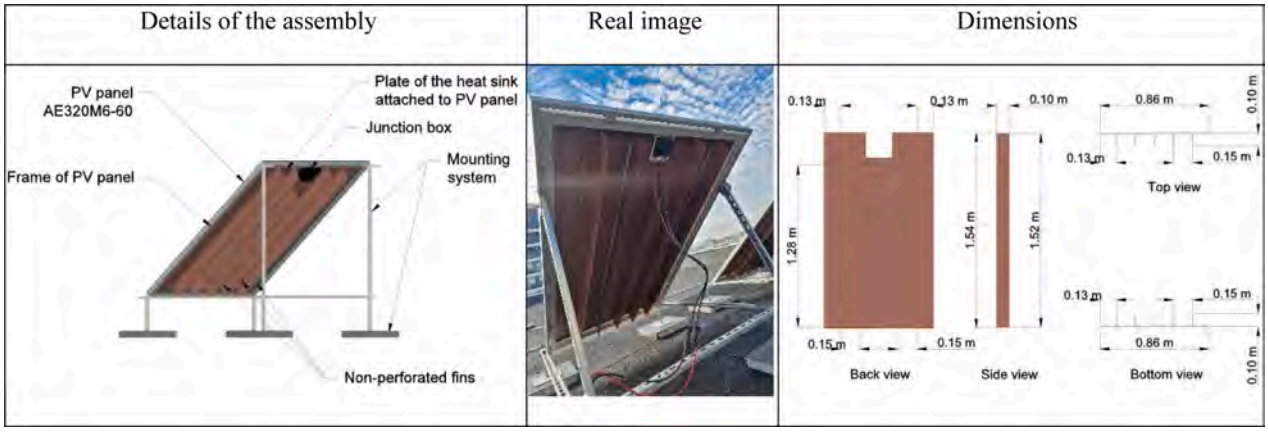


Table 4
Heat sink for cooling photovoltaic panels with vertical fins (***Cool-PV-ANPVF***).

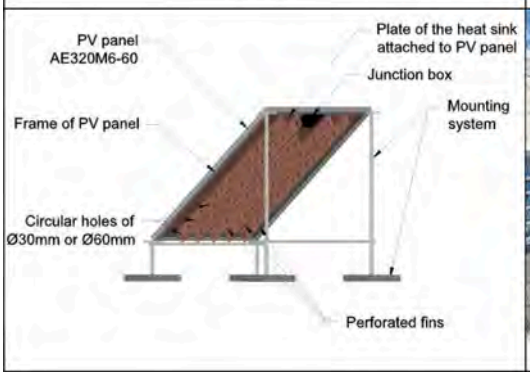
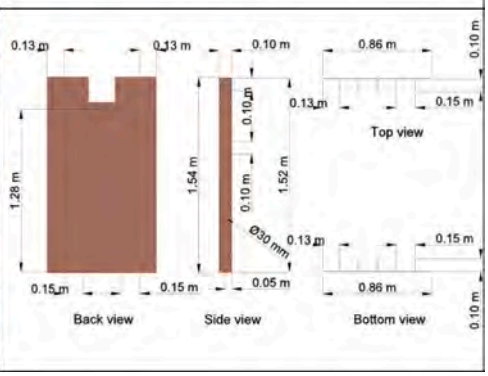


Experimental testing

To obtain accurate data, a versatile measurement infrastructure was created. Therefore, it was realized an automation panel for separating the electrical measurements for each PV panel of the system. Also, the possibility of measuring the open circuit or operating voltage was provided – Fig. 10.

The experimental stand was located outside, in real world conditions, to evaluate all the climatic factors involved during the PV panels operation (solar radiation, air temperature, humidity, wind velocity and direction). All these parameters were monitored throughout the testing.

Table 5
Heat sink for cooling photovoltaic panels with perforated vertical fins (***Cool-PV-APVF30***).

Details of the assembly	Real image	Dimensions
		

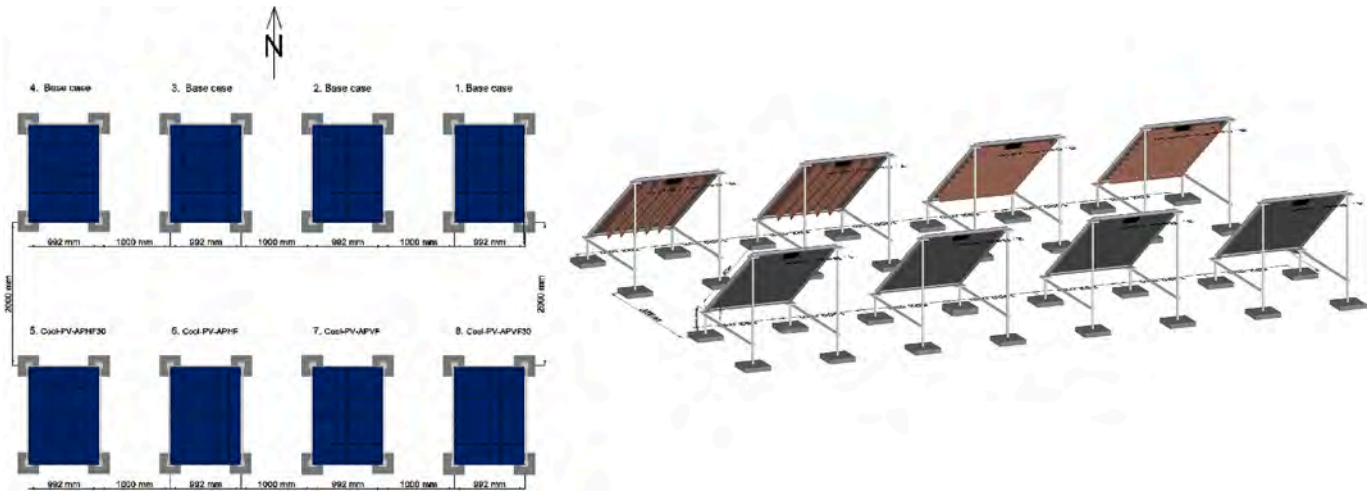


Fig. 9. Spatial arrangement of the PV panels.

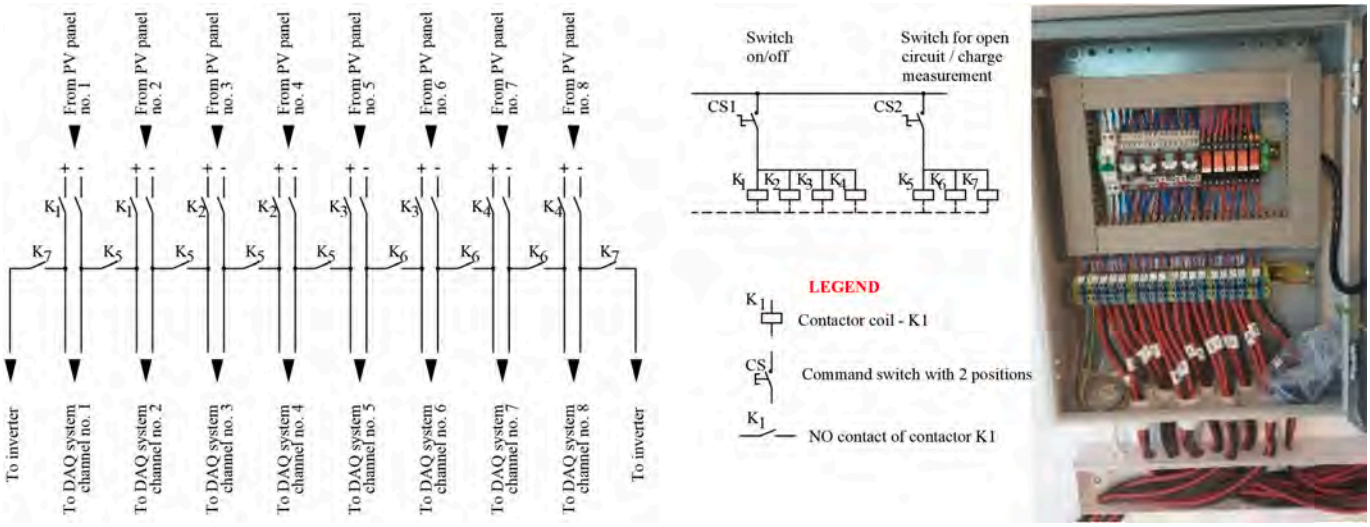


Fig. 10. Automation diagram and electric panel for data acquisition in both open-circuit and under load conditions.

Instrumentation & data acquisition

During the experimental tests, the measurements of the operating temperatures of the photovoltaic panels were made by using K-type contact temperature sensors placed on the back of the photovoltaic panels together with thermal imaging camera coordination [75]. The

Table 6
Characteristics of measurement devices.

Device / Parameter	Unit	Type of device	Measurement range	Accuracy
Data Acquisition Station – Panel Temperatures	–	MS6D Data Logger, simultaneous measurement and recording of temperatures from PT1000	−140…+ 600 °C	2.5 °C around measured value
Data Acquisition Station – Electrical Parameters	V	Sefram BK Precision DAS220	± 100 V	0.1 % within the measured range
Measurement and Recording of the Climatic Parameters (Thermometer, Anemometer, Solar Radiation Sensor)	°C m/s W/ m^2	Weather Station Vantage Pro 2	−40…+65 °C 0.5…89 m/s, 0…1800 W/ m2	±0.5 °C over 20 °C 1 m/s or ± 5 % ± 5 % /1 W/m2
Photovoltaic Panel Temperature	°C	Temperature Sensors PT1000	−50…+ 200 °C	± (0.15 + 0.002*t) °C

Table 7
The uncertainties of the measurement devices.

Device	Measurement range	Accuracy (*a*)	Uncertainty (*u*)
DAS – Panel Temperatures	−140…+600 °C	0.003	0.002
DAS – Electrical Parameters	± 100 V	0.001	0.001
Thermometer	−40…+65 °C	0.005	0.003
Anemometer	0.5…89 m/s,	0.005	0.003
Solar Radiation Sensor	0…1800 W/m^2	0.005	0.003
PT1000 – PV Panel Temperature	−50…+200 °C	0.007	0.004

temperatures were centralized by the aid of a data acquisition system – MS6 Data Logger with 16 channels [76]. The electrical parameters were measured by using PEL 103 equipment [77] and data acquisition systems – Sefram Multipurpose Data Logger – DAS220BAT with 10 channels – for voltage [78] and Chauvin Arnoux CA 8336 Tester [79] and– for current intensity.

The measurement of the intensity of the incident solar radiation on the surface of the photovoltaic panels was carried out with the aid of the pyranometer of the weather station [80].

During the experimental tests, the following physical parameters were measured:

– Solar radiation, air temperature, wind speed, and wind direction.

– Temperatures of the photovoltaic panels (contact temperature probes, thermal imaging camera).

– Electrical parameters: currents, voltages, powers.

All devices used were accompanied by their dedicated software. Table 6 presents the main characteristics of the devices used. The maximum uncertainty of the measurement associated with the instruments is presented in Table 7, while the average percentage is approximately 0,693 %.

The relevant weather data for the experiment's location are presented in Fig. 11 and Fig. 12. In these images, the average solar radiation, air temperatures, wind directions and velocities can be observed. This information was used for preliminary numerical and analytical studies, to establish the optimum characteristics and orientation of the PV panel and for the heat sinks with horizontal or vertical fins.

Results and discussions

The photovoltaic panels with cooling solutions were installed in a structurally and energetically functional photovoltaic system. The focus was on the cooling effect and, consequently, the increase in electrical energy production compared to pilot photovoltaic panels. The testing was conducted during the warm season, with a wide range of climate, energy and electrical data measured and recorded with the specified measuring devices. These data were processed, integrated and correlated as follows.

The cooling effect of the proposed solutions was analyzed for the month of July, characterized by daily average temperatures of 28 °C, highest solar radiation and with typical wind distribution. Considering the need to correlate all the factors involved (personnel, measurement equipment, weather etc.), the experimental results and the effect of the cooling solutions are presented for a representative summer day in Iași – Romania (47.1585° N, 27.6014° E) – 28.07.2024, characterized by clear skies and light winds, Fig. 13.

The wind rose recorded for the studied day and location is presented in Fig. 14.

According to the wind rose, the direction and velocity was on the main axe East-West. This circulation through the PV panels and heat

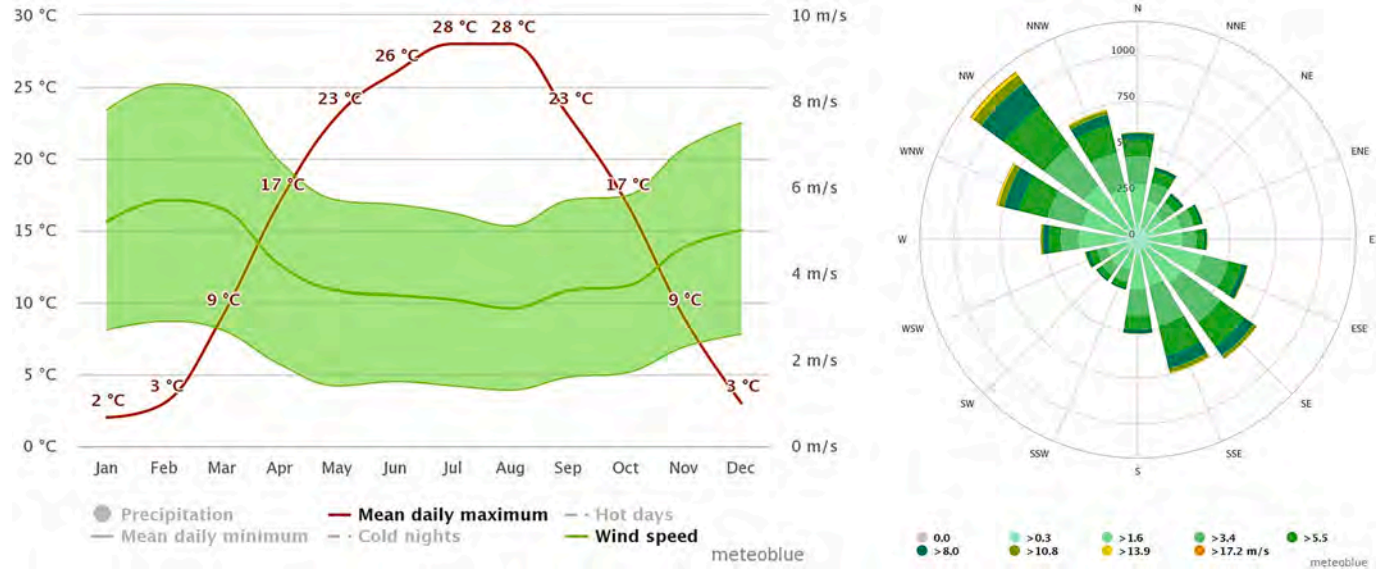


Fig. 11. Typical annual wind speed and temperature distribution [81].

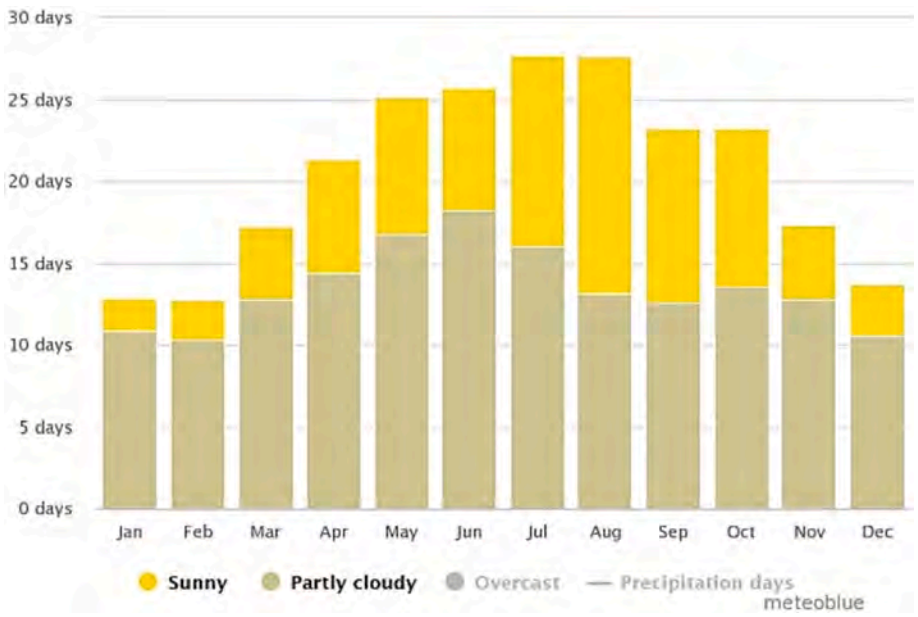


Fig. 12. Typical annual cloudy and sunny days for the study location [81].



Fig. 13. Climate data measured by the weather station in the immediate vicinity of the photovoltaic system on 28.07.2024.

sinks is presented in Fig. 15, which was advantageous both for the base case and air-cooled PV panels.

It can be observed that the electrical energy production of the system on this day follows a typical uniform pattern for a functional photovoltaic system – Fig. 16, which means that the system worked normally and all the photovoltaic panels were operational.

Throughout the measurement day, the electrical parameters of each photovoltaic panel in the functional system were monitored, both for the base case and for the cooling solutions with heat sinks. The cooling analysis was performed during the time interval of 12:00—17:00. During this interval, the higher values of solar radiation led to the generation of electrical energy under relevant operating conditions, but also caused the heating of the external air and of the photovoltaic panels. Therefore, the cooling effect becomes increasingly noticeable as the day progresses. Table 8 shows the maximum increase in the efficiency of photovoltaic panels for each heat sink model compared to the average efficiency in the base cases.

The results of the experimental tests of the proposed models (perforated/non-perforated fin heat sinks) were captured with a thermal imaging camera and illustrated in Figs. 17–19, for the reference case Cool-PV-APHF30 and Cool-PV-APVF30.

Depending on the specific climatic conditions recorded – Fig. 13, the average values of temperature of the PV panels without cooling range between 50…70 °C during the entire interval of study (12.00–17.00 PM, 28.07.2024).

The perforated heat sinks enhanced heat dissipation primarily by promoting convective heat transfer. The perforations increase the surface area exposed to airflow and create turbulence, which disrupts the thermal boundary layer and improves the efficiency of heat removal. Under the average outdoor temperature over 30 °C and the wind velocity of 2 m/s, from the measurement day, the heat sinks reduced the panel's operating temperature by 15 °C. This reduction is attributed to both natural convection and forced convection effects.

Quantitatively, the convective heat transfer coefficient h was calculated using the Nusselt number correlation for perforated surfaces [82]:

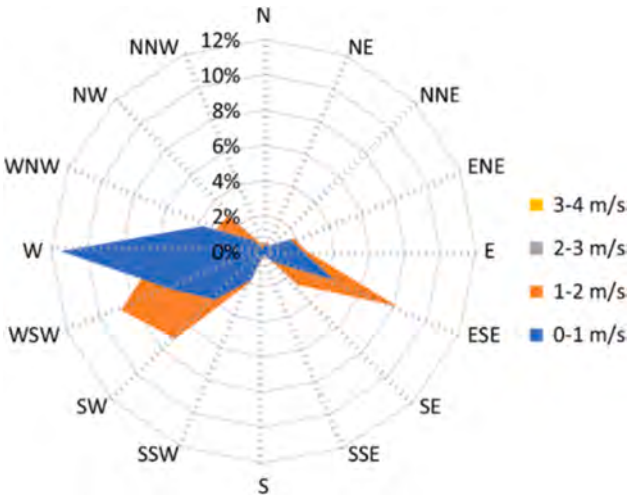


Fig. 14. Wind rose measured at the location of the PV system on 28.07.2024.

$$Nu = C \cdot Re^{n} \cdot Pr^{1/3} \quad (1)$$

Where:
Re – Reynolds number;
Pr – Prandtl number;
were determined based on the airflow properties. The results showed a 20 % increase in h compared to a non-perforated heat sink, directly contributing to the observed reduction in temperature and corresponding efficiency gains of 2.5 %.

Considering that the photovoltaic panels temperature coefficient for the present study is −0.37 %/°C [63], the variation of the average operational temperature and hourly efficiency of the base case PV panels is presented in Fig. 20. The effect of operating temperature on photovoltaic conversion efficiency (η_T) is calculated according to Equation (2).

$$\eta_T = \eta - \eta \cdot \Delta T \cdot \beta \quad (2)$$

Where:
t_{cell} – operating temperature of PV panel (°C);
T_{STC} – operating temperature in standard test conditions (T_{STC} = 25 °C);

Table 8
Increase in the efficiency of PV panels with heat sinks compared to the base case.

Heat Sink Model	Maximum Increase in the Efficiency	Average increase in production during the 12:00—17:00 interval
1. Cool-PV-ANPHF	**5.69 %**	**1.50 %**
2. Cool-PV-APHF30	**5.82 %**	**1.59 %**
3. Cool-PV-ANPVF	**5.28 %**	**1.49 %**
4. Cool-PV-APVF30	**5.92 %**	**1.82 %**

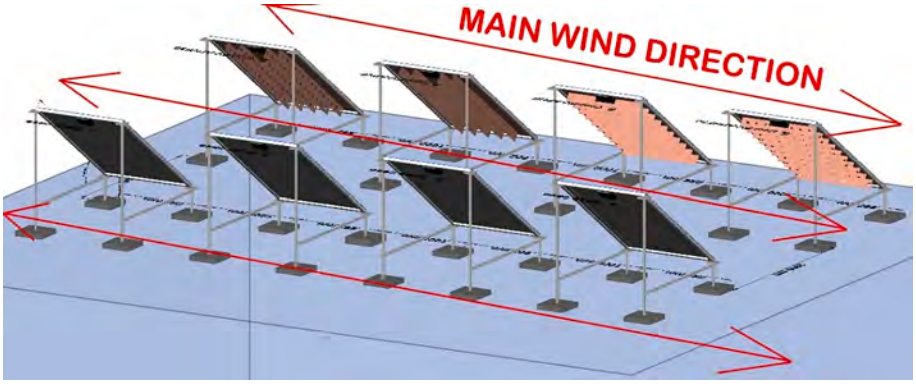


Fig. 15. Main wind direction at the location of the PV panels.

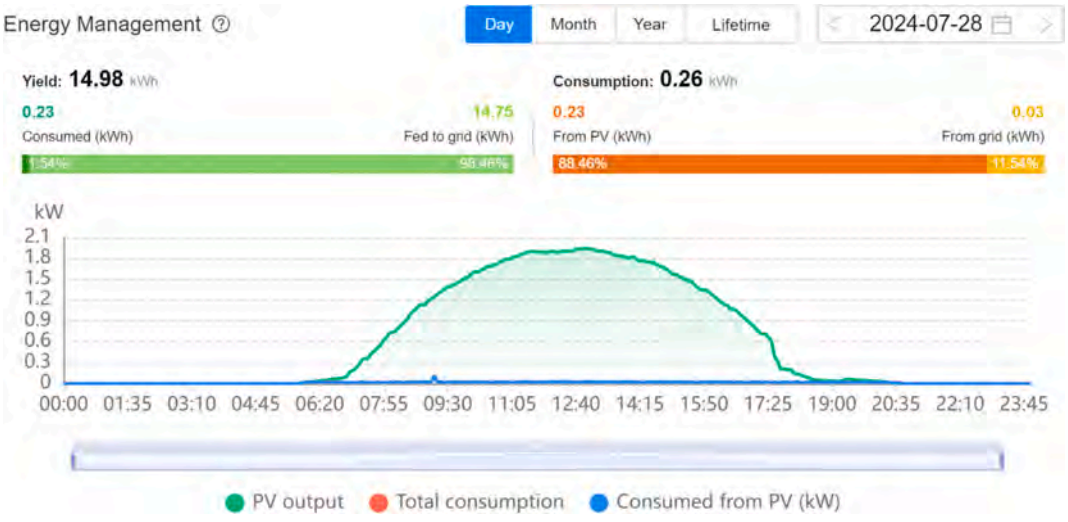


Fig. 16. Electrical energy production of the functional photovoltaic system on 28.07.2024.

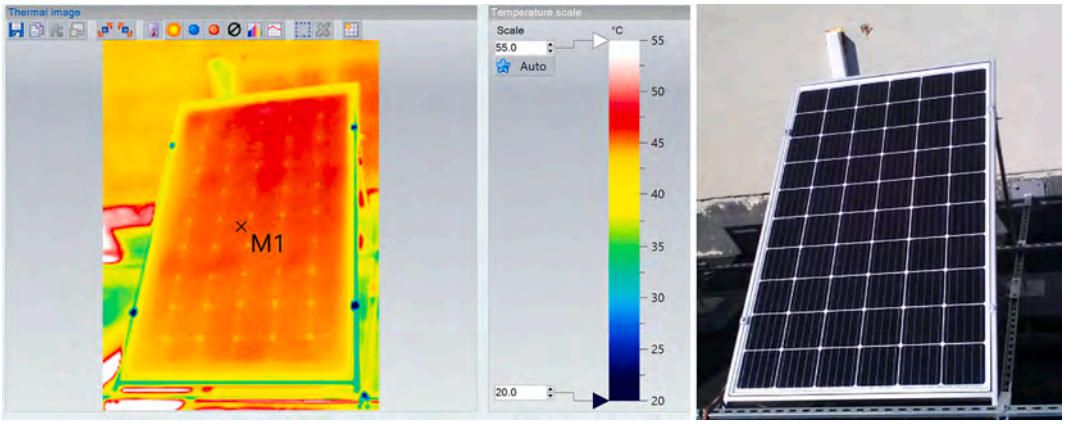


Fig. 17. Thermal imaging camera visualization – base case – without cooling solution.

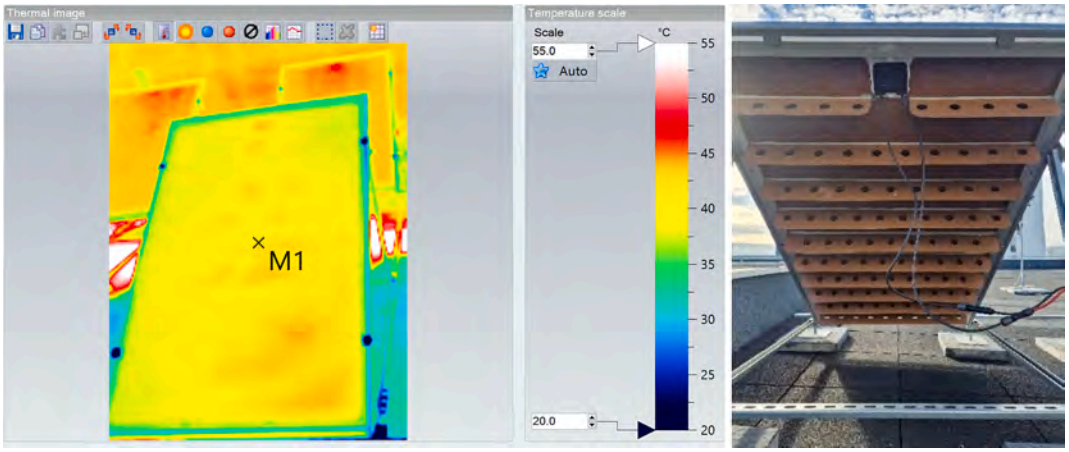


Fig. 18. Thermal imaging camera visualization – air cooling with 30 mm perforated horizontal fin heat sink.

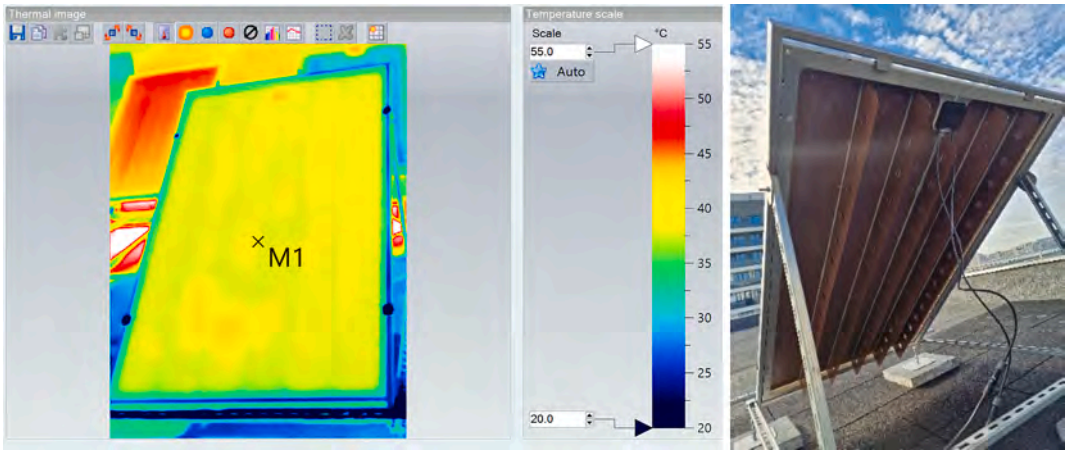


Fig. 19. Thermal imaging camera visualization – air cooling with 30 mm perforated vertical fin heat sink.

ΔT – temperature difference between T_{STC} and t_{cell} (°C);
η_T – PV panel efficiency for temperature T (%);
η – Efficiency of conversion in STC (%);
β – Temperature Coefficient of a PV Cell Efficiency (%/°C).

From a **functional** perspective, all 4 heat sink models result in a significantly similar improvement in the efficiency of photovoltaic panels (in the range of 5.28 % to 5.92 %), with slight advantages observed in the perforated fin heat sinks (5.82 % to 5.92 %) compared to non-perforated ones (5.28 % to 5.69 %). From the constructive and the **economic** perspective, considering the material savings achieved through perforations (approximately 5 %), it is evident that the perforated heat sinks provide superior improvement at a lower cost compared to non-perforated ones. The results have confirmed the anticipated effects and demonstrated the usefulness and feasibility of the proposed models. The prototypes of photovoltaic panel cooling solutions can provide all the required functions of the operational photovoltaic system, leading to an improvement in efficiency as shown in Figs. 21–24.

According to initial expectations [3,22], the proposed heat sink

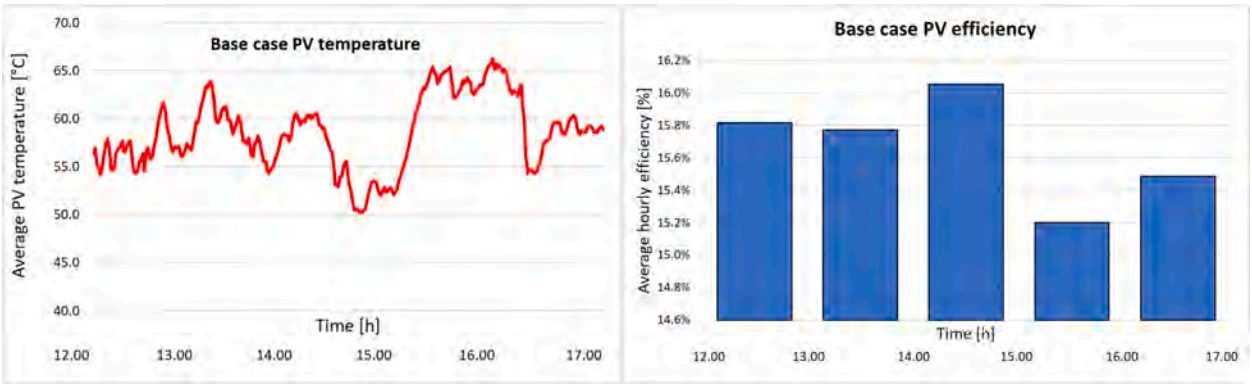
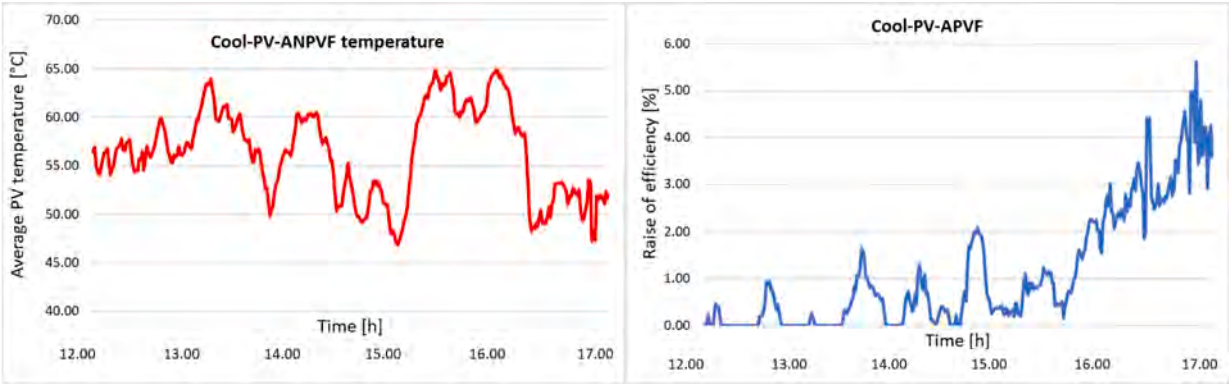
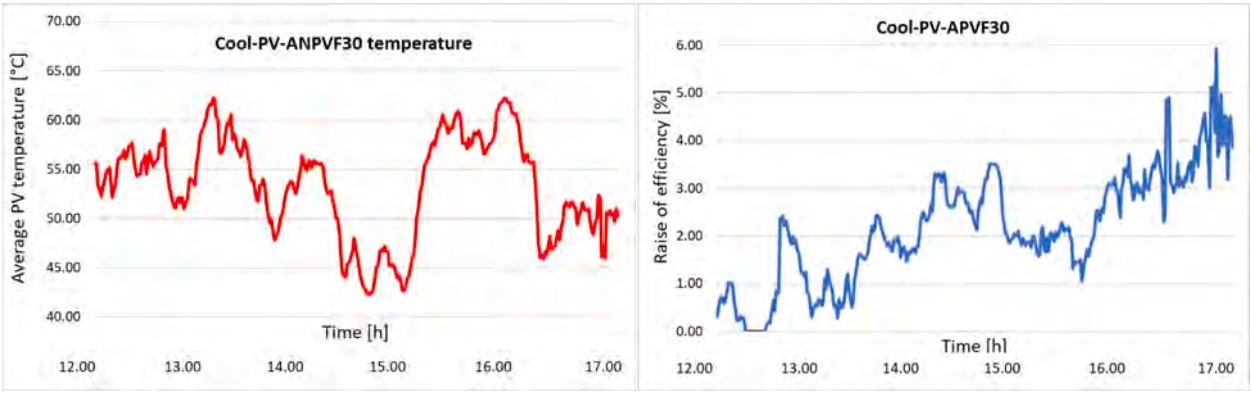


Fig. 20. Evolution of the average operational temperature and efficiency of the base case PV panels.



a) b)

Fig. 21. Operating temperature (a) and PV panel efficiency increase (b) – **ANPVF.**



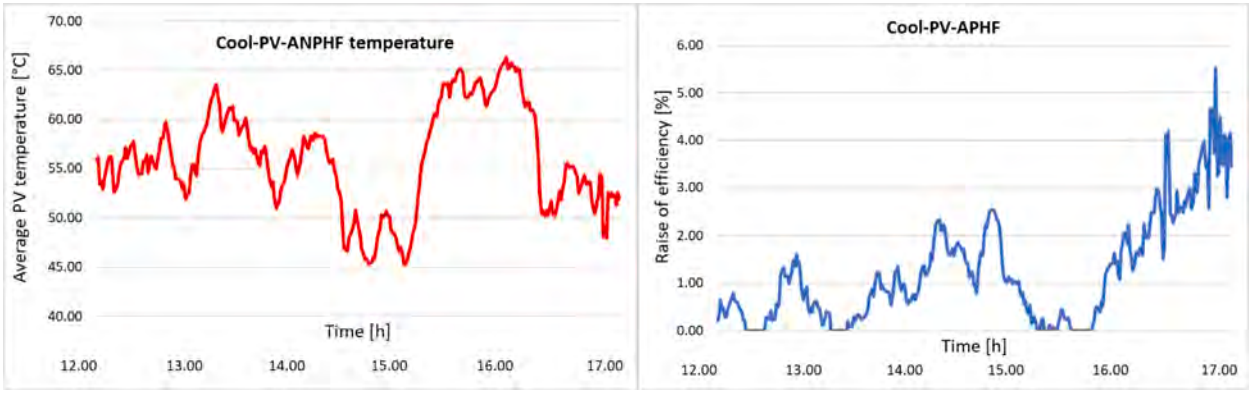
a) b)

Fig. 22. Operating temperature (a) and PV panel efficiency increase (b) – **ANPVF30.**

models were expected to improve the efficiency of photovoltaic panels under optimal conditions by 6.97 % to 7.55 % compared to the base case. According to the experimental results, this increase reaches values between **5.28 %** and **5.92 %.** The recorded differences fall within an acceptable margin, considering the variations that occur between the theoretical models (ideal – constant climatic parameters and stationary thermodynamic regime) and the experimental models (real – variable climatic parameters and variable thermodynamic regime, wind effect on the base case panel was also important).

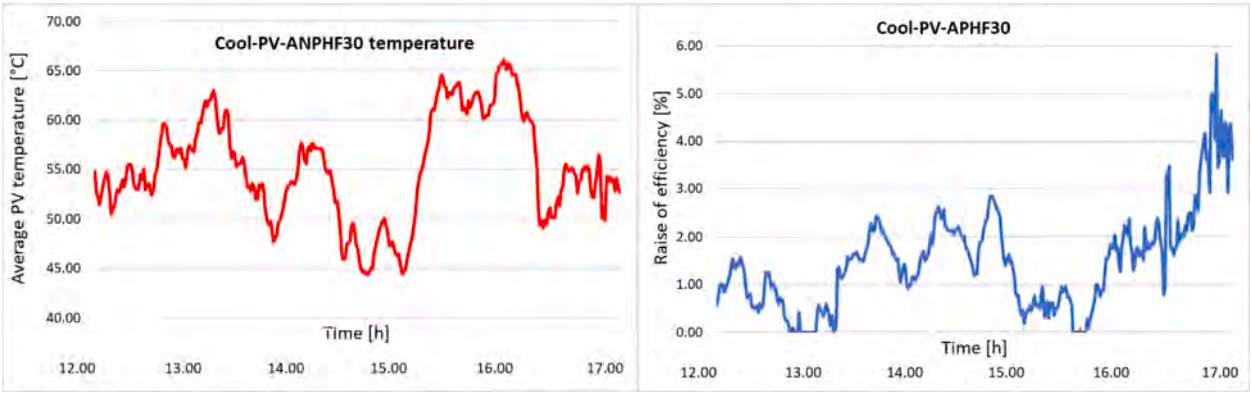
The use of outdoor analysis for perforated heat sinks provides a more realistic evaluation than previous indoor experimental studies [83] or numerical analysis [54,84] on PV air cooling. Unlike existing research in literature [85], this study demonstrates that perforated heat sinks can achieve 5.92 % efficiency improvement under outdoor conditions.

However, considering that the analysis was carried out on a specific condition of a functional photovoltaic system, it is possible that differences could occur compared to the statistical situation of all specific applications in the market. Therefore, a post-implementation SWOT



a) b)

Fig. 23. Operating temperature (a) and PV panel efficiency increase (b) – **ANPHF.**



a) b)

Fig. 24. Operating temperature (a) and PV panel efficiency increase (b) – **ANPHF30.**

analysis was performed, with the following results:

Strengths: – Viable solutions in functional systems.

– Relatively simple labor.

Weaknesses: – Increased material costs.

– Intervention in existing functional equipment.

Opportunities: – Rising electricity prices.

– Use of materials with similar thermophysical characteristics but lower cost.

– Optimal positioning of photovoltaic panels in terms of solar radiation, wind direction, and speed.

Threats: – Heat sinks can only be used with photovoltaic panels that have sufficiently large space at the back for the proposed models.

– Climate and technical uncertainties.

Conclusions

In the study, particular types of copper heat sinks with optimized perforated/non-perforated fins were studied. A novel approach of the cooling effect was integrated by analyzing a real scale photovoltaic system in typical operating conditions – in terms of solar radiation, wind velocity and direction, air temperature, electrical and thermal parameters of the panels. The results presented in this paper are the outcome of several years of phased work, progressing from the formulation of the technological concept to detailed numerical analysis and then to the design of the experimental setup with the presented specifications.

Based on the experimental results, the technological maturity level of the studied models reached a TRL 6 by validating the functionality of the models (heat sinks with perforated and non-perforated fins) under relevant operating conditions. Consequently, the proposed cooling solutions were integrated into a fully functional photovoltaic system installed on the building's terrace and subjected to real climatic conditions. The experimental tests were carried out at full scale in a fully operational system.

General results

The results obtained demonstrated the usefulness and feasibility of the proposed models. They confirmed the anticipated effects and demonstrated the viability of the proposed cooling technologies. All prototypes of photovoltaic panel cooling solutions with heat sinks are capable of operating and fulfilling all the required functions of the operational photovoltaic system, leading to an improvement in efficiency.

Specific results

– Each cooling solution tested in this research improves the efficiency of photovoltaic panels and ensures **uniform** temperature distribution across the panel surface.

– From a functional perspective, all four heat sink models (**Cool-PV-ANPHF, Cool-PV-APHF30, Cool-PV-ANPVF, Cool-PV-APVF30**) result in a significant improvement in photovoltaic panel efficiency (in the range of **5.28 % to 5.92 %**), with slight advantages induced by perforated fin heat sinks (**5.82 % to 5.92 %**) compared to non-perforated

ones (**5.28 % to 5.69 %**).

– From an economical and constructive perspective, considering the material savings (approximately **5 %**) achieved through perforation, it is evident that perforated heat sinks provide superior improvement at a lower cost compared to non-perforated ones.

Improving photovoltaic efficiency using perforated heat sinks contributes to practical applications such as enhancing the performance of solar panels in residential, commercial, or industrial setups; reducing the cooling requirements for photovoltaic systems, leading to cost savings; efficient renewable energy systems and achieving sustainability goals.

CRediT authorship contribution statement

Sebastian-Valeriu Hudișteanu: . **Nelu-Cristian Cherecheș:** Software, Investigation, Conceptualization. **Florin-Emilian Țurcanu:** Investigation, Data curation. **Iuliana Hudișteanu:** Writing – review & editing, Formal analysis. **Marina Verdeș:** Supervision, Conceptualization. **Ana-Diana Ancaș:** Writing – review & editing, Formal analysis.

Declaration of competing interest

The authors declare that they have no known competing financial interests or personal relationships that could have appeared to influence the work reported in this paper.

Acknowledgments

This work was supported by a grant of the Romanian Ministry of Education and Research, CCCDI-UEFISCDI, project number PN-III-P2-2.1-PED-2019-1294, 443PED/2020 within PNCDI III.

Data availability

The data that has been used is confidential.

References

[1] Zaite A, Belouaggadia N, Abid C, Kaiss A, Imghoure O. Performance Enhancement of a Photovoltaic-Thermal Thermoelectric Collector Using Night Radiative Cooling. Appl Energy 2024;364. https://doi.org/10.1016/j.apenergy.2024.123108.
[2] Information available at: www.overshootday.org, last accessed: 12.08.2024.
[3] Hudișteanu SV, Țurcanu FE, Cherecheș N-C, Popovici C-G, Verdeș M, Ancaș D-A, et al. Effect of Wind Direction and Velocity on PV Panels Cooling with Perforated Heat Sinks. Appl Sci 2022;12:9665.
[4] Jha P, Das B, Gupta R, Mondol JD, Ehyaei MA. Review of Recent Research on Photovoltaic Thermal Solar Collectors. Sol Energy 2023;257:164–95. https://doi.org/10.1016/j.solener.2023.04.004.
[5] Information available at: www.transelectrica.ro/widget/web/tel/sen-grafic, last accessed: 12.08.2024.
[6] Photovoltaic (PV) module performance testing and energy rating—Part 1: Irradiance and temperature performance measurements and power rating. In International Standard; IEC 61853-1; Geneva, Switzerland, 2011.
[7] Basak A, Chakraborty S, Behura AK. Tilt angle optimization for bifacial PV module: Balancing direct and reflected irradiance on white painted ground surfaces. Appl Energy 2025;377. https://doi.org/10.1016/j.apenergy.2024.124525.
[8] Baouche FZ, Abderezzak B, Ladmi A, Arbaoui K, Suciu G, Mihaltan TC, et al. Design and Simulation of a Solar Tracking System for PV. Appl Sci 2022;12:9682.
[9] Hudișteanu SV, Cherecheș NC, Popovici CG, Verdeș M, Ciocan V. Effect of cooling on power generated by photovoltaic panels. IOP Conf Ser: Mater Sci Eng 2021; 1141:012008.
[10] Sharaf M, Yousef MS, Huzayyin AS. Review of cooling techniques used to enhance the efficiency of photovoltaic power systems. Environ Sci Pollut Res 2022;29: 26131–59.
[11] Kaneesamkandi Z, Rehman AU. Selection of a Photovoltaic Panel Cooling Technique Using Multi-Criteria Decision Analysis. Applied Sciences (switzerland) 2023;13. https://doi.org/10.3390/app13031949.
[12] Ibrahim OAAM, Kadhim SA, Al-Ghezi MKS. Photovoltaic Panels Cooling Technologies: Comprehensive Review. Archives of Thermodynamics 2023;44: 581–617.
[13] Solanki, R.; Singh, V.; Varshney, L.; Kumar, K. Advanced Cooling Technique to Improve Efficiency of Solar Panel. In Proceedings of the 2023 International Conference on IoT, Communication and Automation Technology, ICICAT 2023; Institute of Electrical and Electronics Engineers Inc., 2023.
[14] Zhou Z, Gentle A, Mohsenzadeh M, Jiang Y, Keevers M, Green M. Long-Term Outdoor Testing of Vortex Generators for Passive PV Module Cooling. Sol Energy 2024;275. https://doi.org/10.1016/j.solener.2024.112610.
[15] Siow LT, Lee JR, Ooi EH, Lau E. Von Application of Graphene and Graphene Derivatives in Cooling of Photovoltaic (PV) Solar Panels: A Review. Renew and Sustainable. Energy Rev 2024;193.
[16] Koohestani SS, Nižetić S, Santamouris M. Comparative Review and Evaluation of State-of-the-Art Photovoltaic Cooling Technologies. J Clean Prod 2023;406. https://doi.org/10.1016/j.jclepro.2023.136953.
[17] Basem A, Mukhtar A, Salem Elbarbary ZM, Atamurotov F, Benti NE. Experimental study on the various varieties of photovoltaic panels (PVs) cooling systems to increase their electrical efficiency. PLoS One 2024;19(9):e0307616.
[18] Kaneesamkandi Z, Almalki MJ, Sayeed A, Haidar ZA. Passive Cooling of PV Modules Using Heat Pipe Thermosiphon with Acetone: Experimental and Theoretical Study. Applied Sciences (switzerland) 2023;13. https://doi.org/10.3390/app13031457.
[19] Kashan ME, Fung AS, Hossein Eisapour A, Swift J. Utilizing Novel Industrialized Heat Exchanger Plate in Air-Based Photovoltaic/Thermal Collectors to Enhance Thermal and Electrical Efficiency. Energy Convers Manage: X 2024;100752. https://doi.org/10.1016/j.ecmx.2024.100752.
[20] Alzgool M. Performance Enhancement by Cooling the PV Panels Using Phase Change Material (RT35): ANSYS Simulation and Experimental Investigation. International Journal of Energy Production and Management 2024;9:73–81. https://doi.org/10.18280/ijepm.090202.
[21] Nguyen DPN, Neyts K, Lauwaert J. Proposed Models to Improve Predicting the Operating Temperature of Different Photovoltaic Module Technologies under Various Climatic Conditions. Appl Sci 2021;11:7064. https://doi.org/10.3390/app11157064.
[22] Hudișteanu SV, Țurcanu FE, Cherecheș NC, Popovici CG, Verdeș M, Hudisteanu I. Enhancement of PV Panel Power Production by Passive Cooling Using Heat Sinks with Perforated Fins. Appl Sci 2021;11:11323. https://doi.org/10.3390/app112311323.
[23] Kazemian A, Khatibi M, Entezari S, Ma T, Yang H. Efficient energy generation and thermal storage in a photovoltaic thermal system partially covered by solar cells and integrated with organic phase change materials. Renew Sustain Energy Rev 2023;188. https://doi.org/10.1016/j.rser.2023.113705.
[24] Chen, L., Baghoolizadeh, M., Basem, A., Ali, S. H., Ruhani, B., Sultan, A. J., Salahshour, S., & Alizadeh, A. (2024). A comprehensive review of a building-integrated photovoltaic system (BIPV). In International Communications in Heat and Mass Transfer (Vol. 159). Ltd. https://doi.org/10.1016/j.icheatmasstransfer.2024.108056.
[25] Beldjani C, Belghar N, Aoues K, Saleh MSM, Boutera Y, Kethiri MA. Efficiency Improvement of Air-Cooled Photovoltaic Modules Utilizing Copper Heat Dissipators. Desalination Water Treat 2022;279:140–6. https://doi.org/10.5004/dwt.2022.29099.
[26] Rousseau P, Nouri H. ANSYS Investigation of Solar Photovoltaic Temperature Distribution for Improved Efficiency. International Journal of Advances in Applied Sciences 2023;12:293–300. https://doi.org/10.11591/ijaas.v12.i3.pp293-300.
[27] Grigore R, Vernica SG, Popa SE, Banu IV. Simulation and Experimental Results for Energy Production Using Hybrid Photovoltaic Thermal Technology. Energies 2024; 17:1422. https://doi.org/10.3390/en17061422.
[28] Shojaeefard MH, Sakran NB, Sharfabadi MM, Hussein OA, Mohammed HA. Experimental and Numerical Investigation of the Effect of Water Cooling on the Temperature Distribution of Photovoltaic Modules Using Copper Pipes. Energies 2023;16:4102.
[29] Prasetyo SD, Arifin Z, Prabowo AR, Budiana EP. Investigation of the Addition of Fins in the Collector of Water/Al2O3-Based PV/T System: Validation of 3D CFD with Experimental Study. Case Stud Therm Eng 2024;60. https://doi.org/10.1016/j.csite.2024.104682.
[30] Babaelahi M, Kazemi A. Optimal energy system configuration for zero energy buildings using hybrid thermal-photovoltaic solar collector. Environ Dev Sustain 2024.
[31] El Fouas C, Cherecheș NC, Hudișteanu SV, Hajji B, Țurcanu EF, Cherecheș ML. Numerical and Parametric Analysis for Enhancing Performances of Water Photovoltaic/Thermal System. Appl Sci 2022;12:646. https://doi.org/10.3390/app12020646.
[32] K. Bilen Erdoğan İ 2023 A Comprehensive Review. Solar Energy Effects of Cooling on Performance of Photovoltaic/Thermal (PV/T) Solar Panels 262.
[33] Hosseini F, Sheikholeslami M, Ghasemian M. Recent Techniques for Cooling of Concentrated Photovoltaic Thermal Systems. J Therm Al Cal 2024;149:3913–35. https://doi.org/10.1007/s10973-024-12984-1.
[34] Ibrahim T, Abou Akrouch M, Hachem F, Ramadan M, Ramadan HS, Khaled M. Cooling Techniques for Enhanced Efficiency of Photovoltaic Panels—Comparative Analysis with Environmental and Economic Insights. Energies 2024;17:713. https://doi.org/10.3390/en17030713.
[35] Dehghan M, Rahgozar S, Pourrajabian A, Aminy M, Halek FS. Techno-economic perspectives of the temperature management of photovoltaic (PV) power plants: A case-study in Iran. Sustainable Energy Technol Assess 2021;45. https://doi.org/10.1016/j.seta.2021.101133.
[36] Ma X, Ghosh A, Cuce E, Saboor S. Building integrated photovoltaic-thermal systems (BIPVT) and spectral splitting technology: A critical review. Next Sustainability 2024;4:100056. https://doi.org/10.1016/j.nxsust.2024.100056.
[37] Ren H, Quan Z, Wang Z, Wang L, Jing H, Zhao Y. Performance simulation and analysis of a multi-energy complementary energy supply system for a novel BIPVT nearly zero energy building. Energ Conver Manage 2023;282. https://doi.org/10.1016/j.enconman.2023.116879.

[38] Information available at: https://www.theheatpumpwarehouse.co.uk/shop/solar/joule-solar-panels, last accessed: 12.08.2024.
[39] Information available at: https://www.solarmastertech.com/?post_type=products&page_id=23920, last accessed: 12.08.2024.
[40] Wang F, Li Z, Liu M, Liu X, Pang D, Du W, et al. Heat-Dissipation Performance of Photovoltaic Panels with a Phase-Change-Material Fin Structure. J Clean Prod 2023;423. https://doi.org/10.1016/j.jclepro.2023.138756.
[41] Sheikh Y, Jasim M, Hamdan MO, Abu-Nabah BA, Gerner F. Design and Performance Assessment of a Solar Photovoltaic Panel Integrated with Heat Pipes and Bio-Based Phase Change Material: A Hybrid Passive Cooling Strategy. J Energy Storage 2024;100. https://doi.org/10.1016/j.est.2024.113706.
[42] Sheikh Y, Jasim M, Qasim M, Qaisieh A, Hamdan MO, Abed F. Enhancing PV Solar Panel Efficiency through Integration with a Passive Multi-Layered PCMs Cooling System: A Numerical Study. International Journal of Thermofluids 2024;23. https://doi.org/10.1016/j.ijft.2024.100748.
[43] Lima-Téllez T, Hinojosa JF, Hernández-López I, Moreno S. Numerical Study of the Thermal Performance of a Single-Channel Cooling PV System Using Baffles and Different Nanofluids. Heliyon 2024;10. https://doi.org/10.1016/j.heliyon.2024.e35413.
[44] Prasetyo SD, Arifin Z, Prabowo AR, Budiana EP. Examining Various Finned Collector Geometries in the Water/Al2O3 Based PV/T System: An Analysis Using Computational Fluid Dynamics Simulation. Int J Heat Technol 2024;42:851–64. https://doi.org/10.18280/ijht.420314.
[45] Wang Q, Yu C, Li T, Wang J, Liu Y, Shi Y, et al. Enhancing the performance of PVT-TEG power generation systems by heat pipes and Fe3O4 nanofluids. Energ Conver Manage 2024;319. https://doi.org/10.1016/j.enconman.2024.118938.
[46] Alktranee M, Al-Yasiri Q, Saeed Mohammed K, Al-Lami H, Bencs P. Energy and exergy assessment of a photovoltaic-thermal (PVT) system cooled by single and hybrid nanofluids. Energy Convers Manage: X 2024;24. https://doi.org/10.1016/j.ecmx.2024.100769.
[47] Dey A, Ahmed ZU, Ramijul Alam M. Thermal and exergy analysis of Pin-finned heatsinks for nanofluid cooled high concentrated photovoltaic thermal (HCPV/T) hybrid systems. Energy Convers Manage: X 2022;16. https://doi.org/10.1016/j.ecmx.2022.100324.
[48] Alajlan AM, Dang S, Gan Q. Enhanced nighttime power generation and photovoltaic cooling in photovoltaic-thermoelectric hybrid systems. Energy Convers Manage: X 2024;22. https://doi.org/10.1016/j.ecmx.2024.100580.
[49] Kuefouet Alexis L, Julius Kewir T, Merlain KB, D., & Segning Harry Bertholt, S.. Experimental study on the electrical and thermal characteristics of a hybrid photovoltaic/thermal water solar collector model using photovoltaic solar modules of different brands. Energy Convers Manage: X 2022;14. https://doi.org/10.1016/j.ecmx.2022.100198.
[50] Abdallah R, Haddad T, Zayed M, Juaidi A, Salameh T. An Evaluation of the Use of Air Cooling to Enhance Photovoltaic Performance. Therm Sci Eng Prog 2024;47. https://doi.org/10.1016/j.tsep.2023.102341.
[51] Al-Azawiey SS, Mohamed MM, Arifin AB. Effectiveness of PV/T Passive Natural Air Cooling by Backside Attached Fins. International Journal of Energy Production and Management 2023;8:55–62. https://doi.org/10.18280/ijepm.080201.
[52] Dunne NA, Liu P, Elbarghthi AFA, Yang Y, Dvorak V, Wen C. Performance evaluation of a solar photovoltaic-thermal (PV/T) air collector system. Energy Convers Manage: X 2023;20. https://doi.org/10.1016/j.ecmx.2023.100466.
[53] Khanalizadeh A, Razi Astaraei F, Heyhat MM, Vaziri Rad MA. Experimental Investigation of a PV/T System Containing a TEG Section between Water-Based Heat Exchanger and Air-Based Heat Sink. Therm Sci Eng Prog 2023;42. https://doi.org/10.1016/j.tsep.2023.101909.
[54] Khosravi K, Mohammed HI, Mahdi JM, Silakhori M, Ebrahimnataj Tiji M, Kazemian A, et al. Optimizing performance of water-cooled photovoltaic-thermal modules: A 3D numerical approach. Sol Energy 2023;264. https://doi.org/10.1016/j.solener.2023.112025.
[55] I.O. Harmailil S.M. Sultan C.P. Tso A. Fudholi M. Mohammad A. Ibrahim A Review on Recent Photovoltaic Module Cooling Techniques: Types and Assessment Methods in Results in Engineering Vol. 22 2024 Elsevier B.V 10.1016/j.rineng.2024.102225.
[56] Mdallal A, Haridy S, Mahmoud M, Alami AH, Olabi AG, Abdelkareem MA. Modelling and optimization of concentrated solar power using response surface methodology: A comparative study of air, water, and hybrid cooling techniques. Energy Conv and Manag 2024;319. https://doi.org/10.1016/j.enconman.2024.118915.
[57] Shaik F, Lingala SS, Veeraboina P. Effect of various parameters on the performance of solar PV power plant: a review and the experimental study. Sustainable Energy Res 2023;10:6.
[58] Del Rio JAS, Ardila YR, Sánchez AR, Quintana EC, Sanin-Villa D, González CA, et al. Numerical Study of the Efficiency of a Solar Panel with Heat Sinks. CFD Lett 2023;15:43–52. https://doi.org/10.37934/cfdl.15.4.4352.
[59] Van Binh D, Vu PQ, Pham MH, Nguyen DT, Nguyen NT, Do QH, et al. Passive Cooling for Photovoltaic Using Heat Sinks: A Recent Research Review. IEEE Inc.; 2023.
[60] Krstic M, Pantic L, Djordjevic S, Radonjic I, Begovic V, Radovanovic B, et al. Passive Cooling of Photovoltaic Panel by Aluminum Heat Sinks and Numerical Simulation. Ain Shams Eng J 2024;15. https://doi.org/10.1016/j.asej.2023.102330.
[61] Razali SN, Ibrahim A, Fazlizan A, Fauzan MF, Ajeel RK, Zairah Ahmad E, et al. Performance Enhancement of Photovoltaic Modules with Passive Cooling Multidirectional Tapered Fin Heat Sinks (MTFHS). Case Stud Therm Eng 2023;50. https://doi.org/10.1016/j.csite.2023.103400.
[62] Hamed MH, Hassan H, Ookawara S, Nada SA. Performance Comparative Study on Passively Cooled Concentrated Photovoltaic (PV) Using Adsorption/Desorption and Heat Sink Cooling Methods: Experimental Investigations. Energy 2024;307. https://doi.org/10.1016/j.energy.2024.132700.
[63] Salehi R, Jahanbakhshi A, Ooi JB, Rohani A, Golzarian MR. Study on the Performance of Solar Cells Cooled with Heatsink and Nanofluid Added with Aluminum Nanoparticle. International Journal of Thermofluids 2023;20. https://doi.org/10.1016/j.ijft.2023.100445.
[64] Cabrera-Escobar R, Vera D, Cabrera-Escobar J, Paredes Godoy MM, Cajamarca Carrazco D, Zumba Llango ER, et al. Finite Element Analysis Method Design and Simulation of Fins for Cooling a Monocrystalline Photovoltaic Panel. Clean Technol 2024;6:767–83. https://doi.org/10.3390/cleantechnol6020039.
[65] Xiao L, Gan LN, Wu SY, Chen ZL. Temperature Uniformity and Performance of PV/T System Featured by a Nanofluid-Based Spectrum-Splitting Top Channel and an S-Shaped Bottom Channel. Renew Energy 2021;167:929–41. https://doi.org/10.1016/j.renene.2020.12.015.
[66] Muneeshwaran M, Sajjad U, Ahmed T, Amer M, Ali HM, Wang CC. Performance Improvement of Photovoltaic Modules via Temperature Homogeneity Improvement. Energy 2020;203. https://doi.org/10.1016/j.energy.2020.117816.
[67] V. Hudisteanu N. Chereches Heat-dissipation device with perforated fins for cooling photovoltaic panels, Patent Assignee: Univ Iasi Tehnica Asachi Gheorghe, Derwent Primary Accession Number 2019 DIIDW:201936097P 2019 36097P.
[68] Popovici CG, Hudișteanu SV, Mateescu TD, Cherecheș NC. Efficiency Improvement of Photovoltaic Panels by Using Air Cooled Heat Sinks. Energy Procedia 2016;85:425–32. https://doi.org/10.1016/j.egypro.2015.12.223.
[69] Information available at: www.google.com/maps/@47.1536636,27.5921657,112m/data=!3m1!1e3? entry=ttu&g_ep=EgoyMDI0MDkyMy4wIKXMDSoASAFQAw%3D%3D, last accessed: 12.08.2024.
[70] last accessed, Information available at 12.08.2024.
[71] Madhi H, Aljabair S, Imran AA, (n.d.).. Comparative numerical study on the effect of fin orientation on the photovoltaic/thermal (PV/T) system performance. International Journal of Thermofluids 2024.
[72] Ehsani H, Roudbari FN, Namaghi SS, Jalili P, Ganji DD. Investigating thermal performance enhancement in perforated pin fin arrays for cooling electronic systems through integrated CFD and deep learning analysis. Results Eng 2024;22. https://doi.org/10.1016/j.rineng.2024.102016.
[73] Rasangika HDK, A., Shakir Nasif, M., & Al-Waked, R.. Numerical investigation on the thermal performance of perforated and non-perforated twisted fins at different twisting angles. Results Eng 2024;23. https://doi.org/10.1016/j.rineng.2024.102332.
[74] Information available at: https://www.davisinstruments.com/products/wireless-vantage-pro2-plus-with-uv-solar-radiation-sens ors-and-weatherlink-console, last accessed: 12.08.2024.
[75] Information available at: https://www.testo.com/en/testo-871/p/0560-8712, last accessed: 12.08.2024.
[76] Information available at: https://www.cometsystem.com/products/sixteen-channel-data-logger-with-alarms/reg-ms6d, last accessed: 12.08.2024.
[77] Information available at: https://www.tme.eu/ro/details/ca-pel103/analizori-calitate-electricitate/chauvin-arnoux/pel-103, last accessed: 12.08.2024.
[78] Information available at: https://ro.farnell.com/sefram/das220bat/handheld-recorder-w-battery-10ch/dp/3010315, last accessed: 12.08.2024.
[79] Information available at: https://www.tme.eu/en/details/ca-8336/power-quality-analyzers/chauvin-arnoux/c-a-8336, last accessed: 12.08.2024.
[80] Information available at: https://www.davisinstruments.com/products/solar-radiation-sensor?srsltid=AfmBOopmf-F0qI3KIdkMAWg5QKHohAikQs14i9i-7GN2uU6aVJIYVrtj, last accessed: 12.08.2024.
[81] Information available at: https://www.meteoblue.com, last accessed: 12.08.2024.
[82] Herwig H. What exactly is the Nusselt number in convective heat transfer problems and are there alternatives? Entropy 2016;18(5). https://doi.org/10.3390/e18050198.
[83] Hudișteanu V-S, Cherecheș N-C, Țurcanu F-E, Hudișteanu I, Romila C. Impact of Temperature on the Efficiency of Monocrystalline and Polycrystalline Photovoltaic Panels: A Comprehensive Experimental Analysis for Sustainable Energy Solutions. Sustainability 2024;16(23):10566. https://doi.org/10.3390/su162310566.
[84] Al Amri F, Al Zohbi G, Al Zahrani M, Aboulebdah M. Analytical Modeling and Optimization of a Heat Sink Design for Passive Cooling of Solar PV Panel. Sustainability 2021;13(6):3490. https://doi.org/10.3390/su13063490.
[85] Arifin Z, Tjahjana DDDP, Hadi S, Rachmanto RA, Setyohandoko G, Sutanto B. Numerical and experimental investigation of air cooling for photovoltaic panels using aluminum heat sinks. Int J Photoenergy 2020;2020. https://doi.org/10.1155/2020/1574274.

sustainability

MDPI

Article

Impact of Temperature on the Efficiency of Monocrystalline and Polycrystalline Photovoltaic Panels: A Comprehensive Experimental Analysis for Sustainable Energy Solutions

Valeriu-Sebastian Hudișteanu *, Nelu-Cristian Cherecheș *, Florin-Emilian Țurcanu, Iuliana Hudișteanu and Claudiu Romila

Faculty of Civil Engineering and Building Services, Gheorghe Asachi Technical University of Iasi, 700050 Iași, Romania; florin-emilian.turcanu@academic.tuiasi.ro (F.-E.Ț.); iuliana.hudisteanu@academic.tuiasi.ro (I.H.); claudiu.romila@academic.tuiasi.ro (C.R.)

* Correspondence: valeriu-sebastian.hudisteanu@academic.tuiasi.ro (V.-S.H.); nelu.chereches@academic.tuiasi.ro (N.-C.C.)

Abstract: The negative effect of the operating temperature on the functioning of photovoltaic panels has become a significant issue in the actual energetic context and has been studied intensively during the last decade. The very high operating temperatures of the photovoltaic panels, even for lower levels of solar radiation, determine a drop in the open-circuit voltage, with consequences over the electrical power generated and PV-conversion efficiency. The temperature effect over the efficiency of monocrystalline and polycrystalline photovoltaic panels by using a double-climatic chamber and a solar simulation device was studied experimentally for two photovoltaic panels, one monocrystalline and another polycrystalline, with the same nominal power of 30 Wp. The double-climatic chamber used is composed of two separate rooms, a cold and a hot one, while the PV panel is placed as a barrier between them. The study is focused on establishing the effect of raising the temperature of PV panels over electrical parameters: voltage, current, and power produced and for efficiency and fill factor to promote sustainable energy consumption. The findings highlight the positive impact of cooling on enhancing system efficiency, with the primary focus on quantifying its overall performance. The operating temperature is controlled by the flow of air on the backside of the PV panel inside the cold room. The level of radiation studied corresponds to a vertical integration of PV panels in building façades. The coefficient of the mean variation of the efficiency with the photovoltaic panels' temperature was −0.52%/°C; for voltage, −0.48%/°C, and for current, +0.10%/°C.

Keywords: PV panel; climatic chamber; efficiency; temperature effect; sustainable solutions

check for updates

Citation: Hudișteanu, V.-S.; Cherecheș, N.-C.; Țurcanu, F.-E.; Hudișteanu, I.; Romila, C. Impact of Temperature on the Efficiency of Monocrystalline and Polycrystalline Photovoltaic Panels: A Comprehensive Experimental Analysis for Sustainable Energy Solutions. *Sustainability* **2024**, *16*, 10566. https://doi.org/10.3390/su162310566

Academic Editor: Domenico Mazzeo

Received: 11 November 2024
Revised: 27 November 2024
Accepted: 29 November 2024
Published: 2 December 2024

Copyright: © 2024 by the authors. Licensee MDPI, Basel, Switzerland. This article is an open access article distributed under the terms and conditions of the Creative Commons Attribution (CC BY) license (https://creativecommons.org/licenses/by/4.0/).

1. Introduction

Climate change has an important impact on the worldwide flora and fauna, including human civilization. To address this issue, sustainable solutions need to be implemented urgently to reduce carbon dioxide emissions [1]. In this context, photovoltaic (PV) technology has important advantages, considering that the energy source is renewable and free and the production of electricity is clean and does not have a negative impact on the environment (CO_2 and NOx emissions, waste, noise, etc.). The generation of electricity is done without moving parts, determining reduced costs of maintenance. When the systems are serving buildings, the energy produced is consumed locally, which results in reduced power losses [1].

Generating electricity with low CO_2 emissions represents an important energetic target, presenting a large European and worldwide interest. In terms of environmental sustainability, PV panels harness solar energy, which is a clean and inexhaustible source. They reduce dependence on fossil fuels and help lower greenhouse gas (GHG) emissions.

The building-integrated photovoltaic (BIPV) concept consists of placing PV panels on the roof or façades of buildings [2]. The integration is justified if one analyzes the main advantages: the local production and consumption of electricity, which imply reduced energy losses and the possibility of complex use of electricity and thermal energy. By increasing energy generation and reducing consumer losses, a reduction in CO_2 and NOx emissions and environmental protection are achieved, maintaining the same comfort conditions for occupants. The implementation of high-efficiency PV systems integrated into buildings and the reduced distance between the source and the consumption point could determine a decrease in environmental pollution and CO_2 emissions [3,4].

One of the main problems concerning the operation of photovoltaic panels is the significant increase in their operating temperature, which causes an important drop in conversion efficiency [5–7]. The decrease in the conversion efficiency related to the increase in the temperature for solar radiation of 1000 W/m^2 has values around $-0.50\%/^\circ$C [8].

Even though monocrystalline and polycrystalline solar panels are structurally different, with a slightly higher efficiency for monocrystalline ones, their operation is similar, and, according to the specialized literature, both are similarly affected by high operating temperatures [8].

The performance characteristics of photovoltaic panels (voltage (V), current intensity (I), electric power generated (P), efficiency (η), and fill factor (FF)) depend on operating temperature (T_{med}) and intensity of solar radiation (G) [9]. It is estimated that around 80% of the solar radiation incident on the photovoltaic panel is converted into heat [10] at operating temperatures in the interval of 65–80 °C, depending on solar radiation intensity [7]. As the power of a photovoltaic cell is influenced by the temperature and radiation levels, the standard test conditions (STC) parameters are defined: T_{med} = 25 °C, G = 1000 W/m^2, AM 1.5, when PV panels generate the nominal power measured in watt-peak (Wp) [11]. A real concern is that in regular operation, at solar radiation levels of 500 . . . 1000 W/m^2 and low air velocities, the photovoltaic panels can reach temperatures of 80 °C [12], leading to a significant decrease in efficiency [13].

The literature provides examples, procedures, and relationships for determining the influence of operating temperature over the efficiency of PV panels, but most of them are related to the STC or NOCT conditions only [11].

A feasible method to increase the efficiency of PV panels consists in using cooling solutions [14,15]. Most of the studies on the cooling of photovoltaic panels are also focused on the usage of the thermal energy extracted because of this process so that the recovery time of the investment is less than that of the stand-alone photovoltaic systems [16]. The simultaneous conversion of solar energy into electric and thermal energy using photovoltaic-thermal panels is known in the literature as PVT (photovoltaic-thermal system) [17]. A particular feature of this solution is the BIPVT concept, which implies the integration of PVT into buildings [3,4].

Detailed studies on the air cooling of photovoltaic panels are carried out in [18,19]. The integration of photovoltaic panels in the building envelope, as the exterior glazing of the double-glazed façades, is also considered a viable solution [20,21]. In this case, the ventilation of the channel can be realized naturally (due to the thermal draft or wind) or mechanically [22].

The use of water as a cooling agent for photovoltaic panels is a solution analyzed in different studies [23–25]. The hybrid photovoltaic panels studied in the literature have attached a water coil with the role of cooling the PV panel and solar collector [26]. Most water-cooling techniques are placed in the category of active cooling solutions and are superior to air cooling, but are more expensive [27].

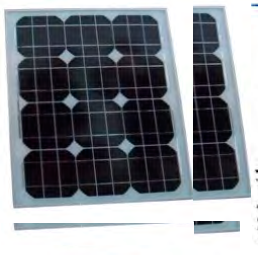
The present study presents an experimental evaluation of the influence of the operating temperature over the most relevant parameters of two silicon PV panels at constant levels of radiation. It highlights the potential for enhancement of the efficiency of photovoltaic systems and emphasizes the importance of further research to promote sustainable energy consumption. The implemented analysis is suitable for building integrated photovoltaics in

energy consumption. The implemented analysis is suitable for building integrated photovoltaics in vertical positions, when solar radiation levels are around 500 W/m², but important heating is still recorded [28].

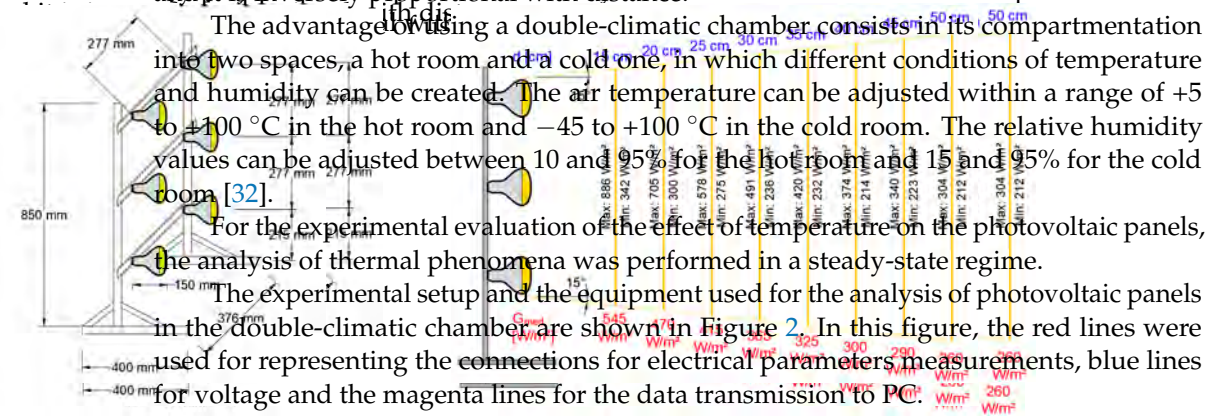
2. Experimental Setup

Comparative tests were performed for two types of photovoltaic panels: monocrystalline and polycrystalline with approximately equal dimensions and of the same nominal power, 30 W, but with slightly different electric characteristics. Within the experimental program carried out by using a Feutron double-climatic chamber (DCC) (Feutron Klima, Sandau/Elbe, Germany) [29], the performance of the photovoltaic panels was analyzed under various conditions by modifying the air temperature. The measured values were the electric V_{mp}, I_{mp}, V_{oc}, and I_{sc} and thermal ones, T_{med} and G_{med}. Additionally, the influence of external parameters on photovoltaic conversion efficiency, η, was determined.

Table 1. Characteristics of photovoltaic panels.

Type of PV Panel	Real Image	Parameters
Monocrystalline photovoltaic panel (Victron Energy)		P_{mp} = 30 Wp V_{mp} = 18.0 V I_{mp} = 1.67 A V_{oc} = 22.5 V I_{sc} = 2.00 A Dimensions ($L \times W \times H$): 430 mm × 540 mm × 25 mm
Polycrystalline photovoltaic panel (Suntech)		P_{mp} = 30 Wp V_{mp} = 17.4 V I_{mp} = 1.74 A V_{oc} = 21.6 V I_{sc} = 1.94 A Dimensions ($L \times W \times H$): 426 mm × 680 mm × 15 mm

The radiation was provided by a solar radiation simulation device (Figure 1) composed of six light bulbs, type OSRAM Ultra Vitalux, of 300 W each, the design, setup and calibration of the device was realized through PhD research in UTAST Romania [30]. The radiation produced by the simulation device does not cover the entire solar radiation spectrum but has satisfactory wavelengths necessary for evaluating PV panel heating and conversion [31]. The radiation produced is nearly uniform on the surface of the PV panel and inversely proportional with distance.



The advantage of using a double-climatic chamber consists in its compartmentation into two spaces, a hot room and a cold one, in which different conditions of temperature and humidity can be created. The air temperature can be adjusted within a range of +5 to +100 °C in the hot room and −45 to +100 °C in the cold room. The relative humidity values can be adjusted between 10 and 95% for the hot room and 15 and 95% for the cold room [32].

For the experimental evaluation of the effect of temperature on the photovoltaic panels, the analysis of thermal phenomena was performed in a steady-state regime.

The experimental setup and the equipment used for the analysis of photovoltaic panels in the double-climatic chamber are shown in Figure 2. In this figure, the red lines were used for representing the connections for electrical parameters measurements, blue lines for voltage and the magenta lines for the data transmission to PC.

The radiation was provided by a solar radiation simulation device (Figure 1) composed of six light bulbs, type OSRAM Ultra-Vitalux, of 300 W each. The design, setup and calibration of the device was realized through PhD research in TUIASI - Romania [30]. The radiation produced by the simulation device does not cover the entire solar radiation spectrum but has satisfactory wavelengths necessary for evaluating PV panel heating and conversion [31]. The radiation produced is nearly uniform on the surface of the PV panel and it is inversely proportional with distance.

Sustainability **2024**, *16*, x FOR PEER REVIEW 4 of 21

The advantage of using a double-climatic chamber consists in its compartmentation into two spaces, a hot room and a cold one, in which different conditions of temperature and humidity can be created. The air temperature can be adjusted within a range of +5 to +100 °C in the hot room and −45 to +100 °C in the cold room. The relative humidity values can be adjusted between 10 and 95% for the hot room and 15 and 95% for the cold room [32].

The advantage of using a double-climatic chamber consists in its compartmentation into two spaces, a hot room and a cold one, in which different conditions of temperature and humidity can be created. The air temperature can be adjusted within a range of +5 to +100 °C in the hot room and −45 to +100 °C in the cold room. The relative humidity values can be adjusted between 10 and 95% for the hot room and 15 and 95% for the cold room [32].

For the experimental evaluation of the effect of temperature on the photovoltaic panels, the analysis of thermal phenomena was performed in a steady-state regime.

For the experimental evaluation of the effect of temperature on the photovoltaic panels, the analysis of thermal phenomena was performed in a steady-state regime.

The experimental setup and the equipment used for the analysis of photovoltaic panels in the double-climatic chamber are shown in Figure 2. In this figure, the red lines were used for representing the connections for electrical parameters measurements, blue lines for voltage and the magenta lines for the data transmission to PC.

The experimental setup and the equipment used for the analysis of photovoltaic panels in the double-climatic chamber are shown in Figure 2. In this figure, the red lines were used for representing the connections for electrical parameters measurements, blue lines for voltage and the magenta lines for the data transmission to PC.

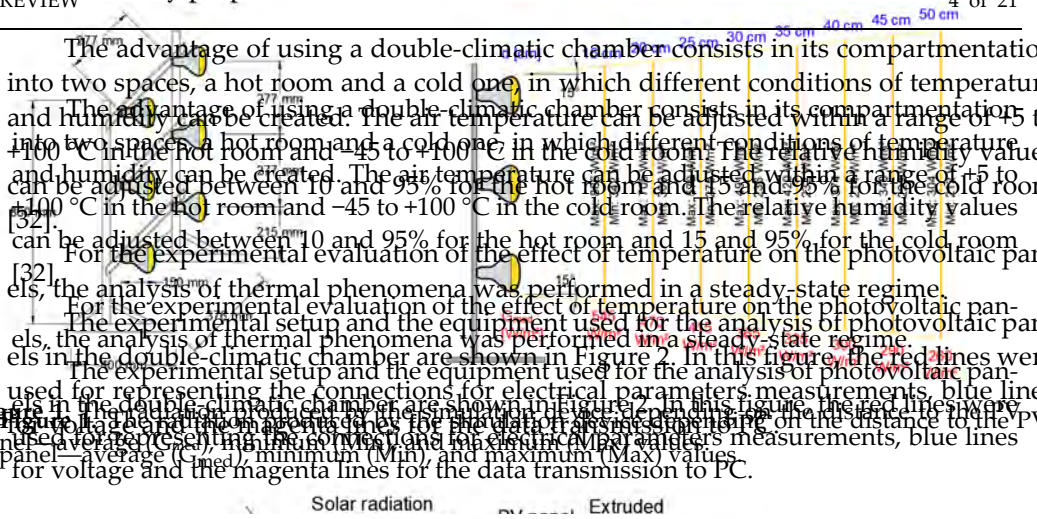


Figure 1. The radiation produced by the simulation device depending on the distance to the PV panel—average (G_{med}), minimum (Min), and maximum (Max) values.

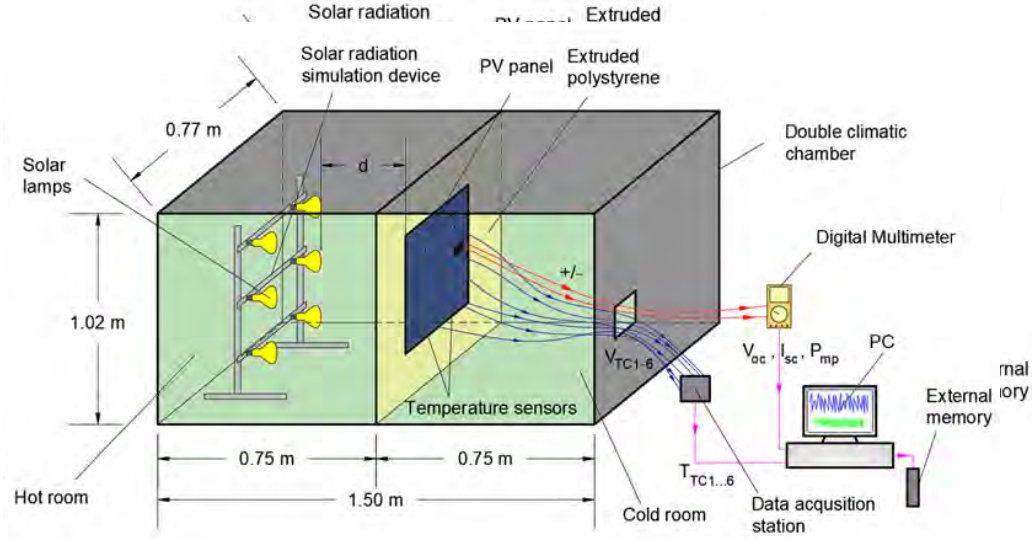


Figure 2. Experimental setup for testing the photovoltaic panels in the double-climatic chamber.

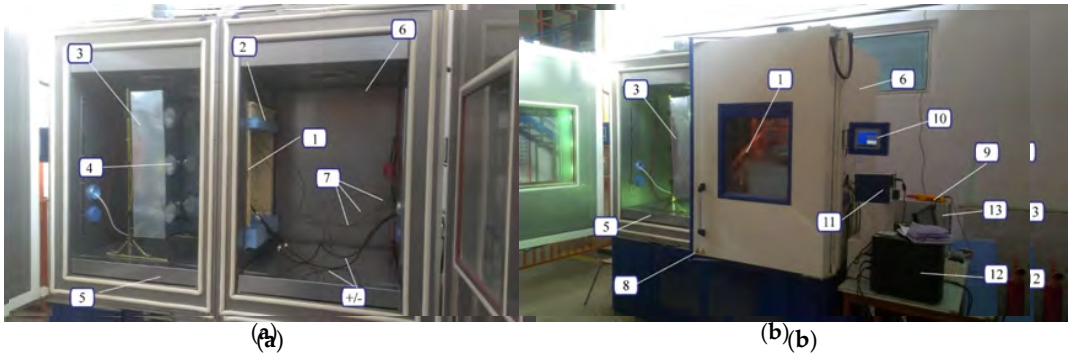
Figure 2. Experimental setup for testing the photovoltaic panels in the double-climatic chamber.

The photovoltaic panels were positioned in the DCC between the two chambers and the cooling is assured by the air from the cold room. The small size of the photovoltaic panels and the solar radiation simulation device were imposed for easy handling and integration in the climatic chamber.

The photovoltaic panels were positioned in the DCC between the two chambers and the cooling is assured by the air from the cold room. The small size of the photovoltaic panels and the solar radiation simulation device were imposed for easy handling and integration in the climatic chamber.

To control the operating temperature of the PV panel exposed to radiation, the solar radiation simulator was placed in the hot room, while the back of the photovoltaic panel was in the cold room (Figure 3). The connections for the measurement of the temperature and the electric parameters were made through a sealed orifice of the climate chamber.

To control the operating temperature of the PV panel exposed to radiation, the solar radiation simulator was placed in the hot room, while the back of the photovoltaic panel was in the cold room (Figure 3). The connections for the measurement of the temperature and the electric parameters were made through a sealed orifice of the climate chamber.



(**a**) (**b**)

Figure 3. Elements of the experimental stand: (**a**) cold room opened (conductors and thermocouples); (**b**) cold room closed (data acquisition devices).

Figure 3. Elements of the experimental stand: (**a**) cold room opened (conductors and thermocouples); (**b**) cold room closed (data acquisition devices).

1—PV panel; 2—extruded polystyrene insulation; 3—solar radiation simulation device; 4—solar lamps; 5—hot room; 6—cold room; 7—conductors from thermocouples; 8—double-climatic chamber; 9—digital multimeter; 10—control panel of DCC; 11—data acquisition station; 12—uninterruptible power supply (UPS); 13—computer; (±)—conductors of PV panels.

The temperature measurement and recording were performed using the data acquisition system provided by COMET Data Logger MS6 (COMET System s.r.o., Rožnov pod Radhoštěm, Czech Republic) with 16 inputs for PT1000 [33] and temperature sensors and (PT1000 thermocouples), while the electrical measurements were achieved by using Fluke multimeters and clamp meters (Fluke Europe B.V., Eindhoven, Netherlands) [34]. The distribution of the temperature was determined using both Testo 871 (Testo SE & Co. KGaA, Baden-Württemberg, Germany) [35] and Thermal PT1000 thermocouples.

When possible, all devices were used together with their dedicated software. The average uncertainty of the measurement associated with the instruments was approximately 0.6%.

During the measurements the following parameters were monitored: the temperature of the photovoltaic panels for the monocrystalline and polycrystalline panels and their electrical parameters; the open-circuit voltage (V_{oc}), the short-circuit current intensity (I_{sc}), and the maximum power produced under the tested conditions (P_{mp}).

The photovoltaic panels were mounted in the boundary area between the two sections of the double-climatic chamber. They were positioned facing the solar radiation simulation device in the hot room (Figure 4b), and the back was in contact with the air in the cold room (Figure 4c). To ensure control of the temperature with the help of the cold room, it was isolated from the hot room by sealing the space around the photovoltaic panel with extruded polystyrene (Figure 4a).

On the rear area of the photovoltaic panel are attached the six contact thermocouples, type PT1000, fixed by means of an adhesive tape, resistant to high temperatures.



(**a**) (**b**) (**c**)

Figure 4. Mounting and testing photovoltaic panels: (**a**) sealing of the PV panel in the double-climatic chamber; (**b**) photovoltaic panel—front view; (**c**) photovoltaic panel—rear view.

A total of 10 measurement setups were conducted for each photovoltaic panel, with different operating temperatures achieved by adjusting the air temperature in the cold room. During this work, the data are presented for measurements in steady-state operation (when radiation level and PV panel temperature were stabilized). Each case required an entire day to obtain these conditions and to remove the influence of the previous scenario.

Radiation Emitted Inside the Climatic Chamber

The results of the average radiation measurements for the positioning of the solar radiation simulation device inside the climatic chamber at a 15 cm distance to the PV panel surface are presented in Table 2. The data were obtained by multiple measurements at each point, both with a solarimeter and pyranometer. The measured values show minor differences compared to the flux emitted when no obstacle is present (Figure 1). These differences are influenced by the reflections that appeared when the simulator was introduced into the climatic chamber, characterized by shiny and highly reflective metal surfaces.

Table 2. Coefficients of dependence of V_{oc}, I_{sc}, P_{mp}, η, and FF with temperature.

	G_{med} = 560 W/m^2
$\Delta V_{oc}/\Delta T$ (%/°C)	−0.48
$\Delta I_{sc}/\Delta T$ (%/°C)	0.16
$\Delta P_{mp}/\Delta T$ (%/°C)	−0.52
$\Delta \eta/\Delta T$ (%/°C)	−0.55
$\Delta FF/\Delta T$ (%/°C)	−0.15

Due to the small differences between the dimensions of the two photovoltaic panels (monocrystalline and polycrystalline) and the limitations introduced by the size of the climate chamber and the solar radiation simulator, the average radiation recorded on their surfaces presents some differences for the same distance of 15 cm. The average radiation intensity incident on the PV panels surface mounted in DCC was 560 W/m^2 for the monocrystalline panel and 520 W/m^2 for the polycrystalline panel.

This level of radiation used during the experiment simulates the integration of PV panels in the building's façade with good accuracy, while the operating temperatures were controlled through the double-climatic chamber operation in order to analyze the cooling effect for these specific conditions.

3. Results

3.1. Experimental Results—Monocrystalline Photovoltaic Panel

3.1.1. Distribution of Incident Radiation on the Monocrystalline Photovoltaic Panel

Figure 5 presents the distribution curves of the radiation levels on the surface of the monocrystalline photovoltaic panel for 15 cm imposed on the solar simulator. Radiation intensity measurements had the following black points of identification:

- the delimiting area between the two rooms of the DCC: 1, 3, 5, 8, 11, 13, 15, 18;
- photovoltaic panel frame: 21, 22, 23, 28, 33, 38, 43, 42, 41, 36, 31, 26;
- the inner surface of the photovoltaic panel: 24, 25, 27, 29, 30, 32, 34, 35, 37, 39, 40.

Throughout the paper, the figures representing the distribution of the radiation and/or temperatures are reported on the front face of PV panels. The plots were generated based on numerical data from measurements by using TOPO LT tool integrated in AutoCAD software. The colors used in these images has the following meaning: Blue text—used for marking the values in the measurement points; Blue lines—marking the edge of the PV panels; Red text—used for marking the values of the isolines for temperature/radiation; Red lines—isolines for temperature/radiation. Apart from the ϖαλυεσ μεασυρεδ at the points of identification, the other ones were determined through interpolation.

Figure 5 shows some areas where the maximum incident radiation values are recorded. These coincide with the position of the solar lamps, and the effect of non-uniformity generated is inversely proportional to the distance. Additionally, a radiation gradient is observed, with higher values in points 29 and 34, and lower in points 30 and 35. This phenomenon is determined by the reflective effect of the climate chamber wall in that area.

The minimum values of the measured radiation were at least 80% of the average value and the maximum at 130%.

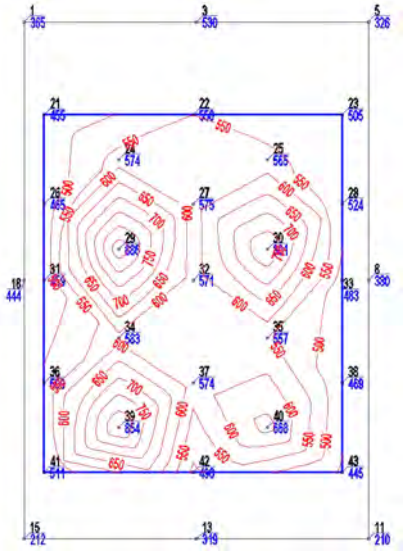


Figure 5. Distribution of radiation on monocrystalline PV for the distance of d = 15 cm/G_{med} = 560 W/m^2 = 560 W/m^2.

3.1.2. Temperature Distribution on the Monocrystalline Photovoltaic Panel

The measurements revealed the appearance of two temperature gradients, one vertically, with higher temperatures in the upper area, and one horizontal, with higher temperatures near the stainless-steel wall, which has high reflective characteristics (Figures 6 and 7). The vertical temperature gradient is determined by the thermal stratification of the air in the immediate vicinity of the photovoltaic panel, while the horizontal differences are determined by the higher levels of radiation in these areas.

The distribution of the average temperatures measured on the surface of the photovoltaic panel is presented in Section 3.1.3. The average temperatures of the PV were calculated as an arithmetic mean of the six thermocouples (TCs), positioned two by two in the upper, middle, and lower areas behind it.

Regarding the temperature of PV on its two faces, one exposed to radiation and the other in contact with cold air, it was found that the temperatures vary practically instantaneously and the differences between them fall in smaller intervals of degree 1 °C.

The images captured using the thermal imaging camera led to a better qualitative and quantitative analysis of the results, confirming the temperature distribution on the photovoltaic panels in Figures 8 and 9. Validation of the temperature distribution obtained using thermocouples was performed for the average panel temperature of 40 °C (Figure 9).

Figure 9 shows the phenomenon of overheating of the photovoltaic panel around its connection box. It can be observed that at an average temperature of 40 °C in the vicinity of the points, this portion records values about 10 °C higher. This phenomenon is determined by the thermal insulation effect produced by the presence of the box, causing the low cooling in that area. The heating of the photovoltaic cells in the respective areas of the panel has a negative effect on overall efficiency when all the cells are interconnected in series. This phenomenon determines an important local decrease in efficiency that is extended to the entire PV panel operation and also a risk of fire [38].

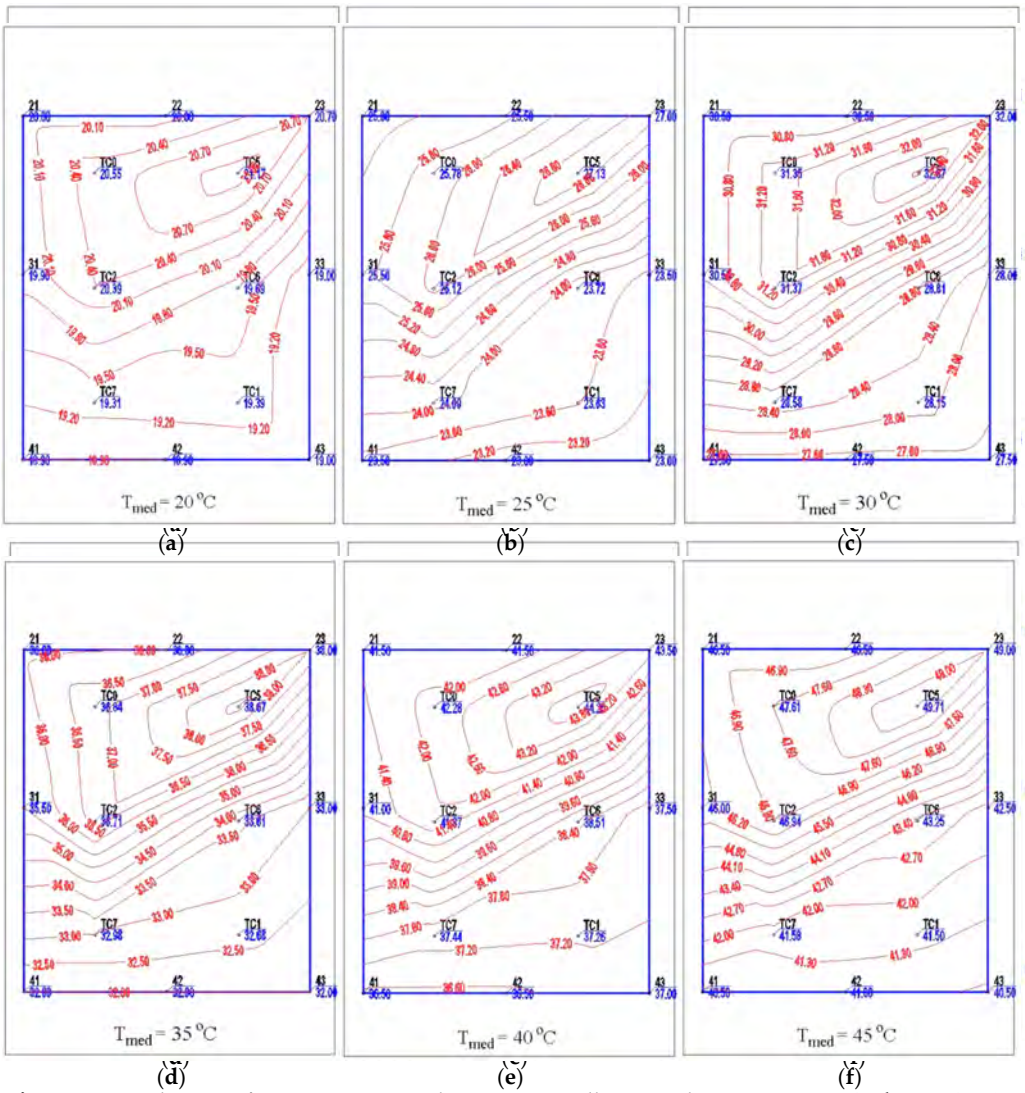


Figure 6. Distribution of temperatures on the monocrystalline panel at T_{med}: (**a**) 20 °C; (**b**) 25 °C; (**c**) 30 °C; (**d**) 35 °C; (**e**) 40 °C; (**f**) 45 °C.

Figure 6. Distribution of temperatures on the monocrystalline panel at T_{med}: (**a**) 20 °C; (**b**) 25 °C; (**c**) 30 °C; (**d**) 35 °C; (**e**) 40 °C; (**f**) 45 °C.

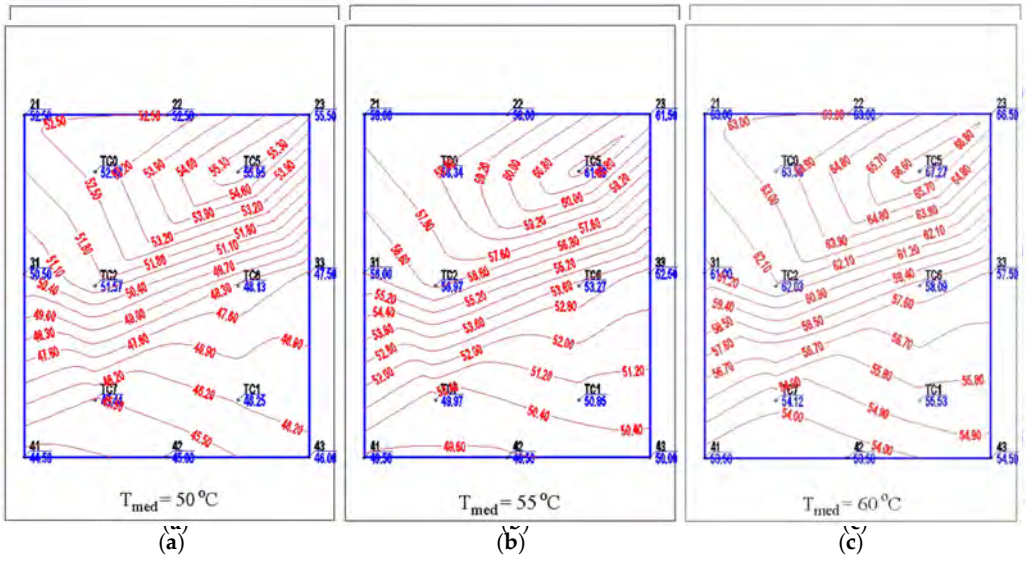


Figure 7. *Cont.*

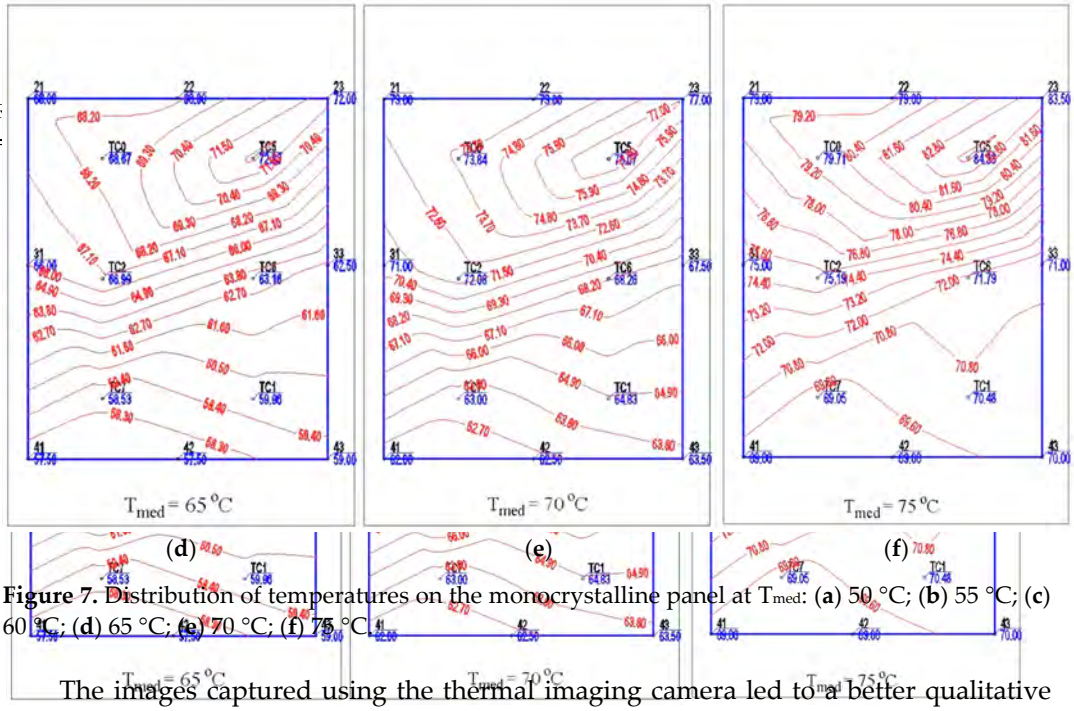


Figure 7. Distribution of temperatures on the monocrystalline panel at T_{med}: (**a**) 50 °C; (**b**) 55 °C; (**c**) 60 °C; (**d**) 65 °C; (**e**) 70 °C; (**f**) 75 °C.

The images captured using the thermal imaging camera led to a better qualitative and quantitative analysis of the results, confirming the temperature distribution on the photovoltaic panels in Figures 8 and 9. Validation of the temperature distribution obtained using thermocouples was performed for the average panel temperature of 40 °C (Figure 9).

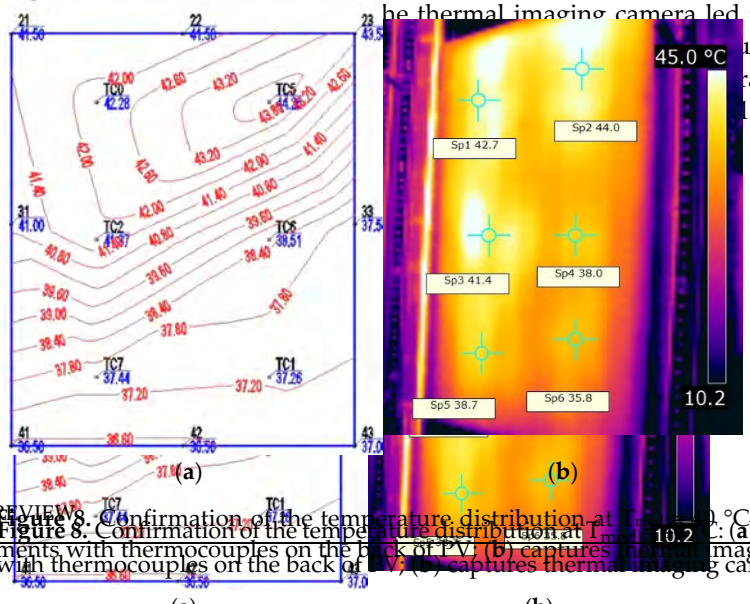


Figure 8. Confirmation of the temperature distribution at T_{med} = 40 °C: (**a**) based on the measurements with thermocouples on the back of PV; (**b**) captures thermal imaging camera.

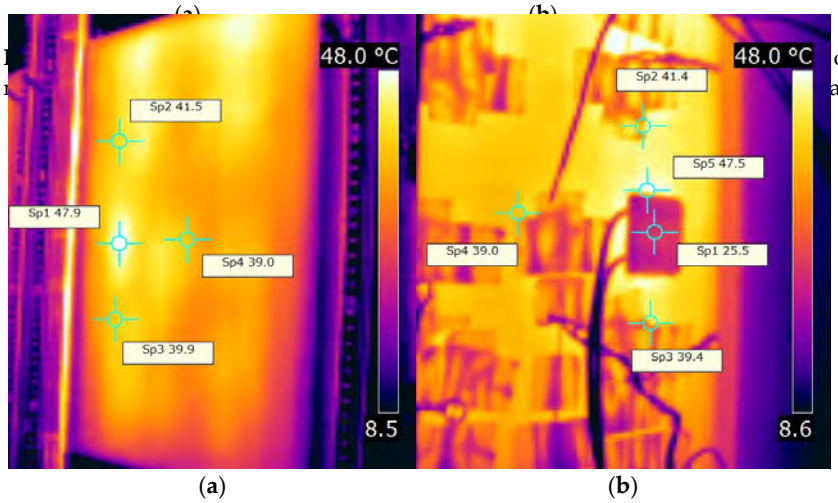


Figure 9. Overheating of photovoltaic cells in the connection box area: (**a**) front view; (**b**) rear view.

Figure 9 shows the phenomenon of overheating of the photovoltaic panel around its connection box. It can be observed that at an average temperature of 40 °C in the vicinity of the points, this portion records values about 10 °C higher. This phenomenon is determined by the thermal insulation effect produced by the presence of the box, causing the low cooling in that area. The heating of the photovoltaic cells in the respective areas of the panel has a negative effect on overall efficiency when all the cells are interconnected in

mined by the thermal insulation effect produced by the presence of the box, causing the low cooling in that area. The heating of the photovoltaic cells in the respective areas of the panel has a negative effect on overall efficiency when all the cells are interconnected in series. This phenomenon determines an important local decrease in efficiency that is extended to the entire PV panel operation and also a risk of fire [38].

3.1.3. Variation of the Parameters of the Monocrystalline Photovoltaic Panel with the Operating Temperature

The maximum power produced, P_{mp}, by the photovoltaic panels was determined by testing the power dissipated by them on linear resistors with variable resistance, using the characteristic resistance method, R_{ch} [39]. For each value of the radiation intensity, three values of the electrical resistance were tested, thus resulting in the maximum power point. Figure 10 shows the variation of the power generated by the monocrystalline photovoltaic panel for the three values of the resistance and various temperatures, at a radiation intensity of 560 W/m^2. There is a reduction in the power produced when the operating temperature is increased for each value of the electrical resistance.

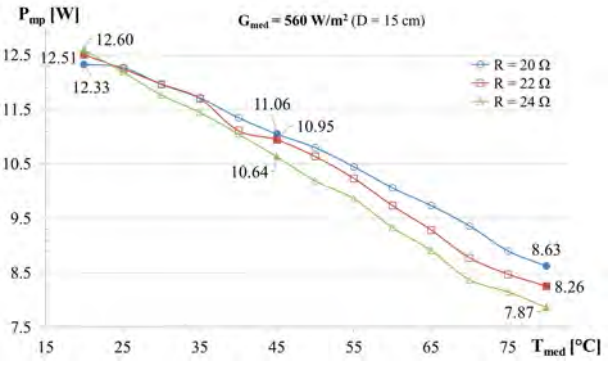


Figure 10. Maximum power output depending on the monocrystalline PV panel temperature and resistive load for G_{med} = 560 W/m^2.

The variation of two of the most important parameters of the photovoltaic panel, the open-circuit voltage, V_{oc}, and the short-circuit current, I_{sc}, for a radiation level of 560 W/m^2 is shown in Figure 11. The increase in temperature can be observed to have a significantly greater impact on V_{oc} than on I_{sc}.

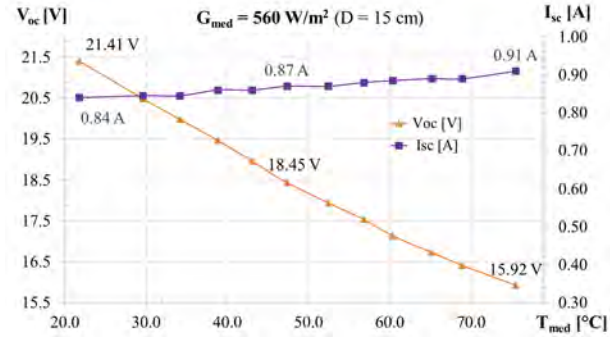
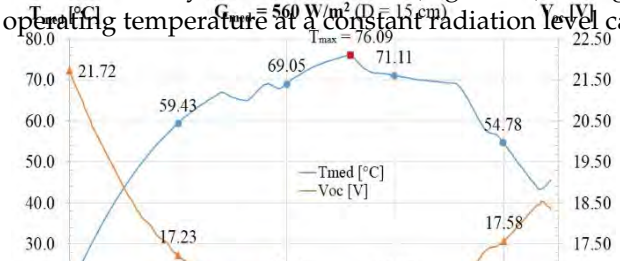


Figure 11. Variation of open-circuit voltage and short-circuit current of monocrystalline PV panel with temperature for G_{med} = 560 W/m^2.

Figure 12 illustrates how the open-circuit voltage and the operating temperature of the photovoltaic panel change over time, while the radiation remains constant. It is found that the maximum values of the voltage are recorded at minimum temperatures and the reverse effect. Additionally, it is important to note the very short reaction time of the PV panel operation related to the temperature change. This behavior is advantageous, as significant efficiency gains can be achieved instantly by cooling when a temperature rise is noticed.

The effect of the operating temperature of the photovoltaic panel is also observed on the efficiency variation curves (Figure 13). A significant influence of the increase in operating temperature at a constant radiation level can be observed.



nificant efficiency gains can be achieved instantly by cooling when a temperature rise is noticed.

the photovoltaic panel change over time, while the radiation remains constant. It is found that the maximum values of the voltage are recorded at minimum temperatures and the reverse effect. Additionally, it is important to note the very short reaction time of the PV . This behavior is advantageous, as sig- by cooling when a temperature rise is

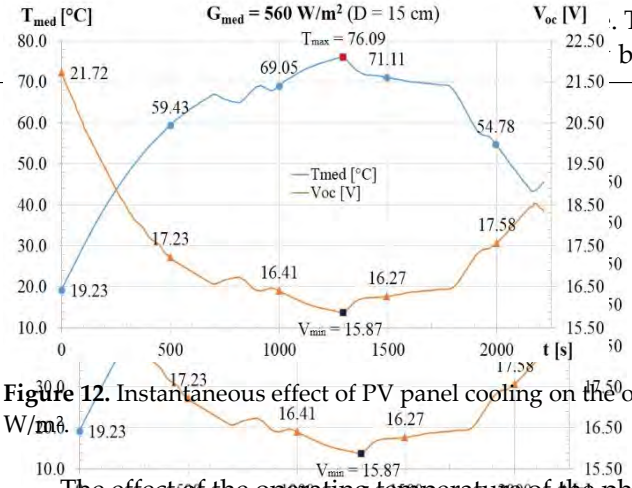


Figure 12. Instantaneous effect of PV panel cooling on the open-circuit voltage for G_{med} = 560 W/m².

Figure 12. Instantaneous effect of PV panel cooling on the open-circuit voltage for G_{med} = 560 W/m².

The effect of the operating temperature of the photovoltaic panel is also observed on the efficiency variation curves (Figure 13). A significant influence of the increase in operating temperature at a constant radiation level can be observed.

photovoltaic panel is also observed on ficant influence of the increase in oper- be observed.

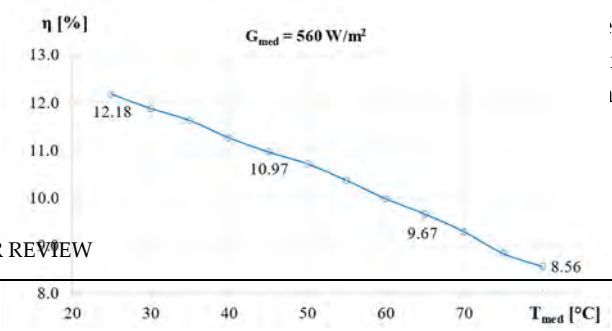


Figure 13. Variation of the efficiency of the PV panel with the operating temperature for G_{med} = 560 W/m².

Figure 13. Variation of the efficiency of the PV panel with the operating temperature for G_{med} = 560 W/m².

3.1.4. Coefficients of Variation of the Parameters of the Monocrystalline Photovoltaic Panel with the Operating Temperature

The detailed analysis of the experimental results is presented as coefficients of the influence of the operating temperature on the parameters of the photovoltaic panel, c_T. The coefficients are calculated by comparing the PV panel parameters, X, for temperature intervals of ΔT = 5 °C starting with 25 °C:

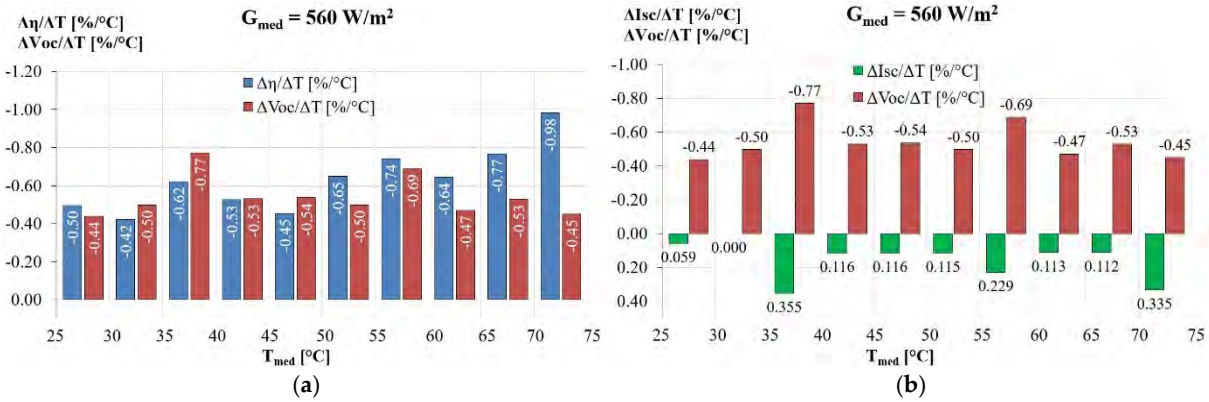
$$c_T = \frac{\Delta X}{\Delta T} \ [\%/°C] \quad (1)$$

The detailed analysis of the experimental results is presented as coefficients of the influence of the operating temperature on the parameters of the photovoltaic panel, c_T. The coefficients are calculated by comparing the PV panel parameters, X, for temperature intervals of ΔT = 5 °C starting with 25 °C:

$$c_T = \frac{\Delta X}{\Delta T} \ [\%/°C] \quad (1)$$

The results are determined for a constant level of radiation of 560 W/m² in Figures 14–16.

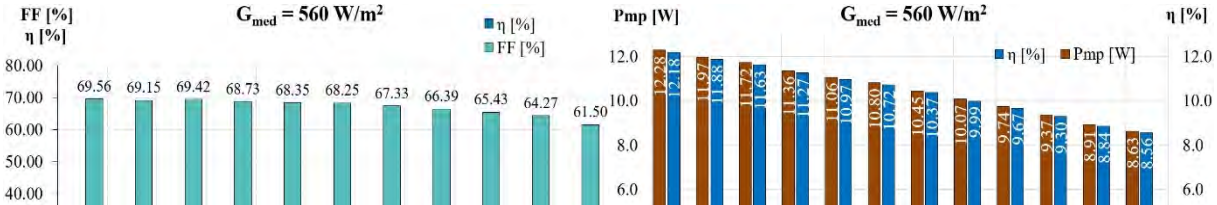
The results are determined for a constant level of radiation of 560 W/m² in Figures 14–16.

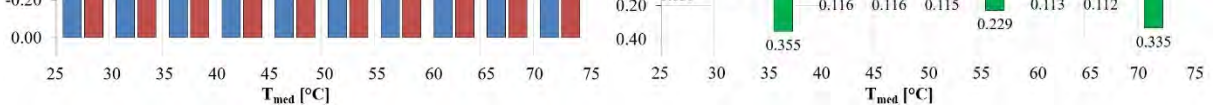


(**a**) (**b**)

Figure 14. Coefficients of variation on temperature intervals at G_{med} = 560 W/m² for (**a**) efficiency and open-circuit voltage; (**b**) short-circuit current and open-circuit voltage.

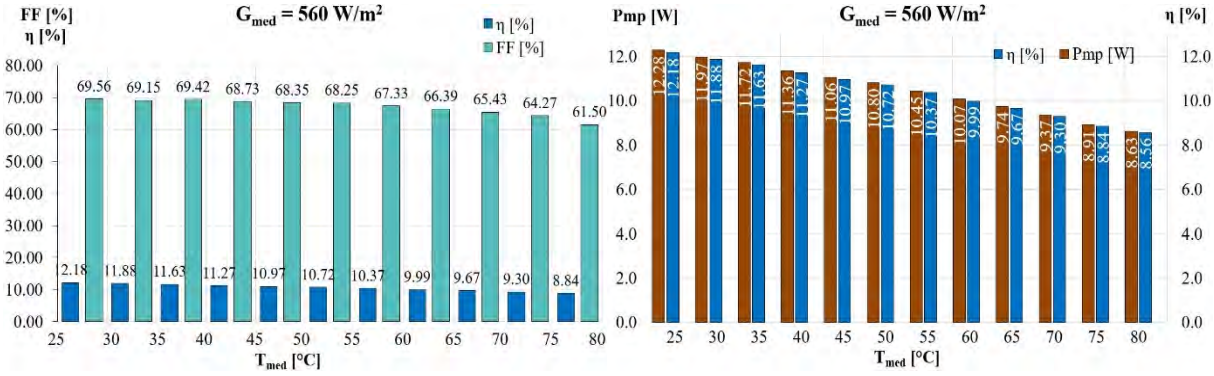
Figure 14. Coefficients of variation on temperature intervals at G_{med} = 560 W/m² for (**a**) efficiency and open-circuit voltage; (**b**) short-circuit current and open-circuit voltage.





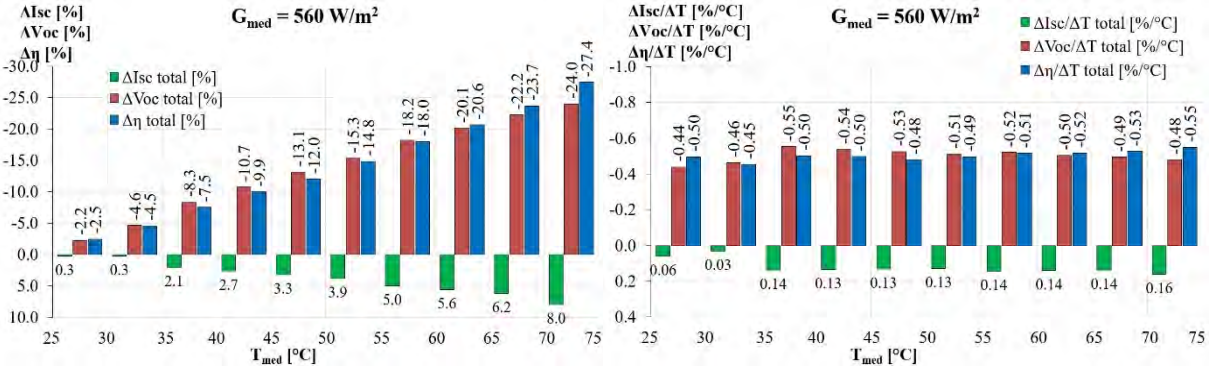
(**a**) (**b**)

Figure 14. Coefficients of variation on temperature intervals at G_{med} = 560 W/m² for (**a**) efficiency and open-circuit voltage; (**b**) short-circuit current and open-circuit voltage.



(**a**) (**b**)

Figure 15. Influence of the temperature variation at G_{med} = 560 W/m² over (**a**) efficiency and fill factor; (**b**) power generated and efficiency.



(**a**) (**b**)

Figure 16. Influence of the temperature variation at G_{med} = 560 W/m² over short-circuit current, open-circuit voltage, and PV panel efficiency: (**a**) total values; (**b**) average values.

Figure 14 shows the coefficients of variation of efficiency, open-circuit voltage, and short-circuit current as a function of operating temperature. The results in Figure 14 are presented for average values over analysis intervals of 5 °C. The negative influence of the panel temperature on the efficiency and the open-circuit voltage is registered for all studied intervals. Additionally, the short-circuit current has positive coefficients of variation on the analogous intervals.

Figure 15 shows the results for the maximum power output, and the percentage values of efficiency and the filling factor. These are presented for a constant radiation intensity of 560 W/m² for temperatures in the range of 25–80 °C. It can be observed that all three parameters are negatively influenced by temperature rise.

The total variation of the open-circuit voltage, short-circuit current, and efficiency, at intervals between 25 °C and 75 °C is shown in Figure 16a. It is observed that there is a constant decrease in efficiency and the open-circuit voltage and an increase in the short-circuit current, compared to the temperature of 25 °C. For temperatures around 75 °C, the total efficiency decrease is 27.4%, and for the open-circuit voltage it is 24.0%.

Figure 16b shows the effect of temperature as coefficients of variation mediated per interval. Using these charts, for any temperature chosen, the coefficients of variation with temperature (%/°C) can be determined.

The coefficients of the influence of the operating temperature on efficiency (−0.52 %/°C), voltage (−0.48 %/°C), and current intensity (+0.14 %/°C) can be approximated with satisfactory accuracy according to Table 2.

3.2. Experimental Results—Polycrystalline Photovoltaic Panel

3.2.1. Distribution of Incident Radiation on the Polycrystalline Photovoltaic Panel

As in the case of the monocrystalline PV panel, Figure 17 presents the distribution of the radiation for *d* = 15 cm imposed on the polycrystalline photovoltaic panel. A slightly lower average level of radiation is obtained for the polycrystalline (520 W/m²), compared to the monocrystalline one (560 W/m²), determined by the elongated shape and the larger

3.2. Experimental Results—Polycrystalline Photovoltaic Panel

3.2.1. Distribution of Incident Radiation on the Polycrystalline Photovoltaic Panel

As in the case of the monocrystalline PV panel, Figure 17 presents the distribution of the radiation for d = 15 cm imposed on the polycrystalline photovoltaic panel. A slightly lower average level of radiation is obtained for the polycrystalline (520 W/m^2), compared to the monocrystalline one (560 W/m^2), determined by the elongated shape and the larger surface. The analysis was implemented at this level of radiation because the quantitative increase in radiation would be obtained by an important decrease in the uniformity of radiation on the surface of the PV panel.

Sustainability **2024**, *16*, x FOR PEER REVIEW 14 of 21

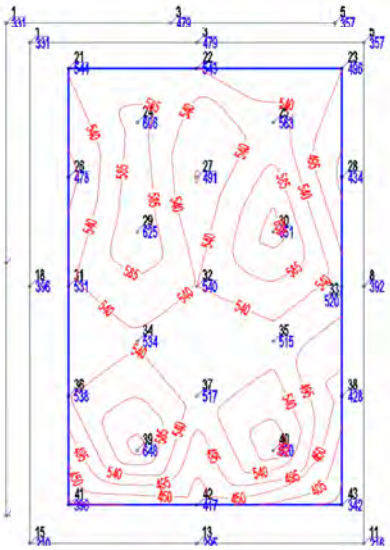


Figure 17. Distribution of radiation on polycrystalline PV for the distance G_{med} = 520 W/m^2.

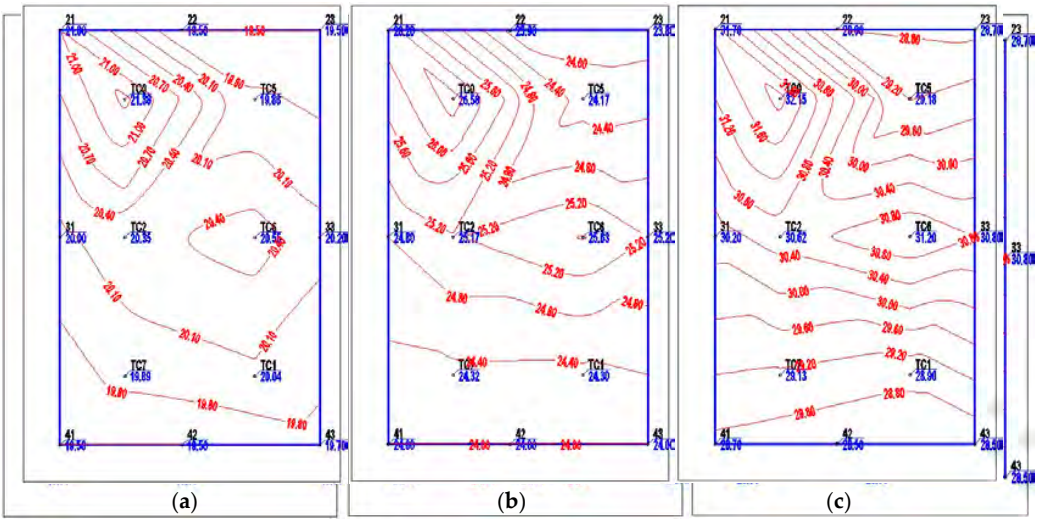
Figure 17. Distribution of radiation on polycrystalline PV for the distance G_{med} = 520 W/m^2.

3.2.2. Temperature Distribution on the Polycrystalline Photovoltaic Panel

3.2.2. Temperature Distribution on the Polycrystalline Photovoltaic Panel

The distribution of the operating temperatures measured on the surface of the polycrystalline photovoltaic panel for the reference mean temperature values is shown in Figures 18 and 19. The average temperature of the PV panel was calculated as the arithmetic mean of the values from six thermocouples (TC) positioned in pairs in the upper, middle, and lower sections on the back of the panel, as shown in Figures 18 and 19.

The distribution of the operating temperatures measured on the surface of the polycrystalline photovoltaic panel for the reference mean temperature values is shown in Figures 18 and 19. The average temperature of the PV panel was calculated as the arithmetic mean of the values from six thermocouples (TC) positioned in pairs in the upper, middle, and lower sections on the back of the panel, as shown in Figures 18 and 19.



(**a**) (**b**) (**c**)

(**a**) (**b**) (**c**)

Figure 18. *Cont.*

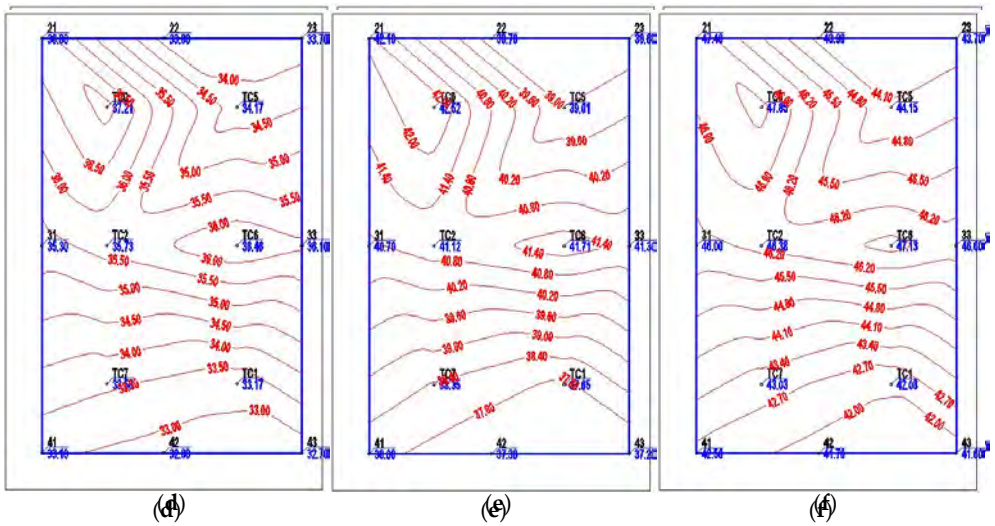


Figure 18. Distribution of temperatures on the polycrystalline panel at T_{med}: (**a**) 20 °C; (**b**) 25 °C; (**c**) 30 °C; (**d**) 35 °C; (**e**) 40 °C; (**f**) 45 °C.

Figure 18. Distribution of temperatures on the polycrystalline panel at T_{med}: (**a**) 20 °C; (**b**) 25 °C; (**c**) 30 °C; (**d**) 35 °C; (**e**) 40 °C; (**f**) 45 °C.

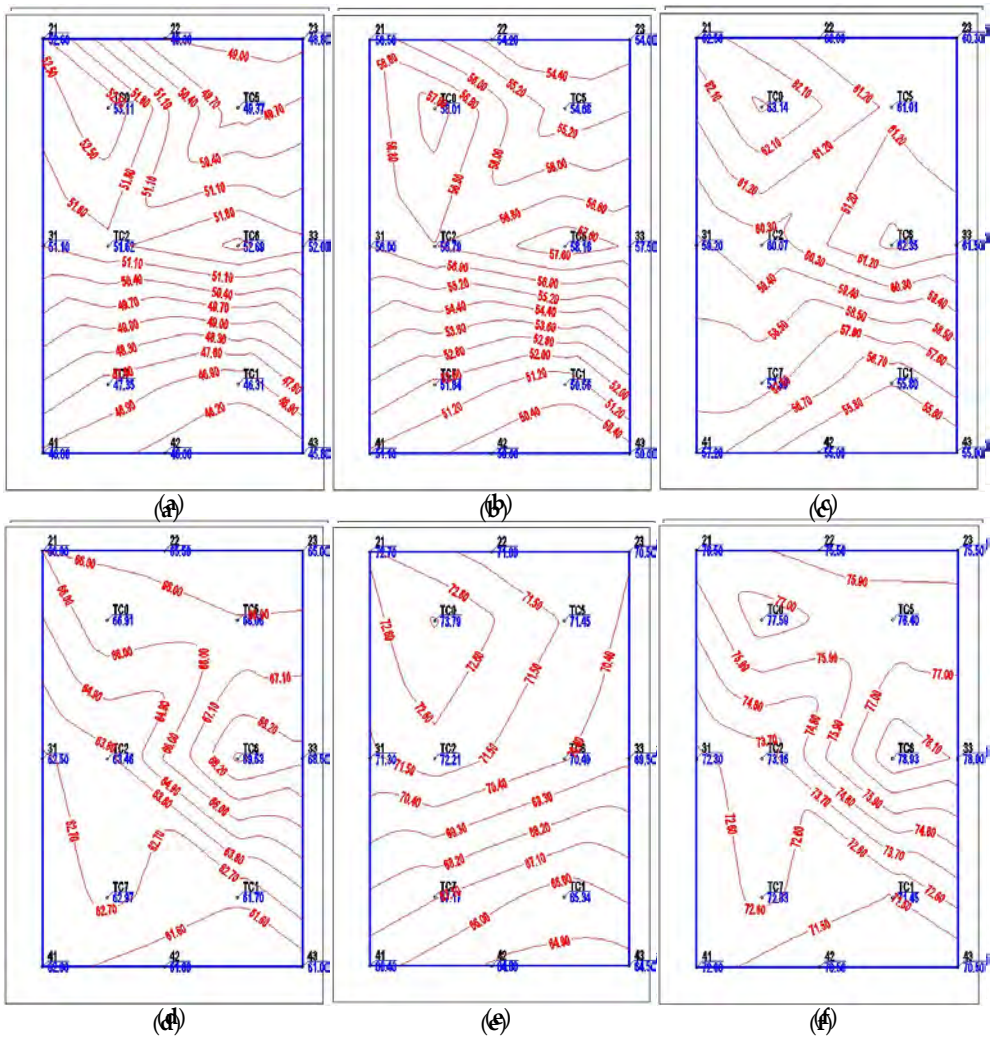


Figure 19. Distribution of temperatures on the polycrystalline panel at T_{med}: (**a**) 50 °C; (**b**) 55 °C; (**c**) 60 °C; (**d**) 65 °C; (**e**) 70 °C; (**f**) 75 °C.

Figure 19. Distribution of temperatures on the polycrystalline panel at T_{med}: (**a**) 50 °C; (**b**) 55 °C; (**c**) 60 °C; (**d**) 65 °C; (**e**) 70 °C; (**f**) 75 °C.

3.2.3. Variation of the Parameters of the Polycrystalline Photovoltaic Panel with the Operating Temperature

During the present study, the focus was on determining the trends of variation of the parameters of the photovoltaic panels on temperature and radiation intervals and less on punctual values. Figures 20–22 show the variation of the P_{mp}, V_{oc}, and I_{sc} of the polycrystalline photovoltaic panel for the three values of the resistance and various temperatures at a radiation intensity of 520 W/m^2.

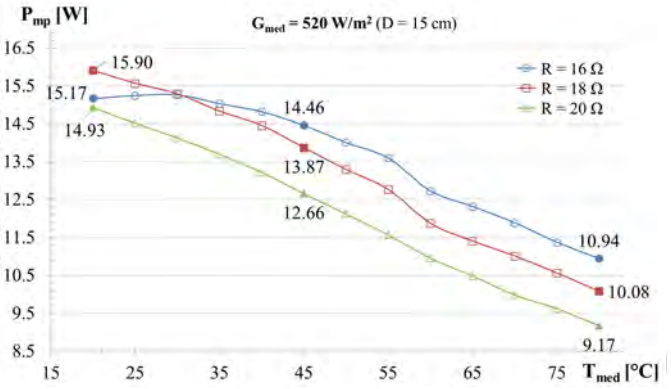


Figure 20. Maximum power output depending on the polycrystalline PV panel temperature and resistive load for G_{med} = 520 W/m^2.

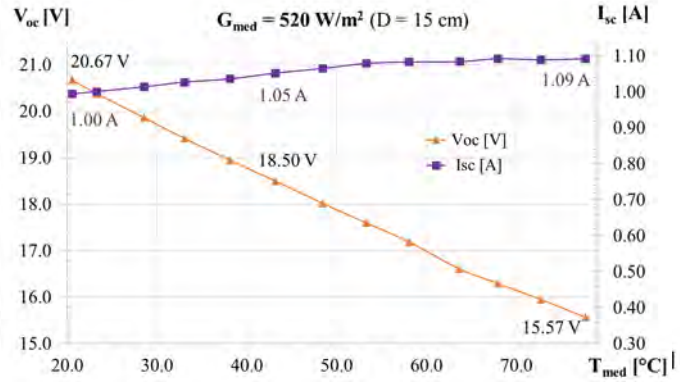


Figure 21. Variation of open-circuit voltage and short-circuit current of polycrystalline PV panel with temperature for G_{med} = 520 W/m^2.

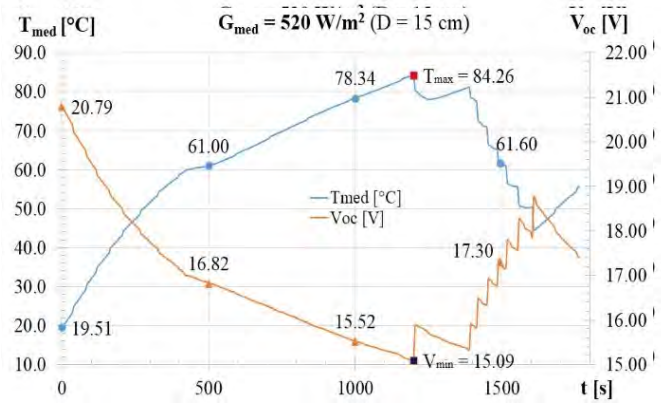


Figure 22. Instantaneous effect of polycrystalline PV panel cooling on the open-circuit voltage for G_{med} = 520 W/m^2.

3.2.4. Coefficients of Variation of the Parameters of the Polycrystalline Photovoltaic Panel with the Operating Temperature

Sustainability **2024**, *16*, x FOR PEER REVIEW 17 of 21

Sustainability **2024**, *16*, x FOR PEER REVIEW 17 of 21

3.2.4. Coefficients of Variation of the Parameters of the Polycrystalline Photovoltaic Panel with the Operating Temperature

Figure 23 shows the variation of the efficiency of the polycrystalline photovoltaic panel with the temperature for the radiation level of 520 W/m². When the operating temperature increases, the efficiency of the photovoltaic panel is reduced almost linearly.

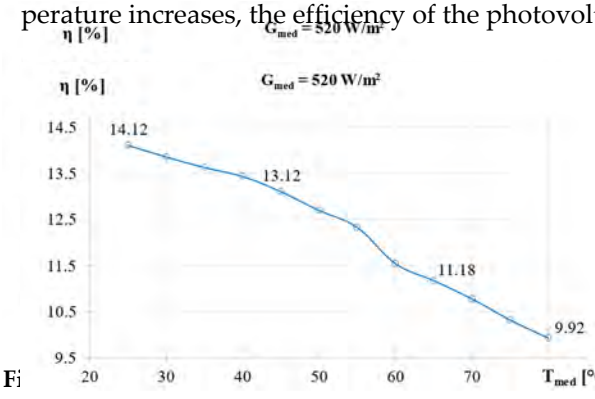


Figure 23. Variation of the efficiency of the PV panel with the operating temperature for G_{med} = 520 W/m².

Figures 24–26 represent the coefficients of variation of PV panel parameters with temperature.

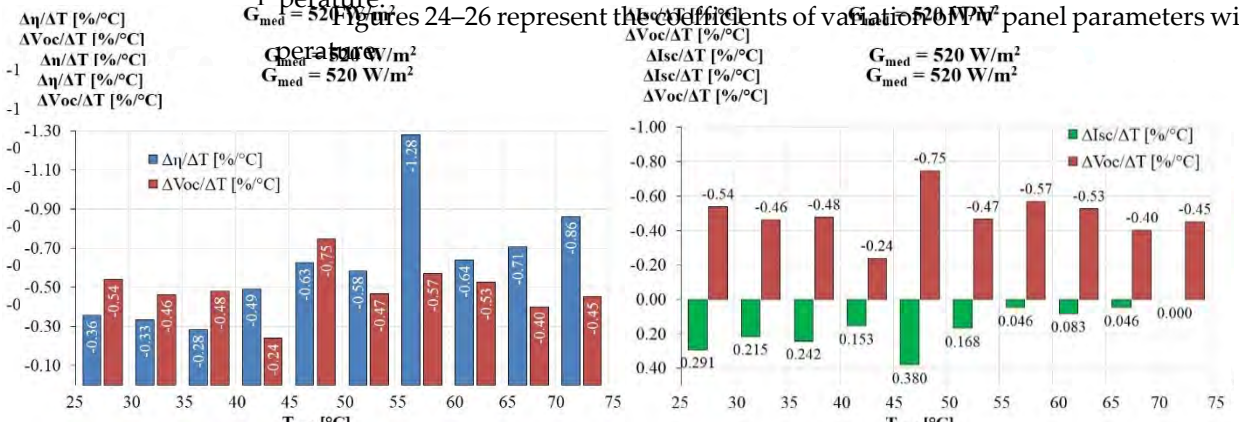


Figure 24. Coefficients of variation on temperature intervals at G_{med} = 520 W/m² for (**a**) efficiency and open-circuit voltage; (**b**) short-circuit current and open-circuit voltage.

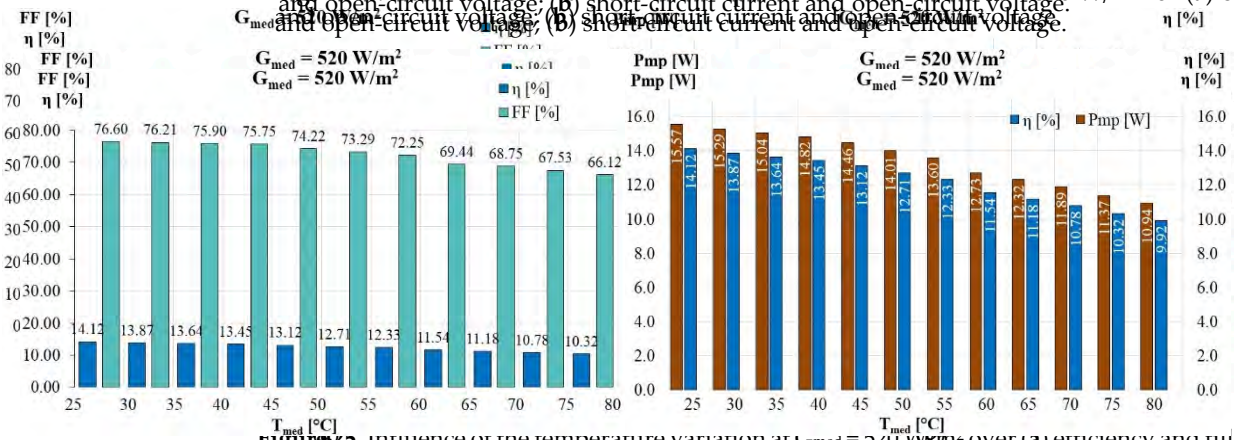


Figure 25. Influence of the temperature variation at G_{med} = 520 W/m² over (**a**) efficiency and fill factor; (**b**) power generated and efficiency.

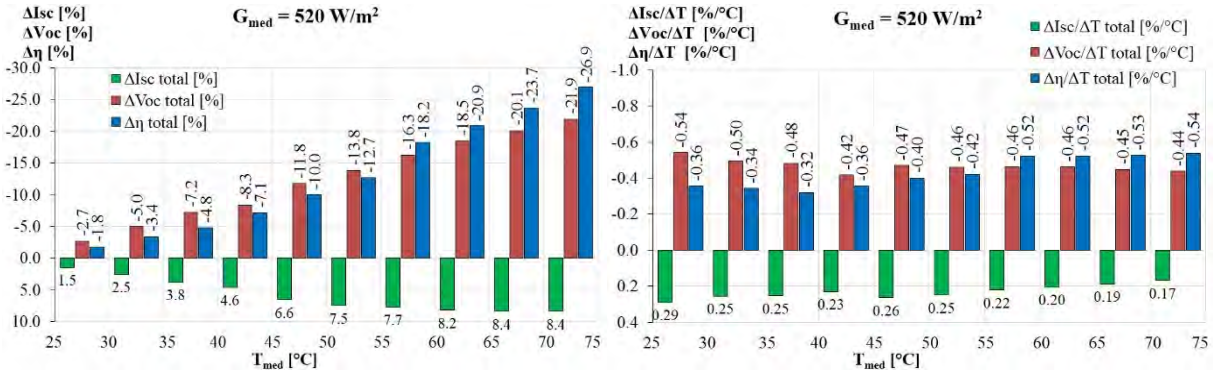


Figure 26. Influence of the temperature variation at G_{med} = 520 W/m² over short-circuit current, open-circuit voltage, and PV panel efficiency: (**a**) total values; (**b**) average values.

Table 3 presents the coefficients of dependence of the parameters of the photovoltaic panels with the operating temperature. According to these data, the decrease in efficiency with temperature has average values of about −0.50%/°C.

Table 3. The values of the dependence coefficients of V_{oc}, I_{sc}, P_{mp}, η, and FF with temperature.

G_{med}	520
$\Delta V_{oc}/\Delta T$ (%/°C)	−0.44
$\Delta I_{sc}/\Delta T$ (%/°C)	0.17
$\Delta P_{mp}/\Delta T$ (%/°C)	−0.52
$\Delta \eta/\Delta T$ (%/°C)	−0.54
$\Delta FF/\Delta T$ (%/°C)	−0.27

4. Conclusions and Discussion

During the experiment, a series of important insights were gained regarding the behavior of two different photovoltaic panels under various operating temperature conditions. The coefficients of influence of operating temperature on power, efficiency, voltage, current intensity, and fill factor were determined. In all cases studied, the coefficients were quantified both as general average values and over specific study intervals.

The study focuses on the performance of monocrystalline and polycrystalline panels under specific irradiation conditions but does not consider other potential influencing factors (e.g., humidity or wind speed). Therefore, there are some limitations regarding the entire spectrum of influence on the efficiency of PV panels. However, this represents a major interest in future research. The efficiency of PV panels is a significant topic in sustainable energy construction. The findings highlight the positive impact of cooling systems in enhancing system efficiency, with the primary focus on quantifying its overall performance.

The results of the experimental tests revealed a series of differences regarding the behavior of the monocrystalline and polycrystalline photovoltaic panels, as well as certain similar general trends under varying operating temperatures and radiation conditions. In terms of power and efficiency, the results show significant differences (Table 4) determined by the incidence surfaces and the different spectral responses of the two panels to the radiation emitted by the solar simulator.

Table 4. Comparison between the parameters of the two photovoltaic panels.

Panel	P_{mp} (W)	η_{STC} (%)	P_{max} (W)	η_{max} (%)
Mono	30	16.66	12.6	12.70
Poly	30	15.15	15.9	14.42

Table 4. Comparison between the parameters of the two photovoltaic panels.

Panel	P_{mp} (W)	η_{STC} (%)	P_{max} (W)	η_{max} (%)
Mono	30	16.66	12.6	12.70
Poly	30	15.15	15.9	14.42

However, regarding the general trend, there have been some results with important similarities. The variation of the parameters of the two photovoltaic panels with the temperature is presented in Table 5.

Table 5. Variation of PV panel parameters with operating temperature.

Panel	$\Delta P_{mp}/\Delta T$ (%/°C)	$\Delta\eta/\Delta T$ (%/°C)	$\Delta V_{oc}/\Delta T$ (%/°C)	$\Delta I_{sc}/\Delta T$ (%/°C)
Mono	−0.47	−0.46	−0.45	0.14
Poly	−0.50	−0.50	−0.43	0.16

According to Table 5, the decrease in the efficiency of the photovoltaic panel with the operating temperature had values of −0.46–−0.50%/°C, and of the power produced by it with −0.47–−0.50%/°C, for both types of panels. These values were obtained based on the initial predictions, highlighting that the manufacturing material (silicon) has an independent influence, regardless of the technology or type of panel used, whether polycrystalline or monocrystalline. During the present research, a slight advantage is reported for the monocrystalline photovoltaic panels in terms of temperature effect, being preferable for integration into buildings.

The dependence of the power produced by the photovoltaic panel on the operating temperature is largely influenced by the variation of the voltage generated by the photovoltaic panel and less by the current produced. The coefficients of variation of the open-circuit voltage have values in the range −0.43–− 0.45%/°C, very close to those corresponding to efficiency (Table 5).

The present study demonstrates the important effect of improving the efficiency of PV panels through cooling, together with the instant effect of applying this technique.

Author Contributions: Conceptualization, V.-S.H., F.-E.Ț. and N.-C.C.; methodology, V.-S.H., F.-E.Ț. and N.-C.C.; software, V.-S.H. and F.-E.Ț.; validation, V.-S.H., F.-E.Ț., N.-C.C. and I.H.; formal analysis, V.-S.H. and I.H.; investigation, V.-S.H., C.R., N.-C.C. and I.H.; resources, V.-S.H. and F.-E.Ț.; data curation, V.-S.H., F.-E.Ț. and I.H.; writing—original draft preparation, V.-S.H., F.-E.Ț., N.-C.C. and I.H.; writing—review and editing, V.-S.H., C.R., N.-C.C. and I.H.; visualization, V.-S.H. and I.H.; supervision, V.-S.H.; project administration, V.-S.H.; funding acquisition, V.-S.H. All authors have read and agreed to the published version of the manuscript.

Funding: This research received no external funding.

Institutional Review Board Statement: Not applicable.

Informed Consent Statement: Not applicable.

Data Availability Statement: Data are contained within the article.

Conflicts of Interest: The authors declare no conflicts of interest.

Nomenclature

STC	Standard test conditions
NOCT	Nominal operating cell temperature
AM	Air mass
c_T	Coefficient of variation with temperature
ΔT	Difference between the t_{STC} and T_{med} (°C)
ΔX	PV panel parameters

T_{med}	Operating cell temperature (°C)
d	Distance between solar simulator and PV (cm)
G_{med}	Average radiation on PV panel surface (W/m^2)
R_{ch}	Characteristic resistance (Ω)
t_{NOCT}	Cell temperature in NOCT conditions (°C)
t_{STC}	Cell temperature in STC conditions (°C)
P_{mp}	Maximum power produced (Wp)
V_{mp}	Voltage at P_{mp} (V)
I_{mp}	Current at P_{mp} (A)
V_{oc}	Open-circuit voltage (V)
I_{sc}	Short-circuit current (A)
η	PV panel efficiency (%)
FF	Fill factor
β	PV panel temperature coefficients (%/°C)
L	Length of PV panel (mm)
l	Width of PV panel (mm)
H	Height of the PV panel (mm)

References

1. Zaite, A.; Belouaggadia, N.; Abid, C.; Kaiss, A.; Imghoure, O. Performance Enhancement of a Photovoltaic-Thermal Thermoelectric Collector Using Night Radiative Cooling. *Appl. Energy* **2024**, *364*, 123108. [CrossRef]
2. Hudișteanu, S.V.; Țurcanu, F.E.; Chereches, N.-C.; Popovici, C.-G.; Verdeș, M.; Ancaș, D.-A.; Hudișteanu, I. Effect of Wind Direction and Velocity on PV Panels Cooling with Perforated Heat Sinks. *Appl. Sci.* **2022**, *12*, 9665. [CrossRef]
3. Ma, X.; Ghosh, A.; Cuce, E.; Saboor, S. Building integrated photovoltaic-thermal systems (BIPVT) and spectral splitting technology: A critical review. *Next Sustain.* **2024**, *4*, 100056. [CrossRef]
4. Ren, H.; Quan, Z.; Wang, Z.; Wang, L.; Jing, H.; Zhao, Y. Performance simulation and analysis of a multi-energy complementary energy supply system for a novel BIPVT nearly zero energy building. *Energy Convers. Manag.* **2023**, *282*, 116879. [CrossRef]
5. Solanki, R.; Singh, V.; Varshney, L.; Kumar, K. Advanced Cooling Technique to Improve Efficiency of Solar Panel. In Proceedings of the 2023 International Conference on IoT, Communication and Automation Technology, ICICAT 2023, Gorakhpur, India, 23–24 June 2023.
6. Beldjani, C.; Belghar, N.; Aoues, K.; Saleh, M.S.M.; Boutera, Y.; Kethiri, M.A. Efficiency Improvement of Air-Cooled Photovoltaic Modules Utilizing Copper Heat Dissipators. *Desalination Water Treat.* **2022**, *279*, 140–146. [CrossRef]
7. Rousseau, P.; Nouri, H. ANSYS Investigation of Solar Photovoltaic Temperature Distribution for Improved Efficiency. *Int. J. Adv. Appl. Sci.* **2023**, *12*, 293–300. [CrossRef]
8. Perin Gasparin, F.; Detzel Kipper, F.; Schuck de Oliveira, F.; Krenzinger, A. Assessment on the variation of temperature coefficients of photovoltaic modules with solar irradiance. *Sol. Energy* **2022**, *244*, 126–133. [CrossRef]
9. Basem, A.; Mukhtar, A.; Salem Elbarbary, Z.M.; Atamurotov, F.; Benti, N.E. Experimental study on the various varieties of photovoltaic panels (PVs) cooling systems to increase their electrical efficiency. *PLoS ONE* **2024**, *19*, e0307616. [CrossRef]
10. Alzgool, M. Performance Enhancement by Cooling the PV Panels Using Phase Change Material (RT35): ANSYS Simulation and Experimental Investigation. *Int. J. Energy Prod. Manag.* **2024**, *9*, 73–81. [CrossRef]
11. *IEC 61853-1*; Photovoltaic (PV) Module Performance Testing and Energy Rating—Part 1: Irradiance and Temperature Performance Measurements and Power Rating. International Electrotechnical Commission: Geneva, Switzerland, 2011.
12. Ebhota, W.S.; Tabakov, P.Y. Influence of photovoltaic cell technologies and elevated temperature on photovoltaic system performance. *Ain Shams Eng. J.* **2023**, *14*, 101984. [CrossRef]
13. Hudișteanu, S.V.; Chereches, N.C.; Popovici, C.G.; Verdeș, M.; Ciocan, V.; Balan, M.C.; Țurcanu, F.E.; Scurtu, I.C. Effect of cooling on power generated by photovoltaic panels. *IOP Conf. Ser. Mater. Sci. Eng.* **2021**, *1141*, 012008. [CrossRef]
14. Ahmed, Y.E.; Maghami, M.R.; Pasupuleti, J.; Danook, S.H.; Basim Ismail, F. Overview of Recent Solar Photovoltaic Cooling System Approach. *Technologies* **2024**, *12*, 171. [CrossRef]
15. Ma, S.; Jin, Y.; Alam, F. Heat Pipe-Based Cooling Enhancement for Photovoltaic Modules: Experimental and Numerical Investigation. *Energies* **2024**, *17*, 4272. [CrossRef]
16. Kazemian, A.; Khatibi, M.; Entezari, S.; Ma, T.; Yang, H. Efficient energy generation and thermal storage in a photovoltaic thermal system partially covered by solar cells and integrated with organic phase change materials. *Renew. Sustain. Energy Rev.* **2023**, *188*, 113705. [CrossRef]
17. Grigore, R.; Vernica, S.G.; Popa, S.E.; Banu, I.V. Simulation and Experimental Results for Energy Production Using Hybrid Photovoltaic Thermal Technology. *Energies* **2024**, *17*, 1422. [CrossRef]
18. Hudisteanu, S.V.; Popovici, C.G. Experimental investigation of the wind direction influence on the cooling of photovoltaic panels integrated in double skin facades. *E3S Web Conf.* **2019**, *111*, 03045. [CrossRef]
19. Bilen, K.; Erdoğan, İ. Effects of Cooling on Performance of Photovoltaic/Thermal (PV/T) Solar Panels: A Comprehensive Review. *Sol. Energy* **2023**, *262*, 111829. [CrossRef]

20. Abdallah, R.; Haddad, T.; Zayed, M.; Juaidi, A.; Salameh, T. An Evaluation of the Use of Air Cooling to Enhance Photovoltaic Performance. *Therm. Sci. Eng. Prog.* **2024**, *47*, 102341. [CrossRef]
21. Al-Azawiey, S.S.; Mohamed, M.M.; Arifin, A.B. Effectiveness of PV/T Passive Natural Air Cooling by Backside Attached Fins. *Int. J. Energy Prod. Manag.* **2023**, *8*, 55–62. [CrossRef]
22. Homa, M.; Sornek, K.; Goryl, W. Experimental and Numerical Study on Air Cooling System Dedicated to Photovoltaic Panels. *Energies* **2024**, *17*, 3949. [CrossRef]
23. Maatallah, T.; Houcine, A.; Saeed, F.; Khan, S.; Ali, S. Simulated Performance Analysis of a Hybrid Water-Cooled Photovoltaic/Parabolic Dish Concentrator Coupled with Conical Cavity Receiver. *Sustainability* **2024**, *16*, 544. [CrossRef]
24. Hudisteanu, V.S.; Chereches, N.C.; Verdes, M.; Ciocan, V.; Popovici, C.G.; Turcanu, F.E.; Balan, M.C. Analysis of an innovative water-cooling solution for photovoltaic-thermal systems. *IOP Conf. Ser. Earth Environ. Sci.* **2021**, *664*, 012025. [CrossRef]
25. Shalaby, S.M.; Elfakharany, M.K.; Moharram, B.M.; Abosheiasha, H.F. Experimental study on the performance of PV with water cooling. *Energy Rep.* **2022**, *8*, 957–961. [CrossRef]
26. Khosravi, K.; Mohammed, H.I.; Mahdi, J.M.; Silakhori, M.; Ebrahimnataj Tiji, M.; Kazemian, A.; Ma, T.; Talebizadehsardari, P. Optimizing performance of water-cooled photovoltaic-thermal modules: A 3D numerical approach. *Sol. Energy* **2023**, *264*, 112025. [CrossRef]
27. Ibrahim, T.; Abou Akrouch, M.; Hachem, F.; Ramadan, M.; Ramadan, H.S.; Khaled, M. Cooling Techniques for Enhanced Efficiency of Photovoltaic Panels—Comparative Analysis with Environmental and Economic Insights. *Energies* **2024**, *17*, 713. [CrossRef]
28. Attoye, D.E.; Tabet Aoul, K.A.; Hassan, A. A Review on Building Integrated Photovoltaic Façade Customization Potentials. *Sustainability* **2017**, *9*, 2287. [CrossRef]
29. Hudisteanu, S.V.; Pruteanu, M.; Mateescu, T.D.; Vasilache, M. Experimental investigation of temperature effects on the parameters of photovoltaic panels. *Environ. Eng. Manag. J.* **2017**, *16*, 1643–1648.
30. Hudisteanu, S.V.; Chereches, C.N.; Turcanu, F.E.; Taranu, N.; Verdes, M.; Ancas, A.D.; Hudisteanu, I.; Ungureanu, D.; Polcovnicu, R.A. Solar radiation simulation device for investigation of thermal and photovoltaic panels. *Int. J. Mod. Manuf. Technol.* **2022**, *14*, 76–85. [CrossRef]
31. Available online: https://www.osram.com/ecat/ULTRA-VITALUX%20UV-A-UV-A-Ultraviolet%20lamps-Industry-Specialty%20Lighting/com/en/GPS01_1028569/ZMP_60829 (accessed on 7 November 2024).
32. Available online: https://www.feutron.de/en/double-climate-test-chamber (accessed on 7 November 2024).
33. Available online: https://www.cometsystem.com/products/sixteen-channel-data-logger-with-alarms/reg-ms6d (accessed on 7 November 2024).
34. Available online: https://www.tme.eu/ro/details/flk-355/contoare-si-adaptoare-cu-clema-ac-dc/fluke/fluke-355 (accessed on 7 November 2024).
35. Available online: https://www.testo.com/en/testo-871/p/0560-8712 (accessed on 7 November 2024).
36. Available online: https://www.soselectronic.com/ro-ro/products/voltcraft/pl-110sm-152318 (accessed on 7 November 2024).
37. Available online: https://bestech.com.au/wp-content/uploads/RE550_V71.pdf (accessed on 7 November 2024).
38. Constantin, A.I.; Iosif, G.; Chihaia, R.A.; Marin, D.; Shehadeh, G.U.A.; Karahan, M.; Gerikoglu, B.; Stavrev, S. Importance of Preventive Maintenance in Solar Energy Systems and Fault Detection for Solar Panels based on Thermal Images. *Electroteh. Electron. Autom.* **2023**, *71*, 1–12. [CrossRef]
39. Durán, E.; Galán, J.; Andujar, J.M.; Sidrach-de-Cardona, M.A. A New Method to Obtain I-V Characteristics Curves of Photovoltaic Modules Based on SEPIC and Cuk Converters. *EPE J.* **2008**, *18*, 5–15. [CrossRef]

Disclaimer/Publisher's Note: The statements, opinions and data contained in all publications are solely those of the individual author(s) and contributor(s) and not of MDPI and/or the editor(s). MDPI and/or the editor(s) disclaim responsibility for any injury to people or property resulting from any ideas, methods, instructions or products referred to in the content.

JOURNAL OF APPLIED ENGINEERING SCIENCES
ISSN: 2247-3769 / e-ISSN: 2284-7197
sciendo
VOL. 14(27), ISSUE 1/2024
ART.NO. 389 pp. 1-10

GRAPHICAL INTERFACE FOR ELECTRICAL DIMENSIONING OF AN ON-GRID PHOTOVOLTAIC SYSTEM

M. Alexa[a]*, N.Ţăranu[a], S.V.Hudişteanu[a], N.C. Cherecheş[a], Fl.E.Ţurcanu[a], Diana Ancaş[a], Marina Verdeş[a], C.G. Popovici[a], V. Ciocan[a], Iuliana Hudişteanu[a]

[a*]Technical University "Gheorghe Asachi" of Iasi, Faculty of Civil Engineering and Building Services, Prof. D. Mangeron 1, 700050, Iasi, Romania; E-mails: *marius.alexa@student.tuiasi.ro, nicolae.taranu@academic.tuiasi.ro, valeriu-sebastian.hudisteanu@academic.tuiasi.ro, nelu.chereches@academic.tuiasi.ro, florin-emilian.turcanu@academic.tuiasi.ro, ancas05@yahoo.com, verdesmarina2003@yahoo.com, catalinpopovici@climatherm.ro, vciocan2005@yahoo.com, iuliana.hudisteanu@academic.tuiasi.ro

Received: 27.01.2024 / Accepted: 09.02.2024 / Revised: 15.02.2024 / Available online: 31.05.2024

DOI: 10.2478/jaes-2024-0001

KEY WORDS: photovoltaic panels, solar energy, dimensioning, design, electricity.

ABSTRACT:

Energy is an essential element in the development of mankind and is the engine that has made possible all the discoveries and innovations of recent decades. It is found behind the comfort we have in everyday life, whether at home, at the office, or when traveling: an optimal temperature in the room, light at anytime, appliances to ease us and make our lives more beautiful. An energy system based on renewable energy has the ability to provide electricity in an economical, sustainable, long-term, non-polluting way and can serve the increasing population. One such example is represented by photovoltaic (PV) panels, which produces electricity from captured solar energy and is one of the solutions considered for reducing energy. The dimensioning of a photovoltaic system, from a technical and economic efficiency point of view, involves the analysis of input data, output data and hence the characteristics of an efficient system. The analysis can be done analytically, but also with the help of dedicated software, the result being, in the end, a safe system in terms of preventive operation and maintenance. In the article was made the dimensioning of a system, analytical and automatic – using software application – to determine if the result obtained – the photovoltaic system – is the same regardless of the method used.

1. INTRODUCTION

Energy is an essential element in the development of mankind and is the engine that has made possible all the discoveries and innovations of recent decades. It is found behind the comfort we have in every day life, whether at home, at the office, or when traveling: an optimal temperature in the room, light at any time, appliances to ease us and make our lives more beautiful.

An energy system based on renewable energy has the ability to provide electricity in an economical, sustainable, long-term, non-polluting way and can serve a population in full population explosion. One such example is represented by photovoltaic (PV) panels, which produces electricity from captured solar energy, is one of the solutions considered for reducing energy consumption and is considered the fastest growing technology for electric power production and pollutant reduction (Aguilar-Jimenez, 2020).

The dimensioning of a photovoltaic system, from a technical and economic efficiency point of view, involves the analysis of input data, output data and hence the characteristics of an efficient system.

The analysis can be done analytically, but also with the help of dedicated software, the result being, in the end, a safe system in terms of preventive operation and maintenance (Gomaa, 2020).

Renewable energy is also an optimal solution to the problem of global warming. In terms of energy sources and combating the lack of energy, the renewable energy could represent an adequate solution. The development of renewable energy sources can also boost employment by creating jobs in new 'green' technologies. In recent years, but especially in the current period, in the context of policy changes at regional / global level, renewable energy, sustainable development and environmental protection have become main topics, of first urgency (Hudişteanu, 2021).

2. THEORETICAL CONSIDERATIONS

2.1 Solar energy

Solar energy is the most abundant energy resource on Earth. It can be captured and used in many ways, and as a renewable energy source it is an important part of our clean future.

Corresponding author: Alexa Marius, Eng., PhD Student/
Faculty of Civil Engineering and Building Services, Iasi, RO, e-mail: marius.alexa@student.tuiasi.com

The sun provides us with solar radiation during the day and does much more for us, so every particle of solar radiation (photon) that reaches Earth contains energy that powers our planet (Math, 2015).

Solar energy can be harnessed and transformed into usable energy using photovoltaic panels or solar thermal panels. Although solar energy accounts for only a small amount of global energy consumption, the low cost of installing solar panels means that more people in more places can take advantage of solar energy (Sornek, 2022).

2.2 Photovoltaic conversion

The photovoltaic effect namely the transformation of solar energy ("photon") into electricity ("volt") was discovered in 1839 by physicist A.Becquerel. To achieve these conversion devices called solar cells are used, made up of semiconductor materials in which a constant electric field has been artificially created (Johnston, 2021; Selimli, 2021).

The photovoltaic effect is the generation of voltage and electric current in a material upon exposure to light. It is a physical and chemical phenomenon (Barkat, 2020).

Photovoltaic/thermal (PV/T) systems are innovative cogeneration systems that ensure the cooling of photovoltaic (PV) (Hudişteanu, 2022). The photovoltaic effect is closely related to the photoelectric effect. In both cases, light is absorbed, causing an electron or other charge carrier to excite to a higher energy state. The main distinction is that the term photoelectric effect is usually used when the electron is ejected from the material (usually in a vacuum), and the term photovoltaic effect is used when the excited charge carrier is still contained in the material.

In both cases, an electric potential (or voltage) is produced by charge separation, and the light must have sufficient energy to overcome the potential barrier of excitation. In addition to direct excitation of free electrons, a photovoltaic effect can occur due to heating caused by light absorption. Heating leads to an increase in the temperature of the semiconductor material, this is accompanied by temperature gradients.

A common way for property owners to take advantage of solar energy is with a solar photovoltaic (PV) system. With the help of a solar photovoltaic system, photovoltaic panels convert sunlight into electricity (Hudişteanu, 2020). The electricity obtained from the transformation of solar energy can be used immediately, which is stored in a solar battery (Aguilar-Jimenez, 2020). Solar radiation produced by the sun, which is captured by solar panels, hits a semiconductor material (usually silicon) and knocks electrons open, setting them in motion and generating a direct electric current that can be captured with wiring and converted into alternating current using a solar inverter.

Solar photovoltaic energy was not wide spread in 1999. After that, the grow was of major importance, reaching 43.4% between 2002 and 2003. The installed capacity in the European Union was 562.3 MW in 2003. Leading the list of EU countries were Germany (397.6 MW), the Netherlands (48.63 MW), Spain (27.26 MW) and Italy (26.02 MW). For comparison, here are the installed powers in several other countries in 2003: France (21.71 MW), Portugal (2.07 MW) and Belgium (1.06 MW), as seen in Figure 1. It is noted that it is not the countries located in southern Europe that develop the photovoltaic chain the most (Ghosh, 2021).

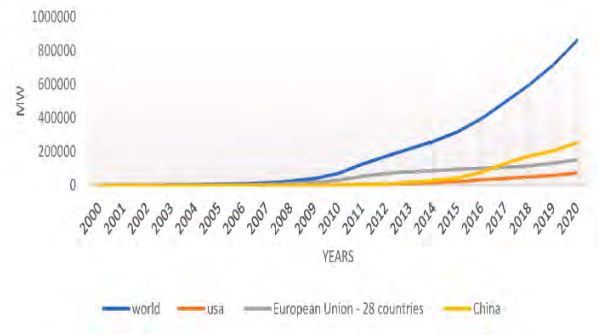


Figure 1. Solar photovoltaic capacity (Mega Watt) in the world, China, the EU and the USA

Starting with 2011 most countries started to implement PV and the most significant changes took place. As a result of changes in PV capacity, in 2023 production increased to 150.502 MW in the EU (EU) countries. More than one-third of PV capacity is produced in Germany, followed by Italy and Austria, Spain, and France (Irena, 2021; Borawski, 2023).

2.3 Photovoltaic panel efficiency

The photovoltaic cell represents an electronic device, made of semiconductor materials, which generates electron pairs and free holes by absorbing light, the charge carriers being spatially separated due to a potential barrier formed by internal discontinuities that drive electrons in the opposite direction to the gaps (Arifin, 2020).

Separating the charge carriers results in a voltage at the cell terminals and a current through a load resistance, so that the photovoltaic cell functions as an electric generator.

The efficiency of a photovoltaic cell is determined as the ratio between the power generated by the cell at the output at a specified temperature and the power of solar radiation (Al-Amri, 2021; Selimi, 2021; Hudişteanu, 2021):

$$\eta = \frac{P_M}{S \cdot E} \qquad (1)$$

where P_M = cell electrical power [Wp];
S = cell/module area [m^2];
E = global radiation incident on the surface of the cell or module [W/m^2]

3. NUMERICAL PHOTOVOLTAIC SYSTEM DIMENSIONING

3.1 General input data

For example it considers a configuration of a grid-connected photovoltaic system with **150 kWp** installed power.

The choice of location. Orientation of photovoltaic panels:
- location: 47° 8' 57" North, 27° 37' 48" East (47.149, 27.629 - Iaşi);
- correct placement of the system in order to avoid shading;
- system orientation: South, fixed tilt 35°.

The installed power in photovoltaic modules is:

$$P_{inst} = 150\ [kWp]$$

Calculation of the number of panels: choose a monocrystalline solar panel with the following technical characteristics (table no 1):

Maximum power STC (P_{max})	500 Wp
Maximum supply voltage P_{max} (V_{mp})	42,2 V
Maximum power current P_{max} (I_{mp})	11,12 A
Open circuit voltage (V_{oc})	49,9 V
Short circuit current (I_{sc})	11,95 A
Module efficiency (%)	21,2
P_{max} temperature coefficient (C_{tPmax})	- 0,45 %/°C
V_{oc}temperature coefficient (C_{tVoc})	- 0,27 %/°C
I_{sc}temperature coeficient (C_{tIsc})	0,05%/°C
Maximum systemvoltage	1500 V
Maximum recommended value for maximum current protection safety	20 A
Operating temperature	- 40°C ÷ +85°C
Nominal Operating Cell Temperature (NOCT)	45°C
Dimensions	2108x1048x40 mm
Height	24 kg

Table 1. Technical characteristics of the photovoltaic panel

$$N_P = \frac{P_{inst}}{P_{max}} = \frac{150000}{500} = 300\ PV \qquad (2)$$

Calculation of the surface area of the photovoltaic system (Gomaa, 2020):

$$A_{SPV} = N_P \cdot A_P = N_P \cdot L_P \cdot l_P \qquad (3)$$

$$A_{SPV} = 300 \cdot 2{,}108 \cdot 1{,}048 = 662{,}75\ [m^2]$$

For the installation of solar panels, an area of at least 662,75 m^2 facing south is needed. Basically, the occupied area will be larger because mounting distances from the roof edges and certain technological distances necessary for the maintenance of the photovoltaic system must be provided.

3.2 Case studies

Choosing the connection diagram of panels: 3 connection variants will be analyzed to configure the subsystems, as follows:

Case 1: N_S = **6 strings**, each string with N_{PS} = **25 PV** linked in series

Case 2: N_S = **5 strings**, each string with N_{PS} = **30 PV** linked in series

Case 3: N_S = **3 strings**, each string with N_{PS} = **50 PV** linked in series

Calculation of photovoltaic generator characteristics
Maximum power DC (P_{maxDC}) represents the maximum power generated by the DC photovoltaic system. It must be less than or equal to the power accepted by the inverter on the DC input.

$$P_{\max DC} = N_p \cdot P_{max} = 150 \cdot 500 = 75\ kW \qquad (4)$$

Maximum voltage DC (V_{maxDC}) represents the maximum voltage of the photovoltaic generator. It must be less than or equal to the voltage accepted by the inverter at the DC input.

In determining this parameter, account shall be taken of:
- the number of panels in the string;
- the value of the idle voltage of one panel;
- the correction thermal coefficient for voltage;
- the minimum working temperature of the panels.

The computational relationship is as follows (Bica, 2019):

$$V_{\max DC} = N_{ps} \cdot V_{oc} \cdot \left[1 + \frac{C_{tV_{oc}}}{100} \cdot (T_{min} - T_{STC})\right] \qquad (5)$$

where: N_{ps} = number of panels connected in series
C_{tVoc} = thermal correction coefficient for idle voltage
V_{oc} = idle voltage of a panel
T_{STC} = standard temperature T_{STC} =25°C
T_{min} (20°C) = minimum temperature in the area.

3.3 System dimensioning

Case 1: N_{ps} = 25

$$V_{\max DC} = 25 \cdot 49{,}9\left[1 + \frac{-0{,}27}{100}(-20 - 25)\right] = 1.398{,}5\ [V]6)$$

Case 2: N_{ps} = 30

$$V_{\max DC} = 30 \cdot 49{,}9\left[1 + \frac{-0{,}27}{100}(-20 - 25)\right] = 1.678{,}1[V]\ 7)$$

Case 3: N_{ps} = 50

$$V_{\max DC} = 50 \cdot 49{,}9\left[1 + \frac{-0{,}27}{100}(-20 - 25)\right] = 2.796{,}9\ [V]8)$$

Minimum voltage DC (V_{minDC}) represents the minimum voltage of the photovoltaic generator. It must be greater than or equal to the minimum voltage (accepted by the inverter at the DC input) from which the inverter starts the conversion from DC to AC.

In determining this parameter, account shall be taken of:
- the number of panels in the string;
- the value of the voltage of one panel at maximum power;
- the correction thermal coefficient for voltage;
- the maximum working temperature of the panels.

The computational relationship is as follows (Bica, 2019):

$$V_{\min DC} = N_{ps} \cdot V_{mp} \cdot \left[1 + \frac{C_{tV_{oc}}}{100} \cdot (T_{max} - T_{STC})\right] \quad (9)$$

where: N_{ps} = number of panels connected in series,
C_{tVoc} = thermal correction coefficient for idle voltage,
V_{mp} = voltage panel for P_{max},
T_{STC} = standard temperature T_{STC} = 25°C,
T_{max} (+70°C) = maximum temperature in the area.

Case 1: N_{ps} = 25

$$V_{min\,DC} = 25 \cdot 42{,}2 \cdot \left[1 + \frac{-0{,}27}{100}(70 - 25)\right] = 926{,}3 \text{ [V]} (10)$$

Case 2: N_{ps} = 30

$$V_{min\,DC} = 30 \cdot 42{,}2 \cdot \left[1 + \frac{-0{,}27}{100}(70 - 25)\right] = 1.112 \text{ [V]} (11)$$

Case 3: N_{ps} = 50

$$V_{min\,DC} = 50 \cdot 42{,}2 \cdot \left[1 + \frac{-0{,}27}{100}(70 - 25)\right] = 1.853 \text{ [V]} (12)$$

Maximum power current ($I_{\max DC}$) represents the maximum current of the photovoltaic generator. It shall be less than or equal to the maximum current accepted by the inverter at the DC input(s).

The computational relationship is as follow (Bica, 2019):

$$I_{\max DC} = N_s \cdot I_{sc} \cdot \left[1 + \frac{C_{tI_{sc}}}{100} \cdot (T_{max} - T_{STC})\right] \quad (13)$$

where: N_s = number of strings connected in parallel to one inverter input,
V_{mp} = voltage panel for P_{max},
C_{tIsc}= thermal correction coefficient for idle current,
T_{STC} = standard temperature T_{STC} = 25°C,
T_{max} = +70°C - maximum temperature in the area.

Case 1: N_s = 6

$$I_{maxDC} = 6 \cdot 11{,}95 \cdot \left[1 + \frac{0{,}05}{100}(70 - 25)\right] = 73{,}3 \text{ [A]} (14)$$

Case 2: N_s = 5

$$I_{maxDC} = 5 \cdot 11{,}95 \cdot \left[1 + \frac{0{,}05}{100}(70 - 25)\right] = 61{,}1 \text{ [A]} (15)$$

Case 3: N_s = 3

$$I_{maxDC} = 3 \cdot 11{,}95 \cdot \left[1 + \frac{0{,}05}{100}(70 - 25)\right] = 36{,}6 \text{ [A]} (16)$$

Inverter dimensioning:

For the choice of inverter, five criteria will be taken into account:
- compliance with the minimum technical conditions imposed by legislation: in order to be allowed to connect to the electricity distribution network, it is necessary that the inverter complies with the grid connection requirements established by ANRE Order 228/28.12.2018 (Ghosh, 2021).

- maximum input power $P_{\max DC}$: the inverter must accept at the DC input a power greater than or equal to **150 kW**.

- maximum input voltage ($V_{\max DC}$) for which the inverter must accept at the DC input a **voltage greater than or equal** to minimum input voltage ($V_{\min DC}$) for which the inverter begins to convert from DC to AC must be less than or equal and the maximum input current ($I_{\max DC}$) representing the maximum allowable inverter current on a DC input shall be equal to or greater than the values in the table 2:

	Case 1	Case 2	Case 3
$V_{\max DC}$ [V]	1.398	1.678	2.797
$V_{\min DC}$ [V]	926	1.112	1.853
$I_{\max DC}$ [A]	73	61	36

Table 2. Values of electrical input characteristics for the inverter

Taking into account the five criteria, one inverter was selected that meet the conditions set out above, according to the table 3.

Parameter/Type of inverter	**Inverter 75KTL-C1**
Maximum input power	84.200 W
Maximum input voltage	1100 V
Operating voltage range	200-1000 V
Maximum input current (per MPPT)	25 A
Maximum input current (per STRING)	18 A
Maximum short-circuit current (1 MPPT)	39 A
Full power MPPT voltage range	625-850 V
Rated input voltage	750V
Number of inputs	12
Number of MPP trackers	6

Table 3. Technical characteristics for the inverter

The total power (150kWp) will be split with 2 inverters; it will come from each string to an MPPT input of the inverter. Inverters with several independent inputs have the advantage of greater operational safety, the failure of one string or input not affecting the operation of the others (the photovoltaic

system will still produce less electricity. Also, this type of inverters is recommended for optimizing production when panel strings have different orientations.

3.4 Cable dimensioning

Solar cables are designed to have a life span of 40 years or more and at the same time minimize energy losses. It must also with stand temperatures between 20 and 80°C. The correct choice of cable is very important, because if it has too small a section, it will heat up and fail.
It will determine the maximum DC voltage generated by a row of photovoltaic panels as the product of the number of panels in a string, the voltage of a panel and a correction coefficient that depends on the permissible temperature of the cable (table no 4):

No.	Ambient temperature °C	Correction coefficient with conductor temperature	
		75°C	90°C
1	21÷25	1.05	1.04
2	26÷30	1.00	1.00
3	31÷35	0.94	0.96
4	36÷40	0.88	0.91
5	41÷45	0.82	0.87
6	46÷50	0.75	0.82
7	51÷55	0.67	0.76
8	56÷60	0.58	0.71
9	61÷70	0.33	0.58
10	71÷80	0.00	0.41

Table. 4 Temperature correction coefficient

The maximum DC voltage:

$$U_{PV} = N_{ps} \cdot U_p \cdot k_t \text{ [V]} \quad (17)$$

where: N_{ps} = number of PV ;
U_p = maximum supply voltage for PV;
k_t = correction coefficient with temperature;

Case 1: $U_{PV} = 25 \cdot 42{,}2 \cdot 0{,}75 = 791{,}2$ [V] (18)

Case 2: $U_{PV} = 30 \cdot 42{,}2 \cdot 0{,}75 = 949{,}5$[V] (19)

Case 3: $U_{PV} = 50 \cdot 42{,}2 \cdot 0{,}75 = 1.582{,}5$[V] (20)

- it will determine the acceptable voltage drop on the cable, normally 2-3%, which will be used to calculate the cable cross section:

$$\Delta U = 0{,}02 \cdot U_{pv} \text{ [V]} \quad (21)$$

Case 1: $\Delta U = 0{,}02 \cdot 791{,}2 = 15{,}8$ [V] (21)

Case 2: $\Delta U = 0{,}02 \cdot 949{,}5 = 19{,}0$ [V] (22)

Case 3: $\Delta U = 0{,}02 \cdot 1.582{,}5 = 31{,}6$ [V] (23)

- it will calculate the maximum direct current which shall be taken to be 1,25 times the rated short-circuit current Isc of the module:

I_{SC} = 11,95 A => maximum value = 1,25 · 11,95 = 15 [A]

- it will calculate the maximum direct current flowing through the conductor, taking into account the worst case:

$$I_{nom} = 1{,}25 \cdot 15 = 18{,}7 \text{ [A]}$$

The current determined above is at a temperature of 70°C. In order to determine the current value to be taken into account in the calculation of the conductor section, the temperature shall be taken into account by the correction coefficient with temperature $\mathbf{k_t}$ (table 4) and the number of conductors in a cable by the correction coefficient $\mathbf{k_c}$ (table 5):

No. of current-carrying	Adjustment factor
1-3 conductors	1.00
4-6 conductors	0.80
7-9 conductors	0.70
10-20 conductors	0.50

Table 5. Correction factor in a cable

For the numerical example presented, the ambient temperature will be considered 61÷70 °C and the cable temperature will be considered 75 °C (k_t =0,33). It will consider 3 conductors in a cable (k_c =1), the calculating current of the conductor section being (Bica, 2019):

$$I_{calc} = \frac{I_{nom}}{k_t k_c} = \frac{18{,}7}{0{,}33 \cdot 1} = 56{,}6 \text{ [A]} \quad (24)$$

Next it will calculate the cross-sectional area:

Consider a 10 m copper cable with resistivity ρ=1.724*10^{-8} Ωm. The total resistance of the cable will be (there are two cables, one carrying and one returning between the panels and the charging controller)

$$R = 2 \cdot \frac{\rho \cdot l}{s} \quad (25)$$

From the relationship of the allowable voltage drop on the cable:

$$\Delta U = R \cdot I_{calc} = 2 \cdot \frac{\rho \cdot l}{s} \cdot I_{calc} \quad (26)$$

The minimum conductor cross section it will determined:

$$s = 2\frac{\rho \cdot l \cdot I_{calc}}{\Delta U} = \frac{2 \cdot 1{,}724 \cdot 10^{-8} \cdot 10 \cdot 56{,}6}{4{,}56} = 4{,}78\ mm^2 \quad (27)$$

It will choose a cable with a standard section of 6 [mm^2].

Cable sizing between inverter and consumers (network):
An allowable voltage drop of 2% shall be considered and the length of the connecting cable shall be 20 m:

$$\Delta U = 0{,}02 \cdot 230 = 4{,}6 \text{ [V]} \quad (28)$$

For three-phase case (for powers greater than 6-7 kW). From the relationship of inverter power:

$$P_{nec} = 3 \cdot U \cdot I \qquad (29)$$

result the value of electricity:

$$I = \frac{P_{nec}}{3U} = \frac{15.000}{3 \cdot 230} = 21{,}74\ [A] \quad (30)$$

From the relationship of the allowable voltage drop:

$$\Delta U = RI = \frac{\rho l}{s} I \qquad (31)$$

Finnaly it will determine the minimum conductor crosssection (copper)

$$s = \frac{\rho l I}{\Delta U} = \frac{1{,}724 \cdot 10^{-8} \cdot 20 \cdot 21{,}74}{4{,}6} = 1{,}63\ [mm^2] \qquad (32)$$

It will choose a cable with a standard section of 2,5 [mm^2].

4. GRAPHICAL INTERFACE FOR PHOTOVOLTAIC SYSTEM DIMENSIONING

4.1 General presentation

Cool-PV software is an application developed at Faculty of Civil Engineering and Building Services – Technical University „Ghe. Asachi" of Iasi. It is realized in the Microsoft Visual Studio platform C#, with its own resources and is intended for analyzing, performing calculations and dimensioning of a photovoltaic system, depending on the number and type of electrical receivers or estimated energy consumption (kWh / month) for a household or non-household consumer (view at http://www.cool-pv.ci.tuiasi.ro/).

Another function of the software is the economic calculation of investment amortization, after an analysis that takes into account all input data (location, PV orientation, tilt angle, etc.) and output data (average energy production of photovoltaic panels and photovoltaic system) over a period of 20 years.

The start page of the software is divided into 3 sections, on modules and the steps that the beneficiary must go through are materialized, in order to obtain the most accurate information, according to figure 2. The steps to be taken by the user are for information purposes only; if the application user does not intervene on predefined input data, the software warns him about not completing the algorithm entirely, but this does not mean that the output data is erroneous.

These are calculated and made available to the user according to the input data, both those predefined by the application, on which the user has not intervened, and according to the modified / entered data by the beneficiary.

In section no. 1 it can be find the main dimensioning key of the photovoltaic system (energy requirements) and the logo of the CoolPV software.

Input data:
The energy requirement can be calculated by accessing one of the 3 options:
1. number of electrical consumers owned by the beneficiary
2. power demanded (kWp)
3. estimated energy consumption (kWh/month)

In order to record the value of the **requested power** or the value of the **estimated energy consumption**, it is enough to check the desired option (ticking the radio-button corresponding to the chosen option), enter a numerical value in the text-box attached to the option and validate the value by pressing the **OK** button. After validating the estimated energy consumption or the requested power, its value can be found in the *readonly text-box* **Estimated energy consumption**, located at the bottom of section 2.

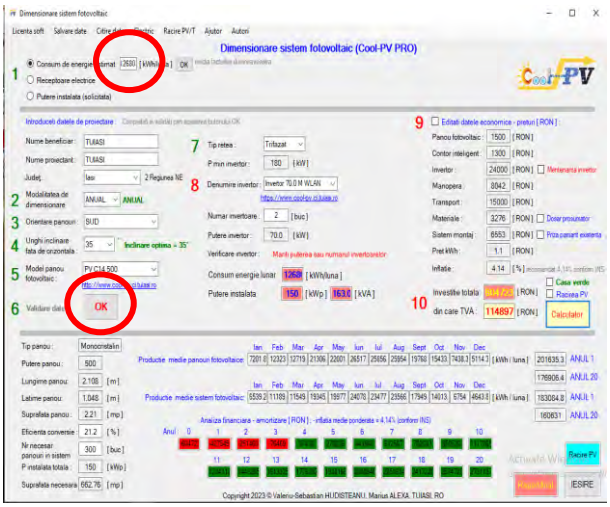


Figure 2. Photovoltaic system dimensioning CoolPV software

After the user has entered all the data that most faithfully represents his own conditions and the sizing method of the photovoltaic system (calculation of electricity needs depending on the degree of energy independence), he must validate this data, which will lead to the next step in the sizing algorithm. The validation is done by pressing the **OK** button with the left-click, button located immediately below *Dimensioning method* (figure no. 2).

After the data is validated, by pressing the OK button (it is recommended to review the information entered in the dedicated fields), the text-box fields in SECTION 3 will be populated with data strictly related to photovoltaic panels.

The *Panel Type* field will be populated with the photovoltaic panel type (monocrystalline, polycrystalline, amorphous, hybrid), this characteristic being read from the manufacturer's technical documentation.

The *Panel Power* field will be populated with its power, given in [Wp].

The *Panel Length* and *Panel Width* fields will be populated with the dimensions of a single photovoltaic panel, taken

from the manufacturer's technical documentation and given in [m]. The value in the *Panel Area* field is given by the length multiply by width, in [m^2], in according with:

$$S_{PV} = L_{PV} \cdot l_{PV} \ [m^2] \qquad (33)$$

The *Conversion Efficiency* field is populated with the photovoltaic panel efficiency value, as it is also known in the specialized literature, and the efficiency value is taken from the manufacturer's technical documentation. The efficiency of the photovoltaic panel also plays an essential role in determining the amount of electricity ultimately produced by the entire photovoltaic system.

Number of panels required in the system: the calculation of electricity production is made by the value of electricity produced by 1 mp of photovoltaic panel, but in direct relation to the intensity of solar radiation in a certain area.

The total area of photovoltaic panels must be dimensioned so that it **covers the value of electricity needs**:

$$S_{total} = \frac{E_{nec}}{E_{mp} * \frac{\sigma_{PV}}{\sigma_{standard}}} \qquad (34)$$

where:

S_{total}= total area producing electricity;
E_{nec} = estimated energy consumption (electricity requirements)
E_{mp} = electricity produced by 1 mp of PV;

$\frac{\sigma_{PV}}{\sigma_{standard}}$ = ratio of PV yield and correction coefficient (0,202)

After identifying the total area needed to cover the estimated energy consumption, the number of photovoltaic panels will be given by the ratio between the total area and the area of a single panel:

$$N_{PV} = \frac{S_{total}}{S_{PV}}; \qquad (35)$$

where:

N_{PV} = number of photovoltaic panels
S_{total} = total area producing electricity;
S_{PV} = the surface of a single photovoltaic panel.

Total power installed represents the power of all photovoltaic panels, in kWh and is given by the sum of the installed power of all photovoltaic panels:

$$P_{i\,total} = \sum_{i=1}^{n} P_{PV\,i}; \qquad (36)$$

The required area represents the minimum area available for the installation of all photovoltaic panels. In order to activate the component responsible for economic calculation, regarding the design and operation of the photovoltaic system, the user must activate, with a left click, the checkbox assimilated to economic data. The economic calculation was made taking into account the annual inflation rate, reported to the annual consumer price index, according to data of the National Institute of Statistics. This index is determined as the ratio, expressed as a percentage, between the average price index of the current year and the average index of the previous year (or other year chosen as reference period).

As from 1992 onwards, the average price index of a given year shall be determined as the simple arithmetic average of the monthly indices for that year, calculated against the same base (October 1990=100).The annual inflation rate is calculated by subtracting 100 from the annual consumer price index, as presented on the website of the National Institute of Statistics (INS). After activating the checkbox assimilated to economic data, numerical values of materials, workmanship, etc., including the selling price of one kWh, can be entered. The calculation, the payback period and the level of return on investment are made according to the numerical values entered here.

The calculation of electricity production, separately on the 2 components (production of photovoltaic panels and production of photovoltaic system) was done in 2 ways:

1. In the first case, the **real mode** of electricity production was taken into account, with the decrease in time of the efficiency of photovoltaic panels, according to the manufacturer's technical documentation.
2. In second case, the **ideal mode** of production was taken into account; the decrease in the efficiency of photovoltaic panels over time (without degradation of photovoltaic cells over time) was not taken into account.

4.2 Electrical dimensioning module

The module dedicated to the electrical dimensioning of the photovoltaic system is accessed by pressing the "*Electric*" button in the menu bar, after the entire photovoltaic system has been dimensioned, as shown in figure no 3.

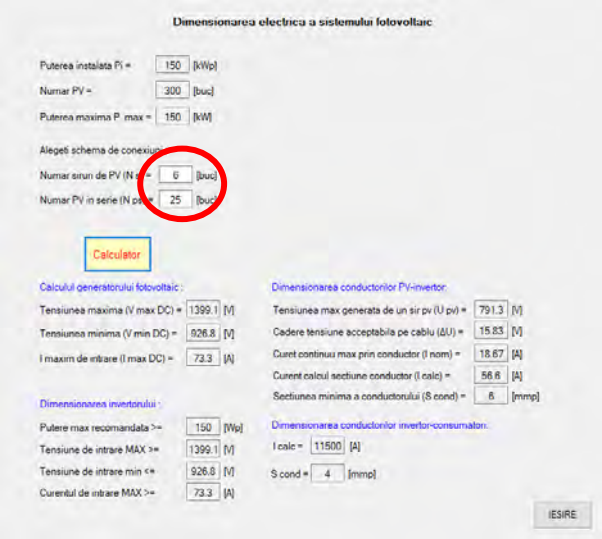


Figure 3. Electrical dimensioning of the photovoltaic system

The window that opens after accessing the "*Electric*" button is shown in figure no. 3, 4 and 5 and has the following input data, taken from the photovoltaic system sizing window:
- The value of the installed power of the photovoltaic system (P_i);
- Number of photovoltaic panels in the system (Nr PV);
- Maximum power value of the dimensioned system (P_{max}).

After presenting the values specific to the photovoltaic system, values that represent input data for dimensioning the values of the maximum, minimum voltages and current of the inverter, the section of direct current conductors and the section of alternating current conductors, the user must establish the number of strings and the number of photovoltaic panels connected in series, in a string.

The number of strings and the number of photovoltaic panels linked in series determine the value of the system voltage and current, values that represent input data for the inverter and must be within the range of values with which it works.

Below are presented the values of the electrical dimensioning of the photovoltaic system, on the 3 cases presented at the beginning of the application.

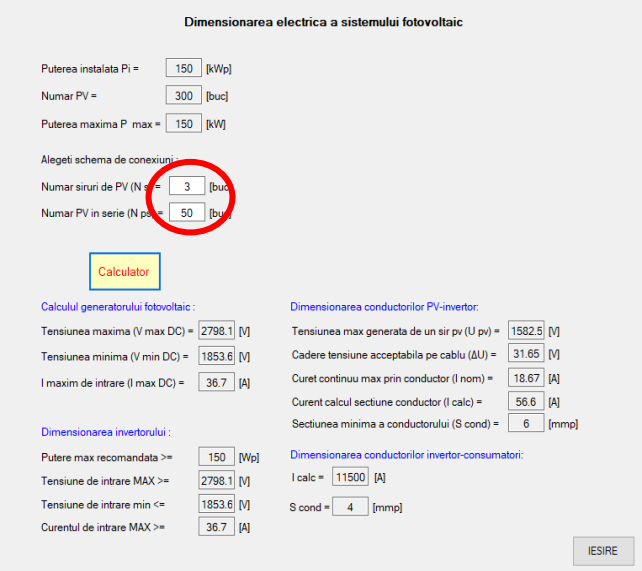


Figure 4. Electrical dimensioning of the photovoltaic system

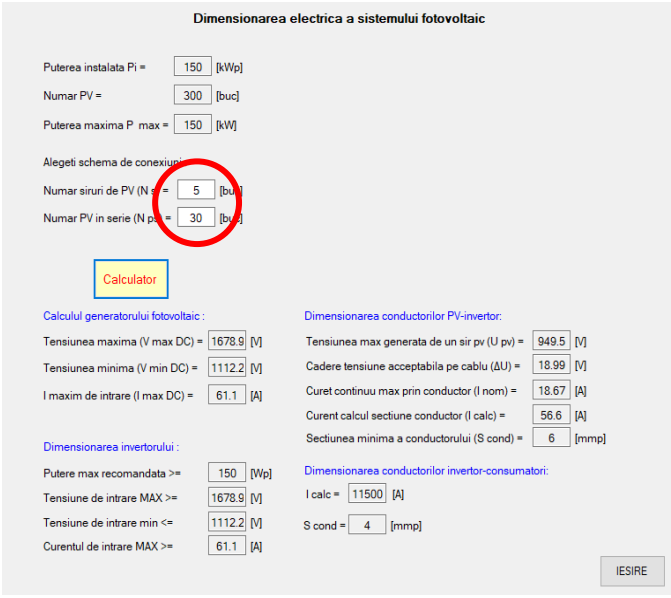


Figure 5. Electrical dimensioning of the photovoltaic system

When the user presses the "*Calculator*" button, the graphical application calculates, after the steps presented in the numerical calculation section, the specific values of the photovoltaic generator, the sizing of the inverter and conductors.

The results obtained with the help of the **Cool-PV** application can be compared with the results obtained by analytical calculation.

4. CONCLUSION

Analyzing the results obtained by numerical calculation, as well as with the help of the Cool-PV application, **the most efficient solution** (table no. 6) is given by placing the photovoltaic panels on **6 rows, 25 pieces in turn**, thus having input on all MPPT channels of the inverter (the inverter has 6 MPPT).

	Case 1 (6x25)	Case 2 (5x30)	Case 3 (3*50)
V_{maxDC} [V]	**1.399**	1.678	2.797
V_{minDC} [V]	**926**	1.112	1.853
I_{maxDC} [A]	**73,3**	61,1	36,6
U_{PV} [V]	**791,2**	949,5	1.582,5
ΔU [V]	**15,8**	19	31,6
I_{nom} [A]	**18,7**	18,7	18,7
I_{calc} [A]	**56,6**	56,6,	56,6,
S [mmp]	**6**	6	6
ΔU [V]	**4,6**	4,6	4,6

Table 6. The final result for PV system management

The **Construction installations field** is no longer a field that is reduced to lighting, utility supply and household or industrial waste disposal.

Another important factor governing construction installations is the level of technology and automation.

In order to ensure optimal living conditions, to ensure conditions according to the norms in force in buildings with special functions, to avoid tragedies and disasters, construction installations are designed, executed and maintained in operation with the help of multiple instruments of a high technological level.

The latest technologies are used in all fields of activity and there are no longer procedures that are not computer-assisted or automated.

That is why specialists in this field must be very good specialists, well anchored in the IT area and very good connoisseurs of automation algorithms.

These specialists can be trained and perfected if simulators are increasingly used.

Also, all stages of design, execution and testing of installations and apparatus in the field of installations can be executed only with the help of simulation systems.

The simulation and dimensioning software of photovoltaic systems is not only a tool to support students, electricians, technicians and installation engineers, but a way to train new specialists, to educate their skills, to improve them, to accustom them to use all the tools in the field of modelling and simulation to obtain maximum efficiency in design and execution.

Finally, we can quote Paulo Coelho who said that "the great mystery that the Divinity revealed to the world was fire. Not just the one capable of warming up, but the one who turns wheat into bread"; and this is precisely the role of modern man: the transformation of wheat into bread.

References

Aguilar-Jimenez J.A., Hernandez-Callejo L., Alonso-Gomez V.; Velazquez N.; Lopez-Zavala R.; Acuna A.; Mariano-Hernandez D., 2020, *Techno-economic analysis of hybrid PV/T systems under different climate scenarios and energy tariffs*, Sol. Energy, 212, 191–202.

Al-Amri F.G., Abdelmagid T.I.M., 2021, *Analytical model for the prediction of solar cell temperature for a high-concentration photovoltaic system*, Elsevier, volume 25, 100890.

Arifin Z., Suyitno S.,Tjahjana D., Juwana W.E., Putra M.R.A., Prabowo A.R., 2020, *The Effect of Heat Sink Properties on Solar Cell Cooling Systems*, Appl. Sci., 10, 7919.

Barkat F., Cheknane A., Guerrero J.M., Lashab A., Istrate M., Banu I.V., 2020, *Hybrid islanding detection technique for single-phase grid-connected photovoltaic multi-inverter systems*, IET Renewable Power Generation, vol. 14, nr. 18, pp. 3864-3880.

Bica M., 2019, *Photovoltaic system, course support*, Bucharest.

Borawski P., Holden L., Beldycka-Borawska A., 2023, *Perspectives of photovoltaic energy market development in the European Union*, Elsevier Energy, vol. 270, pp. 6.

Gomaa M.R.; Hammad W.; Al-Dhaifallah M.; Rezk H., 2020, *Performance enhancement of grid-tied PV system through proposed design cooling techniques: An experimental study and comparative analysis*, Sol. Energy, 211, 1110–1127.

Ghosh S., Yadav R., 2021, *Future of photovoltaic technologies: A comprehensive review*. Sustain. Energy Technol. Assess.; 47:101410. doi: 10.1016/j.seta.2021.101410.

Hudişteanu S.V., Cherecheş N.C., Chaimae El Fouas, Bekkay Hajji, Ţurcanu E.F., Cherecheş M.L., 2022, *Numerical and parametric analysis for enhancing performances of water photovoltaic/thermal system*, Applied sciences 12 (2): 645.

Hudişteanu S.V., Cherecheş N.C., Verdeş M., Ciocan V., Popovici C.G., Ţurcanu F.E., Bălan M., 2021, *Analysis of an innovative water-cooling solution for photovoltaic-thermal systems*, Faculty of Civil Engineering and Building Services, Gheorghe Asachi Technical University of Iasi.

Hudişteanu S.V., Mateescu T.D., Popovici C.G., 2015, *Comparative study of water film heat exchangers for cooling photovoltaic panels*, Bulletin of the Transilvania University of Braşov.

Hudişteanu S.V., Ţurcanu F.E., Cherecheş N.C., Popovici C.G., Verdeş M., 2022, *Effect of wind direction and velocity on PV panels cooling with perforated heat sinks*, Applied sciences 12 (19): 9665.

Hudişteanu S.V., Ţurcanu F.E., Cherecheş N.C., Popovici C.G., Verdeş M., Hudişteanu I, 2021, *Enhancement of PV panel power production by passive cooling using heat sinks with perforated fins*, Applied Sciences 11 (23): 113213.

Hudişteanu S V, Popovici C G, Verdeş M, Ciocan V, Ţurcanu F. E., 2020, *Case study on the efficiency improvement of photovoltaic panels by cooling*, Techniumvol 2, pp. 85-90.

Hudişteanu S.V., Cherecheş N.C., Popovici G.C., Verdeş M., Ciocan V., Balan M.C., Ţurcanu F.E., Scurtu I.C., 2021, *Effect of cooling on power generated by photovoltaic panels*; IOP Conference Series: Materials Science and Engineering; vol. 1141.

Irena, 2021, *https//publications.jrc.ec.europa.eu/repository/handle/ JRC11805,* view at 01.02.2024.

Johnston E., Szabo P.S.B., Bennett N.S., 2021, *Cooling silicon photovoltaic cells using finned heat sinks and the effect of inclination angle*, Therm. Sci. Eng. Prog., 23, 100902.

Math V.B., Sheregar A., Kavitha G., 2015, *Study of temperature differential in different concrete slabs of varying slab thickness in different regions*, European Journal of Applied Engineering and Scientific Research, 4 (2):35-43.

Selimli S, Dumrul H, Yilmaz S, Akman O, 2021, *Experimental and numerical analysis of energy and exergy performance of photovoltaic thermal water collectors*, Solar Energy, volume 228, pages 1-11.

Sornek K., Goryl W., Figaj R., Dabrowska G., Brezden J., 2022, *Development and Tests of the Water Cooling System Dedicated to Photovoltaic Panels*, Department of Sustainable Energy Development, Faculty of Energy and

Fuels, AGH University of Science and Technology, Mickiewicza Ave. 30, 30-059 Krakow, Poland.

applied sciences

MDPI

Article

Effect of Wind Direction and Velocity on PV Panels Cooling with Perforated Heat Sinks

Sebastian Valeriu Hudișteanu *, Florin Emilian Țurcanu *, Nelu-Cristian Cherecheș *, Cătălin-George Popovici, Marina Verdeș, Diana-Ana Ancaș and Iuliana Hudișteanu

Department of Building Services, Faculty of Civil Engineering and Building Services, Gheorghe Asachi Technical University of Iasi, 700050 Iași, Romania

* Correspondence: sebastian.hudisteanu@tuiasi.ro (S.V.H.); emilian-florin.turcanu@tuiasi.ro (F.E.Ț.); chereches@tuiasi.ro (N.-C.C.)

Abstract: The numerical modeling of the effect of wind direction and velocity over the air cooling of PV panels with heat sinks is realized. During the study, a random PV panel with typical characteristics was analyzed for three different wind directions—towards its back, towards its front and from the side. The analysis was realized on a fixed PV panel, oriented to the south, with an inclination of 45 degrees from the horizontal position. The accuracy of the numerical simulation was achieved by comparison with the experimental studies presented in the literature and by comparing the NOCT conditions. The numerical study is focused on different types of heat sinks attached to a typical PV panel. The fins were distributed both horizontally and vertically. A challenging task consisted in simulation of the real wind conditions around the PV panel by taking into account the entire air domain. The simulations were realized for air velocity v_{air} from 1 m/s to 5 m/s, solar radiation of G = 1000 W/m^2 and ambient temperature t_{air} = 35 °C. The output parameters analyzed were the average temperature of PV panels and their power production. Although the lowest temperatures were achieved for the back wind, the cooling effect was more intense for the side wind. The other direction studied also determined the cooling of PV panels. The passive cooling solutions analyzed introduced a rise of maximum power production between 1.85% and 7.71% above the base case, depending on the wind direction and velocity.

Keywords: CFD analysis; wind direction; PV temperature; air cooling; perforated heat sinks; NOCT validation

check for updates

Citation: Hudișteanu, S.V.; Țurcanu, F.E.; Cherecheș, N.-C.; Popovici, C.-G.; Verdeș, M.; Ancaș, D.-A.; Hudișteanu, I. Effect of Wind Direction and Velocity on PV Panels Cooling with Perforated Heat Sinks. *Appl. Sci.* **2022**, *12*, 9665. https://doi.org/10.3390/app12199665

Academic Editor: Luisa F. Cabeza

Received: 2 September 2022
Accepted: 21 September 2022
Published: 26 September 2022

Publisher's Note: MDPI stays neutral with regard to jurisdictional claims in published maps and institutional affiliations.

Copyright: © 2022 by the authors. Licensee MDPI, Basel, Switzerland. This article is an open access article distributed under the terms and conditions of the Creative Commons Attribution (CC BY) license (https://creativecommons.org/licenses/by/4.0/).

1. Introduction

The current global political, economic and energy context is characterized by high demand and consumption of population, instability, uncertainty and rampant inflation, right in the area of resources and energy [1]. Even without taking into account the current context, there is the well-known concept of Overshoot Day which is "celebrated" each year. In essence, this day represents the moment when humanity had already used up all of the renewable resources of the current year and unfortunately it takes place earlier and earlier each year. For the current year, this day was on 28 July 2022, meaning that from 29 July onwards, we started consuming additional resources compared to how much the planet could regenerate [2].

In this context, the use of solar-related energy could reduce the vulnerability of the European Community and eliminate the dependence of third-party oil or gas producers. Solar energy and its conversion into electricity by using photovoltaic (PV) panels became a major attraction in order to reduce the dependence on fossil fuels. After commissioning, there is obtained a clean and sustainable form of energy [2,3]. The photovoltaic systems could represent a stable and competitive area [4], taking into account both the recent actions in Europe [5] and the general tendency on the energy market that have quickly affected the stability of the world countries.

The advantages of photovoltaic technology are well documented in literature [6], but the control of the PV panels temperature is also an important challenge that could assure the enhancement of their efficiency [7].

The irreversible effect of heat generation in PV panels cannot be avoided, taking into account that the PV panel is constantly exposed to high levels of solar energy. Taking into account the efficiency of recently photovoltaic panels (of 20–25%), it can be stated that the vast majority of the remaining solar energy absorbed is converted into heat. This phenomenon, corroborated with the temperature-dependent variation of the efficiency of PV panels [7], determines a continuous concern on reducing the operating temperature. The data from literature present a decrease of the PV efficiency with the temperature between −0.30 and −0.50%/°C [8,9]. It must be specified that, in contrast to STC (Standard Test Conditions), in normal operation the photovoltaic panels can reach temperatures of 70 °C or higher [8,10,11], at 1000 W/m^2, leading to a significant decrease in their efficiency.

It is well known that, when it is possible, it is recommended to use cooling solutions for improving PV panels' efficiency and develop PVT panels (photovoltaic–thermal) as a consequence [12–15]. There are considerable research studies in the literature regarding the cooling solutions for improving the efficiency of photovoltaic panels by reducing their operating temperature [6,9,10,13–15].

The air-cooling effect using heat sinks is tested for different areas: residential sector, urban and power plants [16,17].

The aim of this study was to analyze the effect of wind direction and velocity over different types of heat sinks attached to PV panels in comparison to the base case (without a cooling solution). The main target of the work was to quantify the cooling effect of various heat sinks in variable wind conditions. The presence of heat sinks is influencing the performance of PV panels, but the wind directions could also be an important factor in this regard. In contrast to the majority of similar studies in the literature, in this paper, the numerical modeling was conducted in more realistic wind conditions and inclination of the PV panel [18]. Taking into account the research from the literature, which concluded that the results for different temperature and radiation threshold are varying linearly for values of 20–35 °C and 600–1000 W/m^2, during this study, the most unfavorable conditions in terms of PV panel heating were detailed: solar radiation G = 1000 W/m^2 and ambient temperature t_{air} = 35 °C [6].

2. Related Research

There are numerous related research studies in the literature, both experimental and numerical, regarding the inverse dependence of the temperature of monocrystalline and polycrystalline PV panels with their efficiency, and consequently the necessity of cooling solutions for removing this shortcoming [6,8,9,11,19,20].

Related research works on PV panels' cooling by using air are presented in the literature, and a large number of technologies and solutions to improve their efficiency are presented [9,21–26]. Recent experimental and numerical studies regarding the passive air cooling of PV panels by using heat sinks [8,27,28] tend to confirm noticeable and promising results [6,8,22,23]. The two main materials used for manufacturing the heat sinks are aluminum and copper [23]. The cooling effect is analyzed through experimental tests under different conditions and the conclusion is that copper has superior results [23]. Also, numerical and experimental analysis showed that the presence of perforations on the fins of the heat sinks can improve the efficiency of the PV panels by reducing their operating temperature [6,23]. The predicted temperature drop, due to the use of these solutions, can reach values between 7 °C and 10 °C [23].

Numerical simulations regarding the wind direction towards the back, front and side of heat sinks attached to PV panels showed a potential of operating temperature reduction towards 10 °C below the basic case temperature (when no cooling is applied) [8,11,15,29,30]. The improvement of the PV panels' performance was determining a rise of normalized power production up to 0.90 of the standard test conditions one [31]. As an average, the

normalized power generation of photovoltaic panels can reach about 0.70–0.83 compared to the STC rating [18].

3. Materials and Methods

3.1. Problem Description

The study was focused on determining the effect of wind direction and velocity over the resulting operating temperatures of PV panels both in cooling and non-cooling conditions (base case). Taking into account the variety of PV panels on the market, a typical one is analyzed (with a power production of 320 W_p and a surface of 1.6 m^2). The PV panel is a monocrystalline Si-based one—AE320HM6-60—Table 1 [32], inclined at 45° from the horizontal position, in constant solar radiation G = 1000 W/m^2, constant ambient temperature of t_{air} = 35 °C and variable wind direction (from the back, front and side of the PV panel) and velocity (from 1 m/s to 5 m/s). This configuration is also used for validation of the model in NOCT (Nominal Operating Cell Temperature) conditions [31].

Table 1. The electrical and dimensional characteristics of the photovoltaic panel studied.

AE Solar AE320HM6-60 PV Panel [32]	
Maximum power P_{mp}	320 W_p
Voltage at maximum power V_{mp}	33.40 V
Current at maximum power I_{mp}	9.59 A
Open-circuit voltage V_{oc}	40.90 V
Short-circuit current I_{sc}	10.15 A
Efficiency η_{STC}	19.30%
Temperature factor of efficiency β	−0.37%/°C
Nominal operating cell temperature t_{NOCT}	47 °C
Dimensions of PV panel (length L × width l × height h)	1665 mm × 996 mm × 35 mm

During the study, there were different stages of analysis of the heat sinks attached to the PV panel. The study was initiated with the validation of the model for the base case (no cooling system attached to the photovoltaic panel). After that, a total of six configurations of heat sinks were attached to the PV panel and studied. The various heat sinks were obtained by changing the configuration of their fins. Therefore, for each type of fins (horizontal and vertical), there were the following cases: non-perforated fins vs. fins with perforations of 30 mm and 60 mm diameter (Φ).

The proposed heat sinks are placed in the backside of the PV panel. The contact region is represented by a copper sheet (plate). Perforated or non-perforated copper fins are connected to this plate in order to improve the heat transfer by amplifying the turbulence from the PV panel to the surrounding air (see Figure 1). Therefore, the perforations assure a quantitative and qualitative effect against the heating of the PV panel and could improve the photovoltaic efficiency.

Appl. Sci. 2022, 12, 9665 4 of 19

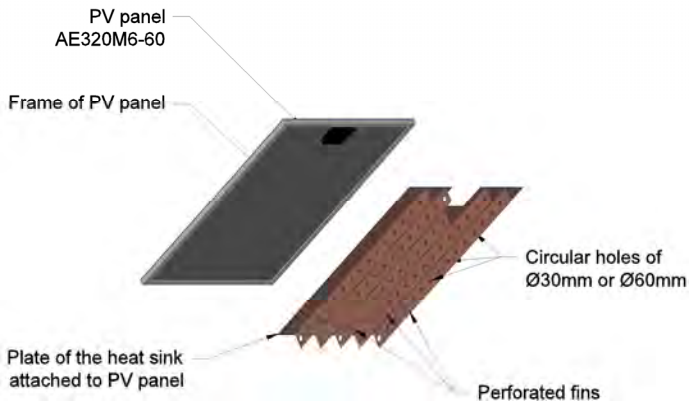


Figure 1. The PV panel—heat sink ensemble—Case of vertical fins with perforations.

The literature analysis showed that the circular holes made in the fins of the heat sinks have the potential to produce promising results for cooling the PV panels [6,8,22,23,29]. In this case, the resulting temperatures are lower by 2–3 °C than those obtained by using other shapes for perforations [18]. In the literature are presented various

The literature analysis showed that the circular holes made in the fins of the heat sinks have the potential to produce promising results for cooling the PV panels [6,8,22,23,29]. In this case, the resulting temperatures are lower by 2–3 °C than those obtained by using other shapes for perforations [18]. In the literature are presented various types of fins (continuous, discontinuous or staggered) [33]. During this study, continuous fins of 100 mm height were analyzed.

Two main configurations of the heat sinks studied were:

Model 1—**horizontal** fins (3 models: non-perforated, perforated with Φ = 30 mm holes and Φ = 60 mm holes);

Model 2—**vertical** fins (3 models: non-perforated, perforated with Φ = 30 mm holes and Φ = 60 mm holes).

3.2. Numerical Modeling

The ANSYS Fluent platform was used for numerical modeling in steady-state conditions. The geometric model and the mesh were created by using ANSYS Fluent-Meshing and ANSYS SpaceClaim.

Given the particularities of the flow (that is not aligned with the mesh), the simulations were realized in the SIMPLE method. The second-order accuracy was used for solving the governing equations of the phenomena involved [8,34].

The solar radiation was modeled by the aid of the native module of Fluent—Solar Ray Tracing. The conversion of solar radiation into heat is synthesized as an absorption coefficient of the PV panel of α = 0.7 [6,8].

The energy balance between the PV panel–heat sink ensemble and the surroundings were modeled by including both the convection and radiation effects [28]. The turbulence model used for the flowing air was the k–ε realizable model [34].

The geometry of the model was created using SpaceClaim. For all studied cases, after preliminary analysis, the distance between fins was imposed to s = 150 mm. The fins are orthogonal to the heat sink sheet, as shown in Figure 1. The circular perforations had 30 mm or 60 mm in diameter and they are located at 100 mm one to another according to previous research works [6,23]. In this way, a better air circulation is achieved near the heat sink and the cooling effect is enhanced.

It is well known that the accuracy and correctness of the mesh lead to precise CFD (Computational Fluid Dynamics) [34]; therefore, in order to solve the highly orthogonal mesh that could result from a conventional mesh. The polyhedral mesh for surfaces and poly-hex mesh for volumes determined an increase of the simulation time, maintaining the same precision of the results. In order to achieve an appropriate mesh, different refinements are necessary [34]. For the present numerical modeling, the PV panel, heat sink and air volume had a mesh quality as presented in Table 2.

Table 2. The mesh quality of the simulation domain.

Mesh Quality	
Aspect ratio	5.0–60
Skewness	0.4–0.7
Orthogonal quality	0.1–0.3

In order to optimize the number of the cells of the mesh and the simulation time, a mesh independence study was realized. The preliminary simulations showed that 3×10^6 cells for the base case and 5.5×10^6 cells for cases with heat sinks determined accurate results compared to a higher number of elements (see Figure 2).

In order to optimize the number of the cells of the mesh and the simulation time, a mesh independence study was realized. The preliminary simulations showed that 3×10^6 cells for the base case and 5.5×10^6 cells for cases with heat sinks determined accurate results compared to a higher number of elements (see Figure 2).

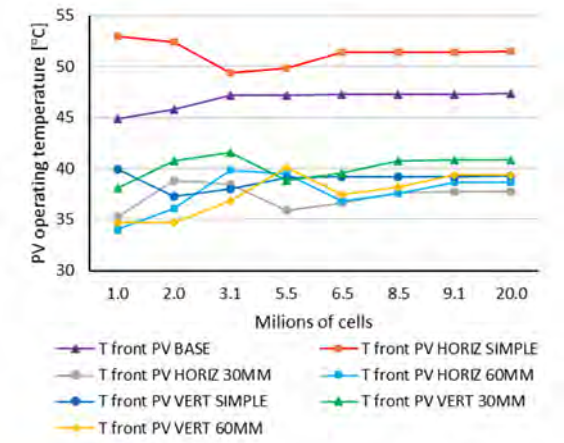


Figure 2. Mesh independence study for the numerical simulation.

3.3. Sensitivity Analysis of Grid Spacing

The spatial discretization error analysis was also performed. The Grid Convergence Index (*GCI*) method was used, according to [35,36]. The *GCI* represents a very accurate method used to evaluate how far the numerical computed values are compared to the asymptotic one [36]. The analysis was implemented on both base and heat sink cases. The following equations present the calculations used and the detailed values obtained. Three grid refinement levels were considered and the following *GCI* values were calculated:

$$GCI_{1-2} = \frac{F_s|\varepsilon_{1-2}|}{\left(r_{1-2}^{p} - 1\right)} \quad (1)$$

and

$$GCI_{2-3} = \frac{F_s|\varepsilon_{2-3}|}{\left(r_{2-3}^{p} - 1\right)} \quad (2)$$

where:

GCI_{1-2}—Grid Convergence Index for fine and medium grids;
GCI_{2-3}—Grid Convergence Index for coarse and medium grids;
F_s—Factor of safety ($F_s = 1.25$ in the present study);
ε—Relative error:

$$\varepsilon_{n-n+1} = \frac{f_{n+1} - f_n}{f_n} \quad (3)$$

p—Order of convergence:

$$p = \frac{\ln\frac{f_{n+2} - f_{n+1}}{f_{n+1} - f_n}}{\ln r} \quad (4)$$

f—Significant parameter chosen for the comparison (f_1—the temperature calculated with the finest grid, f_2—with the medium grid, f_3—with coarsest one);
r—Constant refinement ratio ($r = 2$ in the present study):

$$r_{n-n+1} = \frac{h_{n+1}}{h_n} \quad (5)$$

h—Grid spacing, with:

$$h_1 (= 1\ \text{mm}) < h_2 (= 2\ \text{mm}) < h_3 (= 3\ \text{mm}) \quad (6)$$

For the present study, the f parameter consists in the average operating temperature of the PV panel, t_{PV}.

In order to achieve precise results from numerical simulations by using the lowest number of cells, the following auditing ratio should be as close as possible to 1:

$$\frac{GCI_{2-3}}{r^p GCI_{1-2}} \to 1 \tag{7}$$

In the case of using the finest grid, the predicted value at $h = 0$ is:

$$f = f_1 + \frac{f_1 - f_2}{r_{1-2}^p - 1} \tag{8}$$

For the specific values of the base case analysis ($r = 2, f_1 = 47.28, f_2 = 47.40, f_3 = 47.38$, $F_s = 1.25$), the following values were obtained: the order of convergence $p = 1.68$ and the predicted value $f = 47.31$. Also, $\varepsilon_{1-2} = 0.053\%$ and $\varepsilon_{2-3} = 0.169\%$, while the $GCI_{1-2} = 0.030\%$ and $GCI_{2-3} = 0.096\%$. The calculated auditing ratio is:

$$\frac{GCI_{2-3}}{r^p GCI_{1-2}} = 0.9977 \tag{9}$$

For the specific values of the heat sink case analysis ($r = 2$, $f_1 = 39.39$, $f_2 = 39.44$, $f_3 = 39.49$, $F_s = 1.25$), the following values were obtained: The order of convergence $p = 0.17$ and the predicted value $f = 39.80$. Also, $\varepsilon_{1-2} = 0.116\%$ and $\varepsilon_{2-3} = 0.130\%$, while the $GCI_{1-2} = 1.139\%$ and $GCI_{2-3} = 1.281\%$. The calculated auditing ratio is:

$$\frac{GCI_{2-3}}{r^p GCI_{1-2}} = 0.9975 \tag{10}$$

Therefore, the main verification of the grid quality confirms that the results are in the asymptotic range of convergence and the numerical model was further conducted by using the lowest cell number (coarse grid).

A large number of research studies from the literature are analyzing the photovoltaic panels either in the horizontal [19] or vertical [8,23] position. In addition, the surrounding air is most often simulated as a channel behind the photovoltaic panel [18]. Moreover, studies on cooling inclined photovoltaic panels are present in the literature, but in reduced number [6,11,27].

During this study, the numerical simulations were done considering the air circulation in the vicinity of an inclined PV panel cooled with heat sinks. It was possible due to the high accuracy mesh, which assured a realistic simulation of the airflow and heat transfer from the PV panel to the heat sink and to the surrounding air. In the present study, in order to simplify the numerical model, the influence of the relative humidity of the air was neglected. However, according to literature, the variation of the relative humidity could affect the final results by 4–5% [37]. The thermophysical properties of the materials defined for the simulations are presented in Table 3. The geometry and set-up of the simulation are shown in Figure 3.

Table 3. Thermophysical properties of the materials defined.

Material	g [mm]	λ [W/m·K]	ρ [kg/m^3]	c_p [J/kg·K]
Glass	3.00	1.00	2300	0.50
PV cells	0.35	168	2330	0.757
EVA	0.50	0.35	960	2.09
Tedlar	0.20	0.20	1500	1.20
Copper	1.00	386	8960	0.376
Air	-	0.025	1.20	1.005

where:

g—thickness of the layers composing the PV panel [m];

g—thickness of the layers composing the PV panel [m];
λ—thermal conductivity of the layers composing the PV panel [W/m·K];
ρ—density of the layers composing the PV panel [kg/m^3];
c_p—specific heat of the layers composing the PV panel [J/kg·K].

The steady-state conditions were assumed for the numerical modeling. During the simulations, the following inputs were established:

- **constant**: ambient temperature, t_{air} = 35 °C—worst scenario in terms of heating [6];
- **constant**: solar radiation, G_{med} = 1000 W/m^2—worst scenario in terms of heating [6];
- **variable**: velocity of the air, v_{air} = 1–5 m/s;
- **variable**: wind direction: towards the back, front and side of the PV panel;

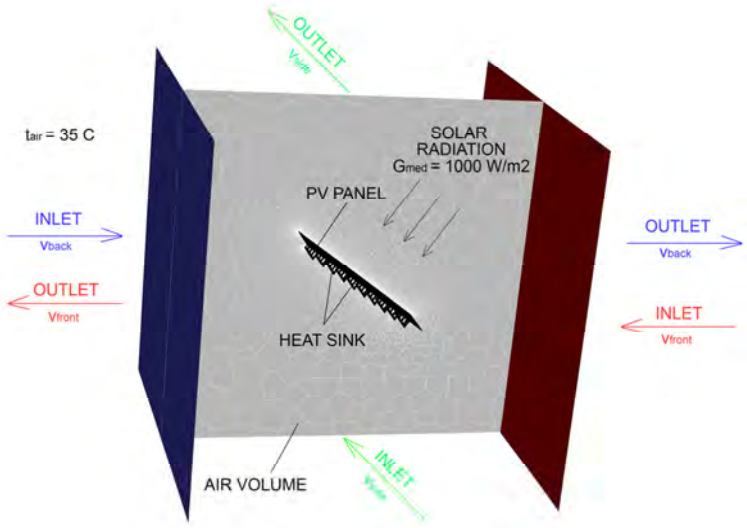


Figure 3. The geometry and set-up of the numerical simulation domain.

The main results obtained from the simulations were:

- operating temperature of the photovoltaic panel;
- normalized power production.

In terms of wind direction, the simulations were made in 3 Scenarios—for each case, different faces of the volume represent the inlet and outlet of the flow—Figure 3. The blue arrows are used for the back wind. The red arrows are used for the front wind. The green arrows are used for the side wind.

The inlet face of the domain varies as the position but has the same boundary conditions for each case: constant air temperature of 35 °C, velocity vector normal to the inlet surface and variable wind velocity, from 1 m/s to 5 m/s. The boundary conditions regarding the flow were the turbulent intensity of 5% and turbulent viscosity ratio of 10.

3.4. Studied Cases

A total of seven cases were studied. The first one is the base case (Case 0), while the other six consist of the heat sinks analyzed:

0. Base case	- no cooling;
1. Horiz Simple	- heat sink and non-perforated horizontal fins;
2. Horiz 30 mm	- heat sink and perforated Φ = 30 mm horizontal fins;
3. Horiz 60 mm	- heat sink and perforated Φ = 60 mm horizontal fins;
4. Vert Simple	- heat sink and non-perforated vertical fins;
5. Vert 30 mm	- heat sink and perforated Φ = 30 mm vertical fins;
6. Vert 60 mm	- heat sink and perforated Φ = 60 mm vertical fins.

The analysis was realized on a fixed PV panel, oriented to the south, with an inclination of 45° from the horizontal position, and wind direction was varied towards the back, front and side of it, as shown in Figure 4.

4. Vert Simple - heat sink and non-perforated vertical fins;
5. Vert 30 mm - heat sink and perforated Φ = 30 mm vertical fins;
6. Vert 60 mm - heat sink and perforated Φ = 60 mm vertical fins.

The analysis was realized on a fixed PV panel, oriented to the south, with an inclination of 45° from the horizontal position, and wind direction was varied towards the back, front and side of it, as shown in Figure 4.

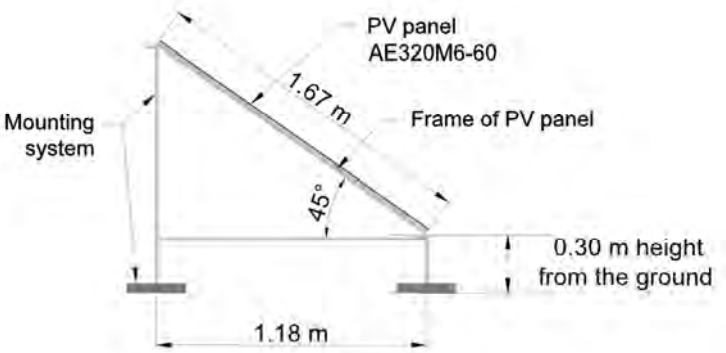
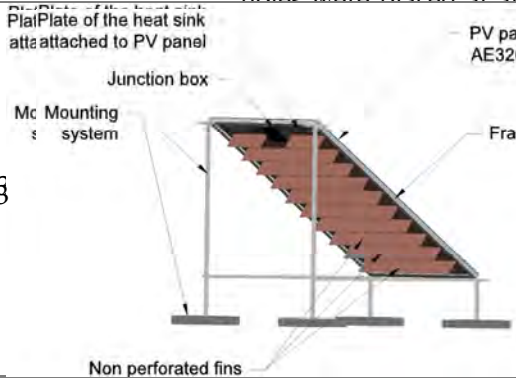
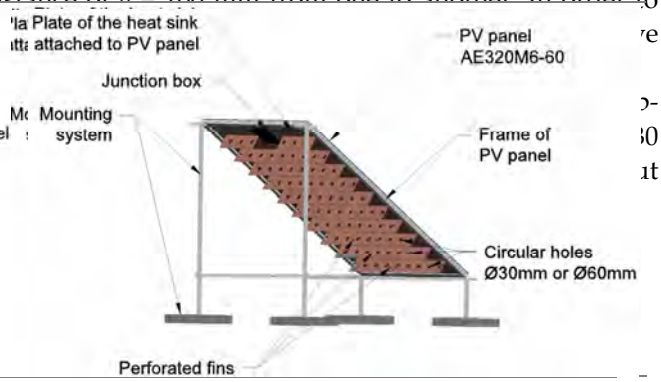
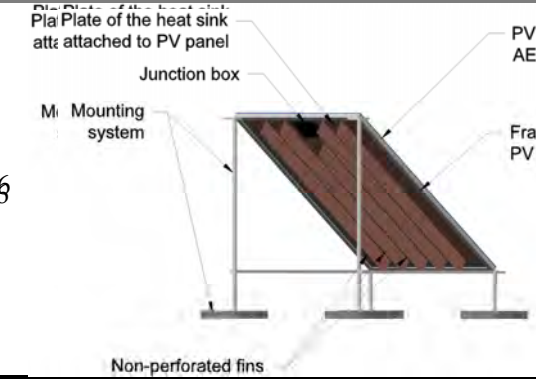
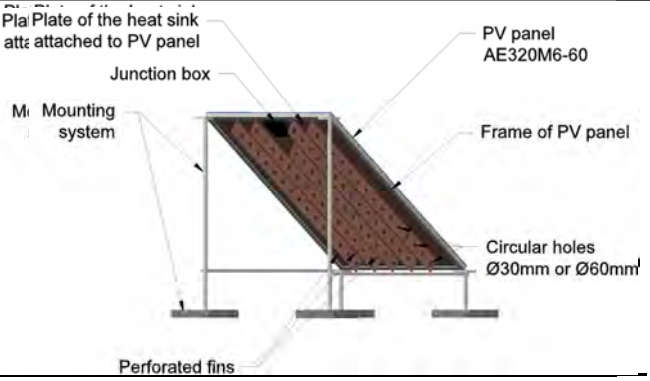


Figure 4. Side view of the set-up of the fixed PV panel, inclined at 45°.

The designed heat sinks consisted of a rectangular metal (copper) sheet with horizontal or vertical equidistant fins (Table 4). The main geometric characteristics of the heat sinks are: h_{fins} = 100 mm (height of all fins implemented), L_{fins} = 1520 mm (length of vertical fins) and L_{fins} = 860 mm (length of vertical fins)—Table 4.

The fins, made of copper, are studied for both perforated and non-perforated cases. The base sheet of the heat sink is in direct contact with the backside of the PV panel. The diameter of the circular perforations of the fins were of 30 mm or 60 mm (Table 4). The holes were placed at an equal distance of p = 100 mm from one to another. In order to assure a staggered circulation, there was imposed an offset of 50 mm between two successive perforated fins.

Table 4. The perspective view of the heat sinks attached to the PV panel.

Case	3D Perspective View
1	
2	
3	
4	

4. Numerical Model Validation

The main cases of cooling solutions analyzed are presented in Table 4: Cases 1–3 represent the horizontal (transversal) fins with no perforations, with perforations of 30 mm and 60 mm, respectively. Cases 4–6 are the vertical fins with no perforations, with perforations of 30 mm and 60 mm, respectively.

According to the literature [38], the average temperature of the PV panel, in these conditions, is 47.16 °C, the model was considered appropriate and the next steps of validation were covered.

A common equation (1) for solar interaction [38,39] was adopted to the NOCT tests and makes the connection between the PV panel temperature (T_c) and solar conditions (air temperature and solar radiation) for a PV panel characterized by its own NOCT:

$$T_c = T_a + \frac{NOCT - 20}{800} \cdot G \quad (1)$$

By comparing the numerical results obtained using Equation (1) with the following

mm and 60 mm. Cases 4–6 are the vertical (longitudinal) ones, both with and without perforations.

4. Numerical Model Validation

4.1. Base Case Validation—Without Heat Sink

The base case was validated in two steps. The first one consisted in analyzing the behavior of the numerical model in NOCT conditions compared to the expected results according to the producer datasheet and literature. The NOCT conditions suppose a PV panel inclined at 45°, direct solar radiation on front of the PV panel of 800 W/m^2, air temperature of 20 °C and the wind velocity of 1 m/s towards the backside of the PV panel [31]. According to the producer of the PV panel [32], in these conditions, the average temperature of the PV panel t_{NOCT} should be 47 °C. Taking into account that the good matching of the PV temperature from simulation was 47.16 °C, the model was considered appropriate and the next steps of validation were covered.

A common Equation (1) from literature [31,38] extrapolates the NOCT results and makes the connection between the PV panel temperature (t_{PV}) and outside conditions (air temperature t_{air} and solar radiation G) for each PV panel, characterized by its own t_{NOCT}. By comparing the numerical results with those obtained with Equation (11), the following tendency of the PV panel temperature was observed (Figure 5).

$$t_{PV} = t_{air} + \frac{t_{NOCT} - 20}{800} \cdot G \quad (11)$$

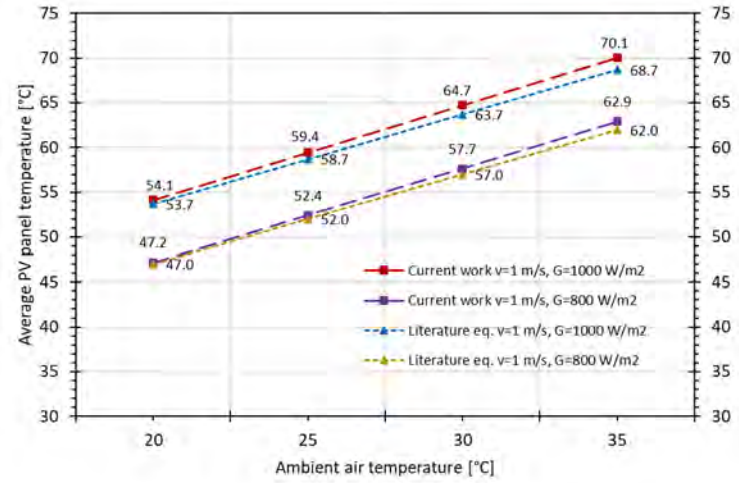
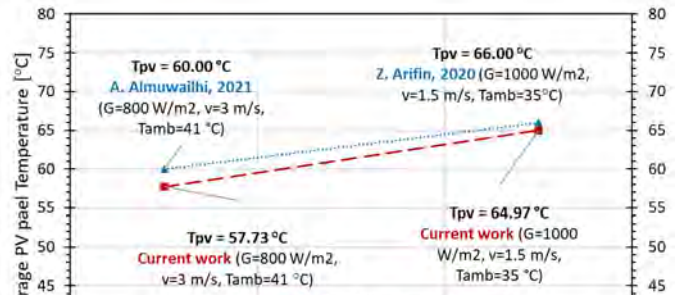


Figure 5. Validation of the numerical model using NOCT conditions and Equation (1).

The differences between the numerical model and Equation (1) were between 0.28 and 1.98%, which represents a very good correlation between them.

Also, experimental studies from literature [11,39] were compared with the present numerical simulation on the base case for different input variables. For the PV panel inclined to 45°, wind velocity of v = 1.5 m/s and solar radiation of G = 837 W/m^2, the difference between the present study (53.68 °C) and the experimental data (51.6 °C) [11] was 3.87%.

Additional results of simulation and experimental studies [23,39] are compared in Figure 6, and a good correlation can be found.



Also, experimental studies from literature [11,39] were compared with the present numerical simulation on the base case for different input variables. For the PV panel inclined to 45°, wind velocity of v = 1.5 m/s and solar radiation of G = 837 W/m², the difference between the present study (53.68 °C) and the experimental data (51.6 °C) [11] was 3.87%.

Additional results of simulation and experimental studies [23,39] are compared in Figure 6, and a good correlation can be found.

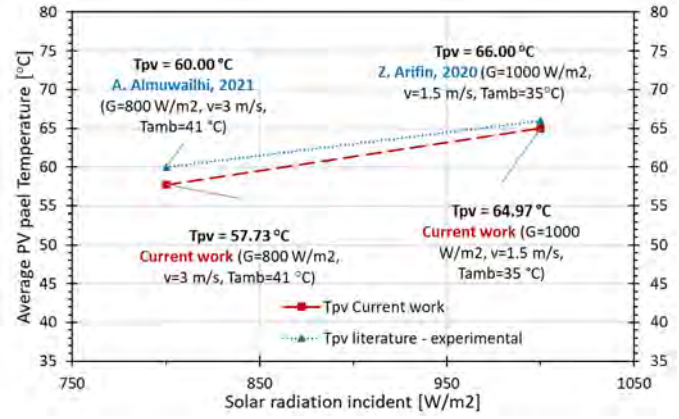


Figure 6. Validation of the numerical simulation—base case—PV panel without heat sink.

Figure 6. Validation of the numerical simulation—base case—PV panel without heat sink.

4.2. PV Panel and Heat Sink Validation

The heat sinks attached to a PV panel were also analyzed for validation. The comparison between experimental data [34] and the present model is presented in Figure 7.

The heat sinks attached to a PV panel were also analyzed for validation. The comparison between experimental data [34] and the present model is presented in Figure 7.

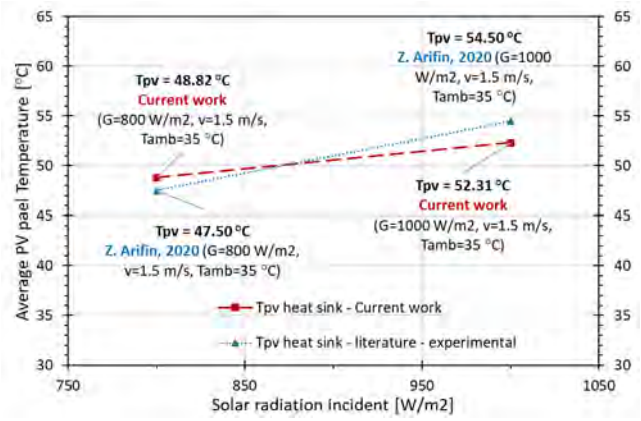


Figure 7. Validation of the numerical simulation—PV panel with heat sink.

Figure 7. Validation of the numerical simulation—PV panel with heat sink.

In order to improve the accuracy, the model validation was realized also for various values of solar radiation and air temperature. The differences between the present numerical model and experiments from literature were from −5.18% to +4.03%. The narrow range of variation is considered acceptable [30], supporting the validity of the study. Therefore, the numerical modelling was considered to have little risk of error and the study was continued.

In order to improve the accuracy, the model validation was realized also for various values of solar radiation and air temperature. The differences between the present numerical model and experiments from literature were from −5.18% to +4.03%. The narrow range of variation is considered acceptable [30], supporting the validity of the study. Therefore, the numerical modelling was considered to have little risk of error and the study was continued.

5. Results and Discussion

5. Results and Discussion

The present simulations have a higher level of accuracy compared to the majority of literature, because the air circulation around the PV panel–heat sink ensemble causes a change in temperatures distribution and non-homogeneous heat transfer. While the majority of existent studies are realized by using a constant convective heat transfer coefficient (h_c) in order to replace the air circulation around an object [18], in the present paper, the airflow near the photovoltaic panel and heat sink ensemble is also considered. This approach produces more realistic results and could represent a good starting point for future research in the literature, representing the connection between air velocity, direction and the power production obtained for these conditions.

The present simulations have a higher level of accuracy compared to the majority of literature, because the air circulation around the PV panel–heat sink ensemble causes a change in temperatures distribution and non-homogeneous heat transfer. While the majority of existent studies are realized by using a constant convective heat transfer coefficient (h_c) in order to replace the air circulation around an object [18], in the present paper, the airflow near the photovoltaic panel and heat sink ensemble is also considered. This approach produces more realistic results and could represent a good starting point for future research in the literature, representing the connection between air velocity, direction and the power production obtained for these conditions.

The PV panel operating temperature and normalized power production were obtained. In Figures 8–10, there are presented qualitative and quantitative results regarding the average temperatures of the photovoltaic panels obtained for each model of the heat sink and various wind velocities and directions. These results are obtained by varying the set-up: t_{air} = 35 °C, v_{air} = 1–5 m/s and G = 1000 W/m² and three wind directions (Table 5).

The PV panel operating temperature and normalized power production were obtained. In Figures 8–10, there are presented qualitative and quantitative results regarding the average temperatures of the photovoltaic panels obtained for each model of the heat sink and various wind velocities and directions. These results are obtained by varying the set-up: t_{air} = 35 °C, v_{air} = 1–5 m/s and G = 1000 W/m² and three wind directions (Table 5).

These values could represent a good marker in order to choose, when possible, the right positioning of the PV panels related to the dominant wind in a certain geographical area. The best temperatures of the heat sinks were obtained when the wind was towards the heat sink—in the backside of the PV panel—determining a decrease of the average

the average operating temperatures of the PV panel measured in °C. The tendency registered for 1 m/s is also manifesting for higher velocities: 2–5 m/s, with the highest temperatures recorded for the base case (T front PV BASE) and the lowest ones for the horizontal heat sink with 30 mm perforations (T front PV HORIZ 30MM).

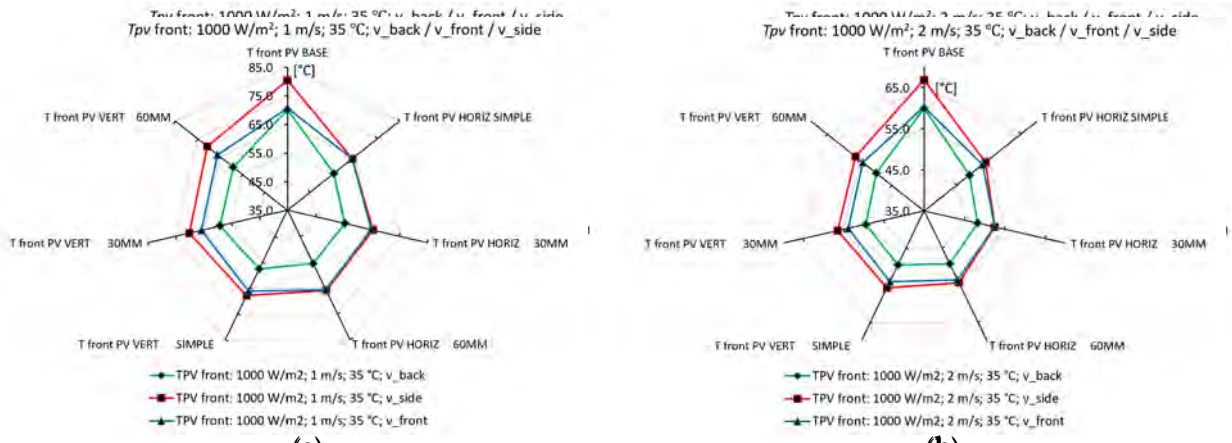


Figure 8. Variation of average operating temperature for (**a**) v_{air} = 1 m/s; (**b**) v_{air} = 2 m/s.

Figure 8. Variation of average operating temperature for (a) v_{air} = 1 m/s; (b) v_{air} = 2 m/s.

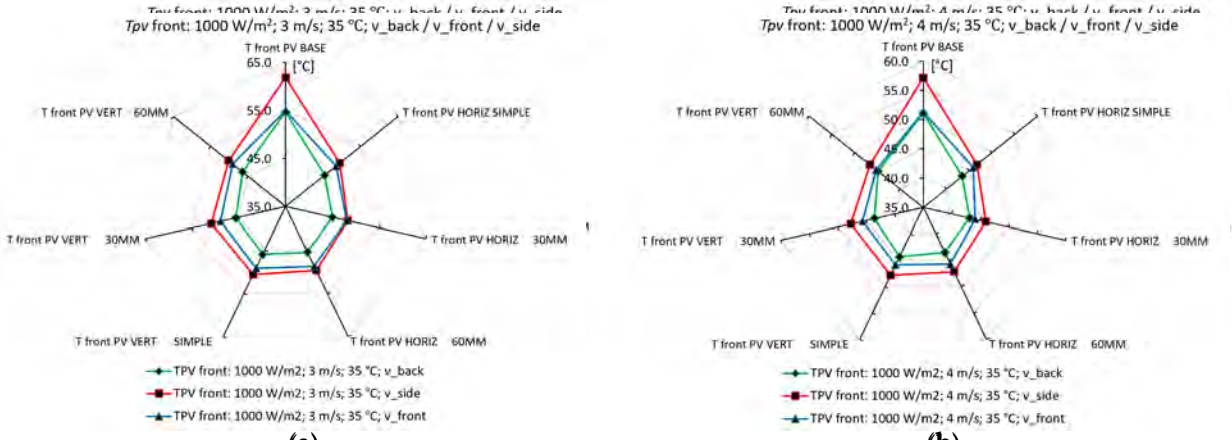


Figure 9. Variation of average operating temperature for (**a**) v_{air} = 3 m/s; (**b**) v_{air} = 4 m/s.

Figure 9. Variation of average operating temperature for (a) v_{air} = 3 m/s; (b) v_{air} = 4 m/s.

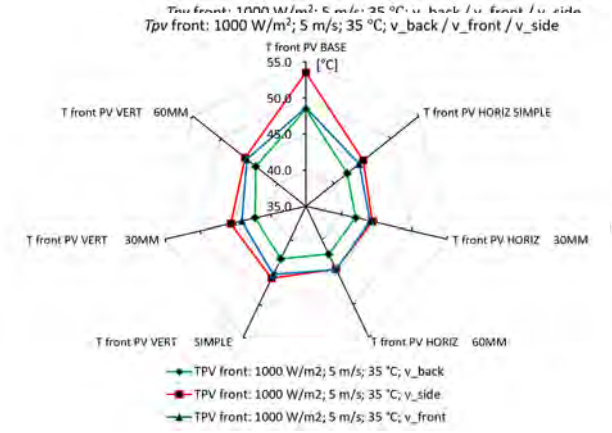


Figure 10. Variation of average operating temperature for v_{air} = 5 m/s.

Figure 10. Variation of average operating temperature for v_{air} = 5 m/s.

Table 5. Operating temperature of PV panel for studied cases.

Case	v_{air}	Back Wind		Front Wind		Side Wind	
		Drop of t_{PV} Compared to Base Case, for t_{air} = 35 °C					
		°C	%	°C	%	°C	%
0. Base Case	1 m/s	70.1 °C	-	70.7 °C	-	80.4 °C	-
1. Horiz Simple		−14.46 °C	−20.6%	−6.88 °C	−9.7%	−16.56 °C	−20.6%
2. Horiz 30 mm		−14.61 °C	−20.9%	−5.85 °C	−8.3%	−14.89 °C	−18.5%
3. Horiz 60 mm		−14.54 °C	−20.8%	−5.03 °C	−7.1%	−14.46 °C	−18%
4. Vert Simple		−12.4 °C	−17.7%	−4.42 °C	−6.2%	−12.54 °C	−15.6%
5. Vert 30 mm		−10.93 °C	−15.6%	−4.85 °C	−6.9%	−10.27 °C	−12.8%
6. Vert 60 mm		−10.87 °C	−15.5%	−4.53 °C	−6.4%	−9.73 °C	−12.1%
0. Base Case	2 m/s	59.9 °C	-	60.2 °C	-	66.8 °C	-
1. Horiz Simple		−10.88 °C	−18.2%	−7.14 °C	−11.9%	−12.86 °C	−19.3%
2. Horiz 30 mm		−11.7 °C	−19.5%	−7.71 °C	−12.8%	−14.28 °C	−21.4%
3. Horiz 60 mm		−10.68 °C	−17.8%	−6.65 °C	−11%	−12.53 °C	−18.8%
4. Vert Simple		−10.38 °C	−17.3%	−6.17 °C	−10.2%	−11.15 °C	−16.7%
5. Vert 30 mm		−10.42 °C	−17.4%	−6.42 °C	−10.7%	−10.33 °C	−15.5%
6. Vert 60 mm		−10.13 °C	−16.9%	−6.27 °C	−10.4%	−10.67 °C	−16%
0. Base Case	3 m/s	54.7 °C	-	54.9 °C	-	61.9 °C	-
1. Horiz Simple		−9.33 °C	−17.1%	−6.45 °C	−11.8%	−12.46 °C	−20.1%
2. Horiz 30 mm		−9.7 °C	−17.7%	−6.85 °C	−12.5%	−13.59 °C	−22%
3. Horiz 60 mm		−9.2 °C	−16.8%	−6.13 °C	−11.2%	−12.14 °C	−19.6%
4. Vert Simple		−8.69 °C	−15.9%	−5.64 °C	−10.3%	−11.25 °C	−18.2%
5. Vert 30 mm		−9.04 °C	−16.5%	−5.94 °C	−10.8%	−10.99 °C	−17.8%
6. Vert 60 mm		−8.21 °C	−15%	−5.75 °C	−10.5%	−11.64 °C	−18.8%
0. Base Case	4 m/s	51.1 °C	-	51.3 °C	-	57.2 °C	-
1. Horiz Simple		−7.57 °C	−14.8%	−5.36 °C	−10.5%	−10.43 °C	−18.2%
2. Horiz 30 mm		−7.94 °C	−15.5%	−7.21 °C	−14.1%	−11.21 °C	−19.6%
3. Horiz 60 mm		−7.58 °C	−14.8%	−5.59 °C	−10.9%	−10.03 °C	−17.5%
4. Vert Simple		−6.8 °C	−13.3%	−5.41 °C	−10.6%	−9.4 °C	−16.4%
5. Vert 30 mm		−7.56 °C	−14.8%	−5.62 °C	−11%	−9.49 °C	−16.6%
6. Vert 60 mm		−6.24 °C	−12.2%	−5.98 °C	−11.7%	−10.52 °C	−18.4%
0. Base Case	5 m/s	48.5 °C	-	48.6 °C	-	53.5 °C	-
1. Horiz Simple		−6.15 °C	−12.7%	−4.23 °C	−8.7%	−8.36 °C	−15.6%
2. Horiz 30 mm		−6.41 °C	−13.2%	−4.57 °C	−9.4%	−9.12 °C	−17%
3. Horiz 60 mm		−6.21 °C	−12.8%	−4.03 °C	−8.3%	−9 °C	−16.8%
4. Vert Simple		−5.47 °C	−11.3%	−3.21 °C	−6.6%	−7.57 °C	−14.1%
5. Vert 30 mm		−6.26 °C	−12.9%	−4.57 °C	−9.4%	−7.87 °C	−14.7%
6. Vert 60 mm		−4.61 °C	−9.5%	−3.21 °C	−6.6%	−7.78 °C	−14.5%

These values could represent a good marker in order to choose, when possible, the right positioning of the PV panels related to the dominant wind in a certain geographical area. The best temperatures of the heat sinks were obtained when the wind was towards the heat sink—in the backside of the PV panel—determining a decrease of the average

operating temperature of approximately 15 °C. On the other hand, the best cooling effect was registered for the side wind, due to the higher temperatures resulted in the base case—when no cooling is applied. Although the lowest temperatures were achieved for the back wind, the cooling effect was more intense for the side wind. If, in the case of wind velocity, the effect of cooling evolves almost linearly from 1 m/s to 5 m/s, in terms of the wind direction, there is a slightly different behavior. Therefore, there are present some recirculation areas that modify the distribution of velocities and temperatures on the PV panel–heat sink ensemble. The worst wind direction, from this point of view, is the side one, causing a non-uniform temperature distribution, which is influencing the entire PV panel efficiency.

The quantitative results for v_{air} = 1 m/s, air temperature t_{air} = 35 °C and solar radiation G = 1000 W/m^2 for each case are presented in the following graphs: Figures 8–10. In these figures, the values displayed on the plots (35, 45, 55, 65, 75 and 85) represent the scale for the average operating temperatures of the PV panel measured in °C. The tendency registered for 1 m/s is also manifesting for higher velocities: 2–5 m/s, with the highest temperatures recorded for the base case (T front PV BASE) and the lowest ones for the horizontal heat sink with 30 mm perforations (T front PV HORIZ 30MM).

A remarkable result is found for the convective heat transfer coefficients. Therefore, the global air circulation determined by the presence of the heat sinks with horizontal fins is also improving the heat transfer coefficients h_c on the front of the PV. In this case, the h_c in front of the PV panel have closer values to the ones recorded on the back. This phenomenon is less intense for the vertical fins. The wind direction seems to change the best configuration (Case 2—horizontal 30 mm) only for particular cases. The temperature reduction determined for this case is presented in Table 5.

A general tendency of the data obtained showed that the horizontal (transversal fins) are superior to those vertical (longitudinal) for each wind direction and velocity, while the best wind direction for improving the cooling of the PV panel–heat sink ensemble is towards the back of the PV panel. Also, if analyzed separately, the smaller holes (Φ = 30 mm) determine better results for horizontal fins, while the larger ones (Φ = 60 mm) are suitable for the vertical ones.

The cooling effect over the global energy production is quantified as efficiency improvement, taking into account the data available from the producer data sheet—a linear reduction of the efficiency by −0.37%/°C [32]. Therefore, for these disadvantageous external conditions (t_{air} = 35 °C, G = 1000 W/m^2), the normalized power generation was calculated—as the ratio of the maximum theoretical power P_{STC} obtained in Standard Test Conditions.

The results regarding the power production are normalized and presented as a fraction of maximum theoretic power (320 Wp in STC conditions). Therefore, each degree of temperature above the standard test conditions temperature t_{STC} = 25 °C determines lower efficiencies compared to the STC one (η_{STC} = 19.30%) [32].

The visual effect over the improvement of the PV panel power generation determined by the heat sinks is presented in Figures 11–13. These figures present the normalized power productions as a ratio of the power produced in STC (considering the STC power as equal to 1). Each figure shows the amount of power produced in each case (from Case 0 to Case 6) for different wind directions (Figure 11—back wind, Figure 12—front wind and Figure 13—side wind. These charts present the results obtained for each case for the air velocity of 1 m/s. This trend is maintained for higher velocities, Table 6, but the effect compared to the base case is attenuated.

ized power productions as a ratio of the power produced in STC (considering the STC power as equal to 1). Each figure shows the amount of power produced in each case (from Case 0 to Case 6) for different wind directions (Figure 11—back wind, Figure 12—front wind and Figure 13—side wind. These charts present the results obtained for each case for the air velocity of 1 m/s. This trend is maintained for higher velocities, Table 6, but the effect compared to the base case is attenuated.

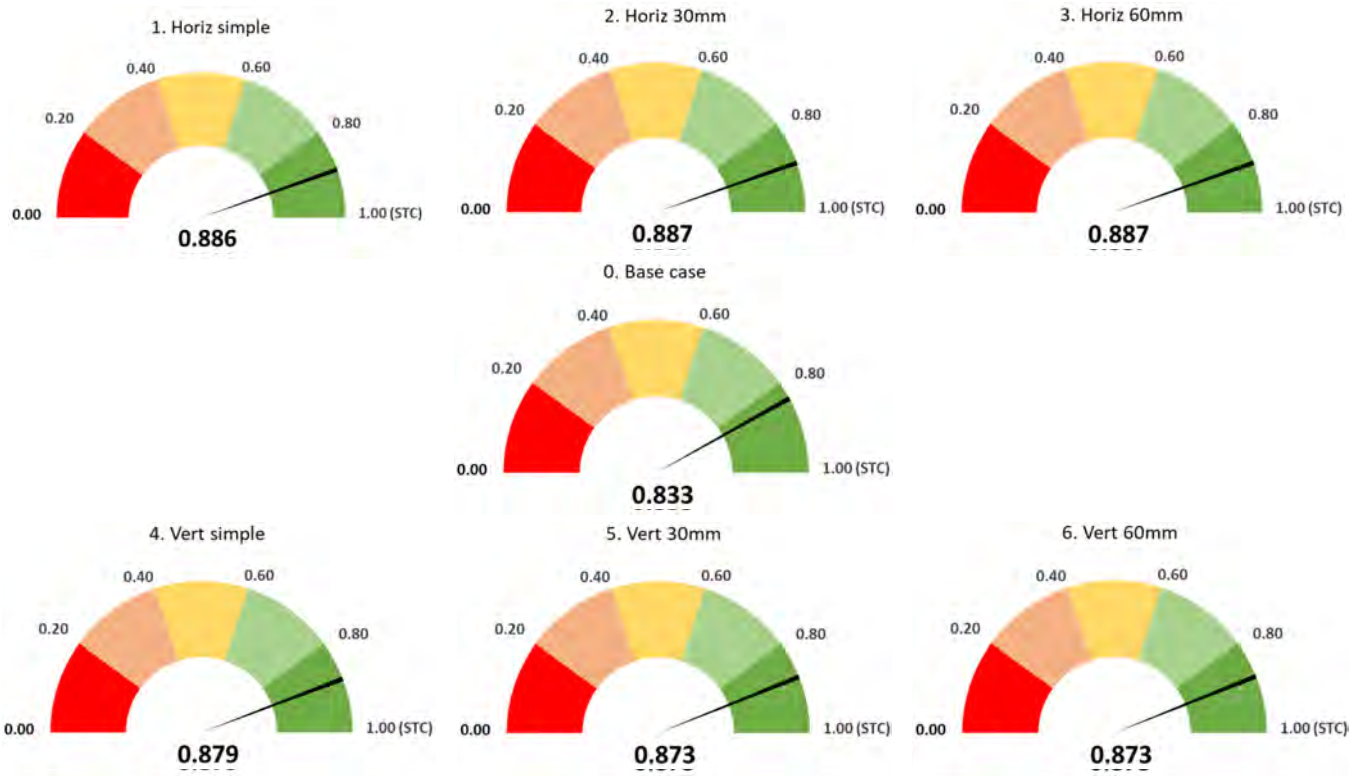


Figure 11. Normalized power production for **back wind**, v_{back} = 1 m/s, t_{air} = 35, G = 1000 W/m^2.

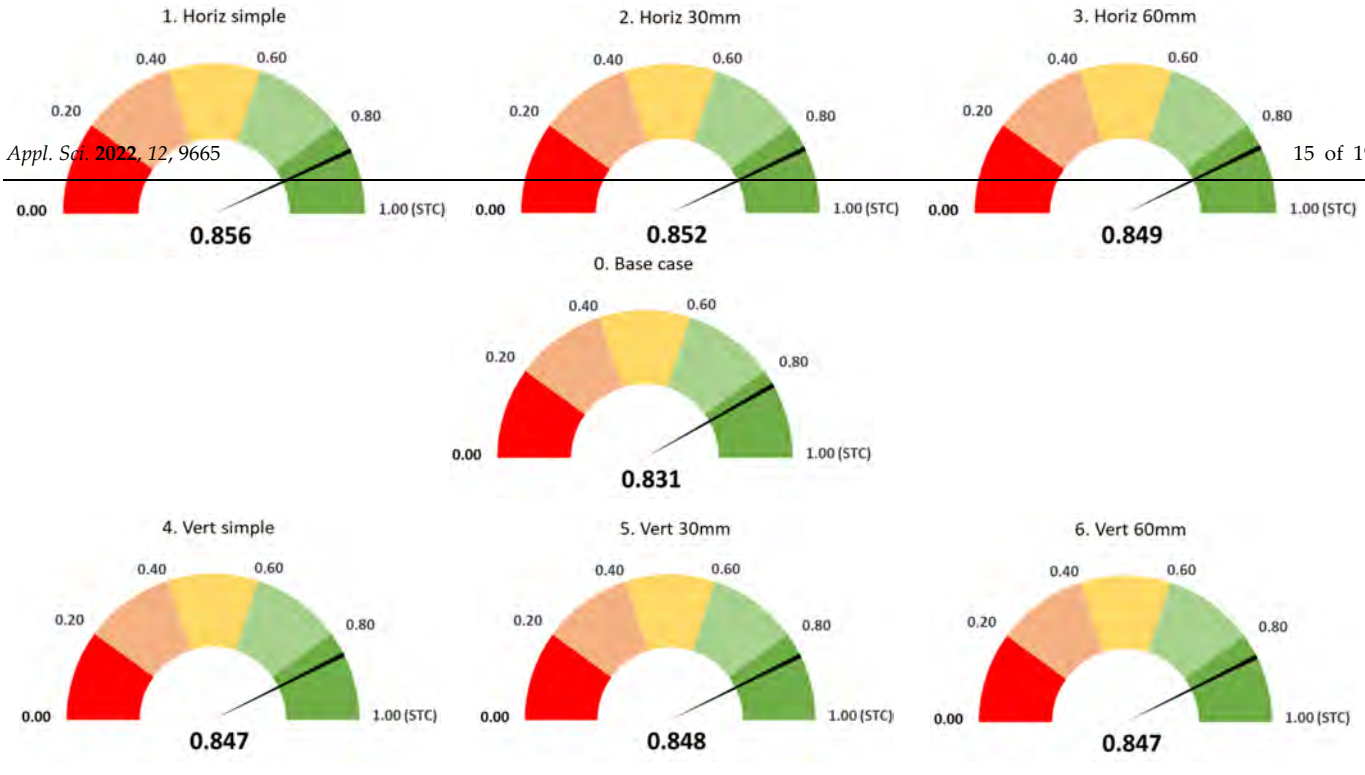


Figure 12. Normalized power production for **front wind**, v_{front} = 1 m/s, t_{air} = 35, G = 1000 W/m^2.

Even if the highest energy production is obtained in the case of the wind direction behind the panel, for the horizontal heat sink with perforated fins, it should be specified that the most important impact in terms of cooling compared to the base case is recorded when the wind blows from the side.



Figure 12. Normalized power production for **front wind**, v_{front} = 1 m/s, t_{air} = 35, G = 1000 W/m^2.

Even if the highest energy production is obtained in the case of the wind direction behind the panel, for the horizontal heat sink with perforated fins, it should be specified that the most important impact in terms of cooling compared to the base case is recorded when the wind blows from the side.

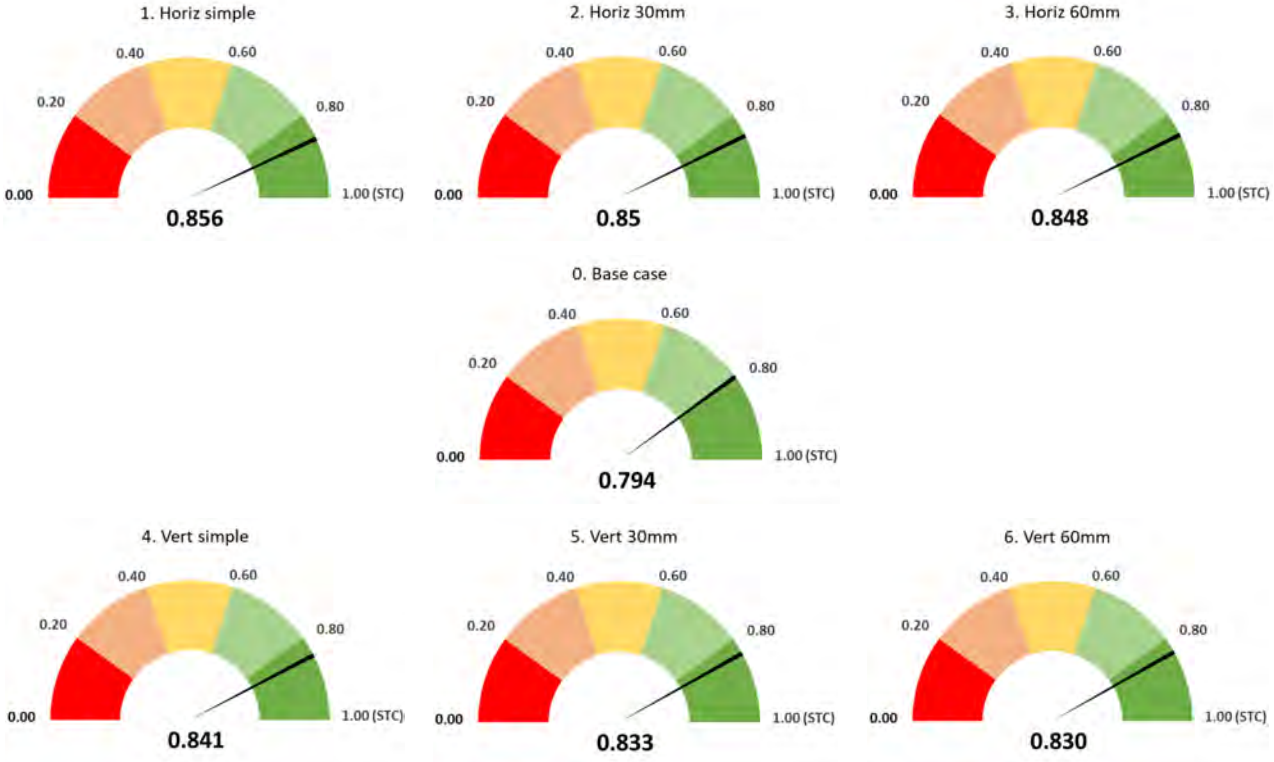


Figure 13. Normalized power production for **side wind**, v_{side} = 1 m/s, t_{air} = 35, G = 1000 W/m^2.

Table 6. Normalized power production of the PV panel for each model analyzed.

Case	v_{air}	Back Wind	Front Wind	Side Wind
		Normalized Power, for t_{air} = 35 °C		
		P_{STC} = 1.00 (320 Wp)		
0. Base Case	1 m/s	0.8333	0.8310	0.7949
1. Horiz Simple		0.8868	0.8564	0.8562
2. Horiz 30 mm		0.8874	0.8526	0.8500
3. Horiz 60 mm		0.8871	0.8496	0.8485
4. Vert Simple		0.8792	0.8473	0.8413
5. Vert 30 mm		0.8737	0.8489	0.8330
6. Vert 60 mm		0.8735	0.8478	0.8309
0. Base Case	2 m/s	0.8709	0.8697	0.8453
1. Horiz Simple		0.9111	0.8961	0.8929
2. Horiz 30 mm		0.9142	0.8982	0.8981
3. Horiz 60 mm		0.9104	0.8943	0.8917
4. Vert Simple		0.9093	0.8925	0.8865
5. Vert 30 mm		0.9094	0.8934	0.8835
6. Vert 60 mm		0.9083	0.8929	0.8848

Table 6. *Cont.*

Case	v_{air}	Back Wind	Front Wind	Side Wind
		Normalized Power, for t_{air} = 35 °C		
		P_{STC} = 1.00 (320 Wp)		
0. Base Case	3 m/s	0.8901	0.8894	0.8636
1. Horiz Simple		0.9246	0.9133	0.9097
2. Horiz 30 mm		0.9260	0.9148	0.9139
3. Horiz 60 mm		0.9241	0.9121	0.9086
4. Vert Simple		0.9223	0.9103	0.9053
5. Vert 30 mm		0.9236	0.9114	0.9043
6. Vert 60 mm		0.9205	0.9107	0.9067
0. Base Case	4 m/s	0.9035	0.9028	0.8809
1. Horiz Simple		0.9315	0.9226	0.9195
2. Horiz 30 mm		0.9329	0.9294	0.9224
3. Horiz 60 mm		0.9315	0.9234	0.9181
4. Vert Simple		0.9286	0.9228	0.9157
5. Vert 30 mm		0.9314	0.9236	0.9160
6. Vert 60 mm		0.9266	0.9249	0.9199
0. Base Case	5 m/s	0.9132	0.9125	0.8944
1. Horiz Simple		0.9359	0.9282	0.9254
2. Horiz 30 mm		0.9369	0.9294	0.9282
3. Horiz 60 mm		0.9361	0.9275	0.9277
4. Vert Simple		0.9334	0.9244	0.9225
5. Vert 30 mm		0.9363	0.9294	0.9236
6. Vert 60 mm		0.9302	0.9244	0.9232

Even if the highest energy production is obtained in the case of the wind direction behind the panel, for the horizontal heat sink with perforated fins, it should be specified that the most important impact in terms of cooling compared to the base case is recorded when the wind blows from the side.

It can be remarked that, for the simulated external conditions, t_{air} = 35 °C, G = 1000 W/m^2 and low air velocity v_{air} = 1 m/s, the normalized power production for the base case is between 0.79 and 0.83. Meanwhile, in the best cooling conditions for each wind directions, it could reach values from 0.85 to 0.88 (Case 3—horizontal 30 mm). The improvement in power generation is between 3.06% and 7.71% compared to the base case (when no cooling is applied).

It should be highlighted that the best configuration of heat sink is the low velocity conditions for various conditions of wind velocity and direction. Therefore, Case 3—Horizontal 30 mm determines the most important effect of cooling of the PV panel. The improvement of power production is important both for low velocities (1–2 m/s) and higher ones (3–5 m/s), but the effect is lower for higher velocities (1.85–5.82%), due to the suitable cooling of the PV panel in the base case.

In terms of wind direction, the lowest cooling effect is registered for the front wind. For these cases, the presence of the heat sink does not have a significant effect, determining a raise of power production between 1.85% and 3.06% compared to the base case.

6. Conclusions

The goal of this study was to deploy a numerical analysis regarding the air cooling of photovoltaic panels by using heat sinks with perforated and non-perforated fins. A random PV panel with typical characteristics was analyzed for different wind directions—towards its back, front and from the side. The PV panel is mounted in fixed position, facing south, inclined at 45 degrees from the horizontal. The input constants were the solar radiation G = 1000 W/m^2 and ambient temperature t_{air} = 35 °C, while the parameters varied during the study were the wind direction (towards its back, front and from the side of PV panel) and velocity v_{air} = 1–5 m/s.

The base case of the numerical model was calibrated according to the NOCT conditions, while the accuracy of the numerical simulation was achieved by comparison with the experimental studies from literature. The numerical study is focused on six types of heat sink with perforated and non-perforated fins attached to a typical PV panel. The fins were distributed both horizontally and vertically. A challenging task consisted in simulation of the real wind conditions around the PV panel by taking into account the entire air domain. The main results obtained were the average temperature of PV panels and the respective efficiency.

The passive cooling solutions analyzed introduced a rise of maximum power production between 1.85% (wind towards the front—worse case) and 7.71% (wind towards the side—best case) above the basic set-up, depending on the wind direction and velocity. The maximum power increase for each wind direction was of 7.71% for the side wind, 6.49% for the backside wind and 3.06% for the front wind. The effect is more intense for lower velocities. This phenomenon is achieved because of the lower convection near the PV panel in the base case, compared to usage of the heat.

Author Contributions: Conceptualization, S.V.H., F.E.Ț. and N.-C.C.; methodology, S.V.H., F.E.Ț. and N.-C.C.; software, S.V.H. and F.E.Ț.; validation, S.V.H., F.E.Ț., N.-C.C. and I.H.; formal analysis, S.V.H., D.-A.A. and I.H.; investigation, S.V.H., F.E.Ț., N.-C.C., C.-G.P., M.V., D.-A.A. and I.H.; resources, S.V.H., F.E.Ț. and C.-G.P.; data curation, S.V.H., F.E.Ț. and I.H.; writing—original draft preparation, S.V.H., F.E.Ț., N.-C.C., C.-G.P., M.V., D.-A.A. and I.H.; writing—review and editing, S.V.H., F.E.Ț., N.-C.C., C.-G.P., M.V. and I.H.; visualization, S.V.H., D.-A.A. and I.H.; supervision, S.V.H. and M.V.; project administration, S.V.H.; funding acquisition, S.V.H. All authors have read and agreed to the published version of the manuscript.

Funding: This work was supported by a grant of the Romanian Ministry of Education and Research, CCCDI-UEFISCDI, project number PN-III-P2-2.1-PED-2019-1294, within PNCDI III.

Institutional Review Board Statement: Not applicable.

Informed Consent Statement: Not applicable.

Data Availability Statement: Not applicable.

Acknowledgments: We would like to acknowledge the invaluable support provided by the FCI-TUIASI infrastructure in writing this article.

Conflicts of Interest: The authors declare no conflict of interest.

References

1. Available online: https://ec.europa.eu/eurostat/statistics-explained/index.php?title=Electricity_price_statistics (accessed on 15 August 2022).
2. Available online: https://www.overshootday.org (accessed on 15 August 2022).
3. AlAmri, F.; AlZohbi, G.; AlZahrani, M.; Aboulebdah, M. Analytical Modeling and Optimization of a Heat Sink Design for Passive Cooling of Solar PV Panel. *Sustainability* **2021**, *13*, 3490. [CrossRef]
4. Available online: https://www.euronews.com/2021/10/28/why-europe-s-energy-prices-are-soaring-and-could-get-much-worse (accessed on 15 August 2022).
5. Available online: https://www.nature.com/articles/d41586-022-00969-9 (accessed on 15 August 2022).
6. Hudișteanu, S.V.; Țurcanu, F.E.; Chereches, N.C.; Popovici, C.G.; Verdeș, M.; Hudisteanu, I. Enhancement of PV Panel Power Production by Passive Cooling Using Heat Sinks with Perforated Fins. *Appl. Sci.* **2021**, *11*, 11323. [CrossRef]

7. Hudișteanu, S.V.; Popovici, C.G. Numerical analysis of the efficiency and energy production of the building integrated photovoltaics for various configurations. In Proceedings of the CLIMA 2019 Congress, E3S Web of Conferences, Bucharest, Romania, 26–29 May 2019; Volume 111, p. 03044.
8. Popovici, C.G.; Hudisteanu, S.V.; Mateescu, T.D.; Chereches, N.C. Efficiency improvement of photovoltaic panels by using air cooled heat sinks. *Energy Procedia* **2016**, *85*, 425–432. [CrossRef]
9. Hernandez-Perez, J.G.; Carrillo, J.G.; Bassam, A.; Flota-Banuelos, M.; Patino-Lopez, L.D. A new passive PV heatsink design to reduce efficiency losses: A computational and experimental evaluation. *Renew. Energy* **2020**, *147*, 1209–1220. [CrossRef]
10. Gomaa, M.R.; Hammad, W.; Al-Dhaifallah, M.; Rezk, H. Performance enhancement of grid-tied PV system through proposed design cooling techniques: An experimental study and comparative analysis. *Sol. Energy* **2020**, *211*, 1110–1127. [CrossRef]
11. Colarossi, D.; Principi, P. Indoor and Outdoor Performance of an Enhanced Photovoltaic Panel through Graphene/Fins/Phase Change Materials. *Appl. Sci.* **2021**, *11*, 8807. [CrossRef]
12. Hudișteanu, S.V.; Cherecheș, N.C.; Popovici, C.G.; Verdeș, M.; Ciocan, V. Effect of cooling on power generated by photovoltaic panels. In *IOP Conference Series: Materials Science and Engineering, Proceedings of the Computational Civil Engineering (CCE 2021), Iasi, Romania, 27–29 May 2021*; IOP Publishing: Bristol, UK; Volume 1141, p. 012008.
13. Branoaea, M.; Burlacu, A.; Verdeș, M.; Ciocan, V.; Costel Balan, M.; Ștefan Vizitiu, R. Hybrid photovoltaic-thermic system with enhanced cell energy efficiency. In Proceedings of the CLIMA 2022 The 14th REHVA HVAC World Congress, Rotterdam, The Netherlands, 22–25 May 2022. [CrossRef]
14. Albatayneh, A.; Jaradat, M.; Al-Omary, M.; Zaquot, M. Evaluation of Coupling PV and Air Conditioning vs. Solar Cooling Systems—Case Study from Jordan. *Appl. Sci.* **2021**, *11*, 511. [CrossRef]
15. Hudișteanu, S.V.; Popovici, C.G. Experimental investigation of the wind direction influence on the cooling of photovoltaic panels integrated in double skin façades. In Proceedings of the CLIMA 2019 Congress, E3S Web of Conferences, Bucharest, Romania, 26–29 May 2019; Volume 111, p. 03045.
16. Hammami, M.; Torretti, S.; Grimaccia, F.; Grandi, G. Thermal and Performance Analysis of a Photovoltaic Module with an Integrated Energy Storage System. *Appl. Sci.* **2017**, *7*, 1107. [CrossRef]
17. Hudisteanu, S.V.; Mateescu, T.D.; Popovici, C.G.; Chereches, C.N. *The Influence of the Building Integrated Photovoltaic Panels Positions on the Conversion Efficiency*; Buletinul Institutului Politehnic din lasi: Sectia Constructii, Arhitectura, 2016.
18. Pérez Escobar, B.L.; Pérez Hernández, G.; Ocampo Ramírez, A.; Rojas Blanco, L.; Díaz Flores, L.L.; Vidal Asencio, I.; Hernández Perez, J.G.; Ramírez Morales, E. Analysis of Thermomechanical Stresses of a Photovoltaic Panel Using a Passive System of Cooling. *Appl. Sci.* **2021**, *11*, 9806. [CrossRef]
19. Arifin, Z.; Tjahjana, D.; Hadi, S.; Rachmanto, R.A.; Setyohandoko, G.; Sutanto, B. Numerical and Experimental Investigation of Air Cooling for Photovoltaic Panels Using Aluminum Heat Sinks. *Int. J. Photoenergy* **2020**, *2020*, 1574274. [CrossRef]
20. Bevilacqua, P.; Bruno, R.; Rollo, A.; Ferraro, V. A novel thermal model for PV panels with back surface spray cooling. *Energy* **2022**, *255*, 124401. [CrossRef]
21. Kuznetsov, P.; Yuferev, L.; Voronin, D.; Panchenko, V.A.; Jasiński, M.; Najafi, A.; Leonowicz, Z.; Bolshev, V.; Martirano, L. Methods Improving Energy Efficiency of Photovoltaic Systems Operating under Partial Shading. *Appl. Sci.* **2021**, *11*, 10696. [CrossRef]
22. Hudișteanu, S.V.; Mateescu, T.D.; Chereches, N.C.; Popovici, C.G. Numerical study of air cooling photovoltaic panels using heat sinks. *Rom. J. Civ. Eng.* **2015**, *6*, 11–20.
23. Arifin, Z.; Suyitno, S.; Tjahjana, D.; Juwana, W.E.; Putra, M.R.A.; Prabowo, A.R. The Effect of Heat Sink Properties on Solar Cell Cooling Systems. *Appl. Sci.* **2020**, *10*, 7919. [CrossRef]
24. Duan, J. A novel heat sink for cooling concentrator photovoltaic system using PCM-porous system. *Appl. Therm. Eng.* **2021**, *186*, 116522. [CrossRef]
25. Bayrak, F.; Oztop, H.F.; Selimefendigil, F. Effects of different fin parameters on temperature and efficiency for cooling of photovoltaic panels under natural convection. *Sol. Energy* **2019**, *188*, 484–494. [CrossRef]
26. Johnston, E.; Szabo, P.S.B.; Bennett, N.S. Cooling silicon photovoltaic cells using finned heat sinks and the effect of inclination angle. *Therm. Sci. Eng. Prog.* **2021**, *23*, 100902. [CrossRef]
27. Amr, A.A.R.; Hassan, A.A.M.; Abdel-Salam, M.; El-Sayed, A.M. Enhancement of photovoltaic system performance via passive cooling: Theory versus experiment. *Renew. Energy* **2019**, *140*, 88–103. [CrossRef]
28. El Fouas, C.; Cherecheș, N.C.; Hudișteanu, S.V.; Hajji, B.; Țurcanu, E.F.; Cherecheș, M.L. Numerical and Parametric Analysis for Enhancing Performances of Water Photovoltaic/Thermal System. *Appl. Sci.* **2022**, *12*, 646. [CrossRef]
29. Vittorini, D.; Cipollone, R. Fin-cooled photovoltaic module modeling—Performances mapping and electric efficiency assessment under real operating conditions. *Energy* **2019**, *167*, 159–167. [CrossRef]
30. Mattar, S.J.; Kavian Nezhad, M.R.; Versteege, M.; Lange, C.F.; Fleck, B.A. Validation Process for Rooftop Wind Regime CFD Model in Complex Urban Environment Using an Experimental Measurement Campaign. *Energies* **2021**, *14*, 2497. [CrossRef]
31. Photovoltaic (PV) module performance testing and energy rating—Part 1: Irradiance and temperature performance measurements and power rating. In *International Standard*; IEC 61853-1; International Electrotechnical Commission: Geneva, Switzerland, 2011.
32. Available online: https://ae-solar.com/wp-content/uploads/2018/10/AE_Eclipse-Ultra-Black_HM6-60_310W-320W.pdf (accessed on 15 August 2022).
33. Nizetic, S.; Papadopoulos, A.M.; Giama, E. Comprehensive analysis and general economic-environmental evaluation of cooling techniques for photovoltaic panels, Part I: Passive cooling techniques. *Energy Convers. Manag.* **2017**, *149*, 334–354. [CrossRef]

34. Ansys Fluent Documentation, 2021-R2. Available online: https://www.ansys.com/products/fluids/ansys-fluent (accessed on 15 August 2022).
35. Malvoni, M.; Baglivo, C.; Congedo, P.M.; Laforgia, D. CFD modeling to evaluate the thermal performances of window frames in accordance with the ISO 10077. *Energy* **2016**, *111*, 430–438. [CrossRef]
36. Congedo, P.M.; Lorusso, C.; De Giorgi, M.G.; Laforgia, D. Computational Fluid Dynamic Modeling of Horizontal Air-Ground Heat Exchangers (HAGHE) for HVAC Systems. *Energies* **2014**, *7*, 8465–8482. [CrossRef]
37. Szodrai, F. Heat Sink Shape and Topology Optimization with Pareto-Vector Length Optimization for Air Cooling. *Energies* **2020**, *13*, 1661. [CrossRef]
38. Nguyen, D.P.N.; Neyts, K.; Lauwaert, J. Proposed Models to Improve Predicting the Operating Temperature of Different Photovoltaic Module Technologies under Various Climatic Conditions. *Appl. Sci.* **2021**, *11*, 7064. [CrossRef]
39. Almuwailhi, A.; Zeitoun, O. Investigating the cooling of solar photovoltaic modules under the conditions of Riyadh. *J. King Saud Univ.-Eng. Sci.* **2021**, *186*, 116522. [CrossRef]

applied sciences

MDPI

Article

Design and Simulation of a Solar Tracking System for PV

Fatima Zohra Baouche [1,*], Bilal Abderezzak [1,*], Abdennour Ladmi [2], Karim Arbaoui [2], George Suciu [3], Traian Candin Mihaltan [4], Maria Simona Raboaca [5,6,7,*], Sebastian Valeriu Hudișteanu [8,*] and Florin Emilian Țurcanu [8,*]

1 Laboratoire de l'Énergie et des Systèmes Intelligent (LESI), University of Khemis Miliana, Road of Theniet el Had, Khemis Miliana 44225, Algeria
2 Department of Technology, Faculty of Sciences and Technology, University of Khemis Miliana, Road of Theniet el Had, Khemis Miliana 44225, Algeria
3 R&D Department Beia Consult International Bucharest, 041386 Bucharest, Romania
4 Faculty of Building Services, Technical University of Cluj-Napoca, 400114 Cluj-Napoca, Romania
5 National Research and Development Institute for Cryogenic and Isotopic Technologies—ICSI Rm. Vâlcea, Uz-inei Street, No. 4, P.O. Box 7 Râureni, 240050 Rm. Vâlcea, Romania
6 Faculty of Electrical Engineering and Computer Science, Ștefan cel Mare University, 720229 Suceava, Romania
7 Doctoral School, University Politehnica of Bucharest, Splaiul Independentei Street, No. 313, 060042 Bucharest, Romania
8 Faculty of Civil Engineering and Building Services, Gheorghe Asachi Technical University of Iasi, 700050 Iași, Romania
* Correspondence: f.baouche@univ-dbkm.dz (F.Z.B.); b.abderezzak@univ-dbkm.dz (B.A.); simona.raboaca@icsi.ro (M.S.R.); valeriu-sebastian.hudisteanu@academic.tuiasi.ro (S.V.H.); florin-emilian.turcanu@academic.tuiasi.ro (F.E.Ț.)

Abstract: After installing a solar panel system, the orientation problem arises because of the sun's position variation relative to a collection point throughout the day. It is, therefore, necessary to change the position of the photovoltaic panels to follow the sun and capture the maximum incident beam. This work describes our methodology for the simulation and the design of a solar tracker system using the advantages that the orientation and efficiency of the PV panel offer due to the latitude and the number of hours of sunshine in the testing area. This proposed methodology is experimentally validated through the implementation of a single-axis solar tracker at a specific location (36.261° latitude), which allowed the incorporation of a high-availability tracking mechanism, low precision, and low cost. Based on the results, the feasibility of this type of solar tracker for latitudes close to 36° was demonstrated, as this tracking system costs less than traditional commercial systems. Furthermore, this system increased the collection efficiency compared to a fixed device. Our results provide an excellent platform for engineering technology researchers and students to study the design theory of a sun-tracking solar system.

Keywords: prototype of a single-axis solar tracker; Simulink; Arduino card; LDR; photovoltaic panels

check for updates

Citation: Baouche, F.Z.; Abderezzak, B.; Ladmi, A.; Arbaoui, K.; Suciu, G.; Mihaltan, T.C.; Raboaca, M.S.; Hudișteanu, S.V.; Țurcanu, F.E. Design and Simulation of a Solar Tracking System for PV. *Appl. Sci.* **2022**, *12*, 9682. https://doi.org/10.3390/app12199682

Academic Editors: Ilinca Nastase and Florin Ioan Bode

Received: 23 August 2022
Accepted: 23 September 2022
Published: 27 September 2022

Publisher's Note: MDPI stays neutral with regard to jurisdictional claims in published maps and institutional affiliations.

Copyright: © 2022 by the authors. Licensee MDPI, Basel, Switzerland. This article is an open access article distributed under the terms and conditions of the Creative Commons Attribution (CC BY) license (https://creativecommons.org/licenses/by/4.0/).

1. Introduction

Much scientific research has been carried out, not only in the field of solar energy conversion in general but also in a very specific sector of the latter, which is none other than photovoltaic technology. In this case, the design, optimization, and realization of systems based on this technology are current issues since they can lead to better exploitation of solar energy if they are correctly done. One of the paths taken is increasing the solar radiation captured since maximum efficiency is achieved when the incident light is perpendicular to the cells of the photovoltaic panels: this is the concept of "solar tracking". Therefore, the energy efficiency of these systems depends on the climate conditions of solar radiation, ambient temperature, and wind speed, the matching of the system with the load, and the appropriate placement of the solar panels. Most solar panels are used in a stationary

position and therefore do not consistently output the maximum amount of power they can produce.

To obtain the maximum efficiency from photovoltaics panels, it was necessary to study the problem of PV orientation, which requires using a solar tracker connected to the photovoltaic system. A solar tracker will track the sun throughout the day and adjust the angle of the solar panel so that the sun is normal, typical to the solar panels at all times. There are two ways to maximize the useful energy rate: by optimizing the conversion and degree of absorption and increasing the incident radiation rate by employing mechanical steering systems. In this context, in our project, we decided to realize such a system, which is commonly called a "solar tracker".

A solar tracker is a photovoltaic installation placed on a supporting structure composed of a motor. It makes it possible to direct the solar panels throughout the day toward the sun to capture the maximum sunshine. Therefore, solar trackers can be classified into two main categories depending on the type of control and the sensitivity of the sensors or the positioning system they incorporate [1–3]. They can also be distinguished by two tracking techniques: The MPPT (maximum power point tracking) method which is based on an algorithm to find the maximum power curve of the photovoltaic panel, or the sun tracking system, which is based on the orientation of solar panels throughout the day to better exploit the photovoltaic cells [4,5].

Much research was conducted to improve and increase the production of electrical energy through the transformation of solar energy. Among this research, we can cite the work of Robert H. Dold and F. R. Rubio et al. [6]. In 2007, they described a 2-axis solar tracker capable of withstanding extreme weather conditions, which tracks the elevation and azimuth movement. In 2008, J.Rizk [6] indicated the potential advantages of a simple solar tracking system using a stepper motor and light sensor. A solar tracking system was designed, implemented, and experimentally tested with fairly conclusive results. Hossein Mousazadeh, in 2009 [6], discussed the different sun tracking systems' advantages and disadvantages. The most effective sun tracking device was found in the form of polar and azimuth/elevation axes. In 2010, Nader Barsoum [6] reported that his research has proven that the single-axis sun tracking system can increase the energy output by about 20%, while the dual-axis tracking system can increase the output by 40%. In 2012, L. Kancevica [6] noted that thanks to the sun tracking device, the solar radiation continuously hit perpendicular to the collector of the flat plate, which finally produced 1.4 times more thermal energy on average compared to the collector stationary of the same size. In 2013, Mostefa Ghassoul [6] described constructing and testing a cost-effective, innovative sun tracking system to extract maximum solar energy. The latter was designed to be driven by a PIC 18F452 microcontroller. The system was based on two mechanisms: the first is the search mechanism (PILOT), which locates the position of the sun and the second mechanism (intelligent PANELS) aligns with the PILOT only if the maximum possible energy could be extracted.

Thereby, the research results from the article [7–11] confirm that the orientation of solar panels can increase the efficiency of the conversion system by 20% up to 50%, which significantly increases electricity production. In [11], there was a study of a three-phase inverter representing an essential part of the photovoltaic systems, which allowed us to take an idea on the conditioning and the simulation of the motor used in our realized prototype. Afterward, many research works have studied the optimization and design of the sun tracking method to maximize the exposure of cells to sunlight by keeping the solar module's active surface perpendicular to the solar radiation. In 2018, the authors of the article [12] presented a comprehensive examination of the solar tracking system's potential in solar energy applications. Their explanation helps to give an overview of drive system design parameters, construction, types, and techniques covering different applications of use. They explained the two main types of solar tracking systems: the single-axis solar tracking system and the dual-axis solar tracking system. Their paper shows that in recent research studies, 42.57% of the studies have discussed and presented single-axis tracking

systems, while 41.58% of these studies reported on dual-axis tracking systems. As well as in the solar tracking techniques, azimuth and elevation tracking reached 16.67% utilization, horizontal tracking 16.67%, azimuth tracking 10%, polar tracking 16.67%, and utilization 4.44%. This encouraged us to continue to improve the modeling results of the different blocks of our methodology and improve the other blocks' modeling results [13].

Several electronic systems for the control and piloting of bi-axial solar trackers of photovoltaic power plants were developed and tested by [14–16]. As in our case, the tracking is managed by a PC software application with a user-friendly graphical interface. The software's design is designed to calculate the circadian orbit of the sun and consequently to move the solar panels to keep the panel surface always perpendicular to the solar rays, thus improving the efficiency of energy production. For example, a new photovoltaic (PV) sun tracker design methodology has been explained and relied on by [14], who used the advantages that the orientation and efficiency of the PV panel offer due to the latitude of the installation zone. They experimentally validated the proposed design methodology and proposed a design methodology via the implementation of a solar tracker with dual axes at a specific location (27.5° latitude). Their method enables the incorporation of a high-availability, low-accuracy, and low-cost tracking mechanism. From their results, we can conclude that this system increases the collection efficiency by 24% with respect to a fixed device. Based on an orientation efficiency chart, the proposed methodology can be applied to control our solar tracker system.

The scientific content of [16] allowed us to get a general idea of the most commonly used solar tracking systems, and we identified the systems that provide benefits such as higher efficiency, higher tracking accuracy, easy installation, and cost-effectiveness. Their study reveals that double axis ST in the form of polar-axis and azimuth/elevation featuring the solar movement models and the dynamic closed-loop feedback control is the most effective and generally gives more than a 40% improvement in energy return compared to fixed PV panels. Moreover, they showed that large systems significantly reduce costs and save on materials. The energy consumed by the moving fixtures is mostly low (2–5% of the collected energy), but this could be higher if no optimization is performed. That is why we have optimized all power-saving hardware and software settings from the early stages of system development to avoid waste of material and over-consumption of power by tracking units.

Another study by [17] presents an overview of the advancements realized in the world of solar tracking systems. They emphasized the performance analysis of dual-axis solar tracking systems equipped with different designs and techniques that have evolved in recent years. Some conclusions drawn in their paper are stated below: the dual-axis solar tracking systems are generally more efficient than their single-axis and fixed counterparts. These systems also demand maintenance due to the presence of rotating components. Furthermore, these systems contain more complex design and control mechanisms. The solar system's performance depends on many physical factors and so does the choice of use of tracking.

In this paper, we present the steps of designing and implementing the prototype of a single-axis solar tracker that we designed and built at our university. The design of the single-axis solar tracker has been made by several researchers, as mentioned in the previous summary of the literature. But still, some shortcomings must be avoided to improve the system, especially concerning the geographical parameters of each installation area. Our project was put into reality following the need of our university for this system to be used in the various premises containing PV panels. This necessity forced us to start collecting knowledge in circuit theory, power electronics, microcontrollers, machine electricity, and solar energy to design and simulate the system. The Matlab/Simulink simulation provided an excellent platform to explore different designs for the sun-tracking solar energy system. After testing and verification using simulations, a prototype system was built in the laboratory using our hardware and programs. The university's weather station collects parameters and real-time data on the installation area. Given the high

number of models created and the mathematical calculations performed, we present only a part of the scientific result obtained in this paper. Our complete prototype of the single-axis solar tracker is characterized by the fact that it contains in the control circuit a control device assembled and programmed by us in the laboratory to allow the pivoting of the photovoltaic panel and force it to follow the sun's curve. Thus, we have developed our mathematical models allowing translating of the behavior of the components constituting the prototype, such as the model of the direct current motor block (servomotor); the model of the quantity of effective radiation; the model of the sun, and the model of the photovoltaic panel.

In particular, our work aims to optimize an existing, designed by us, fully-hardware setup by completely replacing the classic electronic board with the designed software to communicate, using a serial port, with Arduino electronic boards for tracker motors driving. The models were developed using MATLAB/Simulink to track a photovoltaic module and achieve optimal operational efficiency. The multi-controller is programmed to detect sunlight by LDR and operate two actuators to position the solar panel where it can receive maximum sunlight.

2. Methodology

This paper collects some results of research work, part of which is carried out as part of a research project, "PRFU: University Training Research Project", with the participation of [18]. The simulation of our models was carried out using the software "MATLAB-SIMULINK", which allowed us to create a library of specialized simulation blocks. The annual meteorological data was collected through the meteorological station installed at the University of Khemis Miliana. The prototype allowed tracking the movement of the sun in real-time.

To maximize actual PV production in the field, solar trackers must meet several dimensions during the different phases of the PV project life: design, installation, operation, and maintenance. The challenges are many and diverse, ranging from the lay of the land to the need for local content, local workforce skills, weather conditions, and budget constraints. The efficient performance of a solar tracker requires comprehensive realizations.

Our work is based on a new idea by designing an automatic microcontroller-based solar tracker with a hybrid algorithm comprising both active and chronological algorithms for locating the sun's position. This hybrid algorithm combines both mathematical models and sensors to determine the precise sun's position and thereby harness optimal solar energy for all weather conditions.

Experimental results show that the hybrid solar tracking algorithm can yield higher solar power than traditional active and chronological algorithms. The solar tracking process is fully automated, maximizing the collection and management of solar energy for the solar system.

The proposed solar tracker has light-dependent resistors (LDRs), an Arduino microcontroller connected with Wi-Fi, a servo motor, a current sensor, and a solar panel with a supporting metallic servo bracket. This electromechanical system consists of one driver with a servo motor for rotating in east and west directions. The solar panel produces a voltage proportional to the sunlight intensity, while the LDRs determine the system misalignment and send signals to the microcontroller, which in turn automatically adjusts the motors to correct the solar panel position.

Active and chronological algorithms are employed in solar tracking. The active algorithm is a closed-loop tracking mechanism based on the control principle with feedback. A light sensor, which detects sun brightness, acts as the input to the system controller. The acquired values are then analyzed by the microcontroller, which controls the motor motion to orientate the solar panel towards the sun. While the active solar tracker produces high tracking accuracy during clear and sunny days, its performance may degrade when the weather is cloudy or when the light sensor is sheltered. Conversely, the chronological algorithm controls the solar panel movement by identifying the sun's path using sun

tracking mathematical models. The microcontroller calculates the sun's position and directs the motor to move the solar panel towards the sun at preset time intervals.

In summary, with a large-scale implementation, the proposed hybrid solar tracker can harness optimal solar energy for all weather conditions, thereby considerably cutting electricity costs for public and private organizations.

To evaluate the performance of active, chronological, and hybrid algorithms for solar tracking, experiments were conducted. The solar tracker prototype must be in an open field where it can receive sunlight throughout the day. Voltage measurements were taken from the morning at 4 a.m. to the evening at 8 p.m. at every 60-min interval. Readings from the traditional fixed-mount solar panel were also recorded to determine the baseline voltage. Subsequently, an analysis was performed to determine the energy generated, consumed, and gained by the hybrid solar tracker.

2.1. Assumptions

Our research on the tracking system showed us that, in reality, they are from the same capacity compared to a static configuration and will produce more energy at any point in time, but at what cost? When talking about the price, we have to do a test for 10 years of operation. Thus, we must add the cost of the land into the calculations without forgetting to consider the electricity price, which increases every year, and the state degradation of the PV panels, which degrade every year. Therefore, we must consider the average output per kW installed and the maintenance price for the tracking system every year. Finally, we must calculate the cost per watt supplied and installed for the static system and tracker system. Moreover, that question can be asked in reverse. How much does the by-watt price have to drop before the static system becomes more viable than the tracker system?

When comparing to ascertain what is the best system, static versus tracking, many assumptions need to be made in addition to the reality of actual energy production and how it matches with site loads, etc. Our scientific research confirms that many assumptions are common between the static system and the tracker system, but some are not. Based on the assumptions made, we can say that the tracker system is more economically feasible.

Compared to fixed panels, the advantage of mobile panels is that the sun moves continuously during the day, while a PV panel is fixed in its position, thus losing a considerable amount of energy that might be available. When a photovoltaic panel is fixed in relation to the ground and oriented towards the south, its energy yield is not constant during the day. At the start and end of the day, the poor radiation angle of the panel reduces the efficiency of electricity production [11–16,19].

2.2. Block Diagram of a Single-Axis Tracker

The prototype of the tracker that we have realized consists of an electromechanical structure to support the solar panel and direct it in the direction of the perpendicular radiation of the sun on an axis of two East-West directions.

The tracking system essentially consists of two parts: The control or command part (the physical quantities and the solar radiation follow the sun and position the turret optimally) and the operative part (elevation). The control or programming units are used to process the position information of the sun to transmit it to the actuators to track the sun, as well as to detect operating anomalies and perform equipment safety operations. It also performs other functions, such as the control of the system's mechanical movements by limiting the rotation angles from (0° to 180° on the horizontal) and the panel's orientation at the end of the day towards the starting position of the system.

The role of the operating or electronic block is to ensure that the solar radiation is always perpendicular to the panel. It, therefore, relies on systems allowing the reception of orders sent by the calculator, their conversion into electrical signals, their transmission to the articulated mechanical system, and the activation of the motor. As shown in the block diagram in Figure 1, when the tracking system steers the solar panels by rotating them

at the end of the day towards the starting position of the system.

The role of the operating or electronic block is to ensure that the solar radiation is always perpendicular to the panel. It, therefore, relies on systems allowing the reception of orders sent by the calculator, their conversion into electrical signals, their transmission to the articulated mechanical system, and the activation of the motor. As shown in the block diagram in Figure 1, when the tracking system steers the solar panels by rotating them in the direction of the sun and maintaining an ideal angle based on two light-dependent resistors (LDR) and a motor, the electrical power per square meter is maximized [20].

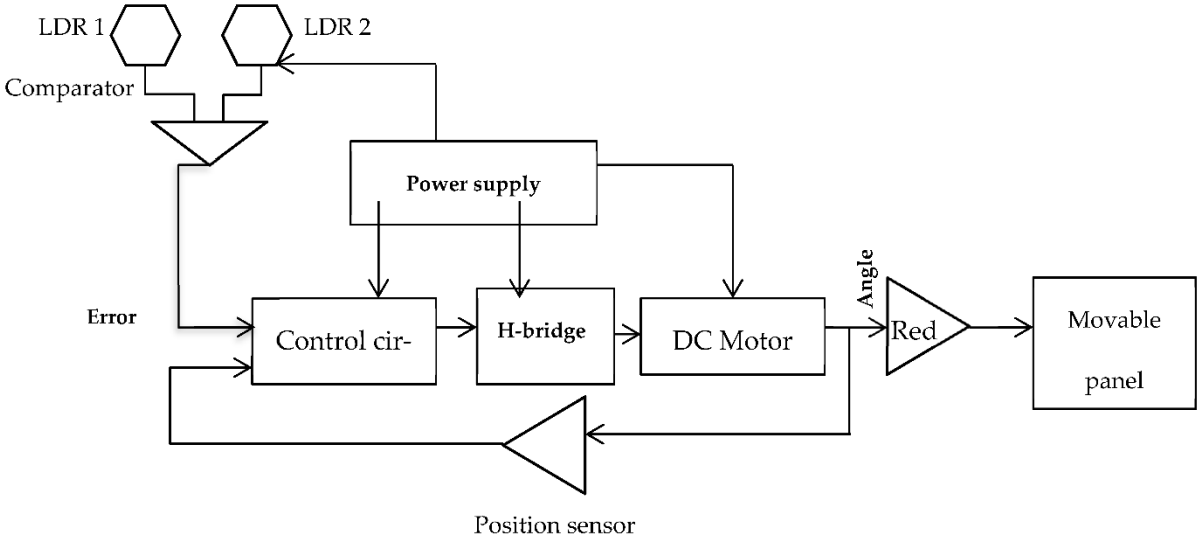


Figure 1. Block diagram of a single-axis tracker.

The two LDRs are used in our work to capture the light in East-West directions. Each LDR will supply the controller an analog signal depending on the lighting through the voltage divider V_{out}, given by Equation (1), with an R_1 resistance LDR and R_2 resistance standard. The controller changes the motor direction [21–25].

$$V_{out} = \frac{R_2}{R_1 + R_2} * Vcc \quad (1)$$

The principle is to notice that the light received by the two LDR photoresistors is identical as soon as the sensor is oriented in the axis of the light. Therefore, we measured the light received by each photoresistor by measuring the voltage at their terminals. This measurement is carried out by connecting the ports pin1 to 2 of the card. The program then compares these voltages ordering the servo motor to rotate in the direction of the photoresistor(s) that receives the least light. We used a resistor of 1 kΩ to measure the voltage change between the photoresistor and a resistor of 1 kΩ (voltage divider) placed on the control unit (Arduino card).

Our MATLAB modeling requires describing the models of the different design blocks [18]: The model of the DC motor (servomotor) with P.I.D. controller (proportional integral derivative), the model of the chopper to vary the voltage, the model of the solar radiation falling on the solar panel, the model of the panel of the photovoltaic panel.

2.3. D.C. Motor Block Controlled by a Chopper

To create the model of the D.C. motor (servomotor), we took into account its 04 constituents and their characteristics which are: A direct current electric motor with rotation in two directions, a reduction gear train actuating the rudder of the out axe, an electronic circuit of the motor control, and a potentiometer.

The creation of our models of the physical system of the engine in the Simulink environment was made using the simulator SimScape (physical systems simulation), which constitutes an effective method for developing the mathematical model of our physical system by creating a multi-domain diagram based on physical connections.

A DC chopper or DC-to-DC converter is the most efficient method as it involves only a one-stage conversion. A fixed D.C. voltage U coming from a power supply is converted into an adjustable D.C. voltage V by a control signal U_{com} with a variable duty cycle. The

chopper's role in the solar tracker system is to vary the rotational speed of the D.C. motors. The equivalent model of a motor contains a resistance (*Rm*), an inductance (*Lm*), and an electromotive force (*E*). In addition, the protection elements such as freewheeling diodes are necessarily added [26–28]. The steps below are taken into consideration while creating the model of the D.C. motor [29].

- Variation of the speed for a motor by the P.W.M. (pulse width modulation) command.
- Voltage reversible chopper.
- The average value of the supply voltage.
- Direction inversion control.

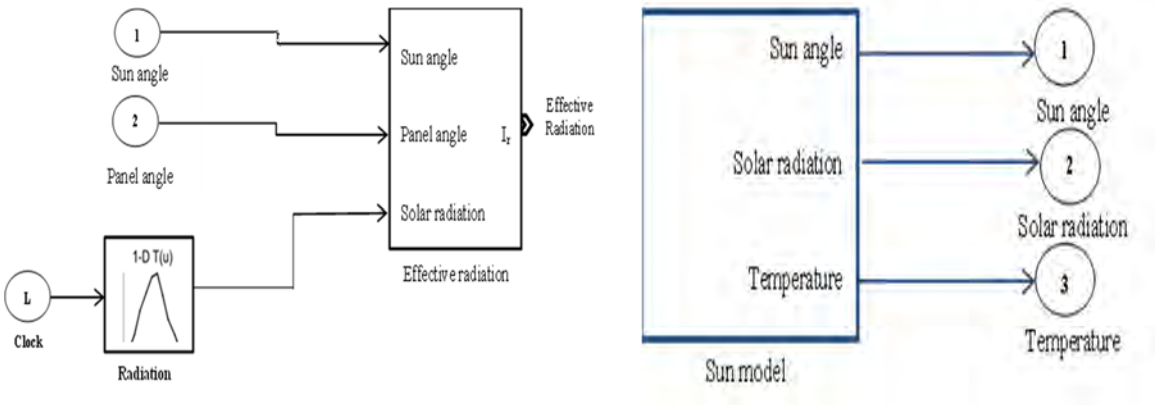
The advantage of a P.I.D. regulator is its dynamic performance, adjustment precision, and stability. The elements of this regulator are a combination of P (proportional), I (integral), and D (derivative) actions chosen according to the type of application. For example, our prototype used it to monitor the motor's position [30].

2.4. Effective Radiation Quantity on the Solar Panel and Calculation of Solar Irradiance

To simulate solar radiation from a different angle than the photovoltaic panel, a simple program was written to obtain the practical relationship between the sun and the falling radiation. Figure 2a shows the equivalent Simulink block diagram that was used to simulate the angle between the sunlight and the photovoltaic panel based on Equation (2) [31,32]. The fixed panel is always parallel to the ground at 45° c.d. 0° for sunrise and 180° for sunset. At sunrise, the sun's angle starts at 0°, and at sunset, it is at 180 °C. To follow the change in the amount of radiation and temperature that falls on the ground during the day, we have created a model that simulates the evolution of the angle of the sun with time using the real data downloaded from the site PV system. Figure 2b represents the Simulink block diagram used.

$$Gef = G * \left(\frac{-(\theta s - \theta p) + 180}{180} \right) \quad (2)$$

where *Gef* is the effective radiation, *G* is the solar radiation, *θs* is the sun angle, and *θp* is the panel angle.



(**a**) (**b**)

Figure 2. Block diagram of (**a**) effective radiation quantity; (**b**) modeling of the sun.

3. Design and Implementation

Our prototype of the solar tracker was made by starting with schematizing its general configuration. As we explained previously, it consists of three large blocks: the electronic control block, which contains the relay module provided by the Arduino card; the mechanical movement block; and the power supply and electrical power block. In the photovoltaic panel design, it was replaced by a wooden frame of size 40 × 27 cm.

3.1. Electronic Control

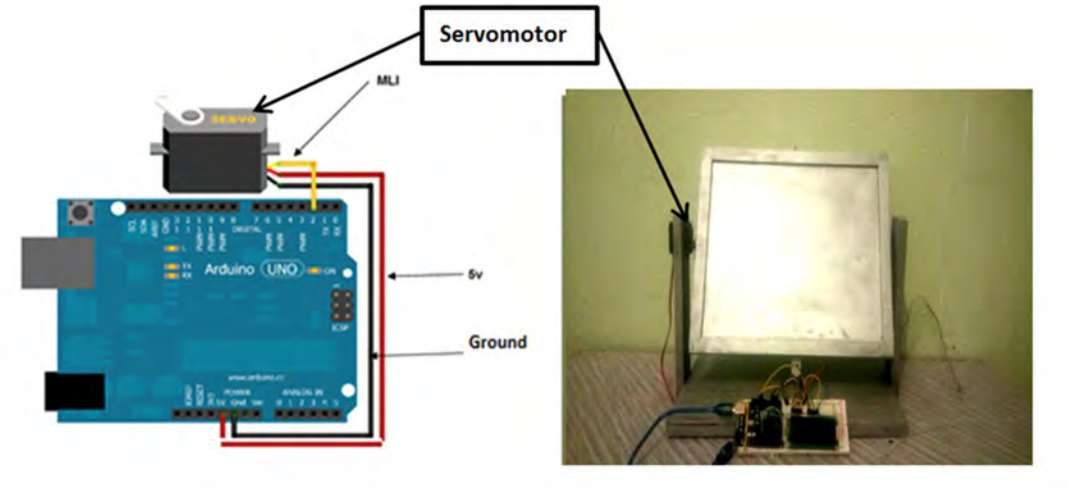
This part mainly includes components and electrical circuits to control our solar tracker system. The latter can be defined as a microprocessor-type information processing unit to which internal peripherals have been added, allowing the assembly to be

3.1. Electronic Control

This part mainly includes components and electrical circuits to control our solar tracker system. The latter can be defined as a microprocessor-type information processing unit to which internal peripherals have been added, allowing the assembly to be carried out without the need for external components [21]. An Arduino board is a brand that covers hardware-free boards on which there is a microcontroller. Their free license allowed us to program microcontrollers that exist in the different cards as we wanted to analyze and produce electrical signals that can be used for different tasks, including the control and management of electronic processes and instruments [21]. Microcontrollers have reduced performance but are small in size and consume little power. Although the Arduino card was chosen because of its open-source architecture and the ease of connecting to the computer with a simple USB cable. This cable provides both the card power supply and serial communication [33–35]. The Arduino card is programmed via a software interface in pseudo-C language. Once the program has been written, it is sent to the card, which can then operate independently (without connection to the computer). To display the numerical or textual information produced by the Arduino card, we connected it to a computer on the one hand and to a liquid crystal display (LCD) on the other hand to be able to operate autonomously away from the computer. In our prototype, we used a display compatible with the Hitachi HD44780 driver.

3.2. Servomotor

Figure 3a shows the mechanical structure of the servomotor. Therefore, Figure 3b shows how we connected the servomotor to the Arduino card. Table 1 collects the characteristic parameters of the servomotor we used in our assembly.



(**a**) (**b**)

Figure 3. (**a**) Servo motor electrical diagram; (**b**) Position of the servo motor compared with the Arduino card.

Table 1. Characteristic parameters of the servomotor used in the construction of the prototype of the single-axis tracker.

Parameters/Characteristics	Values
Weight	14.6 g
Torque	2.5 kg.cm (4.8 v) 2.8 kg.cm (6.0 v)
Operating speed	Operating: 0.11 s/60 degree (4.8 v) 0.09 s/60 degree (6.0 v)
Size	22.5 × 12.2 × 35 mm

To give us a clear idea of the hardware part, it was preferable to use the ISIS program to simulate the block diagram shown in Figure 4. The signal detected at the output of the Arduino card is visualized using the ISIS program, which is used afterward as the servo motor control signal (P.W.M.).

Parameters/Characteristics	Values
Weight	14.6 g
Torque	2.5 kg.cm (4.8 v) 2.8 kg.cm (6.0 v)
Operating speed	Operating: 0.11 sec/60 degree (4.8 v) 0.09 sec/60 degree (6.0 v)
Size	22.5 × 12.2 × 35 mm

To give us a clear idea of the hardware part, it was preferable to use the ISIS program to simulate the block diagram shown in Figure 4. The signal detected at the output of the Arduino card is visualized using the ISIS program, which is used afterward as the servo motor control signal (P.W.M.).

To give us a clear idea of the hardware part, it was preferable to use the ISIS program to simulate the block diagram shown in Figure 4. The signal detected at the output of the Arduino card is visualized using the ISIS program, which is used afterward as the servo motor control signal (P.W.M.).

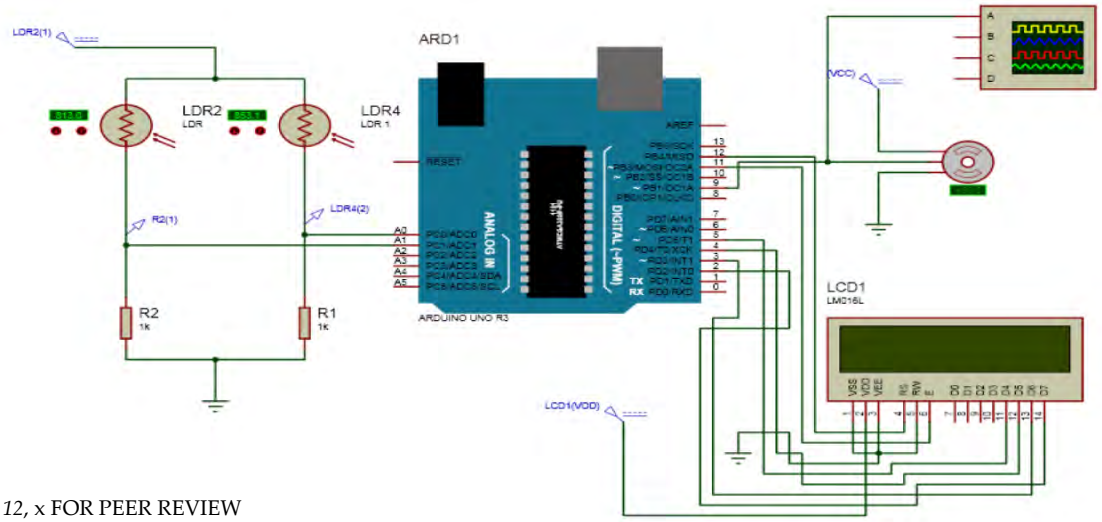


Figure 4. Block diagram used during simulation by ISIS.

Figure 4. Block diagram used during simulation by ISIS.

4. Results and Discussion

4.1. Modeling of a PV Panel

Figure 5 shows the MATLAB-SIMULINK block diagram of the PV panel [18] used in our protocol system.

Figure 5 shows the MATLAB-SIMULINK block diagram of the PV panel [18] used in our protocol system.

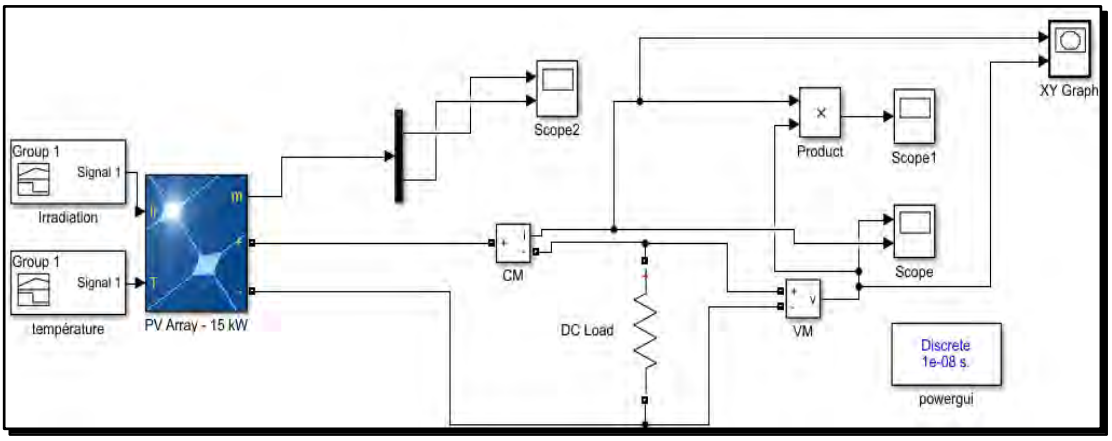


Figure 5. MATLAB-SIMULINK block diagram of a PV panel.

Figure 5. MATLAB-SIMULINK block diagram of a PV panel.

For the modeling of the PV panel block, we chose the Apollo SOLAR ENERGY ASEC-200G6S module available in the Simulink-Matlab library. This module is made up of 54 monocrystalline silicon cells with a maximum power of 200 W. Table 2 contains the parameters that characterize the module under standard conditions (level of solar radiation: G = 1000 W/m², cell temperature: 25 °C, AM = 1.5).

For the modeling of the PV panel block, we chose the Apollo SOLAR ENERGY ASEC-200G6S module available in the Simulink-Matlab library. This module is made up of 54 monocrystalline silicon cells with a maximum power of 200 W. Table 2 contains the parameters that characterize the module under standard conditions (level of solar radiation: G = 1000 W/m², cell temperature: 25 °C, AM = 1.5).

Table 2. Characteristics of the APOLLO SOLAR ENERGY ASEC-200G6S module.

Parameters/Characteristics	Values
Maximum power P_{mpp}[W]	200
Voltage of the maximum power V_{mpp}[V]	25.38
Current of the maximum power I_{mpp} [A]	7.89
Open-circuit voltage $V_{O.C.}$ [V]	33.53
Short-circuit current I_{SC}[A]	8.24
Temperature Coefficient $K_i(I_{SC})$ [%/K]	0.136

Table 2. Characteristics of the APOLLO SOLAR ENERGY ASEC-200G6S module.

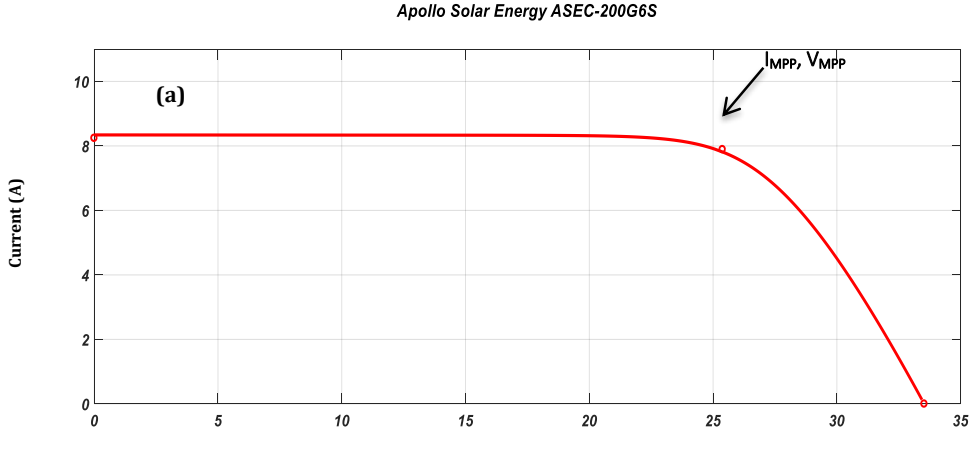
Parameters/Characteristics	Values
Maximum power P_{mpp} [W]	200
Voltage of the maximum power V_{mpp} [V]	25.38
Current of the maximum power I_{mpp} [A]	7.89
Open-circuit voltage $V_{O.C.}$ [V]	33.53
Short-circuit current I_{SC} [A]	8.24
Temperature Coefficient $K_i(I_{SC})$ [%/K]	0.136
Temperature Coefficient $K_i(V_{OC})$ [%/K]	−0.37101
Temperature Coefficient $K_i(P_{mpp})$ [%/K]	−0.47
Length x width x height [mm]	1660 × 990 × 50
Number of cells	54
Cell size [mm]	156 × 156
Cell material	Monocrystalline Si stalling

Current-voltage (I-V) curve and power-voltage curve (P-V) of the PV module (T = 25 °C, G = 1000 W/m^2):

Current-voltage curve (I-V) and power-voltage curve (P-V) of the PV module (T = 25 °C, G = 1000 W/m^2) exhibit a nonlinear relationship with the temperature and irradiance. However, on this characteristic curve (Figure 6a,b), there is a unique point where the entire system can work with maximum efficiency. This point is called the maximum power point M.P.P. It requires calculations, tracking, and control techniques to ensure the PV system is operating at this unique point to achieve the most incredible power harvest. Tracking of the maximum power point (MPPT) is a way to extract the maximum energy from the photovoltaic panels at different irradiance levels. Figure 6 shows the characteristic I-V and P-V of the PV module for a temperature T = 25 °C and a solar radiation G = 1000 W/m^2. We found the short circuit current or the maximum current at zero voltage ISC = 8.24 A and the open circuit voltage or the maximum voltage at zero current VOC = 33.53 V. This result explains the 54 cells that make up the photovoltaic panel. The power delivered by the PV panels depends on the operating point of the generator. The max point represents the maximum power delivered by the generator ($P_{MPP} = I_{MPP}*V_{MPP}$, where V_{MPP} s to the voltage to the maximum power supplied by PMPP, and the IMPP corresponds to the current to the maximum power supplied P_{MPP}).

Appl. Sci. **2022**, *12*, x FOR PEER REVIEW 11 of

1000 W/m^2. We found the short circuit current or the maximum current at zero voltag
ISC = 8.24 A and the open circuit voltage or the maximum voltage at zero current VOC
33.53 V. This result explains the 54 cells that make up the photovoltaic panel. The pow
delivered by the PV panels depends on the operating point of the generator. The ma
point represents the maximum power delivered by the generator (P_{MPP} = I_{MPP}*V_{MPP}
where, V_{MPP} s to the voltage to the maximum power supplied by PMPP, and the IMP
corresponds to the current to the maximum power supplied P_{MPP}).



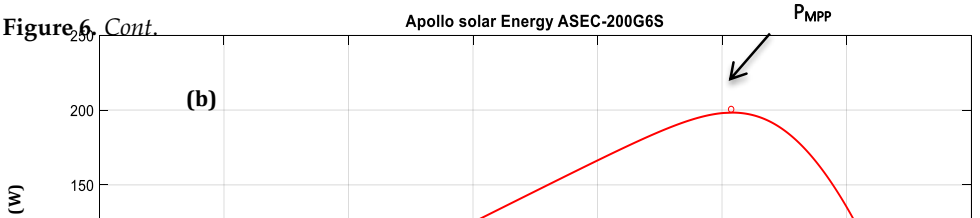


Figure 6. *Cont.*

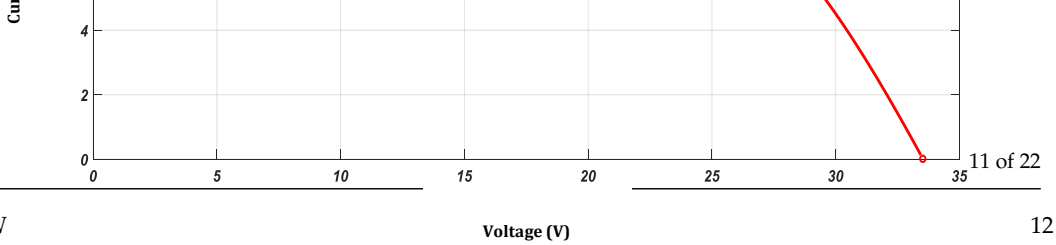


Figure 6. Characteristic curves of the PV module, (**a**) Current-voltage I-V curve, (**b**) Power-voltage curve P-V.

$$I_{SC} = I_{ph} = \alpha(T) \times G \times S \quad (3)$$

where G is the solar radiation in W/m², S is the surface of the cell in m², $\alpha(T)$ is a coefficient depending weakly on the temperature, it is expressed in A/W (in our case α = 0.136/°K). Therefore, we can conclude that the shift of the curve toward the increasing values allows the modeling of the effect of solar radiation on the operation of a PV module because of the temperature sensitivity of the electrical properties of the semiconductor. The characteristic I-V and P-V of a PV module according to the temperature under constant solar radiation (1000 W/m²) is represented in Figure 7a,b. We note that this characteristic I-V varies only slightly when the temperature varies, which means that the temperature has an effect over a long period of operation. It shows that the short-circuit current (I.S.C.) and the maximum voltage (V.O.C.) decrease slightly with the rising temperature. It is also observed that the maximum power (PMPP) of the PV module undergoes a decrease (Sch) when the temperature increases.

Influence of temperature and Irradiance on I-V and P-V characteristics:

The temperature is a very important parameter in the operation of a PV module because of the temperature sensitivity of the electrical properties of the semiconductor. The characteristic I-V and P-V of a PV module according to the temperature under constant solar radiation (1000 W/m²) is represented in Figure 7a,b. We note that this characteristic I-V varies only slightly when the temperature varies, which means that the temperature has an effect over a long period of operation. It shows that the short-circuit current (I.S.C.) and the maximum voltage (V.O.C.) decrease slightly with the rising temperature. It is also observed that the maximum power (PMPP) of the PV module undergoes a decrease (Sch) when the temperature increases.

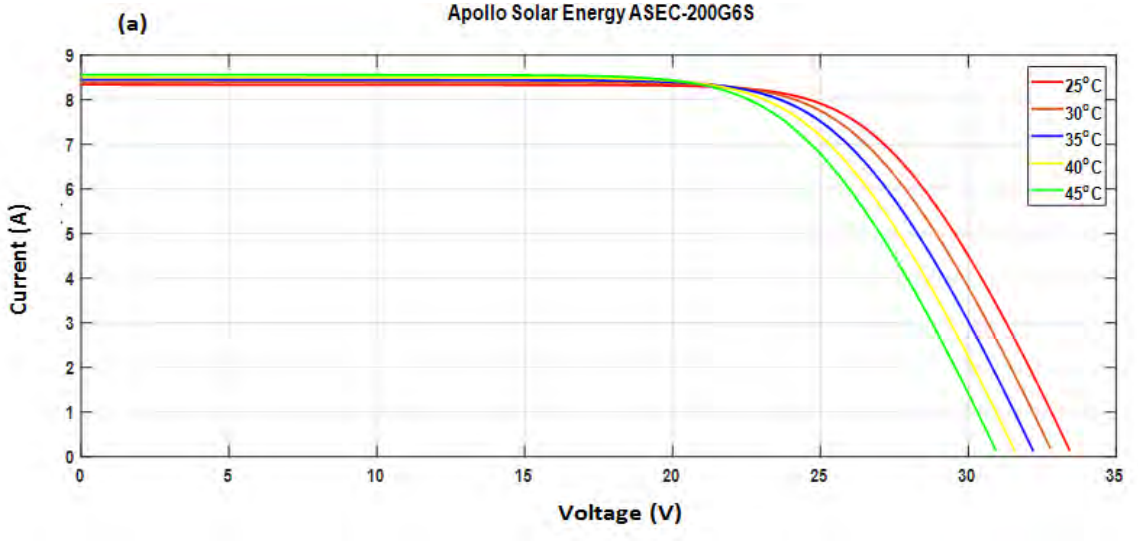


Figure 7. *Cont.*

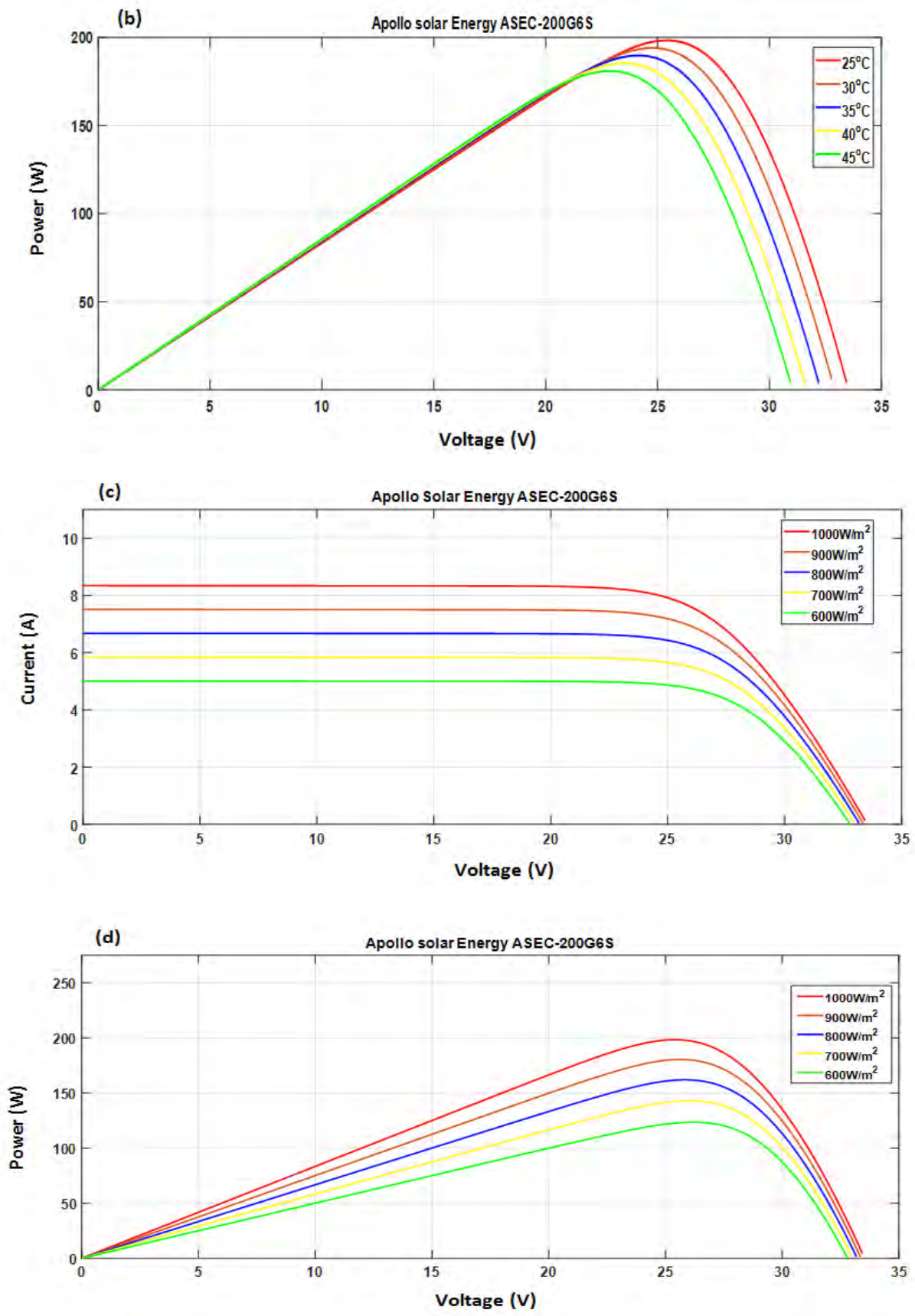


Figure 7. Influence of the variation in the temperature value on (**a**) characteristic I-V; (**b**) characteristic P-V. Influence of variation in the irradiance value on (**c**) characteristic I-V; (**d**) characteristic P-V.

Figure 7. Influence of the variation in the temperature value on (**a**) characteristic I-V; (**b**) characteristic P-V. Influence of variation in the irradiance value on (**c**) characteristic I-V; (**d**) characteristic P-V.

4.2. Command of the Servomotor for Position-Controlled by P.W.M.

The block diagram used in modeling the D.C. motor is shown in Figure 8. For our simulation, we have represented the equation system of a D.C. motor in this block dia-

Figure 7c,d shows the I-V and P-V characteristics of the PV module for different irradiance levels by fixing the temperature value at 25 °C. We noticed that the I-V characteristics undergo a change with the irradiance and that the short-circuit current (I.S.C.) was directly proportional to the incident light intensity according to Equation (3). On the other hand, the increase in illumination causes a slight increase in the open-circuit voltage (V.O.C.). We deduced that the cell could provide an almost correct voltage, even in low light. This implies that the optimal power of the cell (Pmax) is practically proportional to the illumination, and the maximum power points are at approximately the same voltage.

$$I_SC \approx I_ph = \alpha\,(T) \times G \times S \quad (3)$$

where G is the solar radiation in W/m^2, S is the surface of the cell in m^2, $\alpha(T)$ is a coefficient depending weakly on the temperature; it is expressed in A/W (in our case $\alpha = 0.136/°K$). Therefore, we can conclude that the shift of the I-V curves toward the increasing values allows the module to produce greater electrical power. This explains that solar irradiations lead to an increase in power corresponding to the maximum power points (P_{MPP}).

The influence of temperature is smaller compared to that of solar irradiance, but it is no longer negligible on the I-V characteristic of a PV module. For a change in the temperature value, we can see that the voltage variation changes much more than that of the current, which varies very slightly.

4.2. Command of the Servomotor for Position-Controlled by P.W.M.

The block diagram used in modeling the D.C. motor is shown in Figure 8. For our simulation, we have represented the equation system of a D.C. motor in this block diagram. The input parameters are the motor supply voltage (*Ua*), the motor torque (*Cr*), and the accessible output parameters are the motor current (*ia*), the motor torque (*Ce*), and the rotation speed (*Wm*) by calculating the motor angle θ through integrating of the *Wm*.

gram. The input parameters are the supply voltage (*Ua*) and the resistive torque (*Cr*). The accessible output parameters are the motor current (*ia*), the motor torque (*Ce*), and the rotation speed (*Wm*) by calculating the motor angle θ through integrating of the *Wm*.

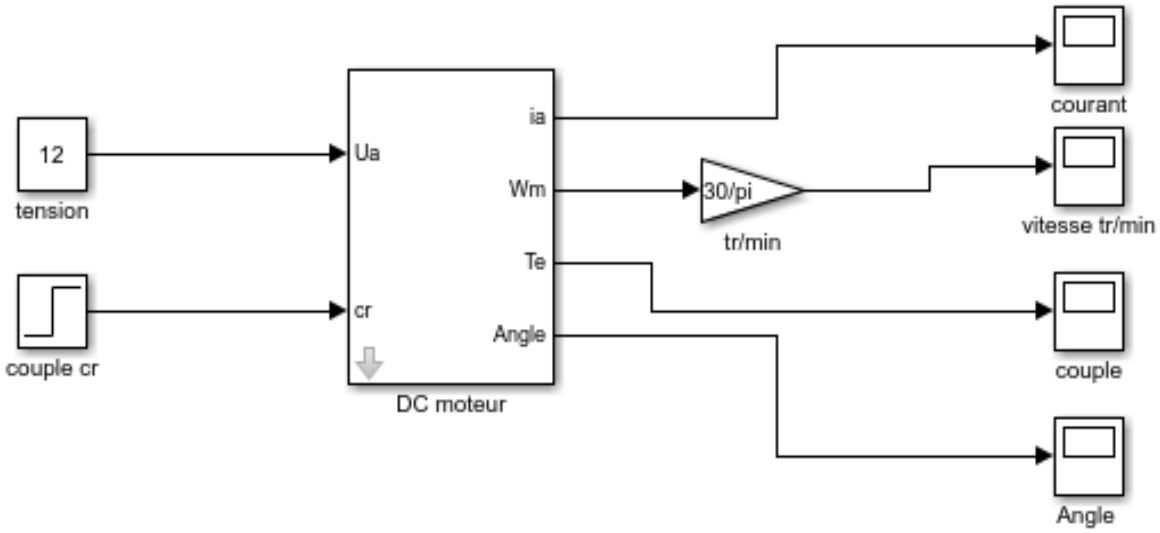
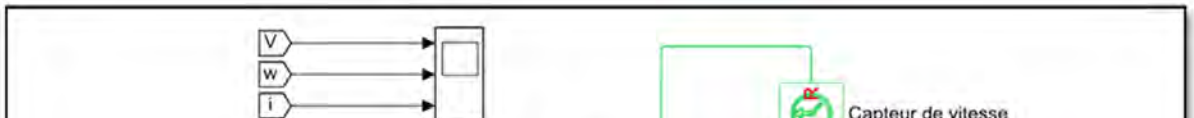


Figure 8. Simulink block model of the servomotor.

Figure 8. Simulink block model of the servomotor.

To facilitate the creation of our servo motor models in the Simulink environment, we used SimScape (physical systems simulation), which is an effective method for developing the mathematical model of the physical system by creating a multi-domain diagram based on physical connections. In addition, SimScape products allowed us to vary the system design without determining and implementing system-level equations. Figure 9 shows the block diagram we used in the SimScape simulation.

To facilitate the creation of our servo motor models in the Simulink environment, we used SimScape (physical systems simulation), which is an effective method for developing the mathematical model of the physical system by creating a multi-domain diagram based on physical connections. In addition, SimScape products allowed us to vary the system design without determining and implementing system-level equations. Figure 9 shows the block diagram we used in the SimScape simulation.



To facilitate the creation of our servo motor models in the Simulink environment, we used SimScape (physical systems simulation), which is an effective method for developing the mathematical model of the physical system by creating a multi-domain diagram based on physical connections. In addition, SimScape products allowed us to vary the system design without determining and implementing system-level equations. Figure 9 shows the block diagram we used in the SimScape simulation.

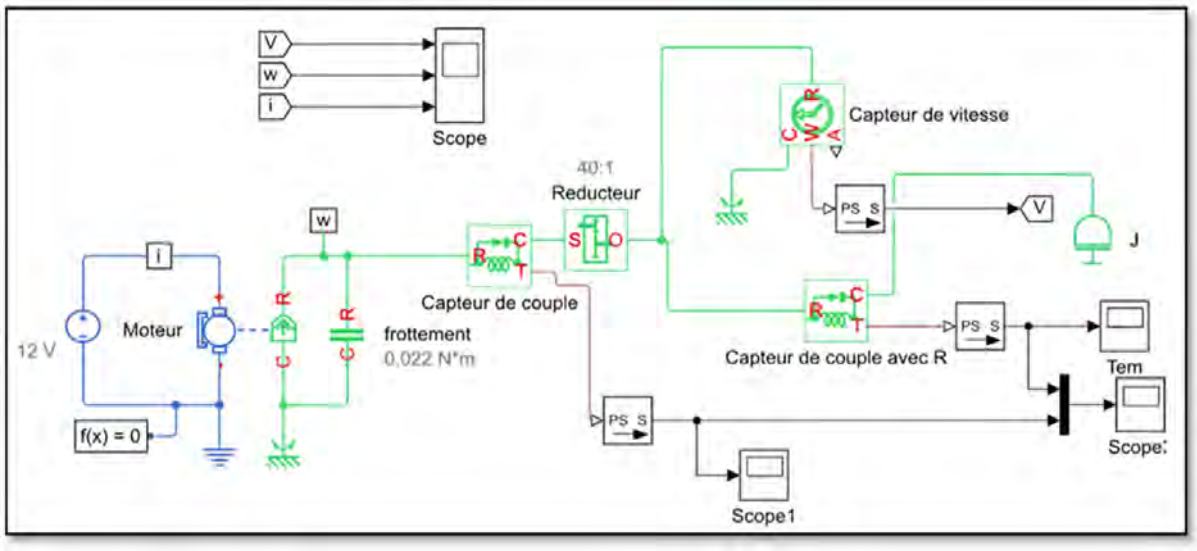


Figure 9. Block model of a voltage-fed motor using SimScape's Simulink.

Figure 9. Block model of a voltage-fed motor using SimScape's Simulink.

Figure 10 shows the simulation results of our servomotor, taking as input the set point (90°) and using the gains of the following P.I.D. controller: Kp = 100, Ki = 1, and Kd = 0 to drive the motor at the desired angle. The step response given in Figure 10 shows that the servomotor reaches its reference position at the angle of 90° for a response time that is less than 1 s. We have chosen a 12 v D.C. motor for our design. The parameters and the simulation results of this motor and the chopper, such as the temporal variation of the speed, current, and torque, the voltage at the chopper output, and the step response of a po

Figure 10 shows the simulation results of our servomotor, taking as input the set point (90°) and using the gains of the following P.I.D. controller: Kp = 100, Ki = 1, and Kd = 0 to drive the motor at the desired angle. The step response given in Figure 10 shows that the servomotor reaches its reference position at the angle of 90° for a response time that is less than 1 s. We have chosen a 12 v D.C. motor for our design. The parameters and the simulation results of this motor and the chopper, such as the temporal variation of the speed, current, and torque, the voltage at the chopper output, and the step response of a po

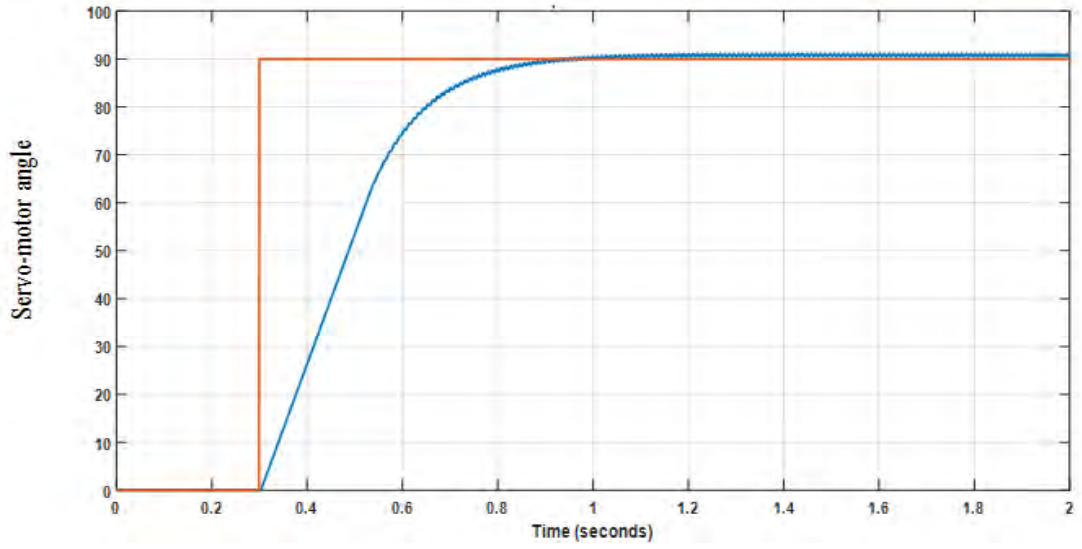


Figure 10. Step responses of a position-control servo motor.

Figure 10. Step responses of a position-control servo motor.

4.3. Simulation of the Sun

Single-axis solar tracker systems rotate on an axis to track the sun, facing east in the morning and west in the afternoon. This type of follower needs seasonal tilt angle adjustment.

Single-axis solar tracker systems rotate on an axis to track the sun, facing east in the morning and west in the afternoon. This type of follower needs seasonal tilt angle adjustment.

The meteorological parameters such as temperature and sunshine of the city of Khemis Miliana were extracted using a PV-system site in real-time and the data of the meteorological station from the university.

The meteorological parameters such as temperature and sunshine of the city of Khemis Miliana were extracted using a PV-system site in real-time and the data of the meteorological station from the university.

The temporal variation of different sun parameters like sun radiation, temperature, and sun angle θ are shown in Figures 11a,b and 12. The simulation was carried out for 16 h from 4:00 a.m. to 8:00 p.m. in May. Where the value of the irradiance used in the study area during the days of the simulation was:

The temporal variation of different sun parameters like sun radiation, temperature, and sun angle θ are shown in Figures 11a,b and 12. The simulation was carried out for 16 h from 4:00 a.m. to 8:00 p.m. in May. Where the value of the irradiance used in the study area during the days of the simulation was:

- Equal to 0 from 00:45 a.m. to 4:45 a.m. and from 8:45 p.m. to 11:45 p.m.;
- Starts increasing by 11 and 1030 from 5:45 a.m. to 13:45 p.m., then decreases from 1030 to 8 from 2:45 p.m. to 7:45 p.m.

As long as the light reappears each morning at sunrise and the temperature rises and begins to disappear at sunset, there is a variation in irradiance during the day, regardless of the season. It can be seen that the irradiance reaches its maximum value at 2:00 p.m. and decreases at sunset when it is colder than during the day. Global irradiation corresponds to the solar energy received in one day; this irradiation is linked to irradiance. It is noted that the temperature and the irradiance vary during the year gradually; they increase from winter until summer and decrease from summer until winter. This is explained by the height of the sun, which varies according to the seasons: the sun is higher at noon in a summer sky than in a winter sky.

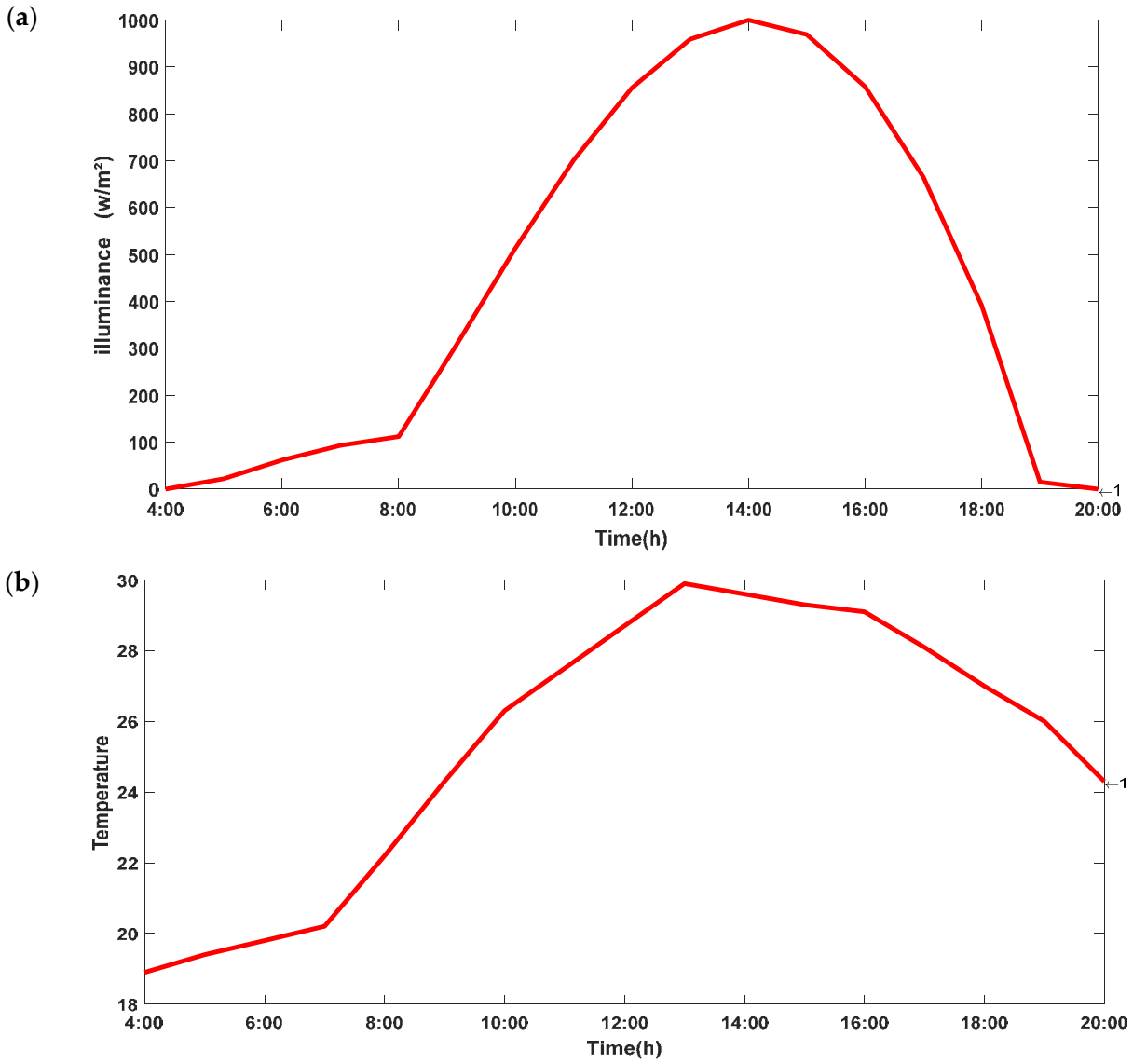


Figure 11. (a) Temporal variation of irradiance during a day; (b) Temporal variation of temperature during a day.

The position of the sun is given by the zenith angle (γs) and the azimuth (αs). The zenith angle is the angle between the local vertical and the line that connects the observer to the sun. The sun's azimuth is the deviation of the sun's position from the south. The zenith and azimuth depend on the local time of day (t), the day of the year (d), and the

The position of the sun is given by the zenith angle (γs) and the azimuth (αs). The zenith angle is the angle between the local vertical and the line that connects the observer to the sun. The sun's azimuth is the deviation of the sun's position from the south. The zenith and azimuth depend on the local time of day (t), the day of the year (d), and the latitude (λ) of the observer (h) [4]. Figure 12 shows that the sun's angle is equal to 90° almost at noon, so the tracker is perpendicular. At 180° at 8:00 p.m., the tracker is at a horizontal position and returns to its starting position.

Appl. Sci. **2022**, *12*, x FOR PEER REVIEW 17 of 23

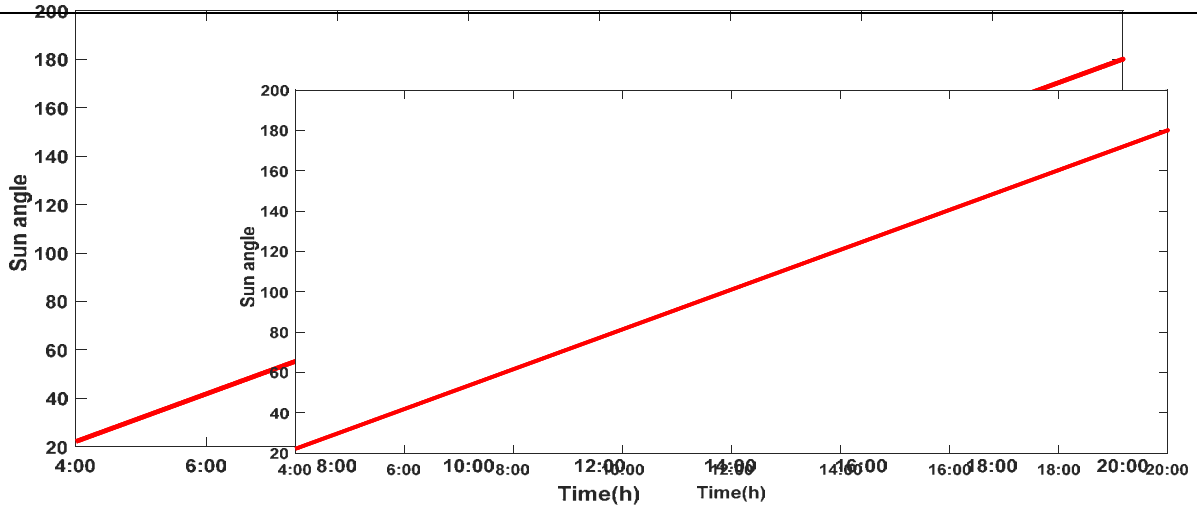


Figure 12. Temporal variation of the sun angle during a day.

Figure 12. Temporal variation of the sun angle during a day.

4.4. Tests of the Tracker

4.4. Tests of the Tracker

After receiving a quantity of light using a lamp, the prototype tracker starts tracking the solar radiation (Figure 13a). Figure 13b shows that the tracker is in the perpendicular position (90° almost at noon).

After receiving a quantity of light using a lamp, the prototype tracker starts tracking the solar radiation (Figure 13a). Figure 13b shows that the tracker is in the perpendicular position (90° almost at noon).



Figure 13. Tests of the position of the solar tracker realized to start tracking of the light. (**a**) Perpendicular position of the solar tracker. (**b**) Position of the solar tracker.

Figure 13. Tests of the position of the solar tracker realized to start tracking of the light. (**b**) Perpendicular position of the solar tracker.

To validate our results, we performed two tests on the prototype of the single-axis solar tracker: the photovoltaic module connected to the prototype of the tracker and checking if it is in its fixed position. Figure 14a,b show the variation of the motor angle (Tracker angle) with respect to the sun angle for the two tests. It can be seen that the solar tracker reaches its reference position (sun angle) in a time of response of less than a second.

To validate our results, we performed two tests on the prototype of the single-axis solar tracker: the photovoltaic module connected to the prototype of the tracker and checking if it is in its fixed position. Figure 14a,b show the variation of the motor angle (Tracker angle) with respect to the sun angle for the two tests. It can be seen that the solar tracker reaches its reference position (sun angle) in a time of response of less than a second.

To validate our results, we performed two tests on the prototype of the single-axis solar tracker: the photovoltaic module connected to the prototype of the tracker and checking if it is in its fixed position. Figure 14a,b show the variation of the motor angle (Tracker angle) with respect to the sun angle for the two tests. It can be seen that the solar tracker reaches its reference position (sun angle) in a time of response of less than a second.

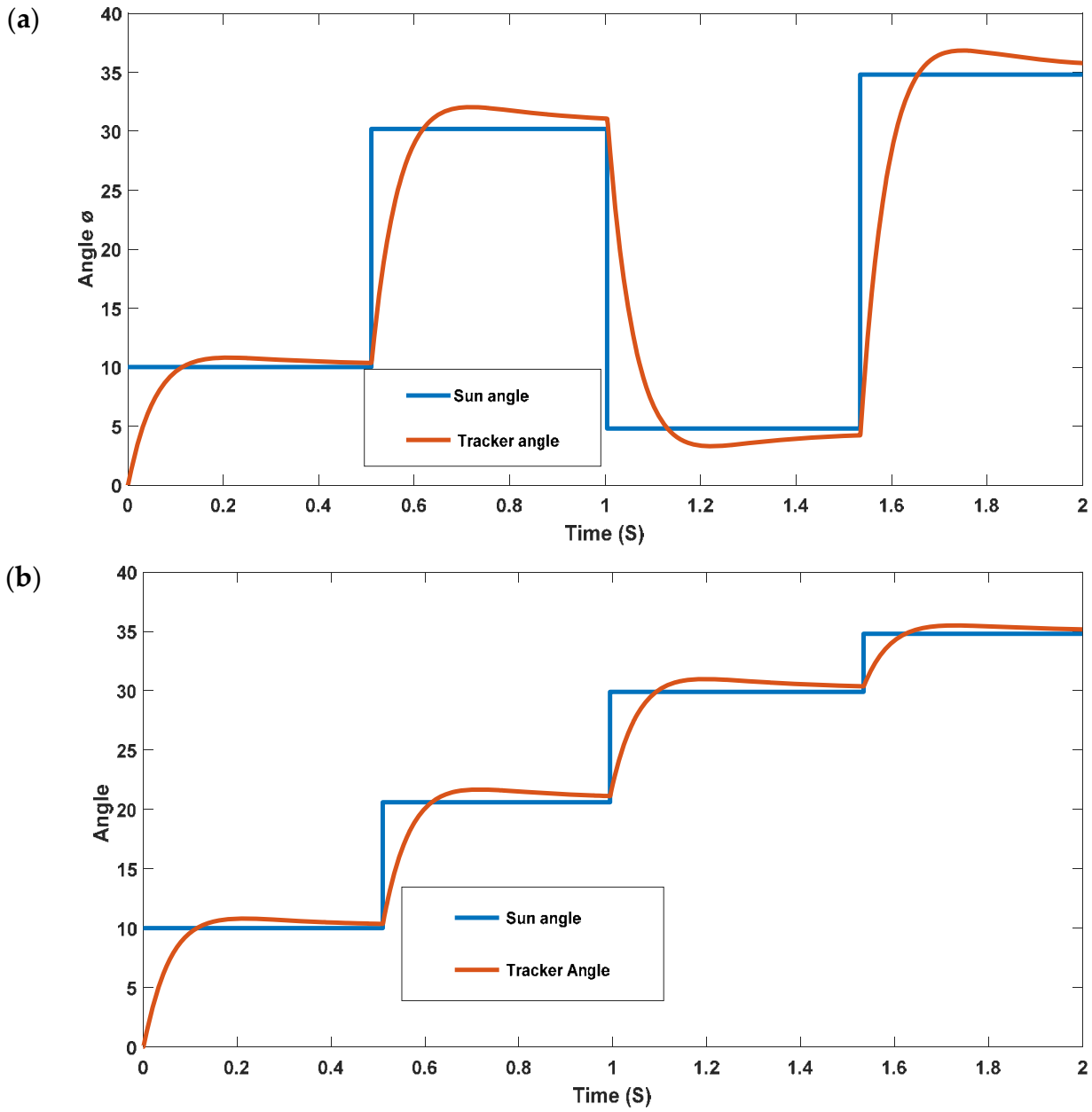


Figure 14. Variation of the motor angle with respect to the sun's angle: (**a**) for test 1; (**b**): for test 2.

Figure 14. Variation of the motor angle with respect to the sun's angle: (a) for test 1; (b): for test 2.

Several studies have analyzed the efficiency of energy production using single-axis trackers compared to fixed panels [35–38]. BAHRAMI et al. [37] determined that the increase in solar production of a PV plant with single-axis trackers compared to fixed-panel system is around 17.22–31.23% [39–41]. That fluctuation in energy production can be reduced depending on the tracker distribution in the PV plant [42–44].

To validate our design, we compared the motor angle and the sun angle over an entire day if the panel is fixed and if the panel is attached to our prototype single-axis tracker. As the sun begins to shine at 5:00 a.m., our system records data until sunset. Figure 15 shows that the solar tracker device maximizes the sun's irradiance by keeping the solar module's active surface vertical at the sun's angle. From noon until sunset, we find that the fixed panel loses a large amount of solar radiation during the day.

Several studies have analyzed the efficiency of energy production using single-axis trackers compared to fixed panels [35–38]. BAHRAMI et al. [37] determined that the increase in solar production of a PV plant with single-axis trackers compared to fixed-panel system is around 17.22–31.23% [39–41]. That fluctuation in energy production can be reduced depending on the tracker distribution in the PV plant [42–44].

To validate our design, we compared the motor angle and the sun angle over an entire day if the panel is fixed and if the panel is attached to our prototype single-axis tracker. As the sun begins to shine at 5:00 a.m., our system records data until sunset. Figure 15 shows that the solar tracker device maximizes the sun's irradiance by keeping the solar module's active surface vertical at the sun's angle. From noon until sunset, we find that the fixed panel loses a large amount of solar radiation during the day.

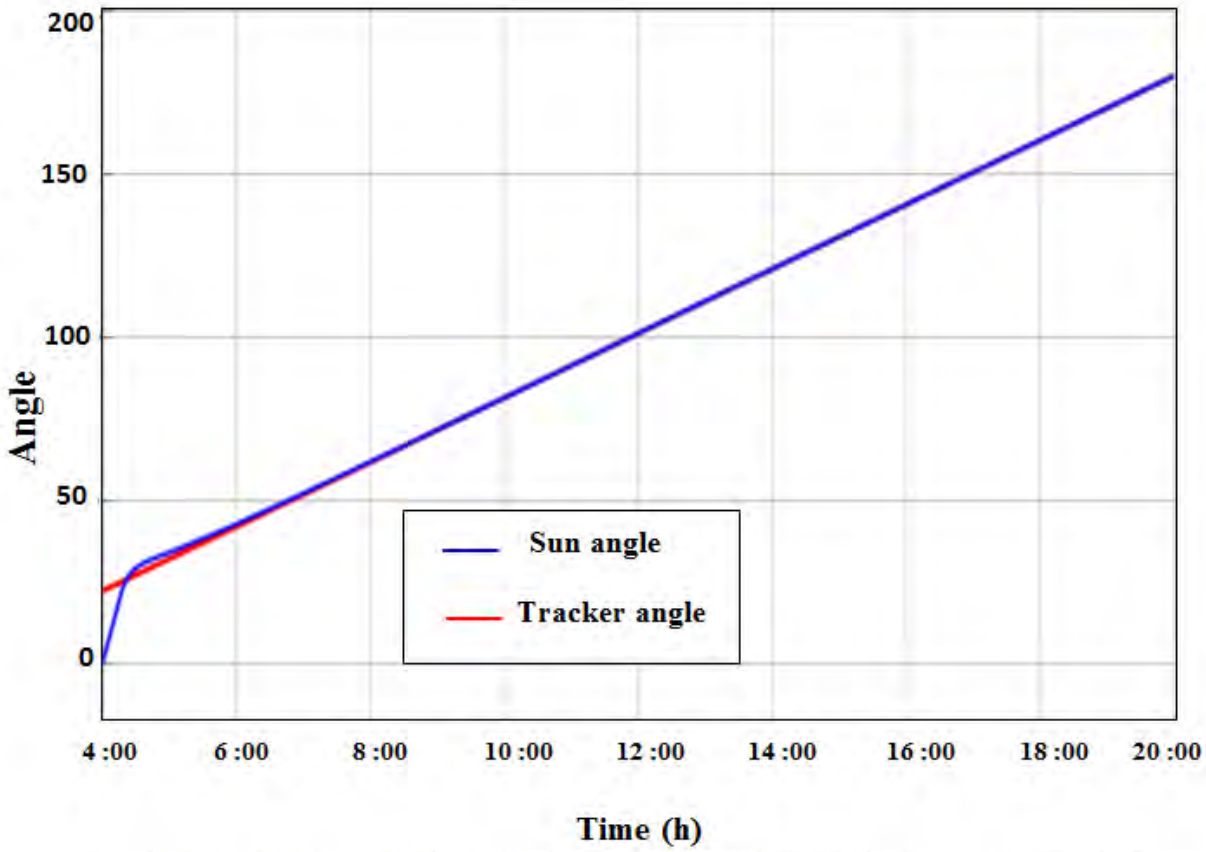


Figure 15. Comparison between sun angle and sun tracker angle.

Time (h)

Figure 15. Comparison between sun angle and sun tracker angle.

Figure 16a–d show the values variation of illuminance, voltage, current, and power of a PV module for two cases (with and without the tracker), which are compared for the period spanning from sunrise to sunset. When the curves are examined between 8:00 a.m. and 11:00 a.m., the voltage, current, and power values are a little close for the two cases. On the other hand, in the afternoon, between 12:00 p.m. and 7:00 a.m., we observed a large difference in the quantity of the voltage, current, and power produced. We concluded that a fixed panel's energy loss was recorded from noon until sunset.

Figure 16a–d show the values variation of illuminance, voltage, current, and power of a PV module for two cases (with and without the tracker), which are compared for the period spanning from sunrise to sunset. When the curves are examined between 8:00 a.m. and 11:00 a.m., the voltage, current, and power values are a little close for the two cases. On the other hand, in the afternoon, between 12:00 p.m. and 7:00 a.m., we observed a large difference in the quantity of the voltage, current, and power produced. We concluded that a fixed panel's energy loss was recorded from noon until sunset.

(**a**)

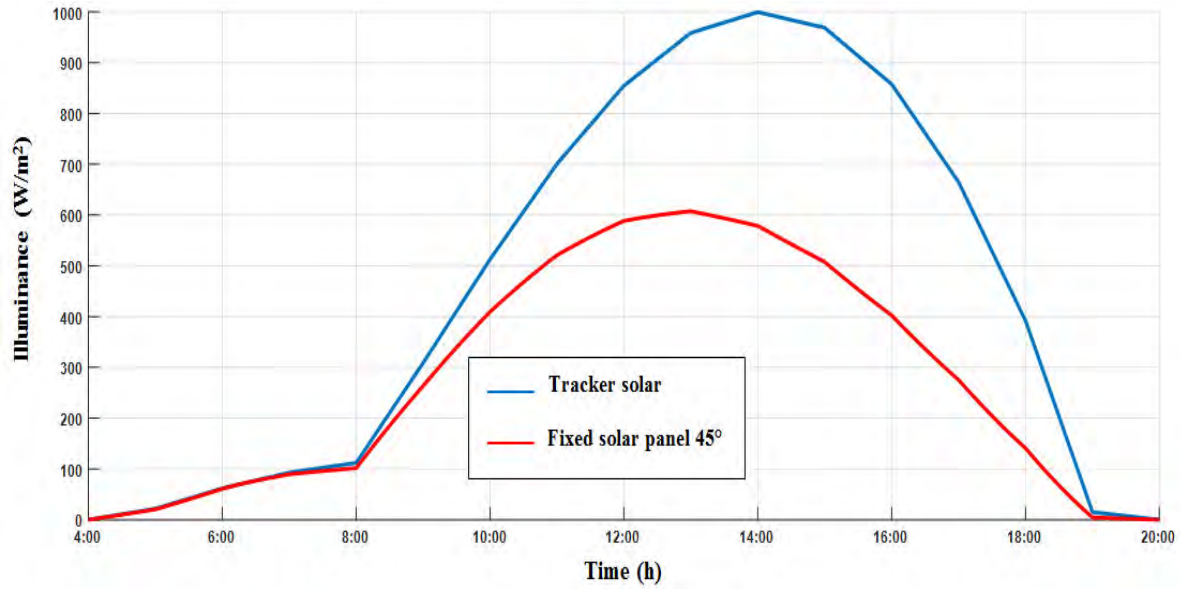


Figure 16. *Cont.*

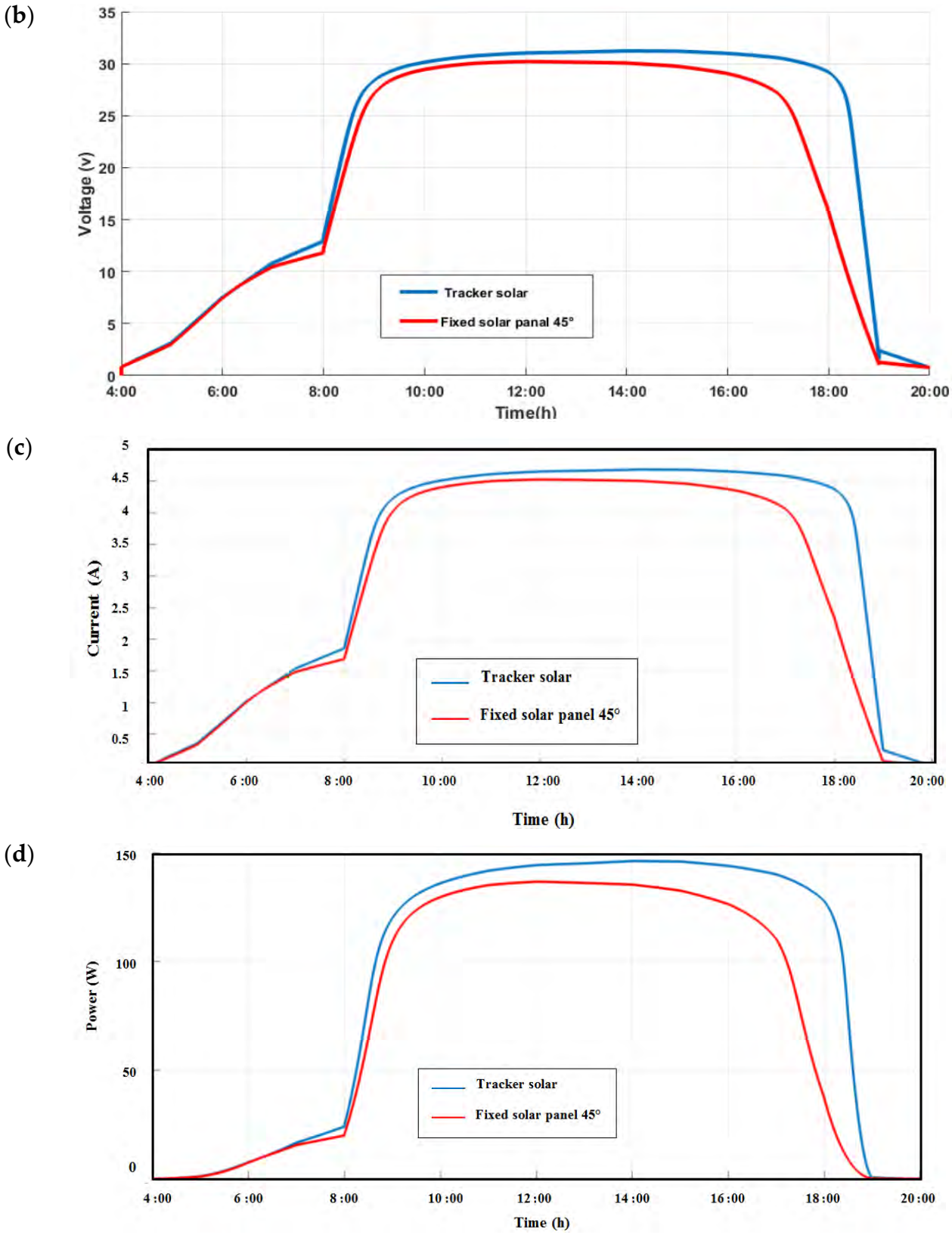


Figure 16. Values of (**a**) solar radiation, (**b**) voltage, (**c**) current, and (**d**) power produced by a PV panel bound with a solar tracker compared to a fixed PV panel.

Figure 16. Values of (a) solar radiation, (b) voltage, (c) current, and (d) power produced by a PV panel bound with a solar tracker compared to a fixed PV panel.

5. Conclusions

The question of sizing and of optimizing the efficiency of the PV solar panel is always a crucial step during their installation. Photovoltaic tracker systems represent an important area in which a significant amount of research has been carried out. However, the field itself is so vast that there is always room for innovation or improvement. This

5. Conclusions

The question of sizing and of optimizing the efficiency of the PV solar panel is always a crucial step during their installation. Photovoltaic tracker systems represent an important area in which a significant amount of research has been carried out. However, the field itself is so vast that there is always room for innovation or improvement. This has prompted us to study this field, enabling the development of PV tracking systems to increase the efficiency of PV modules and, therefore, higher electrical energy production. We have optimized the production of a photovoltaic solar system by using a solar tracker system that we designed on our own. The various elements of our solar tracker were exposed, and we noticed that the part devoted to the control and the electronic command of the maneuvers of this system was the most important. Thanks to the choice of the Arduino board, and the control program that we developed, we could design a complete prototype system by our own configuration, which showed better sensitivity in tracking the trajectory of the sun. The use of an LDR system has enabled us to find a completely autonomous solution that is easy to set up and brings an interesting energy gain, especially during the less sunny hours of the day. The test of the instantaneous energy production through the PV panel that we used showed that following the sun would benefit the future photovoltaic installations that our sun tracking system will support. We can conclude that the photovoltaic tracker systems with appropriate control systems can be considered an important factor in increasing the electrical power by 22 to 56%, compared to the fixed photovoltaic system. This research field is developing very fast; hence, many types of research are ongoing, such as artificial neural networks and fuzzy logic. These tools are used in all fields where fuzzy logic controllers are used for tracking the maximum power point in a photovoltaic system [45].

Currently, cascade control algorithms are used for high-concentration photovoltaics, capable of achieving a sun tracking error of one minute. Scientists and researchers are working on optimizing energy extraction. In doing so, an approach based on deep learning, low-cost open hardware, and computer vision has been developed to reduce the limitations regarding costs and operational issues [46]. Despite many developments, this area still faces some hurdles. Therefore, more work regarding operational efficiency, cost-effectiveness, and feasibility is required. In future perspectives, we plan to develop our tracking system using these new techniques, starting by implementing a manual mode to the automatic control system, as well as a remote access mode and control of PV production of this system.

Author Contributions: Conceptualization, F.Z.B.; Data curation, B.A. and F.Z.B.; Investigation, A.L., T.C.M. and S.V.H.; Project administration, G.S.; Resources, K.A.; Supervision, M.S.R.; Writing—original draft, F.E.Ț. and F.Z.B. All authors have read and agreed to the published version of the manuscript.

Funding: This work was supported by a grant from the Romanian Ministry of Education and Research, CCCDI-UEFISCDI, project number PN-III-P2-2.1-PED-2019-1294, within PNCDI III. 598. This paper was partially supported by the UEFISCDI Romania and MCI through BEIA projects, 599 AISTOR, FinSESco, CREATE, Hydro3D, EREMI, SOLID-B5G, NGI-UAV-AGRO, U-GARDEN and 600 by the European Union's Horizon 2020 research and innovation program under grant agreements No. 601 872172 (TESTBED2) and No. 777996 (SealedGRID). This work is supported by Ministry of Research, Innovation, Digitization from Romania by the National Plan of R & D, Project PN 19 11, Subprogram 1.1. Institutional performance-Projects to finance excellence in RDI, Contract No. 19PFE/30.12.2021 and a grant of the National Center for Hydrogen and Fuel Cells (CNHPC)—Installations and Special Objectives of National Interest (IOSIN).

Institutional Review Board Statement: Romanian Ministry of Education and Research, CCCDI-UEFISCDI, project number PN-III-P2-2.1-PED-2019-1294.

Acknowledgments: This research was partially technically supported by the research laboratory of the University of Khemis Miliana. The authors thank Meriem Saber, a researcher at the "renewable energy development center", for her help in this research.

Conflicts of Interest: The authors declare no conflict of interest.

References

1. Hua, Z.; Ma, C.; Lian, J.; Pang, X.; Yang, W. Optimal capacity allocation of multiple solar trackers and storage capacity for utility-scale photovoltaic plants considering output characteristics and complementary demand. *Appl. Energy* **2019**, *238*, 721–733. [CrossRef]
2. Gómez-Uceda, F.J.; Moreno-Garcia, I.M.; Jiménez-Martínez, J.M.; López-Luque, R.; Fernández-Ahumada, L.M. Analysis of the Influence of Terrain Orientation on the Design of PV Facilities with Single-Axis Trackers. *Appl. Sci.* **2020**, *10*, 8531. [CrossRef]
3. Chong, K.; Wong, C. General Formula for on-axis sun-tracking system and its application in improving tracking accuracy of solar collector. *Sol. Energy* **2009**, *83*, 298–305. [CrossRef]
4. Ferroudji, F. Conception et Optimisation en Dynamique Forcée D'un Nouveau Prototype de Système de Suiveur Solaire à Deux axes. Ph.D. Thesis, University of Batna, Batna, Algeria, 2015.
5. Abu-Khadera, M.; Badranb, O.; Abdallah, S. Evaluating multi-axes sun-tracking system at different modes of operation in Jordan. *Renew. Sustain. Energy Rev.* **2008**, *12*, 864–873. [CrossRef]
6. Available online: http://shodh.inflibnet.ac.in/bitstream/123456789/4251/3/03_liteature%20review.pdf (accessed on 22 August 2022).
7. Alexandru, C.; Pozna, C. Different tracking strategies for optimizing the energetic efficiency of a photovoltaic system. In Proceedings of the 2008 IEEE International Conference on Automation, Quality and Testing, Robotics, Cluj-Napoca, Romania, 22–25 May 2008; Volume 3, pp. 434–439.
8. Natarajan, S.K.; Thampi, V.; Shaw, R.; Kumar, V.S.; Nandu, R.S.; Jayan, V.; Rajagopalan, N.; Kandasamy, R.K. Experimental analysis of a two axis tracking system for solar parabolic dish collector. *Int. J. Energy Res.* **2019**, *43*, 1012–1018. [CrossRef]
9. AL-Rousan, N.; Mat Isa, N.A.; Mat Desa, M.K. Correlation analysis and MLP/CMLP for optimum variables to predict orientation and tilt angles in intelligent solar tracking systems. *Int. J. Energy Res.* **2021**, *45*, 453–477. [CrossRef]
10. Farrar-Foley, N.; Rongione, N.A.; Wu, H.; Lavine, A.S.; Hu, Y. Total solar spectrum energy converter with integrated photovoltaics, thermoelectrics, and thermal energy storage: System modeling and design. *Int. J. Energy Res.* **2021**, *46*, 5731–5744. [CrossRef]
11. El Moubarak Bouzid, A.; Mohammed, A. Dimensionnement D'un Système Photovoltaïque Pour L'alimentation D'une Ferme Étude de L'onduleur Triphasé Lié à Cette Application. Engineer Thesis, University of Oran, Es Senia, Algeria, 2008.
12. Hafez, A.Z.; Yousef, A.M.; Harag, N.M. Solar tracking systems: Technologies and trackers drive types. A review. *Renew. Sustain. Energy Rev.* **2018**, *91*, 754–782. [CrossRef]
13. Merlaud, A.; De Mazière, M.; Hermans, C.; Cornet, A. Equations for Solar Tracking. *Sensors* **2012**, *12*, 4074–4090. [CrossRef]
14. Ruelas, J.; Muñoz, F.; Lucero, B.; Palomares, J. PV Tracking Design Methodology Based on an Orientation Efficiency Chart. *Appl. Sci.* **2019**, *9*, 894. [CrossRef]
15. Visconti, P.; Costantini, P.; Orlando, C.; Lay-Ekuakille, A.; Cavalera, G. Software solution implemented on hardware system to manage and drive multiple bi-axial solar trackers by PC in photovoltaic solar plants. *Measurement* **2015**, *76*, 80–92. [CrossRef]
16. Nsengiyumva, W.; Chen, S.G.; Hu, L.; Chen, X. Recent advancements and challenges in Solar Tracking Systems (S.T.S.): A review. *Renew. Sustain. Energy Rev.* **2018**, *81*, 250–279. [CrossRef]
17. Awasthi, A.; Shukla, A.K.; Manohar S.R., M.; Dondariya, C.; Shukla, K.N.; Porwal, D.; Richhariya, G. Review on sun tracking technology in solar PV system. *Energy Rep.* **2020**, *6*, 392–405. [CrossRef]
18. Ladmi, A.; Arbaoui, K. Modélisation et Optimisation des Performances D'un Suiveur Solaire. Master's Thesis, Faculty of Sciences and Technology, University of Khemis Miliana, Khemis Miliana, Algeria, 2019.
19. Hariri, N.G.; AlMutawa, M.A.; Osman, I.S.; AlMadani, I.K.; Almahdi, A.M.; Ali, S. Experimental Investigation of Azimuth- and Sensor-Based Control Strategies for a PV Solar Tracking Application. *Appl. Sci.* **2022**, *12*, 4758. [CrossRef]
20. Alici, H.; Esenboga, B.; Oktem, I.; Demirdelen, T.; Tumay, M. Chapter 7: Designing and performance analysis of solar tracker system: A case st udy of Çukurova region. In *Design, Analysis, and Applications of Renewable Energy Systems Advances in Nonlinear Dynamics and Chaos (ANDC)*; Academic Press: New York, NY, USA, 2021; pp. 165–184.
21. Balabel, A.; Mahfouz, A.; Salem, F. Design and performance of Solar Tracking Photo-Voltaic system; Research and education. *Int. J. Control Autom. Syst.* **2013**, *1*, 49–55.
22. Etude, K.I. Conception et Réalisation d'un Suiveur de Soleil. Master's Thesis, University of Abou-Bekr Belkaid Tlemcen-Algeria, Chetouane, Algeria, 2018.
23. Chin, C.S.; Babu, A.; McBride, W. Design, modeling and testing of a standalone single axis active solar tracker using MATLAB/Simulink. *Renew. Energy* **2011**, *36*, 3075–3090. [CrossRef]
24. Mousazadeh, H.; Keyhani, A.; Javadi, A.; Mobli, H.; Abrinia, K.; Sharifi, A. A review of principle and sun-tracking methods for maximizing solar systems output. *Renew. Sustain. Energy Rev.* **2009**, *13*, 1800–1818. [CrossRef]
25. Afarulrazi, B.A.; Utomo, W.M.; Liew, K.L.; Zarafi, M. Solar tracker robot using microcontroller. In Proceedings of the 2011 International Conference on Business, Engineering and Industrial Applications, Kuala Lumpur, Malaysia, 5–7 June 2011; pp. 47–50.
26. Nuwayhid, R.Y.; Mrad, F.; Abu-Said, R. The realization of a simple solar tracking concentrator for university research applications. *Renew. Energy* **2001**, *24*, 207–222. [CrossRef]
27. Le Moteur à Courant Continu: Principe, Astuces-Pratiques. 2015. Available online: https://www.astuces-pratiques.fr/electronique/le-moteur-a-courant-continu-principe (accessed on 22 August 2022).

28. Eric, G. Le Servomoteur. 2011. Available online: http://ericaeromodelisme974.unblog.fr/2011/06/04/le-servomoteur (accessed on 22 August 2022).
29. Rabeh, M.B.; Ayoub, D. Conception et Réalisation d'un Suiveur Solaire Bi-axial à Bas De capteurs de lumière. Master's Thesis, University of Kasdi Merbah Ouargla, Ouargla, Algeria, 2016.
30. Electrical Guide 360. *D.C. Chopper or DC-to-DC Converter: Working & Its Function*; Power Electronics: Valencia, Spain, 2021.
31. Solar Angles & Tracking Systems. Photovoltaic Efficiency: Lesson 1, Fundamentals Article; Free STEM Curriculum for K-12. Available online: https://www.TeachEngineering.org (accessed on 22 August 2022).
32. Telidjane, M. Modélisation des Panneaux Photovoltaïques et Adaptation de la Cyclostationarité pour le Diagnostic. Ph.D. Thesis, University of Lyon, Lyon, France, 13 July 2017.
33. Marwan; Anshar, M. Controller Design for Solar Tracking System. In Proceedings of the International Conferences on Information System and Technology (CONRIST 2019), Yogyakarta, Indonesia, 5–6 December 2019; pp. 72–77. [CrossRef]
34. Engr, F. *How to Make a Solar Tracker Using Arduino, Arduino Solar Tracker System Its Circuit and Programming*; Electronic Clinic: Wan Chai, Hong Kong, 2019.
35. Aqib, M. Sun Tracking Solar Panel Using Arduino. Microcontroller-Projects. 2017. Available online: https://Circuitdigest.com (accessed on 22 August 2022).
36. Necir, A.; Bouchaala, A.D.J. Conception et Réalisation d'un Suiveur du Soleil Commandé par une Carte Arduino. Master's Thesis, University of El-Oued, El Oued, Algeria, 2018.
37. Koussa, M.; Cheknane, A.; Hadji, S.; Haddadi, M.; Noureddine, S. Measured and modelled improvement in solar energy yield from flat plate photovoltaic systems utilizing different tracking systems and under a range of environmental conditions. *Appl. Energy* **2011**, *88*, 1756–1771. [CrossRef]
38. Bahrami, A.; Okoye, C.O.; Atikol, U. The effect of latitude on the performance of di erent solar trackers in Europe and Africa. *Appl. Energy* **2016**, *177*, 896–906. [CrossRef]
39. Abdallah, S.; Nijmeh, S. Two axes sun tracking system with PLC control. *Energy Convers. Manag.* **2004**, *45*, 1931–1939. [CrossRef]
40. Antonanzas, J.; Urraca, R.; Martinez-de-Pison, F.J.; Antonanzas, F. Optimal solar tracking strategy to increase irradiance in the plane of array under cloudy conditions: A study across Europe. *Sol. Energy* **2018**, *163*, 122–130. [CrossRef]
41. Batayneh, W.; Bataineh, A.; Soliman, I.; Hafees, S. Investigation of a single-axis discrete solar tracking system for reduced actuations and maximum energy collection. *Autom. Constr.* **2019**, *98*, 102–109. [CrossRef]
42. Manoel Henriques de Sa, C.; Chigueru, T. npTrack: A n-Position Single Axis Solar Tracker Model for Optimized Energy Collection. *Energies* **2021**, *14*, 925.
43. Seme, S.; Stumberger, B.; Hadziselimovic, M.; Sredensek, K. Solar Photovoltaic Tracking Systems for Electricity Generation: A Review. *Energies* **2020**, *13*, 4224. [CrossRef]
44. Kuttybay, N.; Saymbetov, A.; Mekhilef, S.; Nurgaliyev, M.; Tukymbekov, D.; Dosymbetova, G.; Meiirkhanov, A.; Svanbayev, Y. Optimized Single-Axis Schedule Solar Tracker in Different Weather Conditions. *Energies* **2020**, *13*, 5226. [CrossRef]
45. Farajdadian, S.; Hosseini, S.M.H. Conception d'un contrôleur flou optimal pour obtenir une puissance maximale dans un système de production d'énergie solaire. *Solar Energy* **2019**, *182*, 161–178. [CrossRef]
46. Onyeka Okoye, C.; Bahrami, A.; Atikol, U. Evaluating the solar resource potential on different tracking surfaces in Nigeria. *Renew. Sustain. Energy Rev.* **2018**, *81 Pt 1*, 1569–1581. [CrossRef]

applied sciences

MDPI

Article

Numerical and Parametric Analysis for Enhancing Performances of Water Photovoltaic/Thermal System

Chaimae El Fouas [1], Nelu Cristian Chereches [2,*], Sebastian Valeriu Hudisteanu [2,*], Bekkay Hajji [1], Emilian Florin Țurcanu [2,*] and Monica Lilioara Chereches [3]

[1] Laboratory of Renewable Energy, Embedded System and Information Processing, National School of Applied Sciences, Mohammed First University, Oujda 60000, Morocco; c.elfouas@ump.ac.ma (C.E.F.); hajji.bekkay@gmail.com (B.H.)
[2] Department of Building Services, "Gheorghe Asachi" Technical University of Iași, 700050 Iași, Romania
[3] National Institute for Research and Development in Construction, Urban Planning and Sustainable Spatial Development, NR&DI URBAN-INCERC Iasi Branch, 700048 Iasi, Romania; monicachereches@gmail.com
* Correspondence: chereches@tuiasi.ro (N.C.C.); sebastian.hudisteanu@tuiasi.ro (S.V.H.); emilian-florin.turcanu@tuiasi.ro (E.F.Ț.)

Abstract: Photovoltaic/thermal (PV/T) systems are innovative cogeneration systems that ensure the cooling of photovoltaic (PV) backside and simultaneous production of electricity and heat. However, an effective cooling of the PV back is still a challenge that affects electrical and thermal performance of the PV/T system. In the present work, a PV/T numerical model is developed to simulate the heat flux based on energy balance implemented in MATLAB software. The numerical model is validated through the comparison of the three-layer PV model with the NOCT model and tested under the operation conditions of continental temperate climate. Moreover, the effect of velocity and water film thickness as important flow parameters on heat exchange and PV/T production is numerically investigated. Results revealed that the PV model is in good agreement with the NOCT one. An efficient heat transfer is obtained while increasing the velocity and water film thickness with optimal values of 0.035 m/s and 7 mm, respectively, at an inlet temperature of 20 °C. The PV/T system ensures a maximum thermal power of 1334.5 W and electrical power of 316.56 W (258.8 W for the PV). Finally, the comparison between the PV and PV/T system under real weather conditions showed the advantage of using the PV/T.

Keywords: photovoltaic thermal system; water cooling; solar energy; numerical model; electrical efficiency; thermal efficiency

check for updates

Citation: El Fouas, C.; Chereches, N.C.; Hudișteanu, S.V.; Hajji, B.; Țurcanu, E.F.; Chereches, M.L. Numerical and Parametric Analysis for Enhancing Performances of Water Photovoltaic/Thermal System. *Appl. Sci.* **2022**, *12*, 646. https://doi.org/10.3390/app12020646

Academic Editors: Ilinca Nastase and Florin Ioan Bode

Received: 16 November 2021
Accepted: 4 January 2022
Published: 10 January 2022

Publisher's Note: MDPI stays neutral with regard to jurisdictional claims in published maps and institutional affiliations.

Copyright: © 2022 by the authors. Licensee MDPI, Basel, Switzerland. This article is an open access article distributed under the terms and conditions of the Creative Commons Attribution (CC BY) license (https://creativecommons.org/licenses/by/4.0/).

1. Introduction

Increasing energy demand for industrial and domestic purposes has led to greater interest in renewable energy as a substitute for fossil fuels. Sun radiation is the primary source of all types of renewable energy sources. Photovoltaic (PV) technology is one of the common methods of direct converting the solar radiation into electricity [1]. Instead, the performance of PV panels falls by 0.5% for every degree rise in temperature, depending on the type of solar cells used [2]. Since the PV temperatures can reach as high as 80 °C in the summer, it is necessary to find efficient cooling methods to achieve higher heat dissipation rates from PV modules and increase his electrical efficiency and longevity.

An efficient version of the PV module is the photovoltaic–thermal (PV/T) module which uses cooling systems to remove the excess thermal energy. The commercially available technologies are classified into passive and active cooling systems [3]. Active cooling systems use forced circulation of air [4–6], water [7–10], or nanofluids [11] while the passive ones use natural circulation of working fluids in which no external source of power is needed as well as heat pipes [12] or phase change materials (PCMs) to naturally

transport heat through a boiling–condensing process to the ambient air [13]. Some recent related review articles also provide updates on the important aspects of PV/T cooling systems [14–18].

Water cooling methods provide improved performance over air cooling methods due to the increase in heat-carrying capacity of water over air [19]. Nahar et al. [20] studied the performance of a PV/T module with parallel plate flow channel without absorber plate both numerically and experimentally at outdoor conditions. They observed that the overall efficiency increases numerically by 22.1% and experimentally by 20% with an increase in water inlet velocity from 0.0003 to 0.0007 m/s under an irradiation level of 1000 W/m^2 and inlet water temperature of 34 °C.

A novel compound system through connecting a PV/T system with a solar collector in series was proposed by Kazemian et al. [21]. The results showed that using the optimum condition given by Taguchi-based gray relational optimization, electrical, thermal and total power generation of the system increased by 23.86%, 35.78%, and 34.75%, respectively.

A hybrid photovoltaic/thermal (PV/T) collector with serpentine exchanger was studied by Boumaarafa et al. [22] showing that combining both types of heat and electrical offers a better thermal performance with an overall thermal efficiency around 79.43%.

Different parameters for enhancing heat transfer performance of photovoltaic thermal systems was investigated by Nahar et al. [23]. Results revealed that PV/T electrical and thermal efficiency increase with both Reynolds and Prandtl number and a maximum reduction in cell temperature of 10.2 °C was achieved for increasing channel depth from 10 to 20 mm.

Even with the large number of papers related to the PV/T system, there is little research work that treats enhancement of flow parameters, e.g., the inlet velocity and water film thickness simultaneously for an effective cooling of PV cells. This paper presents a transient numerical PV/T model based on an energy balance equation developed in MATLAB software and resolved by the Runge–Kutta numerical method. This model is built based on the three layers PV model validated with the NOCT model. Moreover, the energy balance equations for the cooling unit (absorber 1, fluid, absorber 2) are driven from a PV/T model validated experimentally in previous work [24]. Thus, based on the developed model, a parametric study was conducted to determine the optimal flow parameters.

2. Methodology

2.1. Numerical Model

A numerical model was developed to evaluate the thermal and electrical behavior of a PV/T system, operating in dynamic conditions. The parametric analysis was performed by varying some PV/T key flow parameters, such as the water velocity from 0.01 m/s to 0.035 m/s, water film thickness from 3 mm to 10 mm, and water inlet temperature from 20 °C to 30 °C.

The PV/T system investigated in this work consists mainly of four solid components and cooling liquid (water). According to the PV/T system design shown in cross section in Figure 1a, six sub-numerical models were established as follows:

- Sub-numerical model for the glass cover;
- Sub-numerical model for the PV module;
- Sub-numerical model for the Tedlar layer;
- Sub-numerical model for the upper aluminum layer;
- Sub-numerical model for the water film in channel;
- Sub-numerical model for the lower aluminum layer.

For the six PV/T system sub-models, a heat balance equation was done separately, based on the internal energy variation equation [25] and the heat transfer between layers as shown in Figure 1b. Moreover, the Runge–Kutta numerical method (RK4) was used for resolving the (ODE) governing equations in MATLAB Software. The main advantage of the developed numerical model is allowing the determination of the mean temperature of

- The amount of absorbed solar irradiation that is not converted into electri transferred from the PV cells back to the rest of system;
- The material properties remain constant in the PV/T system, for a tempe limited range;
- The heat flux between PV cells and EVA is supposed to be negligible;
- A perfect contact between PV/T components is supposed;
- The effects of dust and partial shading were neglected.

each PV/T layer (glass cover, PV cells, Tedlar, absorbers, and fluid), based on the different heat exchanges between these ones.

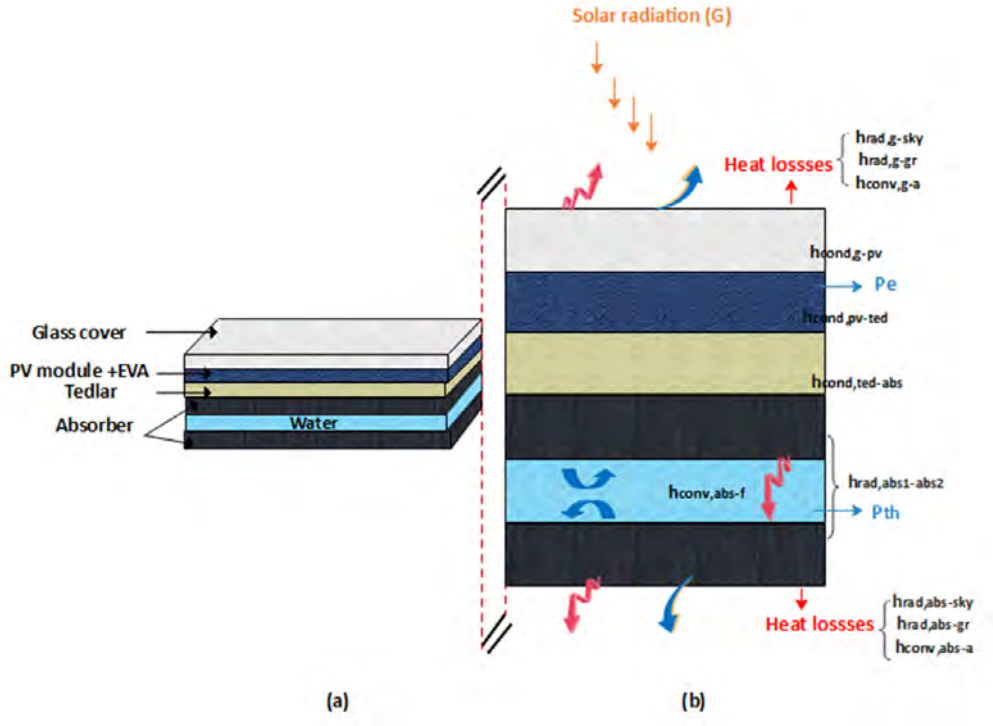


Figure 1. Components (**a**) and heat exchange mechanism in the PV/T system (**b**).

The main PV technical characteristics (applied to Standard Test Conditions of solar irradiance of 1000 W/m² and ambient temperature of 25 °C) and the selected PV/T system properties are reported in Tables 1 and 2. Moreover, the assumptions considered in developing the PV/T model due to its different components were [22,23,26]:

- A (1D) numerical model is built since the layers' thickness are very thin relative to the other dimensions. As a result, heat losses are considered to be neglected at the PV/T sides and average uniform temperature is determined for each layer;
- The amount of absorbed solar irradiation that is not converted into electricity is transferred from the PV cells back to the rest of system;
- The material properties remain constant in the PV/T system, for a temperature limited range;
- The heat flux between PV cells and EVA is supposed to be negligible;
- A perfect contact between PV/T components is supposed;
- The effects of dust and partial shading were neglected.

Table 1. PV module technical characteristics applied to STC.

PV Type	Pmax (W)	Vmp (V)	Imp (A)	Voc (V)	Isc (A)	η_e (%)	NOCT (°C)
AE320HM-60 Mono-crystalline	320	33.40	9.59	40.90	10.15	19.30	45 ± 2

Table 2. PV/T investigated parameters.

Dimensions	1665 × 996 (mm × mm)				
Properties	**Glazing**	**PV Cells**	**Tedlar**	**Alumi Abso**	
Density (kg/m³)	2300	2330	1500	270	
Thermal conductivity (W/m·K)	1.0	168.0	0.2	16	

Table 2. PV/T investigated parameters.

Dimensions	1665 × 996 (mm × mm)			
Properties	**Glazing**	**PV Cells**	**Tedlar**	**Aluminum Absorber**
Density (kg/m^3)	2300	2330	1500	2700
Thermal conductivity (W/m·K)	1.0	168.0	0.2	160
Specific heat (kJ/kgK)	500	757	1200	900
Thickness (m)	0.003	0.00035	0.0015	0.003

2.2. Heat Balance Governing Equations

In the present work, a PV/T transient model was conducted based on a heat balance established for solid and fluid domains. In all solid components (glass, PV module, Tedlar, aluminum absorbers), the heat exchange process occurs by conduction mechanism, while in the flow duct, the thermal transfer to fluid (water) is through the convection mode. For each PV/T layer, the energy balance equation is a function of the layer internal energy variation taking into account some external parameters, e.g., the solar irradiance, ambient temperature, wind speed, and mass flow rate. Thus, the energy governing equations for solid and fluid layers were obtained considering the selected thermo-physical proprieties summarized in Table 2.

2.2.1. Solid Layers

The heat flux for the PV/T solid layers can be obtained using Equation (1). It is a function of the density ρ_S, specific heat capacity $c_{p,S}$ and the thickness δ_s of the selected layer as well the thermal heat exchange coefficient h_s:

$$\rho_S \, \delta_s c_{p,s} \, \frac{\mathrm{dT_s}}{\mathrm{dt}} = \Sigma \, h_s \, \Delta \mathrm{T_s} + \alpha \, E_{sun} - \vartheta E_e \tag{1}$$

where $\Delta \mathrm{T_s}$ is the temperature gradient and E_{sun} is the absorbed solar irradiance for each solid layer. In fact, a significant part of the incident solar irradiance is absorbed by the PV cells and converted to electrical energy E_e while the remainder is lost with environment. Thus, the absorption and electricity production terms for PV cell are $\alpha \neq 0$; $\vartheta = 1$ and for the other solid layers are $\alpha = 0$; $\vartheta = 0$.

The expression of heat exchange coefficient h_s is directly dependent on the heat transfer mechanisms between layers. In case of solid layers *i,j* where heat is transferred by conduction, h_s is given by:

$$h_s = hc_{i,j} = \frac{1}{\left(\frac{\delta_i}{\lambda_i} + \frac{\delta_j}{\lambda_j}\right) A_{i,j}} \tag{2}$$

where: λ_i and δ_i are the thermal conductivity and thickness of the layer *i*; λ_j and δ_j are the thermal conductivity and thickness of the layer *j* and $A_{i,j}$ is the exchange area between the layers *i,j*.

For the front of the PV/T system, three expressions of the heat exchange coefficient h_{s1}, h_{s2}, and h_{s3} are used, due to the heats transfer by radiation between the glass-sky, glass-ground and by convection between the glass-ambient:

$$h_{s1} = hr_{g,sky} = \sigma \varepsilon_g F_{g,sky} \, A\left(T_{sky} + T_g\right) \cdot \left(T_{sky}^2 + T_g^2\right) \tag{3}$$

$$h_{s2} = hr_{g,\mathrm{gr}} = \sigma \varepsilon_g F_{g,gr} \, A\left(T_{gr} + T_g\right) \cdot \left(T_{gr}^2 + T_g^2\right) \tag{4}$$

$$h_{s3} = hv_{g,a} = \left(hv_{forced}{}^3 + hv_{free}{}^3\right)^{1/3} \tag{5}$$

where ε_g, is the glass emissivity; $F_{g,sky}$ and $F_{g,gr}$ are the view factors [24].

The glass-ambient heat transfer coefficient h_{s3} is determined as the sum of the forced and natural convective heat transfer coefficients hv_{forced} and hv_{free}. If $Gr/Re^2 << 1$, the forced convection regime has been evaluated. Thus, the following correlation [27] based on the wind speed velocity w is used:

$$hv_{forced} = 2.8w + 3 \tag{6}$$

Otherwise, for $Gr/Re^2 >> 1$, the correlation of Bejan et al. [28] depending on the air thermal conductivity λa and Nusselt number Nu_{free} is adopted:

$$hv_{free} = \frac{Nu_{free}\ \lambda a}{L} \tag{7}$$

$$Nu_{free} = 0.14\left[(Gr\ Pr)^{\frac{1}{3}} - (Gr_{cr}\ Pr)^{\frac{1}{3}}\right] + 0.56(Gr_{cr} Pr \cos\theta) \tag{8}$$

At the back side of the PV/T system, the heat losses by radiation between the absorber-sky, absorber -ground, and by convection between the absorber–ambient were considered. Moreover, three heat exchange coefficients h_{s1}, h_{s2}, and h_{s3} can be expressed as follows:

$$h_{s1} = hr_{absl,sky} = \sigma\varepsilon_{absl}F_{sky,absl}\ A\left(T_{sky} + T_{absl}\right)\cdot\left(T_{sky}^2 + T_{absl}^2\right) \tag{9}$$

$$h_{s2} = hr_{absl,gr}\ \sigma\varepsilon_{absl}F_{absl,gr}\ \ A\left(T_{gr} + T_g\right)\cdot\left(T_{gr}^2 + T_g^2\right) \tag{10}$$

$$h_{s3} = hv_{a,absl} \tag{11}$$

where ε_{absl}, is heat transfer between the absorber and the ambient.

The heat exchange coefficient $h_{s3} = hv_{absl,a}$ could be calculated as function of the forced or the free convection regime using the following correlations considered in [29].

In case of forced convection:

$$hv_{absl,a} = 5.7\ w \tag{12}$$

While in free convection is determined by:

$$hv_{absl,a} = \frac{Nu_{free}\ \lambda a}{L} \tag{13}$$

$$Nu_{free} = \left\{0.825 + \frac{0.387Ra^{1/6}}{\left[1 + \left(\frac{0.492}{Pr}\right)^{9/16}\right]^{8/27}}\right\}^2 \tag{14}$$

For the duct formed by the two aluminum plates, the heat exchange coefficient h_s is due to the radiation mechanism as expressed in [30].

Table 3 shows the set of governing equations introduced in the numerical model for the solid PV/T layers.

Table 3. Governing equations for the PV/T solid layers.

Layers	Equations	
Glass	$\left(\rho_g \delta_g C_g\right) \frac{dT_g}{dt} = \alpha_g E_{sun} + hr_{g,sky}\left(T_{sky} - T_g\right) + hr_{g,gr}\left(T_{gr} - T_g\right) + hv_{g,a}\left(T_a - T_g\right) + hc_{PV,g} PF\left(T_{PV} - T_g\right) + hc_{Ted,g}(1 - PF)\left(T_{Ted} - T_g\right)$	(15)
PV cells	$PF(\rho_{PV}\delta_{PV}C_{PV})\frac{dT_{PV}}{dt} = \left[\left(\tau_g \alpha_{PV} - \eta_e\right) E_{sun} + hc_{PV,g}\left(T_g - T_{PV}\right) + hc_{Ted,PV}\left(T_{Ted} - T_{PV}\right)\right] PF$	(16)
Tedlar	$(\rho_{Ted}\delta_{Ted}C_{Ted})\frac{dT_{Ted}}{dt} = (1 - PF)\tau_g \alpha_{Ted} + (1 - PF) hc_{Ted,g}\left(T_g - T_{Ted}\right) + PF \cdot hc_{Ted,PV}\left(T_{PV} - T_{Ted}\right) + hc_{abs1,Ted}\left(T_{abs1} - T_{Ted}\right)$	(17)
Absorber 1	$(\rho_{abs}\ \delta_{abs}\ C_{abs})\frac{dT_{abs1}}{dt} = hc_{abs1,Ted}\left(T_{Ted} - T_{absh}\right) + hr_{abs1,abs2}\left(T_{absl} - T_{absh}\right) + hc_{f,abs1}\left(T_f - T_{absh}\right)$	(18)
Absorber 2	$(\rho_{abs}\delta_{abs}C_{abs})\frac{dT_{abs2}}{dt} = hc_{abs2,f}\left(T_f - T_{abs2}\right) + hr_{abs1,abs2}\left(T_{abs2} - T_{abs1}\right) + hr_{abs2,sky}\left(T_{sky} - T_{abs2}\right) + hr_{abs2,gr}\left(T_{gr} - T_{abs2}\right) + hv_{a,absl}\left(T_a - T_{abs2}\right)$	(19)

2.2.2. Fluid Layers

For the cooling fluid flows in the duct of the PV/T system, the energy balance equation is given as:

$$\left(\rho_f \delta_f\ C_f\right)\frac{dT_f}{dt} = hc_{f,abs1}\left(T_{abs1} - T_f\right) + hc_{abs2,f}\left(T_{abs2} - T_f\right) - \dot{m}C_f\ \left(T_{out} - T_{int}\right) \quad (20)$$

where $\dot{m}$, C_f, and T_{int} and T_{out} are respectively the fluid mass flow rate, the fluid specific heat capacity, and the temperature at the inlet and outlet of the PV/T system.

The heat transfer coefficients $hc_{f,abs1}$ and $hc_{f,abs2}$ characterize the convection between the two absorbers and fluid and can be evaluated as a function of the fluid thermal conductivity λ_f, duct hydraulique diameter D_h, and Nusselt number Nu_f:

$$hc_{f,abs1} = hc_{f,abs2} = \frac{Nu_f\ \lambda_f}{D_h} \quad (21)$$

The Nusselt number for water cooling flow between absorber plates is deduced from the correlations of Kudish et al. [31]:

$$Nu_f = 1.86\left[R_e\ P_r\left(\frac{D_h}{L}\right)\right]^{\frac{1}{3}}\left(\frac{\mu_f}{\mu_f\prime}\right)^{0.14}, \text{ case of laminar flow} \quad (22)$$

$$Nu_f = 0.023\ [\ {R_e}^{0.8}{P_r}^{0.33}], \qquad \text{case of turbulent flow} \quad (23)$$

where R_e , P_r, and μ_f are respectively the Reynolds number, Prandlt number, and fluid dynamic viscosity; $\mu_f' = \mu_f(T_p)$ [32].

By rearranging the governing Equations (15)–(20), a set of energy differential equations was built. Thereafter, a MATLAB solution program was developed where the Runge–Kutta (RK4) numerical method was used to solve the energy balance system. Finally, the basic simulation allowed to determine the temperature profile as well as the thermal, electrical, and global performances. The calculation steps in MATLAB software are summarized in flow chart form as shown in Figure 2.

$$\eta_{th} = \frac{E_{th}}{E_{sun}} \quad (28)$$

Combining both electrical and thermal efficiencies, the PV/T global performance was obtained by:

$$\eta_g = \eta_e + \eta_{th} \quad (29)$$

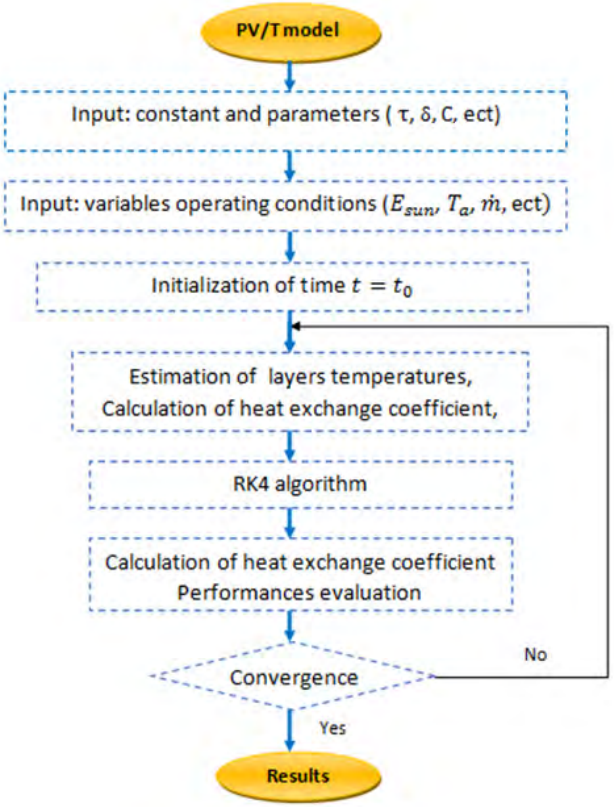


Figure 2. Flow chart of the PV/T numerical modeling.

Figure 2. Flow chart of the PV/T numerical modeling.

2.3. Energy Analysis Method

In order to analyze the developed numerical model for the PV/T system, a performance evaluation is required. Therefore, the solar irradiance as an energy source was supposed uniform and perpendicular on the PV/T surface. Absorbed solar irradiance by the PV cells layer was given as function of the glass layer transmittance τ_c, the cell absorptivity α_{PV}, and the incident solar irradiance E_{sun} by [33]:

$$E'_{sun} = \tau_c \alpha_{PV} E_{sun} \quad (24)$$

The electrical production from the PV cells is determined by Equation (24):

$$E_e = A_{pv}\, \eta_e E'_{sun} \quad (25)$$

For evaluation of the electrical performance, the following expression was used [30]:

$$\eta_e = \eta_{ref}[1 - \beta(T_{PV} - T_{STc})] \quad (26)$$

where η_{ref} is the reference efficiency; β is the temperature coefficient; T_{PV} is the PV cells temperature; and T_{STc} is PV cells temperature at STC conditions equal to 25 °C. According to the AE320HM-60 PV commercial unit with characteristic reported in Table 1, the η_{ref} is about 19.30% and β is equal to 0.0045 C^{-1} [34].

The thermal production of PV/T system is a function of fluid mass flow rate $\dot{m}$, fluid specific heat capacity C_f , and the temperature difference of the fluid at the inlet and outelt of the PV/T system [35]:

$$E_{th} = \dot{m} C_f\, (T_{out} - T_{int}) \quad (27)$$

3. Results and Discussion

In this section, the set of obtained results is presented and discussed. To test the accuracy of the developed PV/T model allowing the prediction of both thermal and electrical behavior of the system, a model validation is processed. Based on the same thermal model, a comprehensive analysis is further performed to assess the effect of some PV/T key parameters on its outputs. Finally, the PV/T optimized model is tested under the real weather data of Iasi, Romania and performance comparison with conventional PV panel is conducted.

For assessment of thermal efficiency, the fraction of the thermal production on the absorbed solar irradiance was conducted according to Equation (28):

$$\eta_{th} = \frac{E_{th}}{E'_{sun}} \tag{28}$$

Combining both electrical and thermal efficiencies, the PV/T global performance was obtained by:

$$\eta_g = \eta_e + \eta_{th} \tag{29}$$

3. Results and Discussion

In this section, the set of obtained results is presented and discussed. To test the accuracy of the developed PV/T model allowing the prediction of both thermal and electrical behavior of the system, a model validation is processed. Based on the same thermal model, a comprehensive analysis is further performed to assess the effect of some PV/T key parameters on its outputs. Finally, the PV/T optimized model is tested under the real weather data of Iasi, Romania and performance comparison with conventional PV panel is conducted.

3.1. Model Validation

3.1. Model Validation

The validation process included the model of the PV unit, mainly formed by the glass, PV cells, and Tedlar (Equations (15)–(17)). This model was tested under different operating conditions, e.g., solar irradiance and outdoor temperature. Furthermore, the results were compared with the data for Nominal Operating Cell Temperature conditions (NOCT: E_{sun} = 800 W/m², T_a = 20 °C and w = 1 m/s). In Figure 3, the PV cells temperature is evaluated for different solar irradiances of 600 W/m², 800 W/m², and 1000 W/m² with an ambient temperature of 20 °C, 25 °C, and 35 °C, respectively. From this figure, the effect of environmental conditions on a PV temperature is clearly shown (a minimum PV temperature was noted at about 39 °C when solar radiation and ambient temperature were lower, about 600 W/m² and 20 °C). It can be also observed that the difference between PV temperature values and NOCT is quite negligible. According to the commercial PV datasheet characteristic summarized in Table 1, the NOCT value was 45 ± 2 °C, while for the three layers model, the PV temperature was 43.96 °C, which proves the effectiveness of PV developed model. For the rest of the PV/T system (absorber 1, fluid and absorber 2), the developed Equations (18)–(20) were written based on the PV/T model validated experimentally in [24].

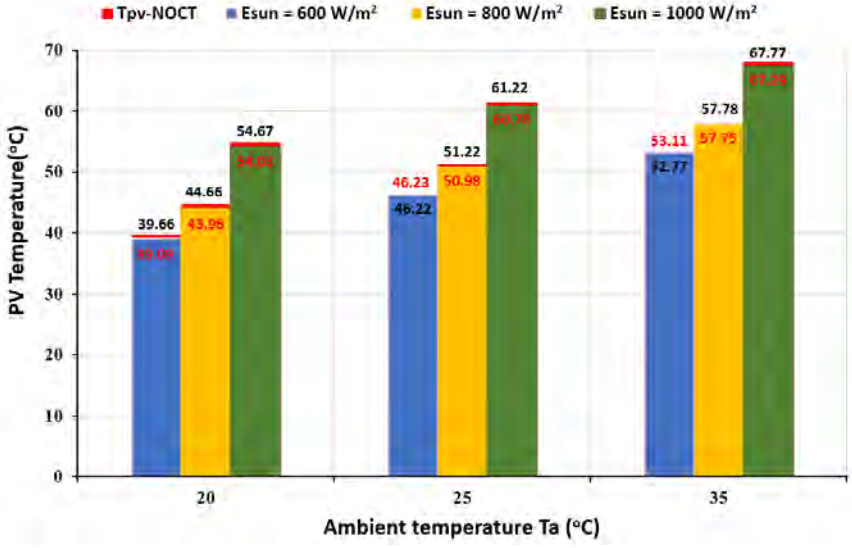


Figure 3. Comparison of the developed PV model and NOCT model.

3.2. Parametric Analysis

3.2.1. Effect of Water Velocity

Based on the developed numerical model, the effect of water velocity on the PV/T performance was analyzed. The environmental conditions involved in this analysis were

3.2. Parametric Analysis

3.2.1. Effect of Water Velocity

Based on the developed numerical model, the effect of water velocity on the PV/T performance was analyzed. The environmental conditions involved in this analysis were a solar irradiance of 1000 W/m^2, an outdoor temperature of 35 °C, and a wind speed of 1 m/s. The fluid velocity as a flow control parameter had a significant effect on the cooling of the PV unit. Hence, Figure 4 investigates the PV temperature evolution as function of water inlet temperature for different water velocities of 0.010 m/s, 0.015 m/s, 0.02 m/s, 0.025 m/s, 0.030 m/s, and 0.035 m/s. As result, it is depicted that by increasing water velocity from 0.010 m/s to 0.035 m/s, a drop in the PV temperature was observed in the four cases, where the water film thickness was 3 mm, 5 mm, 7 mm, and 10 mm. In addition, a minimum value of PV operating temperature about 27.7 °C was observed for an inlet water temperature of 20 °C, water thickness of 7 mm, and highest velocity of 0.035 m/s. This underlines the effective cooling of the PV cells, where a significant heat is extracted from the PV back side while increasing the water velocity.

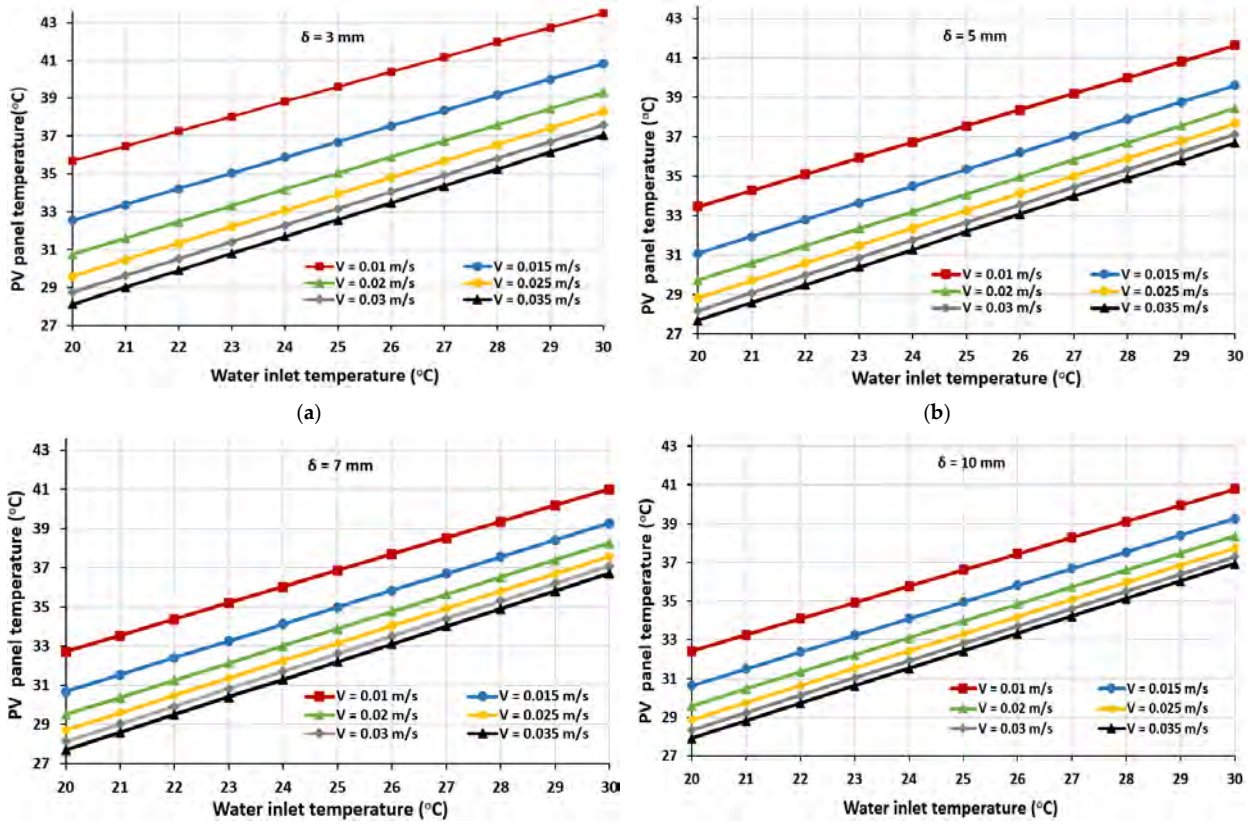


Figure 4. Effect of water velocity on the cooling of the PV cells for different thicknesses: (**a**) δ = 3 mm, (**b**) δ = 5 mm, (**c**) δ = 7 mm, (**d**) δ = 10 mm.

3.2.2. Effect of Water Film Thickness

Among the other geometry parameters for flow, the water film thickness presented an important effect on the optimized cooling of the PV cells and the PV/T electrical and thermal performances. Hence, four water thicknesses of 3 mm, 5 mm, 7 mm, and 10 mm were selected to investigate its impact on the cooling of the PV cells with water velocity and inlet temperature ranging from 0.010 to 0.035 m/s and 20 to 30 °C, respectively. The study was carried out under the same weather conditions mentioned above (solar irradiance of 1000 W/m^2, outdoor temperature of 35 °C, and wind speed of 1 m/s).

As illustrated in Figure 5, as the water film thickness increased (3 mm, 5 mm, 7 mm) for the different water velocity cases, the PV temperature decreased. This is due to the important heat removed from the PV panel, while by further increasing the water film thickness from 10 mm the PV temperature start increasing (inflexion point). As a result, a minimum value of PV temperature was noted to be 27.7 °C for an optimal water film thickness of 7 mm (water inlet temperature and velocity of 20 °C and 0.035 m/s, respectively).

As illustrated in Figure 5, as the water film thickness increased (3 mm, 5 mm, 7 mm) for the different water velocity cases, the PV temperature decreased. This is due to the important heat removed from the PV panel, while by further increasing the water film thickness from 10 mm the PV temperature start increasing (inflexion point). As a result, a minimum value of PV temperature was noted to be 27.7 °C for an optimal water film thickness of 7 mm (water inlet temperature and velocity of 20 °C and 0.035 m/s, respectively).

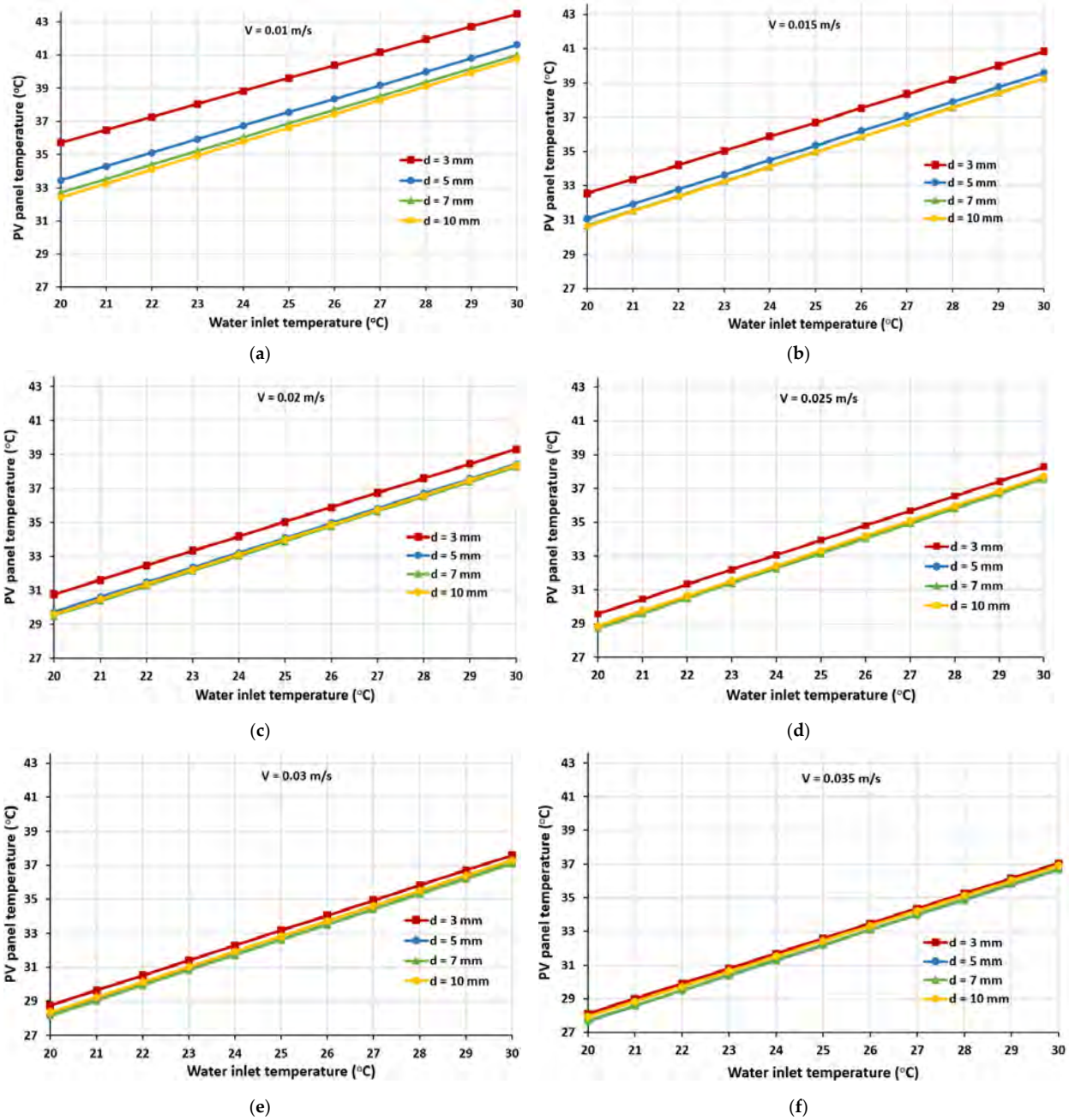


Figure 5. Effect of water thickness on the cooling of the PV cells for different velocities: (**a**) V = 0.01 m/s, (**b**) V = 0.015 m/s, (**c**) V = 0.02 m/s, (**d**) V = 0.025 m/s, (**e**) V = 0.03 m/s, (**f**) V = 0.035 m/s.

In Figure 6, the effect of the water film thickness on the fluid heat transfer coefficient and thermal power is illustrated for variable water velocity and inlet temperature. From this figure, it can be seen that with the increase in water thickness, the heat exchange coefficient dropped which decreases the fluid outlet temperature. However, the thermal power increased and reached a maximum value of 1334.5 W at water thickness of 7 mm (velocity of 0.035 m/s, inlet temperature of 20 °C, and temperature difference of 21.81 °C), Table 4.

mal power increased and reached a maximum value of 1334.5 W at water thickness of 7 mm (water velocity of 0.035 m/s, inlet temperature of 20 °C, and outer temperature of 21.31 °C), Table 4.

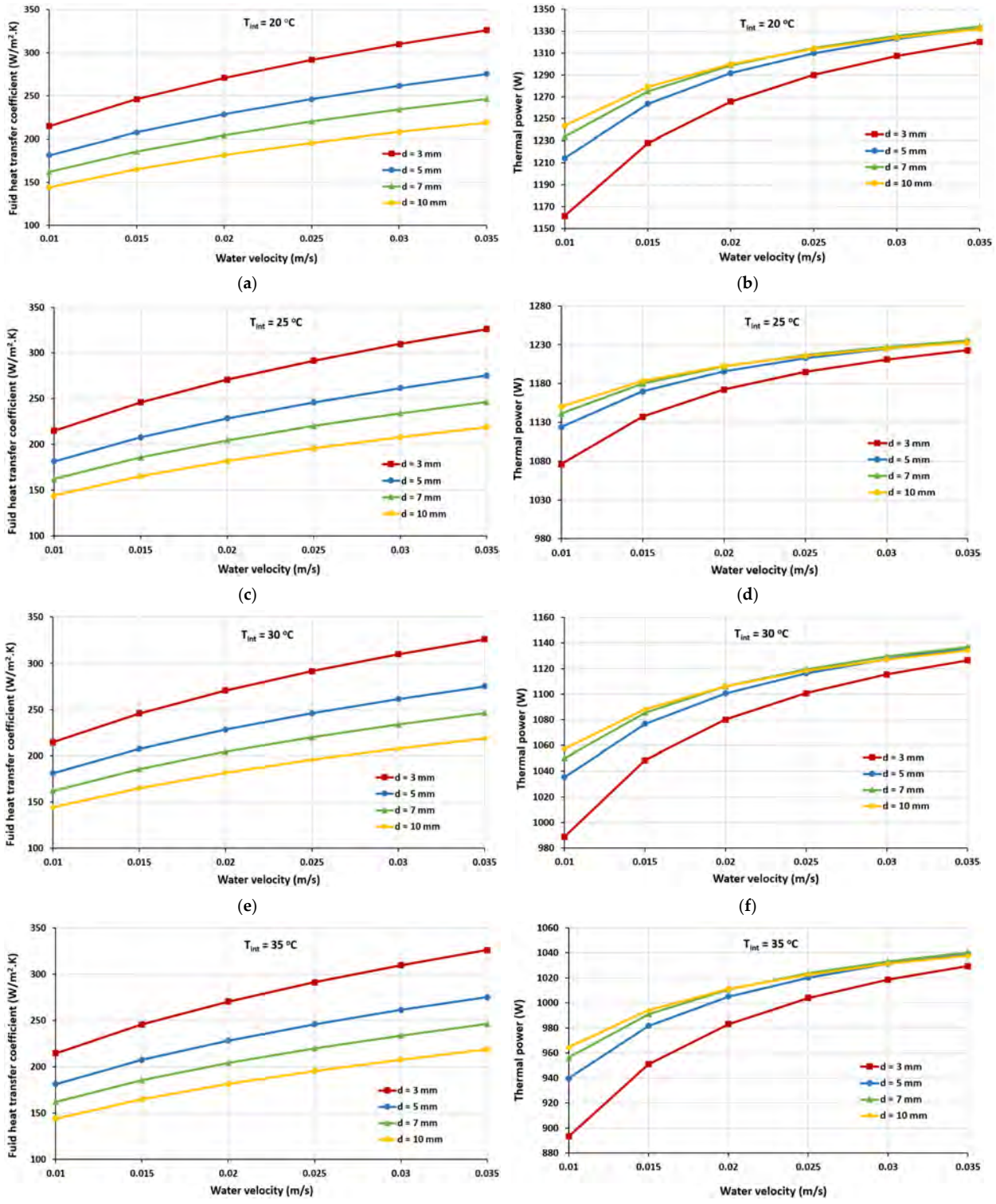


Figure 6. Effect of water thickness on fluid transfer coefficient and thermal power for different inlet temperatures: (**a**,**b**) T_{int} = 20 °C; (**c**,**d**) T_{int} = 25 °C; (**e**,**f**) T_{int} = 30 °C; (**g**,**h**) T_{int} = 35 °C.

weight. Consequently, the PV/T system with a coupled optimum water velocity and thickness of 0.035m/s and 7mm provided the best cooling effect and highest electrical and thermal performances (Table 4).

Table 4. Comparison of PV and PV/T performances at E_{sun} = 1000 W/m², T_a = 35 °C, and T_{int} = 20 °C.

	T_{PV} (°C)	T_{out}(°C)	E_e (W)	E_{th} (W)	η_e (%)	η_{th} (%)
PV	67.7	-	258.8	-	15.60	-
PV/T	27.7	21.31	316,56	1334.5	19.07	80.3

Table 4. Comparison of PV and PV/T performances at E_{sun} = 1000 W/m², T_a = 35 °C, and T_{int} = 20 °C.

	T_{PV} (°C)	T_{out}(°C)	E_e (W)	E_{th} (W)	η_e (%)	η_{th} (%)
PV	67.7	-	258.8	-	15.60	-
PV/T	27.7	21.31	316,56	1334.5	19.07	80.3

The PV and PV/T performances were also depicted and compared under real weathers conditions of Iasi, Romania. A daily simulation was conducted for a typical day of summer (28 July 2016), with weather data involving solar irradiance E_{sun} and ambient temperature T_a, reported by the PVGIS data [36] as shown in Figure 7. During this day, a maximum solar irradiance about 1022 W/m² and ambient temperature of 27.6 °C were noted at 13:00. The simulation was done supposing the inlet water temperature for PV cooling equal to the ambient one with a maximum temperature of 27.6 °C. The optimum case of PV/T system was chosen in terms of water velocity of 0.035 m/s and water film thickness of 7 mm.

Given these weather conditions, the evolution of PV and PV/T temperatures (PV/T at $T_{int} = T_a$) is illustrated in Figure 8. It can be clearly observed that both temperatures presented the same trend during this day. Moreover, the PV/T system provided a lower PV cell temperature of 33.8 °C at 13:00, due to the cooling effect compared with the conventional PV unit (61 °C). According to the negative dependence between electrical production and operating temperature of the PV cells, an effective cooling enhances electrical power. As shown in Figures 9 and 10, the PV/T system provide a better electrical power and efficiency of about 313 W and 18.54% at 13:00, compared with the conventional PV panel.

According to Equation (27) the thermal power is not only depending on difference between the inlet and the outlet temperature, but also a function of the water mass flow rate. At a fixed value of water inlet temperature and velocity, the thermal power is related to the water mass flow rate and the outlet temperature. In this study, the water film thickness increase clearly affected the cooling of the PV unit and the heat gain. Noting that, further increase of water thickness will also affect the cost and the PV/T system heavy weight. Consequently, the PV/T system with a coupled optimum water velocity and thickness of 0.035 m/s and 7 mm provided the best cooling effect and highest electrical and thermal performances (Table 4).

The PV and PV/T performances were also depicted and compared under real weathers conditions of Iasi, Romania. A daily simulation was conducted for a typical day of summer (28 July 2016), with weather data involving solar irradiance E_{sun} and ambient temperature T_a, reported by the PVGIS data [36] as shown in Figure 7. During this day, a maximum solar irradiance about 1022 W/m² and ambient temperature of 27.6 °C were noted at 13:00. The simulation was done supposing the inlet water temperature for PV cooling equal to the ambient one with a maximum temperature of 27.6 °C. The optimum case of PV/T system was chosen in terms of water velocity of 0.035 m/s and water film thickness of 7 mm.

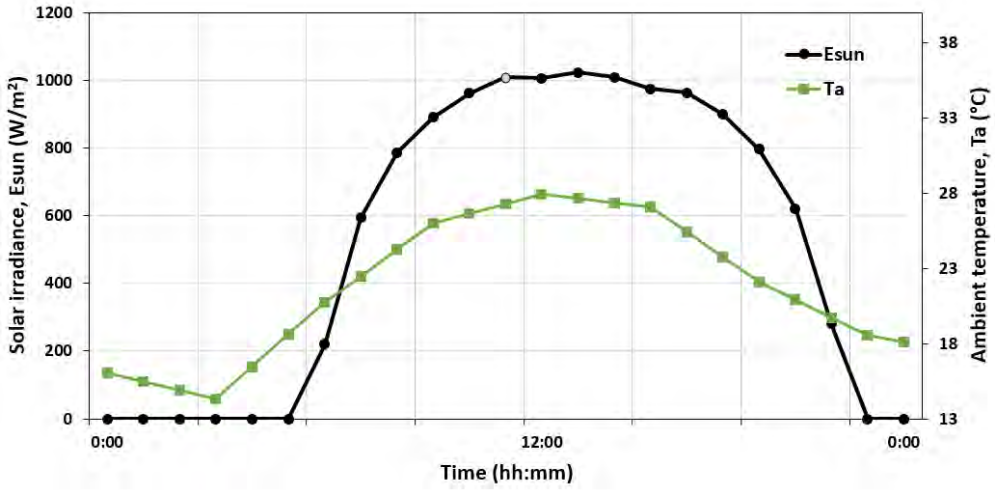


Figure 7. Variation of solar irradiance and ambient temperature (28 July 2016).

Figure 7. Variation of solar irradiance and ambient temperature(28 July 2016).

Given these weather conditions, the evolution of PV and PV/T temperatures (PV/T at $T_{int} = T_a$) is illustrated in Figure 8. It can be clearly observed that both temperatures presented the same trend during this day. Moreover, the PV/T system provided a lower PV cell temperature of 33.8 °C at 13:00, due to the cooling effect compared with the conventional PV unit (61 °C). According to the negative dependence between electrical production and operating temperature of the PV cells, an effective cooling enhances electrical power. As shown in Figures 9 and 10, the PV/T system provide a better electrical power and efficiency of about 313 W and 18.54% at 13:00, compared with the conventional PV panel.

Appl. Sci. 2022, 12, x FOR PEER REVIEW 13 of 17

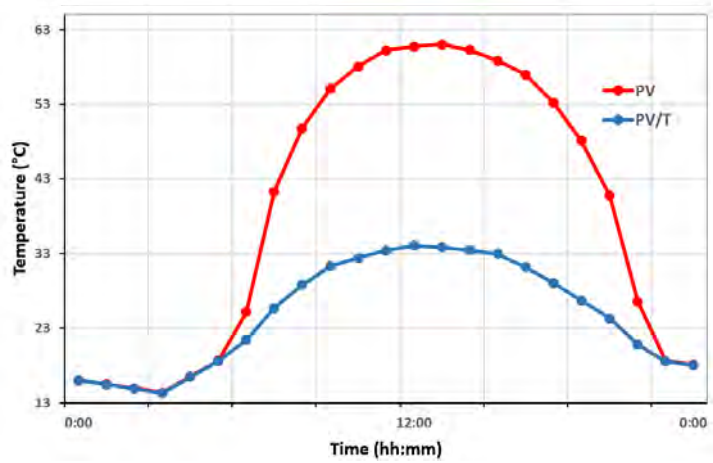


Figure 8. Comparison of PV and PV/T temperatures.
Figure 8. Comparison of PV and PV/T temperatures.

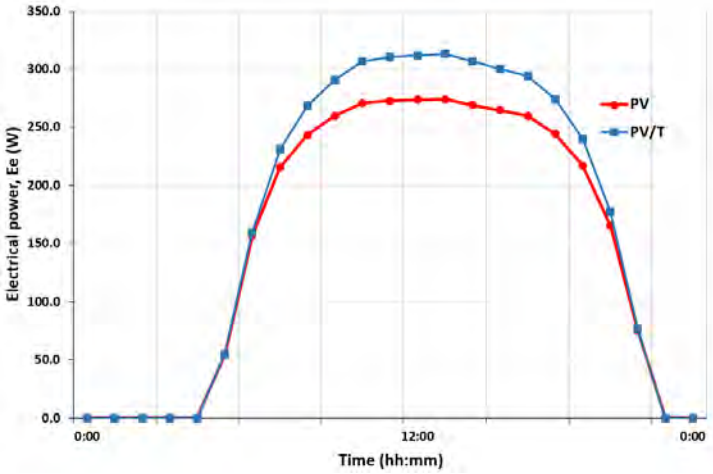


Figure 9. Comparison of PV and PV/T electrical power.
Figure 9. Comparison of PV and PV/T electrical power.

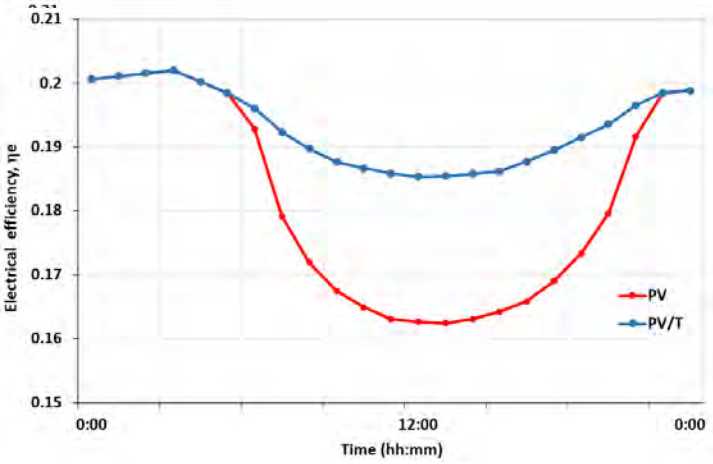


Figure 10. Comparison of PV and PV/T electrical efficiency.
Figure 10. Comparison of PV and PV/T electrical efficiency.

4. Conclusions
4. Conclusions

This work proposes an improved dynamic numerical model for PV/T system based on the heat balance equations established for each layer and solved in MATLAB software. The main obtained outputs of the PV/T model are respectively the temperatures and the electrical and thermal power used for evaluating the advantages of using the PV/T system instead of PV conventional one.
This work proposes an improved dynamic numerical model for PV/T system based on the heat balance equations established for each layer and solved in MATLAB software. The main obtained outputs of the PV/T model are respectively the temperatures and the electrical and thermal power used for evaluating the advantages of using the PV/T system instead of PV conventional one.

This developed model was built regarding the other models presented in literature [37] and validated through comparison of the three layer PV model with the NOCT model and using the equations of the cooling unit, derived from a previous PV/T model validated experimentally in [24]. Consequently, results revealed good agreement. Thus, the model is considered a useful tool for other research works aiming to investigate the PV/T system and analyze its energy yield.

Thereafter, the PV/T model was used to investigate the effect of the water velocity and thickness on the cooling of the PV cells. Next, the improved PV/T model with optimum parameters values was applied in case operating conditions of Iasi, Romania, where the input variables, e.g., solar irradiance and ambient temperature, were given by PVGIS data [36]. Important conclusions of this work can be drawn as below:

- The effectiveness of the developed PV/T model based on the three layer PV model tested at different of solar irradiance and ambient temperature was proven.
- Inlet water temperature had a significant effect on the cooling of the PV panel. A lower PV temperature was noted when the inlet temperature was about 20 °C.
- As the water velocity ranged from 0.010 to 0.035 m/s, the cooling process improved. A lower PV temperature was obtained for water velocity of 0.035 m/s.
- The temperature of the PV panel decreased while increasing the water film thickness from 3 mm to 7 mm and started increasing by 10 mm.
- Optimal cooling of the PV cells (27.7 °C) was ensured, adopting optimum values of water velocity and thickness of 0.035 m/s and 7 mm, respectively, at inlet temperature of 20 °C.
- The improved PV/T model showed a better electrical performance (316.56 W) compared with the conventional PV panel (258.8 W). Furthermore, an important gain of 1334.5 W of thermal production was obtained.

Therefore, the PV/T system designing based on the optimum functional parameters can be an efficient way to produce electrical and thermal energy simultaneously where the electrical and thermal efficiency can reach 19.07% and 80.3%, respectively. Moreover, similar results found in literature [20,21] show economic advantages for implementing such systems in the same climate conditions, where the investment return can be up to 4.25 years with a 75% subsidy in the initial investment and six PV/T modules installed [38].

Future works foresee experimental programs for developing the PV/T model using a real experimental PV/T prototype that is installed on the roof of the Building Services Department, "Gheorghe Asachi" Technical University of Iași, Romania, in order to consider more climatic parameters, such as the wind speed and direction, which also affect the electrical and the thermal energy outputs of the PV/T system.

Author Contributions: Conceptualization, C.E.F., S.V.H., N.C.C. and B.H.; methodology, C.E.F. and B.H.; software, C.E.F.; validation, C.E.F., S.V.H. and E.F.Ț.; formal analysis, C.E.F., S.V.H. and M.L.C.; investigation, C.E.F., N.C.C., S.V.H., B.H., E.F.Ț. and M.L.C.; resources, N.C.C. and M.L.C.; data curation, C.E.F., N.C.C. and B.H.; writing—original draft preparation, C.E.F. and S.V.H.; writing—review and editing, C.E.F. and N.C.C.; supervision, N.C.C. and B.H.; project administration, N.C.C.; funding acquisition, N.C.C. All authors have read and agreed to the published version of the manuscript.

Funding: This paper was financed by the program Internal Grants—Publications granted by the "Gheorghe Asachi" Technical University of Iasi, Romania, project number GI/P35_Publications/2021.

Institutional Review Board Statement: Not applicable.

Informed Consent Statement: Not applicable.

Data Availability Statement: Data are contained within the article.

Acknowledgments: We would like to acknowledge the invaluable support provided by the FCI-TUIASI infrastructure in writing this article. The authors also acknowledge AUF for the support received through the postdoc scholarship for Chaimae El Fouas.

Conflicts of Interest: The authors declare no conflict of interest.

Nomenclature

A	Area (m^2)
C	Specific heat capacity (kJ/kg°C)
Ee	Electrical power (W)
Eth	Thermal power (W)
$F_{j,k}$	View factor between layer i and j
E_{sun}	Solar irradiance (W/m^2)
Gr	Grashof number
$hc_{,i,j}$	Conductive heat exchange coefficient between components i and j (W/m^2K)
$hr_{,j,k}$	Radiative heat exchange coefficient between components i and j (W/m^2K)
$hv_{,i,j}$	Convective heat transfer coefficient between components i and j (W/m^2K)
Isc	Short circuit current (A)
I_{mp}	Maximum current (A)
L	Length (m)
$NOCT$	Nominal operating cell temperature
Nu	Nusselt number
Pr	Prandlt number
P_{max}	Maximum power (W)
PF	Packing factor
Ra	Rayleigh number
Re	Reynolds number
STC	Standard test conditions
t	Time step (s)
T_i	Temperature of layer i (°C)
T_a	Ambient temperature (°C)
V	Water velocity (m/s)
V_{OC}	Open circuit voltage(V)
V_{mp}	Maximum voltage (V)
w	Wind speed (m/s)
Greek symbols	
α	Absorptivity
β	Reference temperature coefficient for efficiency
η_e	Electrical efficiency (%)
η_{th}	Thermal efficiency (%)
λ	Thermal conductivity (W/m K)
ρ	Material density (kg/m^3)
σ	Stefan–Boltzmann constant
Scripts	
Abs	Absorber
f	Fluid
g	Glass
gr	Ground
PV	Photovoltaic
PV/T	Photovoltaic/thermal
Ted	Tedlar

References

1. Markvart, T. *Solar Electricity*, 2nd ed.; John Wiley & Sons: Chichester, UK, 2000.
2. Chandrasekar, M.; Rajkumar, S.; Valavan, D. A review on the thermal regulation techniques for non integrated flat PV modules mounted on building top. *Energy Build.* **2015**, *86*, 692–697. [CrossRef]
3. Makki, A.; Omer, S.; Sabir, H. Advancements in hybrid photovoltaic systems for enhanced solar cells performance. *Renew. Sustain. Energy Rev.* **2015**, *41*, 658–684. [CrossRef]
4. Elminshawy, N.A.S.; Mohamed, A.M.I.; Morad, K.; Elhenawy, Y.; Alrobaian, A.A. Performance of PV panel coupled with geothermal air cooling system subjected to hot climatic. *Appl. Therm. Eng.* **2019**, *148*, 1–9. [CrossRef]
5. Hudisteanu, S.V.; Turcanu, F.E.; Chereches, N.C.; Popovici, C.G.; Verdes, M.; Huditeanu, I. Enhancement of PV Panel Power Production by Passive Cooling Using Heat Sinks with Perforated Fins. *Appl. Sci.* **2021**, *11*, 11323. [CrossRef]

6. Hudisteanu, S.V.; Popovici, C.G.; Mateescu, T.D.; Chereches, N.C. Efficiency analysis of BIPV systems for different locations in Romania. In *Sustainable Solutions for Energy and Environment, Proceedings of the EENVIRO, Bucharest, Romania, 26–28 October 2016*; Elsevier: Amsterdam, The Netherlands, 2017; Volume 112, pp. 404–411.
7. Siecker, J.; Kusakana, K.; Numbi, B.P. Optimal switching control of PV/T systems with energy storage using forced water circulation: Case of South Africa. *J. Energy Storage* **2018**, *20*, 264–278. [CrossRef]
8. Nizetic, S.; Coko, D.; Yadav, A.; Grubisic-Cabo, F. Water spray cooling technique applied on a photovoltaic panel: The performance response. *Energy Convers. Manag.* **2016**, *108*, 287–296. [CrossRef]
9. Hudisteanu, V.S.; Chereches, N.C.; Verdes, M.; Ciocan, V.; Popovici, C.G.; Turcanu, F.E.; Balan, M.C. Analysis of an innovative water-cooling solution for photovoltaic-thermal systems IOP Conference Series: Earth and Environmental Science. *IOP Sci.* **2021**, *664*, 1–10. [CrossRef]
10. Hudișteanu, S.V.; Chereches, N.C.; Popovici, C.G.; Verdeș, M.; Ciocan, V.; Balan, M.C.; Țurcanu, F.E.; Scurtu, I.C. Effect of cooling on power generated by photovoltaic panels IOP Conference Series: Materials Science and Engineering. *IOP Sci.* **2021**, *1141*, 1–12. [CrossRef]
11. Rostami, Z.; Rahimi, M.; Azimi, N. Using high-frequency ultrasound waves and nanofluid for increasing the efficiency and cooling performance of a PV module. *Energy Convers. Manag.* **2018**, *160*, 141–149. [CrossRef]
12. Senthil, R.; Elavarasan, R.M.; Pugazhendhi, R.; Premkumar, M.; Vengadesan, E.; Navakrishnan, S.; Islam, M.R.; Natarajan, S.K. A holistic review on the integration of heat pipes in solar thermal and photovoltaic systems. *Sol. Energy* **2021**, *227*, 577–605. [CrossRef]
13. Chandel, S.S.; Agarwal, T. Review of cooling techniques using phase change materials for enhancing efficiency of photovoltaic power systems. *Renew. Sustain. Energy Rev.* **2017**, *73*, 1342–1351. [CrossRef]
14. Hamzat, A.K.; Sahin, A.Z.; Omisanya, M.I.; Alhems, L.M. Advances in PV and PVT cooling technologies: A review. *Sustain. Energy Technol. Assess.* **2021**, *47*, 1–31. [CrossRef]
15. Bhakre, S.S.; Sawarkar, P.D.; Kalamkar, V.R. Performance evaluation of PV panel surfaces exposed to hydraulic cooling-A review. *Sol. Energy* **2021**, *224*, 1193–1209. [CrossRef]
16. Maleki, A.; Haghighi, A.; Assad, M.E.; Mahariq, I.; Nazari, M.A. A review on the approaches employed for cooling PV cells. *Sol. Energy* **2020**, *209*, 170–185. [CrossRef]
17. Verma, S.; Mohapatra, S.; Chowdhury, S.; Dwivedi, G. Cooling techniques of the PV module: A review. *Mater. Today-Proc.* **2021**, *38*, 253–258. [CrossRef]
18. Reddy, S.R.; Ebadian, M.A.; Lin, C.X. A review of PV-T systems: Thermal management and efficiency with single phase cooling. *Int. J. Heat Mass Transf.* **2015**, *91*, 861–871. [CrossRef]
19. Gomaa, M.R.; Hammad, W.; Al-Dhaifallah, M.; Rezk, H. Performance enhancement of grid-tied PV system through proposed design cooling techniques: An experimental study and comparative analysis. *Sol. Energy* **2020**, *211*, 1110–1127. [CrossRef]
20. Nahar, A.; Hasanuzzaman, M.; Rahim, N.A. Numerical and experimental investigation on the performance of a photovoltaic thermal collector with parallel plate flow channel under different operating conditions in Malaysia. *Sol. Energy* **2017**, *144*, 517–528. [CrossRef]
21. Kazemian, A.; Parcheforosh, A.; Salari, A.; Ma, T. Optimization of a novel photovoltaic thermal module in series with a solar collector using Taguchi based grey relational analysis. *Sol. Energy* **2021**, *215*, 492–507. [CrossRef]
22. Boumaaraf, B.; Boumaaraf, H.; Slimani, M.E.A.; Tchoketch-Kebir, S.; Ait-cheikh, M.S.; Touafek, K. Performance evaluation of a locally modified PV module to a PV/T solar collector under climatic conditions of semi-arid region. *Math. Comput. Simul.* **2020**, *167*, 135–154. [CrossRef]
23. Nahar, A.; Hasanuzzaman, M.; Rahim, N.A.; Parvin, S. Numerical investigation on the effect of different parameters in enhancing heat transfer performance of photovoltaic thermal systems. *Renew. Energy* **2019**, *132*, 284–295. [CrossRef]
24. El Fouas, C.; Hajji, B.; Gagliano, A.; Tina, G.M.; Aneli, S. Numerical model and experimental validation of the electrical and thermal performances of photovoltaic/thermal plant. *Energy Convers. Manag.* **2020**, *220*. [CrossRef]
25. Barbu, M.; Siroux, M.; Darie, G. Numerical model and parametric analysis of a liquid based hybrid photovoltaic thermal (PVT) collector. *Energy Rep.* **2021**. [CrossRef]
26. Rejeb, O.; Dhaou, H.; Jemni, A. A numerical investigation of a photovoltaic thermal (PV/T) collector. *Renew. Energy* **2015**, *77*, 43–50. [CrossRef]
27. El Fouas, C.; El Manssouri, O.; Hajji, B.; Bouselham, L.; Marco Tina, G.; Gagliano, A. Modeling of Dust Deposition Impact on PV/T Hybrid Collector Performances. In Proceedings of the 7th International Renewable and Sustainable Energy Conference (IRSEC), Agadir, Morocco, 27–30 November 2019; pp. 1–6. [CrossRef]
28. Bejan, A.; Kraus, A.D. *Heat Transfer Handbook*; John Wiley & Sons: Hoboken, NJ, USA, 2003.
29. Incropera, F.P.; DeWitt, D.P. *Fundamentals of Heat and Mass Transfer*; John Wiley & Sons: Hoboken, NJ, USA, 2002.
30. El Hocine, H.B.; Touafek, K.; Kerrour, F.; Haloui, H.; Khelifa, A. Model Validation of an Empirical Photovoltaic Thermal (PV/T) Collector. *Energy Procedia* **2015**, *74*, 1090–1099. [CrossRef]
31. Kudish, A.I.; Evseev, E.G.; Walter, G.; Leukefeld, T. Simulation study of a solar collector with a selectively coated polymeric double walled absorber plate. *Energy Convers. Manag.* **2002**, *43*, 651–671. [CrossRef]
32. Rabl, A. *Active Solar Collectors and their Applications*; Oxford University Press: New York, NY, USA, 1985; p. 503.

33. Kazemian, A.; Salari, A.; Hakkaki-Fard, A.; Ma, T. Numerical investigation and parametric analysis of a photovoltaic thermal system integrated with phase change material. *Appl. Energy* **2019**, *238*, 734–746. [CrossRef]
34. Kazemian, A.; Salari, A.; Ma, T. A year-round study of a photovoltaic thermal system integrated with phase change material in Shanghai using transient model. *Energy Convers. Manag.* **2020**, *210*, 112657. [CrossRef]
35. Salari, A.; Taheri, A.; Farzanehnia, A.; Passandideh-fard, M.; Sardarabadi, M. An updated review of the performance of nanofluid-based photovoltaic thermal systems from energy, exergy, economic, and environmental (4E) approaches. *J. Clean. Prod.* **2021**, *282*, 124318. [CrossRef]
36. EU SCIENCE HUB. Available online: https://ec.europa.eu/jrc/en/pvgis (accessed on 15 November 2021).
37. El Fouas, C.; Hajji, M.; Bouselham, L.; Hajji, B.; El Mehdi, A.; Bouali, H. Analysis and Design of an Energy System Based on PV/T Water Collector for Building Application. In Proceedings of the 2017 International Renewable and Sustainable Energy Conference (IRSEC), Agadir, Morocco, 4–7 December 2017; pp. 1–5. [CrossRef]
38. Aguilar-Jimenez, J.A.; Hernandez-Callejo, L.; Alonso-Gomez, V.; Velazquez, N.; Lopez-Zavala, R.; Acuna, A.; Mariano-Hernandez, D. Techno-economic analysis of hybrid PV/T systems under different climate scenarios and energy tariffs. *Sol. Energy* **2020**, *212*, 191–202. [CrossRef]

applied sciences

MDPI

Article

Enhancement of PV Panel Power Production by Passive Cooling Using Heat Sinks with Perforated Fins

Sebastian Valeriu Hudișteanu *, Florin Emilian Țurcanu *, Nelu Cristian Cherecheș *, Cătălin George Popovici, Marina Verdeș and Iuliana Huditeanu

Faculty of Civil Engineering and Building Services, Gheorghe Asachi Technical University of Iasi, 700050 Iași, Romania; catalin-george.popovici@academic.tuiasi.ro (C.G.P.); marina.verdes@academic.tuiasi.ro (M.V.); iuliana.hudisteanu@academic.tuiasi.ro (I.H.)

* Correspondence: sebastian.hudisteanu@tuiasi.ro (S.V.H.); emilian-florin.turcanu@tuiasi.ro (F.E.Ț.); chereches@tuiasi.ro (N.C.C.)

Abstract: This paper presents a numerical model regarding the passive cooling of PV panels through perforated and non-perforated heat sinks. A typical PV panel was studied in a fixed position, tilted at 45 degrees from the horizontal with the wind direction towards its backside. A challenging approach was used in order to calibrate the base case of the numerical model according to the NOCT conditions. Further validation of the accuracy of the numerical simulation consisted of a comparison between the results obtained for the base case, or heat sink, with horizontal non-perforated fins and the experiments presented in the literature. Six types of heat sink attached to the backside of the PV panel were numerically studied. The analyzed configurations focused on heat sinks with both perforated and non-perforated fins that were distributed horizontally and vertically. The CFD simulation was also conducted by modeling the air volume around the PV panel in real wind conditions. The main output parameters were the average temperature and the convective heat transfer coefficient on the front and back of the PV panel. The most important effect of cooling was achieved in low wind conditions and high levels of solar radiation. For v_{air} = 1 m/s, G = 1000 W/m^2 and ambient temperature t_{air} = 35 °C, the percentage of maximum power production achieved 83.33% for the base case, while in the best cooling scenario it reached 88.74%, assuring a rise in the power production of 6.49%.

Keywords: power enhancement; perforated heat sinks; passive cooling; operating PV temperature; NOCT validation; CFD analysis

check for updates

Citation: Hudișteanu, S.V.; Țurcanu, F.E.; Cherecheș, N.C.; Popovici, C.G.; Verdeș, M.; Huditeanu, I. Enhancement of PV Panel Power Production by Passive Cooling Using Heat Sinks with Perforated Fins. *Appl. Sci.* **2021**, *11*, 11323. https://doi.org/10.3390/app112311323

Academic Editors: Ilinca Nastase and Florin Ioan Bode

Received: 16 November 2021
Accepted: 24 November 2021
Published: 30 November 2021

Publisher's Note: MDPI stays neutral with regard to jurisdictional claims in published maps and institutional affiliations.

Copyright: © 2021 by the authors. Licensee MDPI, Basel, Switzerland. This article is an open access article distributed under the terms and conditions of the Creative Commons Attribution (CC BY) license (https://creativecommons.org/licenses/by/4.0/).

1. Introduction

The current global energy context is characterized by the energy consumption of humanity, which has reached impressive values in recent years. Thus, in the current year (2021) the well-known Overshoot Day was "celebrated" on 29 July. This meant that humanity had already used up all of the restorable resources of 2021. From 30 July we started consuming more resources than the planet could regenerate in a year [1]. Therefore, by the end of the year 2021, the energy consumption is projected to reach about 1.73× Earth's resource regeneration capacity. It is a global emergency and every small step in reducing this tendency to over consume energy will become decisive in this fight.

Solar energy is a clean and sustainable source of energy. It is involved directly or indirectly in the vast majority of other renewable energy sources, and it is also related to the conventional fuels—as most of them are the result of photosynthesis. The solar energy incident on the Earth could cover the annual energy demand for the entire world in only 1.5 h [2,3].

Regarding the conversion of solar radiation into electricity, this can be achieved by using photovoltaic (PV) cells or it can be generated through solar thermal technologies [1].

Photovoltaic conversion has important advantages: the energy source is renewable and free, and the processes of electricity production are environmentally friendly (in terms of CO_2 and NOx emissions, waste, noise etc.). The generation of electricity is achieved without the use of moving parts, so the cost of maintenance is reduced. Furthermore, the energy produced is consumed locally, which results in reduced power losses.

By implementing efficient PV systems, the safety of the users of the electricity supply is increased [4,5]. These systems also reduce the vulnerability of European space and could eliminate future energy crises or the lack of an energy supply. Considering the long service life and the low CO_2 emissions of PV systems, they represent a sustainable alternative to electricity production. In addition, the energy market in Europe, which lately has been affected by internal and external factors, could become more stable and competitive by increasing the power it produces and the number of users of photovoltaic systems [6].

The main environmental parameters, which are influencing the efficiency and the lifetime of PV panels are solar radiation, wind velocity and direction, dust, ambient temperature and their operating temperature. Most of these meteorological parameters are random and uncontrollable. From the point of view of the installation methods, the tilt angle, orientation and positioning are very difficult to manage in the case of typical PV systems [7,8]. However, the management of the operating temperature of PV cells has been demonstrated to be a good solution for enhancing their efficiency [9].

Almost 80% of the solar energy incident on the PV panel's surface is converted into heat, and it is well known that the performance of PV panels is temperature-dependent [9,10]. Skoplaki, E. et al. [10] analyzed different methods and relations for calculating the dependence between conversion efficiency and photovoltaic cell temperature; a linear dependence between efficiency and temperature has been proved. The decrease in the efficiency of the produced power related to the increase in the temperature has values between -0.46–$-0.50\%/^{\circ}C$ and -0.47–$-0.50\%/^{\circ}C$, respectively [11–13].

Taking into account that the power of a photovoltaic cell is influenced by the temperature and radiation levels, standard test condition (STC) parameters were defined: t_{PV} = 25 °C, G = 1000 W/m^2, AM1.5 [14]. In STCs the PV panels produce the watt peak power [Wp], but a real concern is that in regular operation, at 1000 W/m^2, the photovoltaic panels can reach extreme temperatures of 70–80 °C [11,15,16], leading to a significant decrease in the efficiency.

Complementary cooling solutions are recommended in order to achieve high productivity [17–21]. The literature presents a large number of papers on different solutions for improving the conversion efficiency by decreasing the temperature of the photovoltaic panels [13,15,20,22–27].

Concepts frequently used in analyzing PV systems are the NOCT (nominal operating cell temperature) conditions. In contrast to STCs, the NOCT conditions are closer to reality, taking into account the following operating conditions: tilt of PV panel = 45°; G = 800 W/m^2; t_{air} = 20 °C; v_{air} = 1 m/s towards the backside of PV panel [15]. According to these conditions, every producer must supply, via the data sheet, the average operating temperature of the PV panel—t_{NOCT}.

The aim of this study was to overcome technological and conceptual barriers that were currently attributed implicitly to photovoltaic systems by improving their efficiency during months with maximum energy production but lower efficiencies due to high operating temperatures. For example, in hot summer days it turned out that the most important cause of the production potential not being reached, when the intensity of solar radiation had the highest values of the year, was the uncontrolled increase in the operating temperatures of the photovoltaic panels.

The improvement in the efficiency of PV panels when air-cooled heat sinks were used, was reasonable for the residential sector, urban areas and power plants [28,29].

The novelty of the present study consisted of analyzing the impact of longitudinal and transversal heat sinks with perforated and non-perforated fins on the performance of PV panels. The impact was analyzed using more realistic wind conditions and tilt of the panel, compared to existing studies in the literature.

2. Related Research

Experimental tests and numerical analyses on monocrystalline or polycrystalline photovoltaic panels show that the decrease in efficiency, as the operating temperature increases, and the necessity of cooling solutions are current concerns in the literature [11–13,16,30,31].

Different technologies to improve the efficiency of photovoltaic panels by passive cooling, using air, are studied in the literature [8,13,32–39]. Detailed studies on air cooling of photovoltaic panels are carried out in the following works [11,40]. Air cooling with heat sinks and perforated fins is studied both numerically [11,32] and experimentally [34]. The characteristic values for multiple photovoltaic panels cooled with aluminum and copper heat sinks were compared through experimental tests under different conditions [34]. The results of the simulation and from the experiment showed that the heat sink with perforated fins can significantly reduce the temperature of the panel and increase its performance; there was an increase in the heat extracted from the photovoltaic cell and a decrease in its temperature, with values between 7 °C and 10 °C [34].

Also, numerical simulations on a particular case of backside ventilation [11,16,41] revealed that the temperature was reduced by 10 °C below the value obtained in the base case. This aspect was favorable for conversion efficiency, determining a generation of approximately 90% of the maximum power produced in STCs [14], while the average power production of PV panels was about 70–80% of P_{mp} in STCs [42].

3. Materials and Methods

3.1. Problem Description

The goal of this work was to develop a numerical model regarding the passive cooling of the PV panels, through perforated and non-perforated heat sinks, and determine the enhancement of operating temperatures compared to the base case (without cooling). A photovoltaic panel with an area of approximately S = 1.6 m^2 was studied in a fixed position and tilted at 45° from horizontal, as well as in variable solar radiation, wind velocity and ambient temperature. This setup, together with the wind direction towards the backside of the PV panel, was established according to NOCT conditions [14] in order to validate the model.

A common monocrystalline Si-based PV panel (AE Solar AE320HM6-60), with an advantageous position of the junction box, was analyzed with the following technical data (Table 1) [43].

Table 1. General characteristic for the considered PV panel.

AE Solar AE320HM6-60 PV Panel	
P_{mp}	320 Wp
V_{mp}	33.40 V
I_{mp}	9.59 A
V_{oc}	40.90 V
I_{sc}	10.15 A
η	19.30%
β	−0.37%/°C
t_{NOCT}	47 °C
Dimensions ($L \times l \times h$)	1665 mm × 996 mm × 35 mm

Dimensions ($L \times l \times h$)	1665 mm × 996 mm × 35 mm

A step-by-step analysis of heat sink usage for cooling PV panels was conducted. After the initial validation of the base case—PV panel without heat sink—a total of six photovoltaic panels with attached heat sinks were analyzed. Two of them were non-perforated, while the other four had perforated fins.

The heat sink consisted of a metal plate with copper attached to the photovoltaic panel and perforated or non-perforated metal fins. Figure 1 The role of the designed holes on the fins was assessed both quantitatively (by reducing the amount of material necessary for device construction) and qualitatively (by amplifying the turbulent and heat transfer intensity at the PV panel).

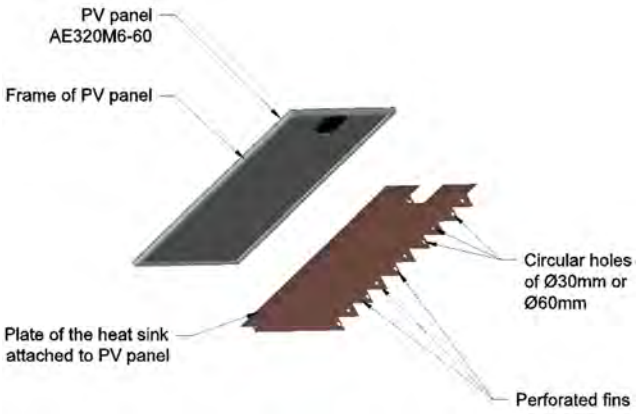


Figure 1. Overview of the components of the heat sink attached to the PV panel for cooling (case with perforated fins).

Due to preliminary analysis and the literature review [1,32,34,41], the 30 mm and 60 mm diameter circular perforations distributed on a single row turned out to be feasible. It emerged that other shapes, dimensions or multiple rows of perforations were heading towards lower performance of the heat sink (the operating temperatures were at least 2–3 °C higher). It must be specified that the literature comprises a diversity of heat sinks with different approaches of fins [42,44]. The present study is focused on using heat sinks with continuous fins.

Two types of heat sinks were analyzed:

Type 1—heat sinks with horizontal (transversal) fins of 100 mm height (with 3 subtypes: non-perforated, $\Phi \equiv 30$ mm perforations, $\Phi \equiv 60$ mm perforations);

Type 2—heat sinks with vertical (longitudinal) fins of 100 mm height (with 3 subtypes: non-perforated, $\Phi = 30$ mm perforations, $\Phi = 60$ mm perforations).

3.2. Numerical Simulation

The numerical simulation was performed using the ANSYS-Fluent 2021-R1 software. The geometry and discretization of the computing domain was performed within the platform using the Fluent-Meshing and SpaceClaim programs.

For simulation the control volume method, SIMPLE pressure–velocity coupling and second-order accuracy for equation solving were used, taking into account that the flow was not aligned with the mesh [45]. This method used a relationship between velocity and pressure corrections to enforce mass conservation and to obtain the pressure field. A fully implicit numerical scheme was employed, in which upwind differences were used for the convective terms and central differences for the diffusion terms [11]. The calculation was iterative, with a convergence criteria of 10^{-6} for the energy equation and 10^{-3} for the pressure, velocities, k, ε and continuity equations.

The simulation of solar radiation was realized using the Solar Ray Tracing model of the Fluent program. The absorption of solar radiation by the front of the PV panel was imposed as a global coefficient $\alpha = 0.7$, taking into account all the layers of the PV panel [11,46].

The simulation of solar radiation was realized using the Solar Ray Tracing model of the Fluent program. The absorption of solar radiation by the front of the PV panel was imposed as a global coefficient α = 0.7, taking into account all the layers of the PV panel [11,46].

The heat transfer balance was set in order to include the convection and radiation with the surroundings [46]. The numerical simulation was realized using the k-ε realizable model [45]. For all studied configurations, the distance between fins was set to 150 mm. The fins were perpendicular to the heat sink plate—Figure 1. For the case of perforated fins, they had circular holes of 30 mm or 60 mm diameter, which were placed at a distance of 100 mm to one to another [34]. Their role was to improve the air circulation near the heat sink and to extract more heat from the PV panel.

The accuracy and the solution time were both highly depend on the characteristic of the mesh. Computational fluid dynamics (CFDs) solvers depended on the highly orthogonal mesh that could be difficult to achieve on different types of geometries. For the present study, a polyhedral mesh was used for the surfaces and a poly-hex core for one of the volumes. The choice of these types of cells was made due to an increase in speed of simulation from 20 to 50% while maintaining the high level of accuracy. In addition, this approach in the simulation opened up the possibility of improving the solver speed and accuracy compared with the tetrahedral cells.

The mesh was realized with different refinements for the heat sink and air volume. The mesh quality achieved for the numerical analysis was as follows:

- Aspect ratio was in the range 5–60;
- Skewness was in the range 0.4–0.7;
- Orthogonal quality was in the range 0.1–0.3.

A mesh independence study was carried out, taking into account the large number of elements that resulted due to modeling the air volume that flowed over the PV panel and heat sinks. Figure 2 presents the mesh independence study, which was achieved for approximately 3 million cells in the base case and over 5.5 million cells for cases with heat sinks and perforated fins.

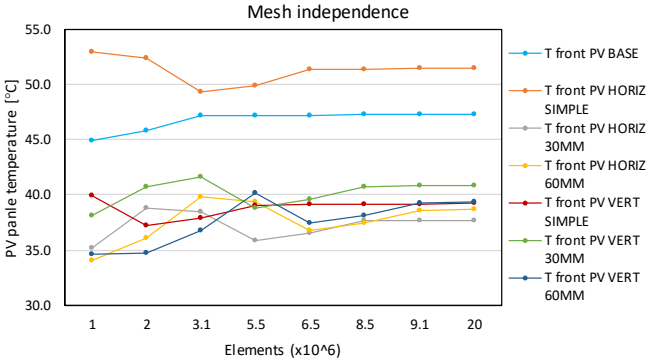


Figure 2. Mesh independence study for each model.

The numerical analysis was conducted on a workstation that had 48 cores, 256 GB of RAM and a graphical computing video card Nvidia Quadro P6000.

Typical approaches from the literature considered the position of the PV panel as either horizontal [31] or vertical [11,34], with a channel simulating the wind behind the PV panel. There were only a few studies on cooling tilted PV panels [16,40].

During this study the modelling was realized by taking into account the air circulation in the vicinity of a tilted PV panel cooled with heat sinks. In this way, by using an optimized resource consumer mesh, the airflow and the heat transfer were more realistic and easier to visualize and understand. The material properties used in the simulations are shown in Table 2, and the sketch of the model is presented in Figure 3.

Table 2. Material properties.

Material	g [mm]	λ [W/m·K]	ρ [kg/m³]	c_p [J/kg·K]
Glass	3.00	1.00	2300	0.50
PV cells	0.35	168	2330	0.757
EVA	0.50	0.35	960	2.09
Tedlar	0.20	0.20	1500	1.20
Copper	1.00	386	8960	0.376
Air	-	0.025	1.20	1.005

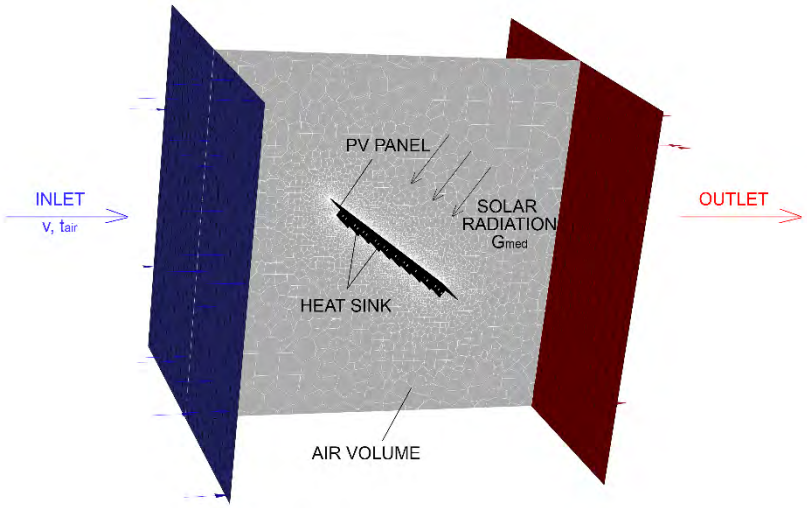


Figure 3. Main components of the numerical model.

During the study, the non-perforated heat sinks were compared with perforated heat sinks in order to determine the optimum configuration for implementation in NOCT conditions of wind.

Simulations were realized in steady state conditions with the following input parameters:

- ambient temperature, t_{air} = 20, 25, 30 and 35 °C;
- velocity of the air towards the back of the photovoltaic panel, v_{air} = 1–5 m/s;
- the normal component of solar radiation varied between 200–1000 W/m², assuming the typical conditions of operation for the PV panel.

It should be mentioned that heat sinks were studied on some of the worst scenarios of temperature operation for the base case. Therefore, some cases with low levels of solar radiation, low ambient temperatures or high wind velocities were excluded from the results presented during the paper.

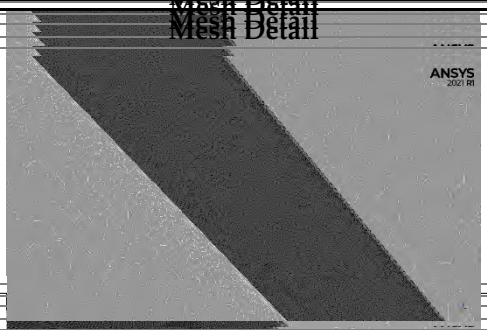
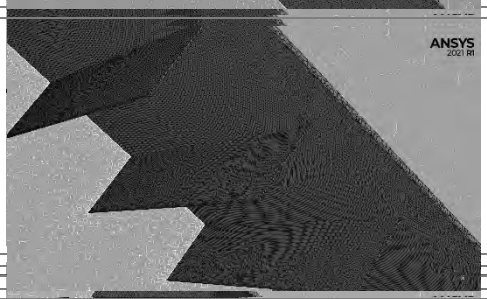
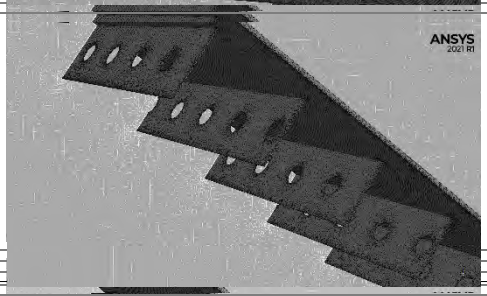
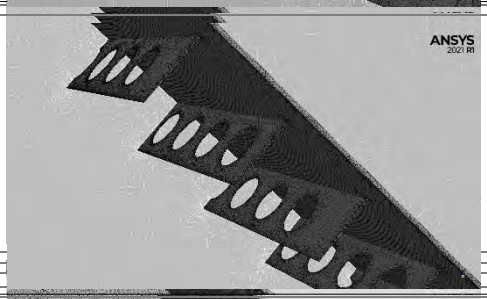
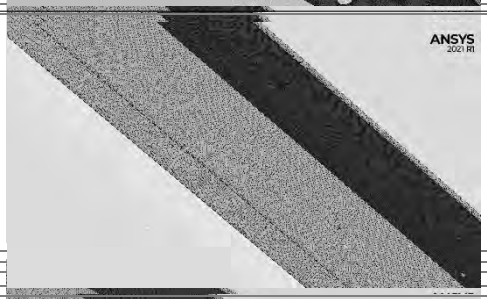
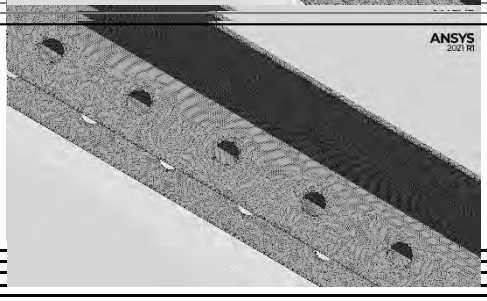
The main outputs of the simulations were:

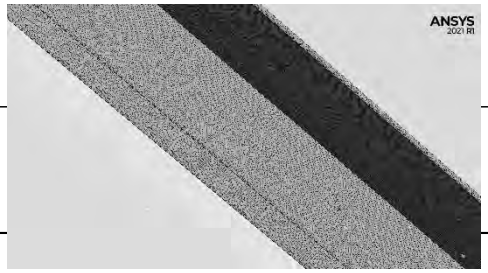
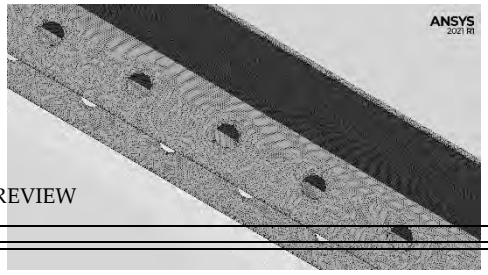
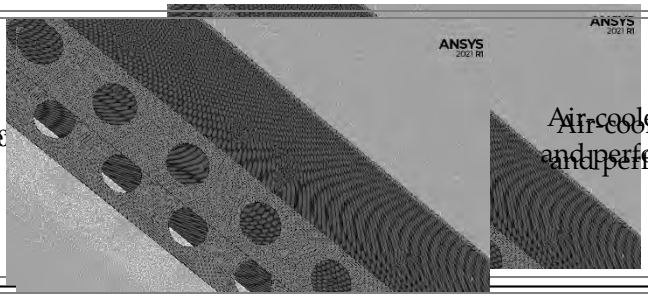
- average temperature of the PV panel;
- convective heat transfer coefficients, achieved for both the front and the back of the PV panel or heat sink.

Studied Cases

A total of six configurations of heat sinks were analyzed, plus the base case, these are shown in Table 3.

Table 3. Studied configurations.

Case	Name	Mesh Detail	Description
0	Base		Pilot photovoltaic panel—normal installation—without cooling solution.
1	Horiz Simple		Air-cooled photovoltaic panel with heat sink non-perforated horizontal (transversal) fins.
2	Horiz 30 mm		Air-cooled photovoltaic panel with heat sink and perforated horizontal (transversal) fins ≡ 30 mm.
3	Horiz 60 mm		Air-cooled photovoltaic panel with heat sink and perforated horizontal (transversal) fins ≡ 60 mm.
4	Vert Simple		Air-cooled photovoltaic panel with heat sink and non-perforated vertical (longitudinal) fins.
5	Vert 30 mm		Air-cooled photovoltaic panel with heat sink and perforated vertical (longitudinal) fins 30 mm.

Case	Name		Description
4	Vert Simple		Air-cooled photovoltaic panel with heat s and non-perforated vertical (longitudinal)
5	Vert 30 mm		Air-cooled photovoltaic panel with heat s and perforated vertical (longitudinal) fins (longitudinal) fins D = 30 mm.
6	Vert 60 mm		Air-cooled photovoltaic panel with heat s and perforated vertical (longitudinal) fins (longitudinal) fins D = 60 mm.

Appl. Sci. 2021, 11, x FOR PEER REVIEW 8
Appl. Sci. 2021, 11, x FOR PEER REVIEW 8 of 20

The position of the PV panel and air circulation was set according to NOCT conditions: the PV panel was tilted at 45° and wind direction toward the backside of the PV panel (Figures 4 and 5).

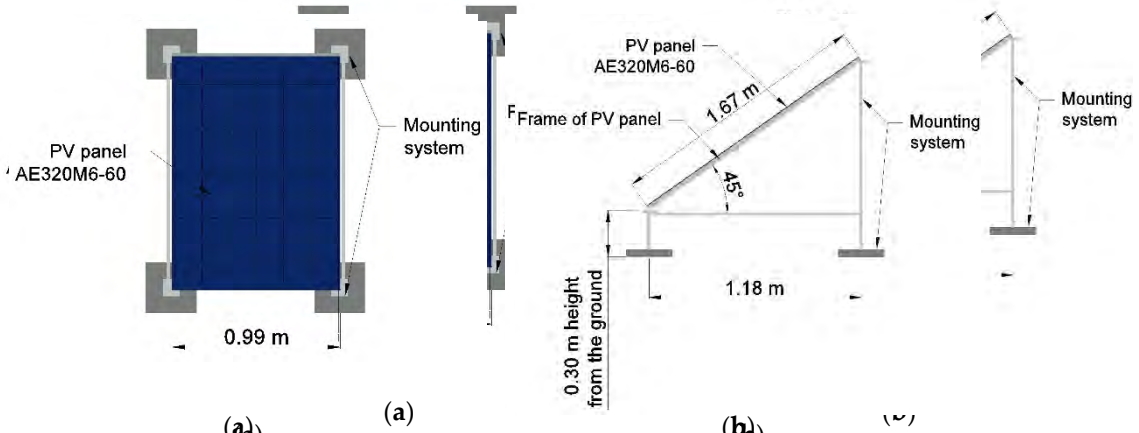


Figure 4. Position of the PV panel (fixed, tilted at 45°): (**a**) top view; (**b**) side view.

Figure 4. Position of the PV panel (fixed, tilted at 45°): (**a**) top view; (**b**) side view.

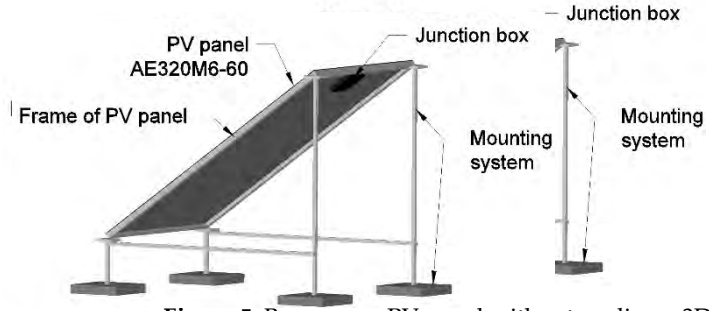


Figure 5. Base case—PV panel without cooling—3D perspective view.

Figure 5. Base case—PV panel without cooling—3D perspective view.

Heat sinks consist of a metal plate and perforated or non-perforated longitudinal or transversal fins arranged at equal distances of 150 mm from each other (Table 4). Both the base plate and the fins were made of copper. The base plate was in direct contact with the back of the photovoltaic panel. The fins had circular perforations with a diameter of 30 or 60 mm (Table 4).

During the study, the fins were arranged longitudinally (vertically—parallel to the length of the PV panel) or transversally (horizontally—parallel to the width of the PV panel). The distance between fins was s = 150 mm, while their height was h_{fins} = 100 mm.

The back side top and bottom view of the heat sinks attached to the PV panel are presented in Figure 2 and the dimensions of the heat sinks are presented in Table 1.

Table 1. Components of the model and overall dimensions of the heat sinks.

Case	Components of the Model	Overall Dimensions of the Heat Sink
Case 1	PV panel AE320M6-60 Plate of the heat sink attached to PV panel Junction box Mounting system Frame of PV panel Non perforated fins	Back view: 0.11 m × 0.15 m × 0.15 m × 0.09 m Side view: 0.10 m × 0.33 m × 0.20 m × 0.10 m Bottom view: 0.10 m × 0.86 m × 0.86 m × 0.10 m
Case 2	PV panel AE320M6-60 Plate of the heat sink attached to PV panel Junction box Mounting system Frame of PV panel Circular holes of Ø30mm or Ø60mm Perforated fins	Back view: 0.11 m × 0.15 m × 0.15 m × 0.09 m Side view: 0.10 m × 0.33 m × 0.08 m × 0.10 m × 0.10 m Bottom view: 0.10 m × 0.86 m × 0.03 m × 0.10 m × 0.86 m × 0.10 m
Case 3	PV panel AE320M6-60 Plate of the heat sink attached to PV panel Junction box Mounting system Frame of PV panel Non-perforated fins	Back view: 0.13 m × 1.28 m × 0.15 m × 0.15 m Side view: 0.13 m × 0.10 m × 1.54 m × 1.52 m Bottom view: 0.10 m × 0.86 m × 0.13 m × 0.15 m × 0.86 m × 0.10 m
Case 4	PV panel AE320M6-60 Plate of the heat sink attached to PV panel Junction box Mounting system Frame of PV panel Circular holes of Ø30mm or Ø60mm Perforated fins	Back view: 0.13 m × 1.28 m × 0.15 m × 0.15 m Side view: 0.13 m × 0.10 m × 1.54 m × 0.10 m × 1.52 m × 0.05 m Bottom view: 0.10 m × 0.86 m × 0.13 m × 0.15 m × 0.86 m × 0.10 m

During the study, the fins were arranged longitudinally (vertically—parallel to the length of the PV panel) or transversally (horizontally—parallel to the width of the PV panel). The distance between fins was s = 150 mm, while their height was h_{fins} = 100 mm.

The approximate length of the fins was L_{fins} = 1520 mm (for longitudinal ones) and L_{fins} = 860 mm (for transversal ones). The number of fins was 11 for the horizontal case and 5 for vertical case (Table 4).

The perforations had a circular shape and a diameter of Φ = 30 mm or Φ = 60 mm. The distance measured on the fins between the centers of the perforations was d = 100 mm. The perforations were staggered by 50 mm between two successive fins.

The back, side, top and bottom view of the heat sinks attached to the PV panel are presented in Table 4. In addition, the main components of the geometry conceptions of the photovoltaic panel, mounting system and heat sinks with perforated and non-perforated fins were easy to follow in 3D perspective views.

4. Validation of the Model

4. Validation of the Model

4.1. NOCT Calibration

4.1. NOCT Calibration

The PV panel tilted at 45° was initially exposed to a direct solar radiation of 800 W/m^2, air temperature of 20 °C and wind velocity of 1 m/s from behind, similar to the NOCT conditions. According to the PV panel data sheet [43], in this scenario, the t_{NOCT} should be 45 ± 2 °C, while the operating temperature from simulation was 47.16 °C. Taking into account the good matching between results and expectation, further validation was conducted. Therefore, by comparing the results from modelling with those obtained by using the acknowledged Equation (1) [14,47], the following variation of the operating temperature was obtained (Figure 6).

The PV panel tilted at 45° was initially exposed to a direct solar radiation of 800 W/m^2, air temperature of 20 °C and wind velocity of 1 m/s from behind, similar to the NOCT conditions. According to the PV panel data sheet [43], in this scenario, the t_{NOCT} should be 45 ± 2 °C, while the operating temperature from simulation was 47.16 °C. Taking into account the good matching between results and expectation, further validation was conducted. Therefore, by comparing the results from modelling with those obtained by using the acknowledged Equation (1) [14,47], the following variation of the operating temperature was obtained (Figure 6).

$$t_{PV} = t_{air} + \frac{t_{NOCT} - 20}{800} \cdot G \quad (1)$$

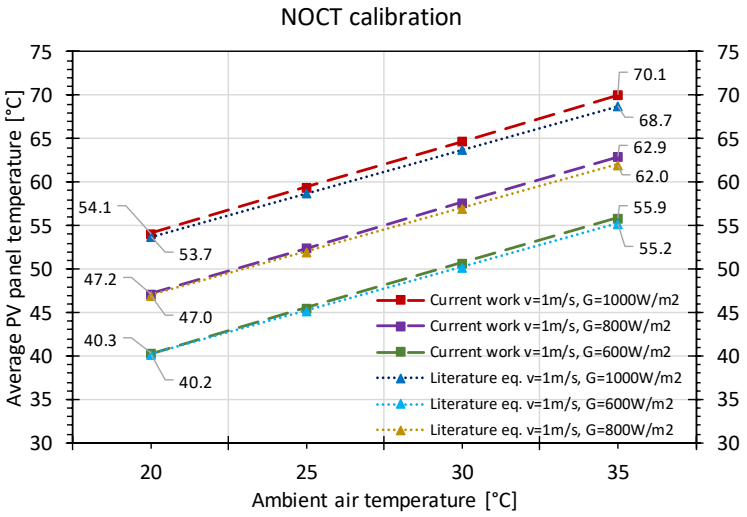


Figure 6. Calibration of the model according to NOCT conditions variation.

Figure 6. Calibration of the model according to NOCT conditions variation.

The results showed that the values computed using the current work differed from those of Equation (1) within the range of 0.28–1.98%.

The results showed that the values computed using the current work differed from those of Equation (1) within the range of 0.28–1.98%.

4.2. Base Case Validation

4.2. Base Case Validation

Nizetic et al. [16] experimentally studied the thermal performance of PV panels on different inclination angles. In Case 1 of their study (45° tilt, v = 1.5 m/s, G = 837 W/m^2) the average temperature of the PV panel was 51.6 °C. For validation, the base case of the present work was set for the same parameters. The average temperature of the PV panel obtained in the current model was 53.68 °C, which represented a variation of 3.87%.

Nizetic et al. [16] experimentally studied the thermal performance of PV panels on different inclination angles. In Case 1 of their study (45° tilt, v = 1.5 m/s, G = 837 W/m^2) the average temperature of the PV panel was 51.6 °C. For validation, the base case of the present work was set for the same parameters. The average temperature of the PV panel obtained in the current model was 53.68 °C, which represented a variation of 3.87%.

Also, experimental studies of Arifin et al. in 2020 [34], and Almuwailhi in 2021 [48], were examined and the correlations with the present work were presented together in Figure 7a.

Also, experimental studies of Arifin et al. in 2020 [34], and Almuwailhi in 2021 [48], were examined and the correlations with the present work were presented together in Figure 7a.

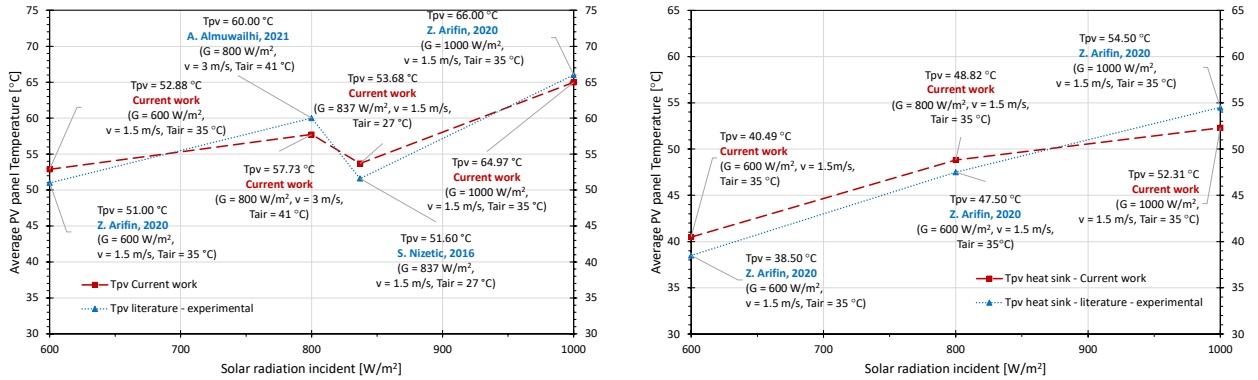


Figure 7. Validation of the model: **(a)** base case—without heat sink; **(b)** PV panel with heat sink.

4.3. Heat Sink Validation

An experimental study on heat sinks attached to a PV panel [34] were used in order to compare the results with the present model (Figure 7b).

A reasonable variation of the simulated PV panel average temperature compared to the literature for low and high ambient temperatures was recorded, in addition to different levels of radiation (Figure 7). The differences recorded were between −5.18% and +4.03%. According to the literature [49], this variation was acceptable so the study was considered consistent and the next step consisted of modelling the heatsinks with perforated fins (Cases 2–6) in the same conditions as those validated above.

5. Results and Discussion

Most simulations in the literature were realized by imposing a constant convective heat transfer coefficient (h_c), which determined a quasi-uniform temperature distribution [50]. In the present work, the simulation of the airflow near the PV panel determined a more realistic temperature distribution on its surface compared with the typical approaches [42], while the convective heat transfer coefficient was varying on the PV panel's surface.

The results of the simulations consisted of the photovoltaic panel temperature and convective heat transfer coefficient variation, depending on the type of the heat sink. The spectra of the operating temperatures of the PV panels and velocity path lines on the cross-sectional plane were obtained (Table 5). The following images present the qualitative visualization of the results for cases simulated in NOCT configuration: t_{air} = 20 °C, v_{air} = 1 m/s, G = 800 W/m² (Table 5).

Appl. Sci. 2021, 11, x FOR PEER REVIEW

Table 5. Temperature distribution on the PV panel and air velocity profile for the NOCT configuration.

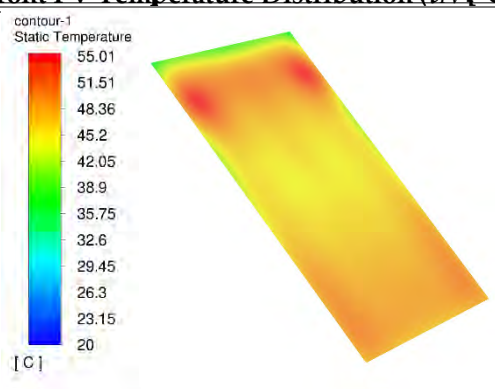
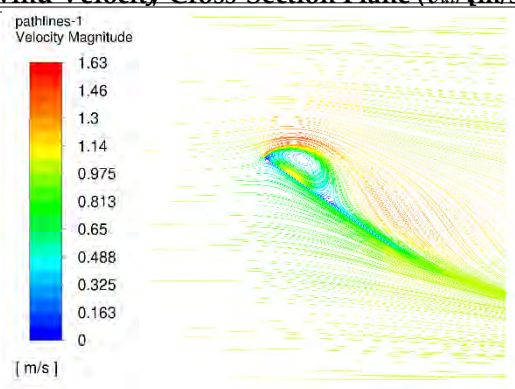
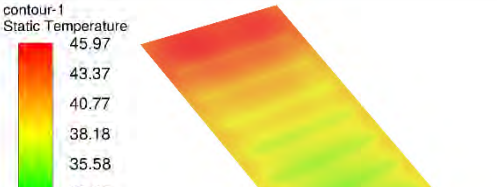
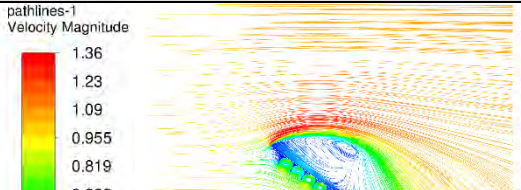
Front PV Temperature Distribution (t_{PV} [°C])	Wind Velocity Cross-Section Plane (v_{air} [m/s])
	
Base case: (a)	(b)
	

Table 5. *Cont.*

Front PV Temperature Distribution (t_{pv} [°C])	Wind Velocity Cross-Section Plane (v_{air} [m/s])
Base case: (a)	(b)
Horizontal simple: (a)	(b)
Horizontal 30 mm: (a)	(b)
Horizontal 60 mm: (a)	(b)
Vertical simple: (a)	(b)
Vertical 30 mm: (a)	(b)

Table 5. *Cont.*

Vertical simple: (a) (b)

Vertical 30 mm: (a) (b)

Vertical 60 mm: (a) (b)

The visual results clarify the temperature distribution achieved for each case analyzed, together with the air velocity field on the crosscut plane. The effect of the heated air recirculation in front of the PV panel is clearly identified in all cases, leading to a decrease in the maximum operating temperature of approximately 10 °C in relation to the base case. Additionally, the airflow is redirected towards the back side of the PV panel, further increasing the convective heat transfer coefficient. Considering the base case, the increase in the convective heat transfer coefficient is 10%, 20%, and 30% for the vertical simple, vertical 30 mm, and vertical 60 mm cases, respectively. Despite the improvement in the heat transfer coefficient, the recirculation areas are detrimental to the PV panel performance, as they are hotter than the rest of the area.

The results for T_{air} = 1 m/s, various inlet temperatures (T_{air} = 20–35 °C), and solar radiation (G = 600–1000 W/m²) were merged in the following plots (Figures 8–10).

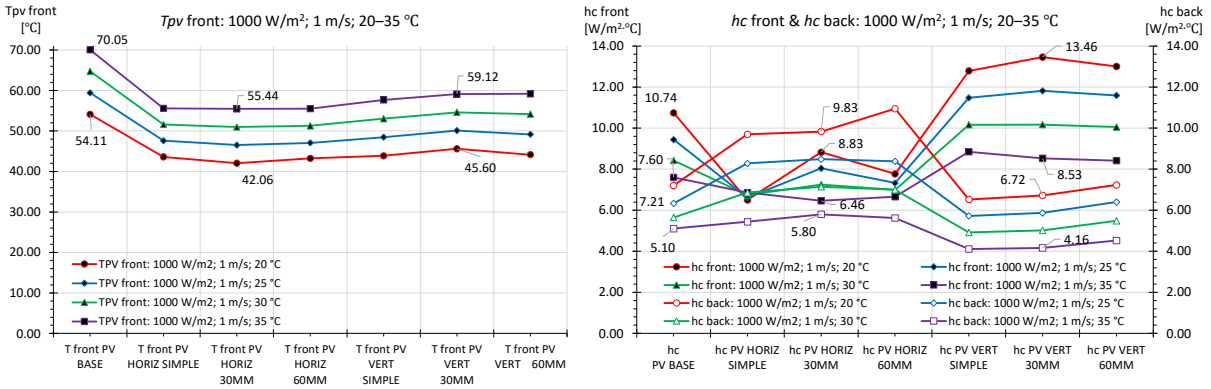
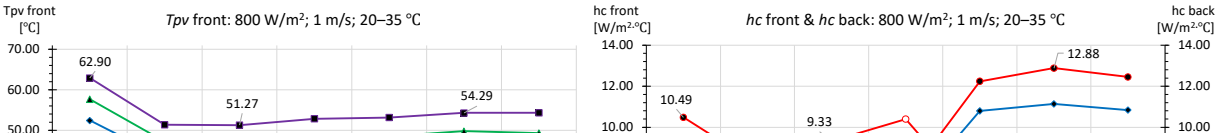


Figure 8. Variation of average operating temperature and convective heat transfer coefficient for studied cases. G = 1000 W/m², u_{air} = 1 m/s, and t_{air} = 20–35 °C.



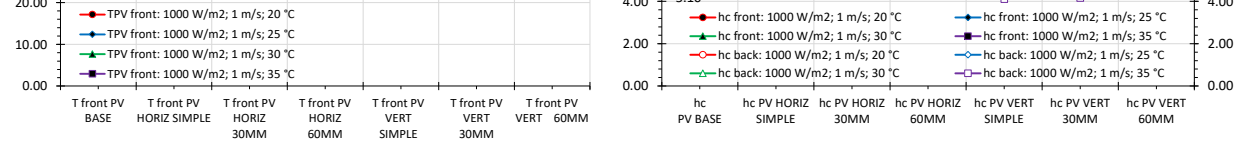


Figure 8. Variation of average operating temperature and convective heat transfer coefficient for studied cases. G = 1000 W/m^2, v_{air} = 1 m/s and t_{air} = 20–35 °C.

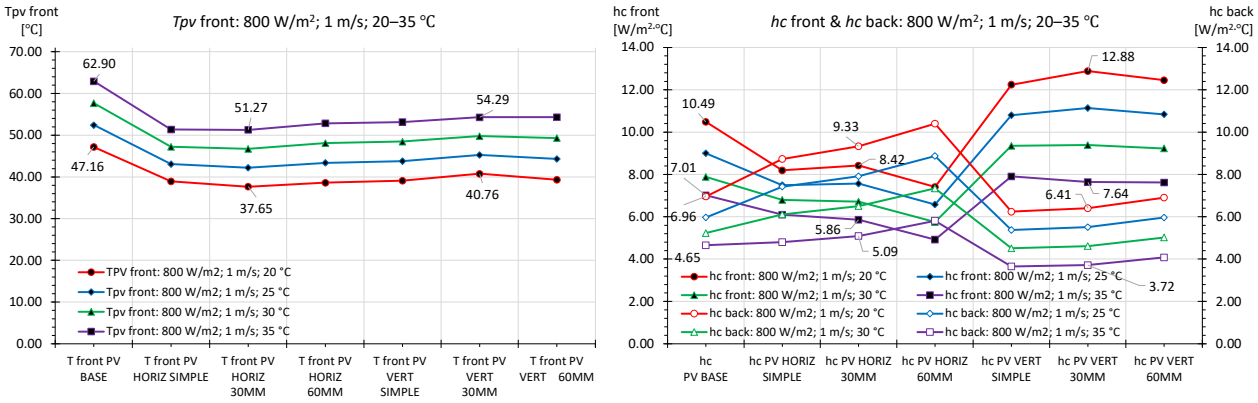


Figure 9. Variation of average operating temperature and convective heat transfer coefficient for studied cases (G = 800 W/m^2, v_{air} = 1 m/s and t_{air} = 20–35 °C).

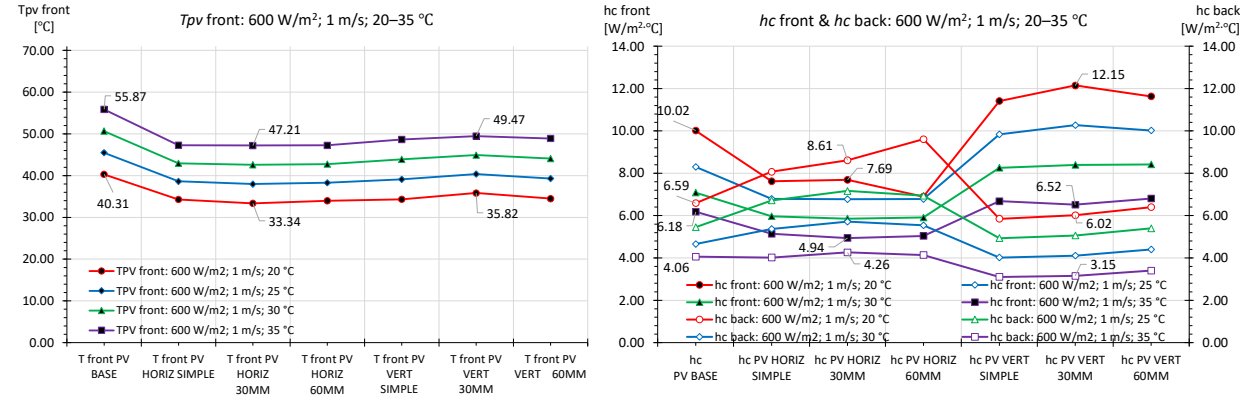


Figure 10. Variation of average operating temperature and convective heat transfer coefficient for studied cases (G = 600 W/m^2, v_{air} = 1 m/s and t_{air} = 20–35 °C).

An interesting aspect was recorded on convective heat transfer coefficients. Therefore, for horizontal heat sinks the h_c on the front of the PV panel were much closer to the h_c on the back, compared to vertical ones, where an important difference was recorded. The ambient temperature variation did not seem to change the best configuration (Case 2—horizontal 30 mm). This configuration determined a drop of temperature as presented in Table 6.

Table 6. Drop of the PV panel operating temperature for ambient air temperatures, t_{air} = 20–35 °C, wind velocity, v_{air} = 1–5 m/s and solar radiation, G = 600–1000 W/m^2.

Case	v_{air}	G = 600 W/m^2		G = 800 W/m^2		G = 1000 W/m^2	
		Drop of t_{PV} Compared to Base Case, for t_{air} = 20–35 °C					
		°C	%	°C	%	°C	%
0. BASE CASE	1 m/s	40.3–55.9	-	47.2–62.9	-	54.1–70.1	-
1. HORIZ SIMPLE		−6.02–−8.59	−14.9–−15.4	−8.22–−11.54	−17.4–−18.3	−10.52–−14.46	−19.4–−26.7
2. HORIZ 30MM		−6.97–−8.66	−17.3–−15.5	−9.51–−11.63	−20.2–−18.5	−12.05–−14.61	−22.3–−27
3. HORIZ 60MM		−6.35–−8.62	−15.8–−15.4	−8.55–−10.05	−18.1–−16	−10.88–−14.54	−20.1–−26.9
4. VERT SIMPLE		−5.98–−7.2	−14.8–−12.9	−8.07–−9.76	−17.1–−15.5	−10.25–−12.4	−18.9–−22.9
5. VERT 30MM		−4.49–−6.4	−11.1–−11.5	−6.4–−8.61	−13.6–−13.7	−8.51–−10.93	−15.7–−20.2
6. VERT 60MM		−5.82–−6.97	−14.4–−12.5	−7.84–−8.59	−16.6–−13.7	−9.97–−10.87	−18.4–−20.1

Table 6. *Cont.*

Case	v_{air}	G = 600 W/m^2		G = 800 W/m^2		G = 1000 W/m^2	
		Drop of t_{PV} Compared to Base Case, for t_{air} = 20–35 °C					
		°C	%	°C	%	°C	%
0. BASE CASE	2 m/s	34.5–49.9	-	39.4–54.9	-	44.3–59.9	-
1. HORIZ SIMPLE		−6.11–−6.18	−17.7–−12.4	−8.52–−8.6	−21.6–−15.7	−10.26–−10.88	−23.2–−18.2
2. HORIZ 30MM		−6.36–−6.79	−18.4–−13.6	−8.51–−9.32	−21.6–−17	−10.7–−11.7	−24.2–−19.5
3. HORIZ 60MM		−6–−6.37	−17.4–−12.8	−8.01–−8.73	−20.3–−15.9	−10.07–−10.68	−22.7–−17.8
4. VERT SIMPLE		−6.67–−6.17	−19.3–−12.4	−7.55–−8.26	−19.2–−15	−9.5–−10.38	−21.5–−17.3
5. VERT 30MM		−5.31–−6.21	−15.4–−12.4	−7.27–−8.3	−18.5–−15.1	−9.26–−10.42	−20.9–−17.4
6. VERT 60MM		−5.59–−4.48	−16.2–−9	−7.47–−8.14	−19–−14.8	−9.39–−10.13	−21.2–−16.9
0. BASE CASE	3 m/s	31.4–46.8	-	35.2–50.7	-	39.1–54.7	-
1. HORIZ SIMPLE		−4.88–−5.24	−15.5–−11.2	−6.72–−7.15	−19.1–−14.1	−8.53–−9.33	−21.8–−17.1
2. HORIZ 30MM		−5.3–−5.77	−16.9–−12.3	−7.17–−7.73	−20.3–−15.2	−9–−9.7	−23–−17.7
3. HORIZ 60MM		−5.11–−5.49	−16.3–−11.7	−6.85–−7.56	−19.4–−14.9	−8.62–−9.2	−22.1–−16.8
4. VERT SIMPLE		−4.59–−5.16	−14.6–−11	−6.33–−6.92	−18–−13.6	−7.96–−8.69	−20.4–−15.9
5. VERT 30MM		−5–−5.38	−15.9–−11.5	−6.7–−7.21	−19–−14.2	−8.41–−9.04	−21.5–−16.5
6. VERT 60MM		−4.53–−5.06	−14.4–−10.8	−6.08–−6.54	−17.2–−12.9	−7.64–−8.21	−19.5–−15
0. BASE CASE	4 m/s	29.2–44.6	-	32.4–47.8	-	35.5–51.1	-
1. HORIZ SIMPLE		−3.92–−4.07	−13.4–−9.1	−5.41–−5.68	−16.7–−11.9	−6.88–−7.57	−19.4–−14.8
2. HORIZ 30MM		−4.25–−4.75	−14.5–−10.6	−5.77–−5.87	−17.8–−12.3	−7.26–−7.94	−20.5–−15.5
3. HORIZ 60MM		−4.16–−4.53	−14.2–−10.2	−5.58–−5.76	−17.2–−12	−7.02–−7.58	−19.8–−14.8
4. VERT SIMPLE		−3.66–−4.05	−12.5–−9.1	−4.92–−5.41	−15.2–−11.3	−6.21–−6.8	−17.5–−13.3
5. VERT 30MM		−4.13–−4.49	−14.1–−10.1	−5.53–−6.02	−17.1–−12.6	−6.95–−7.56	−19.6–−14.8
6. VERT 60MM		−3.46–−3.72	−11.8–−8.3	−4.64–−4.98	−14.3–−10.4	−5.84–−6.24	−16.5–−12.2
0. BASE CASE	5 m/s	27.7–43.1	-	30.4–45.8	-	33–48.5	-
1. HORIZ SIMPLE		−3.15–−3.54	−11.4–−8.2	−4.38–−4.87	−14.4–−10.6	−5.56–−6.15	−16.9–−12.7
2. HORIZ 30MM		−3.64–−3.82	−13.1–−8.9	−4.87–−5.11	−16.1–−11.2	−6.1–−6.41	−18.5–−13.2
3. HORIZ 60MM		−3.41–−3.73	−12.3–−8.7	−4.57–−4.9	−15.1–−10.7	−5.76–−6.21	−17.5–−12.8
4. VERT SIMPLE		−2.95–−3.25	−10.6–−7.6	−3.95–−4.36	−13–−9.5	−4.98–−5.47	−15.1–−11.3
5. VERT 30MM		−3.42–−3.73	−12.3–−8.7	−4.59–−4.99	−15.1–−10.9	−5.75–−6.26	−17.4–−12.9
6. VERT 60MM		−2.62–−2.73	−9.4–−6.3	−3.52–−3.68	−11.6–−8	−4.42–−4.61	−13.4–−9.5

The results showed that for the studied wind conditions, the perforations did not improve the temperature of the PV panel when the fins were vertical. In addition, in the case of vertical fins, the larger perforations (Φ = 60 mm) were better, while for the horizontal fins the smaller ones (Φ = 30 mm) were better.

In terms of efficiency and power production, according to the assumption that the efficiency dropped linearly with the rise in temperature of −0.37%/°C [43], the following power production could be achieved—Table 7.

Table 7. Percentage of maximum power production achieved by the PV panel for each studied case.

Case	v_{air}	G = 600 W/m^2	G = 800 W/m^2	G = 1000 W/m^2
		of P_m at 25 °C, for t_{air} = 20–35 °C		
		%	%	%
0. BASE CASE	1 m/s	94.33–88.58	91.8–85.98	89.23–83.33
1. HORIZ SIMPLE		96.56–91.76	94.84–90.25	93.12–88.68
2. HORIZ 30MM		96.91–91.78	95.32–90.28	93.69–88.74
3. HORIZ 60MM		96.68–91.77	94.96–89.7	93.25–88.71
4. VERT SIMPLE		96.55–91.24	94.79–89.59	93.02–87.92
5. VERT 30MM		96–90.95	94.17–89.16	92.38–87.37
6. VERT 60MM		96.49–91.16	94.7–89.16	92.92–87.35
0. BASE CASE	2 m/s	96.48–90.79	94.68–88.95	92.87–87.09
1. HORIZ SIMPLE		98.74–93.08	97.84–92.13	96.67–91.11
2. HORIZ 30MM		98.83–93.3	97.83–92.39	96.83–91.42
3. HORIZ 60MM		98.7–93.15	97.65–92.18	96.6–91.04
4. VERT SIMPLE		98.95–93.07	97.47–92	96.39–90.93
5. VERT 30MM		98.44–93.09	97.37–92.02	96.3–90.94
6. VERT 60MM		98.55–92.45	97.45–91.96	96.35–90.83
0. BASE CASE	3 m/s	97.63–91.95	95.71–89.19	94.79–89.01
1. HORIZ SIMPLE		99.44–93.88	98.53–92.2	97.95–92.46
2. HORIZ 30MM		99.59–94.08	98.71–92.44	98.12–92.6
3. HORIZ 60MM		99.52–93.98	98.58–92.37	97.98–92.41
4. VERT SIMPLE		99.33–93.85	98.36–92.1	97.74–92.23
5. VERT 30MM		99.48–93.93	98.52–92.22	97.91–92.36
6. VERT 60MM		99.31–93.82	98.26–91.94	97.62–92.05
0. BASE CASE	4 m/s	98.43–92.74	96.54–89.26	96.12–90.35
1. HORIZ SIMPLE		99.88–94.25	99.09–91.94	98.67–93.15
2. HORIZ 30MM		100–94.5	99.25–92.02	98.81–93.29
3. HORIZ 60MM		99.97–94.42	99.16–91.97	98.72–93.15
4. VERT SIMPLE		99.79–94.24	98.85–91.81	98.42–92.86
5. VERT 30MM		99.96–94.41	99.14–92.09	98.69–93.14
6. VERT 60MM		99.71–94.12	98.72–91.61	98.28–92.66
0. BASE CASE	5 m/s	98.98–93.32	97.22–89.21	96.12–90.35
1. HORIZ SIMPLE		100.15–94.63	99.5–91.74	99.11–93.59
2. HORIZ 30MM		100.33–94.74	99.75–91.86	99.31–93.69
3. HORIZ 60MM		100.25–94.7	99.6–91.76	99.18–93.61
4. VERT SIMPLE		100.07–94.52	99.27–91.47	98.9–93.34
5. VERT 30MM		100.25–94.7	99.6–91.8	99.18–93.63
6. VERT 60MM		99.95–94.33	99.05–91.12	98.69–93.02

The power production was calculated as the percentage of maximum power possible, by assuming that at 25 °C the ratio achieved was 100% (320 Wp in STCs). From here on, we considered that the rise of temperature determined a drop in power production for each degree over t_{STC} = 25 °C, according to the PV panel's data sheet [43].

The most important effect of air cooling heat sinks was achieved in low wind conditions and high levels of solar radiation. It could be observed, Table 7, that for v_{air} = 1 m/s, G = 1000 W/m^2 and ambient temperature t_{air} = 35 °C, the percentage of maximum power production achieved was 83.33% for the base case, while the best cooling scenario (Case 3—horizontal 30 mm) could reach 88.74%. This meant a rise in power production of 6.49% compared to the base case.

For the position of the PV panel and wind direction studied in the paper, the best solution of heat sink for various conditions was the following: Case 3—Horizontal 30 mm. For this type of heat sink, the enhancement of power production was also reached for higher wind velocities (2–5 m/s), but with lower impact: from 3.60–4.97%, compared to the base case.

When lower ambient temperatures were involved, the effect of the heat sinks was decreased, this was due to inferior operating temperatures of the PV panel that were reached for base case. Therefore, the improvement of the power production reached values in the range 3.31–4.99%.

6. Conclusions

The goal of this manuscript was to develop and use a numerical model regarding the passive cooling of PV panels through perforated and non-perforated heat sinks. The PV panel was studied in a fixed position and tilted at 45 degrees from the horizontal, with the wind direction towards its backside. The input parameters, such as solar radiation, ambient temperature and wind velocity, were varied during the study. A challenging approach was used in order to calibrate the base case of the numerical model according to the NOCT parameters of the studied PV panel. A second validation of the accuracy of the numerical simulation consisted of comparison between the results obtained for the case of the heat sink with horizontal non-perforated fins and the experiments presented in the literature. Six types of heat sinks attached to the backside of the PV panel were numerically studied. The analyzed configurations focused on heat sinks with both perforated and non-perforated fins that were distributed horizontally and vertically. The CFD simulation was also conducted by modeling the air volume around the PV panel in real wind conditions. The main output parameters were the average temperature and the convective heat transfer coefficient on the front and back of the PV panel. In the best scenario, the perforated heat sink could assure a rise of the photovoltaic panel power production of 6.49%, compared to the base case.

Author Contributions: Conceptualization, S.V.H., F.E.Ț. and N.C.C.; methodology, S.V.H., F.E.Ț. and N.C.C.; software, S.V.H. and F.E.Ț.; validation, S.V.H., F.E.Ț., N.C.C. and I.H.; formal analysis, S.V.H. and I.H.; investigation, S.V.H., F.E.Ț., N.C.C., C.G.P., M.V. and I.H.; resources, S.V.H., F.E.Ț. and C.G.P.; data curation, S.V.H., F.E.Ț. and I.H.; writing—original draft preparation, S.V.H., F.E.Ț., N.C.C., C.G.P., M.V. and I.H.; writing—review and editing, S.V.H., F.E.Ț., N.C.C., C.G.P., M.V. and I.H.; visualization, S.V.H. and I.H.; supervision, S.V.H. and M.V.; project administration, S.V.H.; funding acquisition, S.V.H. All authors have read and agreed to the published version of the manuscript.

Funding: This work was supported by a grant of the Romanian Ministry of Education and Research, CCCDI-UEFISCDI, project number PN-III-P2-2.1-PED-2019-1294, within PNCDI III.

Institutional Review Board Statement: Not applicable.

Informed Consent Statement: Not applicable.

Data Availability Statement: Not applicable.

Acknowledgments: We would like to acknowledge the invaluable support provided by the FCI-TUIASI infrastructure in writing this article.

Conflicts of Interest: The authors declare no conflict of interest.

Nomenclature

STC	Standard test conditions
NOCT	Nominal operating cell temperature
AM	Air mass
t_{PV}	Cell temperature [°C]
G	Solar irradiance [W/m^2]
t_{air}	Ambient temperature [°C]
v_{air}	Wind speed towards backside of PV panel [m/s]
t_{NOCT}	Cell temperature in NOCT conditions [°C]
t_{STC}	Cell temperature in STC conditions [°C]
P_{mp}	Maximum power produced [Wp]
V_{mp}	Voltage at P_{mp} [V]
I_{mp}	Current at P_{mp} [A]
V_{oc}	Open circuit voltage [V]
I_{sc}	Short-circuit current [A]
η	PV panel efficiency [%]
β	P_{mp} temperature coefficient [%/°C]
L	Length of PV panel [m]
l	Width of PV panel [m]
h	Thickness of PV panel [m]
g	Thickness of the layers composing the PV panel [m]
λ	Thermal conductivity of the layers composing the PV panel [W/m·K]
ρ	Density of the layers composing the PV panel [kg/m^3]
c_p	Specific heat of the layers composing the PV panel [J/kg·K]
s	Distance between the fins of PV panel [m]
L_{fins}	Length of the fins [m]
h_{fins}	Height of the fins [m]
Φ	Diameter of the perforations of the fins [m]
d	Distance between the centers of the perforations [m]
$h_{c,front}$	Convective heat transfer coefficient on the front of PV panel [W/m^2·K]
$h_{c,back}$	Convective heat transfer coefficient on the back of PV panel [W/m^2·K]

References

1. 100 Days of Possibility. Available online: https://www.overshootday.org (accessed on 15 November 2021).
2. AlAmri, F.; AlZohbi, G.; AlZahrani, M.; Aboulebdah, M. Analytical Modeling and Optimization of a Heat Sink Design for Passive Cooling of Solar PV Panel. *Sustainability* **2021**, *13*, 3490. [CrossRef]
3. Taylor, M.; Ralon, P.; Ilas, A. The Power to Change: Solar and Wind Cost Reduction Potential to 2025. 2016. Available online: https://www.irena.org/publications/2016/Jun/The-Power-to-Change-Solar-and-Wind-Cost-Reduction-Potential-to-2025 (accessed on 15 November 2021).
4. Kuznetsov, P.; Yuferev, L.; Voronin, D.; Panchenko, V.A.; Jasiński, M.; Najafi, A.; Leonowicz, Z.; Bolshev, V.; Martirano, L. Methods Improving Energy Efficiency of Photovoltaic Systems Operating under Partial Shading. *Appl. Sci.* **2021**, *11*, 10696. [CrossRef]
5. Colarossi, D.; Principi, P. Indoor and Outdoor Performance of an Enhanced Photovoltaic Panel through Graphene/Fins/Phase Change Materials. *Appl. Sci.* **2021**, *11*, 8807. [CrossRef]
6. Why Europe's Energy Prices Are Soaring and Could Get Much Worse. Available online: https://www.euronews.com/2021/10/28/why-europe-s-energy-prices-are-soaring-and-could-get-much-worse (accessed on 15 November 2021).
7. Kamuyu, W.C.L.; Lim, J.R.; Won, C.S.; Ahn, H.K. Prediction Model of Photovoltaic Module Temperature for Power Performance of Floating PVs. *Energies* **2018**, *11*, 447. [CrossRef]
8. Idoko, L.; Anaya-Lara, O.; McDonald, A. Enhancing PV modules efficiency and power output using multi-concept cooling technique. *Energy Rep.* **2018**, *4*, 357–369. [CrossRef]
9. Dubey, S.; Sarvaiya, J.N.; Seshadri, B. Temperature Dependent Photovoltaic (PV) Efficiency and Its Effect on PV Production in the World—A Review. *Energy Procedia* **2013**, *33*, 311–321. [CrossRef]
10. Skoplaki, E.; Palyvos, J.A. On the temperature dependence of photovoltaic module electrical performance: A review of efficiency/power correlations. *Sol. Energy* **2009**, *83*, 614–624. [CrossRef]
11. Popovici, C.G.; Hudisteanu, S.V.; Mateescu, T.D.; Chereches, N.C. Efficiency improvement of photovoltaic panels by using air cooled heat sinks. *Energy Procedia* **2016**, *85*, 425–432. [CrossRef]
12. Berthod, C.; Strandberg, R.; Odden, J.O. Temperature coefficients of compensated silicon solar cells—Influence of ingot position and blend-in-ratio. *Energy Procedia* **2015**, *77*, 15–20. [CrossRef]

13. Hernandez-Perez, J.G.; Carrillo, J.G.; Bassam, A.; Flota-Banuelos, M.; Patino-Lopez, L.D. A new passive PV heatsink design to reduce efficiency losses: A computational and experimental evaluation. *Renew. Energy* **2020**, *147*, 1209–1220. [CrossRef]
14. Photovoltaic (PV) module performance testing and energy rating—Part 1: Irradiance and temperature performance measurements and power rating. In *International Standard*; IEC 61853-1; International Electrotechnical Commission: Geneva, Switzerland, 2011.
15. Gomaa, M.R.; Hammad, W.; Al-Dhaifallah, M.; Rezk, H. Performance enhancement of grid-tied PV system through proposed design cooling techniques: An experimental study and comparative analysis. *Sol. Energy* **2020**, *211*, 1110–1127. [CrossRef]
16. Nizetic, S.; Grubisic-Cabo, F.; Marinic-Kragic, I.; Papadopoulos, A.M. Experimental and numerical investigation of a backside convective cooling mechanism on photovoltaic panels. *Energy* **2016**, *111*, 211–225. [CrossRef]
17. Haidar, Z.A.; Orfi, J.; Kaneesamkandi, Z. Experimental investigation of evaporative cooling for enhancing photovoltaic panels efficiency. *Results Phys.* **2018**, *11*, 690–697. [CrossRef]
18. Herrando, M.; Pantaleo, A.M.; Wang, K.; Markides, C.N. Solar combined cooling, heating and power systems based on hybrid PVT, PV or solar-thermal collectors for building applications. *Renew. Energy* **2019**, *143*, 637–647. [CrossRef]
19. Ibrahim, A.; Fudholi, A.; Sopian, K.; Othman, M.Y.; Ruslan, M.H. Efficiencies and improvement potential of building integrated photovoltaic thermal (BIPVT) system. *Energy Convers. Manag.* **2014**, *77*, 527–534. [CrossRef]
20. Lamnatou, C.; Notton, G.; Chemisana, D.; Cristofari, C. Storage systems for building-integrated photovoltaic (BIPV) and building-integrated photovoltaic/thermal (BIPVT) installations: Environmental profile and other aspects. *Sci. Total Environ.* **2020**, *699*, 134269. [CrossRef]
21. Albatayneh, A.; Jaradat, M.; Al-Omary, M.; Zaquot, M. Evaluation of Coupling PV and Air Conditioning vs. Solar Cooling Systems—Case Study from Jordan. *Appl. Sci.* **2021**, *11*, 511. [CrossRef]
22. Hudișteanu, S.V.; Popovici, C.G. Numerical analysis of the efficiency and energy production of the building integrated photovoltaics for various configurations. In Proceedings of the CLIMA 2019 Congress, *E3S Web of Conf.*, Bucharest, Romania, 26–29 May 2019; Volume 111, p. 03044.
23. Hudișteanu, S.V.; Popovici, C.G. Experimental investigation of the wind direction influence on the cooling of photovoltaic panels integrated in double skin façades. In Proceedings of the CLIMA 2019 Congress, *E3S Web of Conf.*, Bucharest, Romania, 26–29 May 2019; Volume 111, p. 03045.
24. Bahaidarah, H.M.S. Experimental performance evaluation and modeling of jet impingement cooling for thermal management of photovoltaics. *Sol. Energy* **2016**, *135*, 605–617. [CrossRef]
25. Bai, A.; Popp, J.; Balogh, P.; Gabnai, Z.; Palyi, B.; Farkas, I.; Pinter, G.; Zsiboracs, H. Technical and economic effects of cooling of monocrystalline photovoltaic modules under Hungarian conditions. *Renew. Sustain. Energy Rev.* **2016**, *60*, 1086–1099. [CrossRef]
26. Ebrahimi, M.; Rahimi, M.; Rahimi, A. An experimental study on using natural vaporization for cooling of a photovoltaic solar cell. *Int. Commun. Heat Mass Transf.* **2015**, *65*, 22–30. [CrossRef]
27. Eicker, U.; Pietruschka, D.; Schmitt, A.; Haag, M. Comparison of photovoltaic and solar thermal cooling systems for office buildings in different climates. *Sol. Energy* **2015**, *118*, 243–255. [CrossRef]
28. Aelenei, L.; Pereira, R.; Ferreira, A.; Goncalves, H.; Joyce, A. Building Integrated Photovoltaic System with integral thermal storage: A case study. *Energy Procedia* **2014**, *58*, 172–178. [CrossRef]
29. Hammami, M.; Torretti, S.; Grimaccia, F.; Grandi, G. Thermal and Performance Analysis of a Photovoltaic Module with an Integrated Energy Storage System. *Appl. Sci.* **2017**, *7*, 1107. [CrossRef]
30. Bevilacqua, P.; Perrella, S.; Cirone, D.; Bruno, R.; Arcuri, N. Efficiency Improvement of Photovoltaic Modules via Back Surface Cooling. *Energies* **2021**, *14*, 895. [CrossRef]
31. Arifin, Z.; Tjahjana, D.; Hadi, S.; Rachmanto, R.A.; Setyohandoko, G.; Sutanto, B. Numerical and Experimental Investigation of Air Cooling for Photovoltaic Panels Using Aluminum Heat Sinks. *Int. J. Photoenergy* **2020**, *2020*, 1574274. [CrossRef]
32. Hudișteanu, S.V.; Mateescu, T.D.; Chereches, N.C.; Popovici, C.G. Numerical study of air cooling photovoltaic panels using heat sinks. *Rom. J. Civ. Eng.* **2015**, *6*, 11–20.
33. Fatoni, E.K.A.; Taqwa, A.; Kusumanto, R.; Polytechn Sriwijaya, P.S.S.I. Solar Panel Performance Improvement using Heatsink Fan as the Cooling Effect. In Proceedings of the 2nd Forum in Research, Science, and Technology (FIRST), Palembang, Indonesia, 30–31 October 2018.
34. Arifin, Z.; Suyitno, S.; Tjahjana, D.; Juwana, W.E.; Putra, M.R.A.; Prabowo, A.R. The Effect of Heat Sink Properties on Solar Cell Cooling Systems. *Appl. Sci.* **2020**, *10*, 7919. [CrossRef]
35. Fahad, A.-A.; Taher, S.M.; Omar, F.A.-A.; Sajid, A.; Sadaqat, A.; Ijlal, S.A.; Richu, Z.; Tarek, S.K. Innovative technique for achieving uniform temperatures across solar panels using heat pipes and liquid immersion cooling in the harsh climate in the Kingdom of Saudi Arabia. *Alex. Eng. J.* **2021**, *61*, 1413–1424. [CrossRef]
36. Duan, J. A novel heat sink for cooling concentrator photovoltaic system using PCM-porous system. *Appl. Therm. Eng.* **2021**, *186*, 116522. [CrossRef]
37. Bayrak, F.; Oztop, H.F.; Selimefendigil, F. Effects of different fin parameters on temperature and efficiency for cooling of photovoltaic panels under natural convection. *Sol. Energy* **2019**, *188*, 484–494. [CrossRef]
38. Johnston, E.; Szabo, P.S.B.; Bennett, N.S. Cooling silicon photovoltaic cells using finned heat sinks and the effect of inclination angle. *Therm. Sci. Eng. Prog.* **2021**, *23*, 100902. [CrossRef]
39. Mojumder, J.C.; Chong, W.T.; Ong, H.C.; Leong, K.Y.; Abdullah Al, M. An experimental investigation on performance analysis of air type photovoltaic thermal collector system integrated with cooling fins design. *Energy Build.* **2016**, *130*, 272–285. [CrossRef]

40. Amr, A.A.R.; Hassan, A.A.M.; Abdel-Salam, M.; El-Sayed, A.M. Enhancement of photovoltaic system performance via passive cooling: Theory versus experiment. *Renew. Energy* **2019**, *140*, 88–103. [CrossRef]
41. Vittorini, D.; Cipollone, R. Fin-cooled photovoltaic module modeling—Performances mapping and electric efficiency assessment under real operating conditions. *Energy* **2019**, *167*, 159–167. [CrossRef]
42. Pérez Escobar, B.L.; Pérez Hernández, G.; Ocampo Ramírez, A.; Rojas Blanco, L.; Díaz Flores, L.L.; Vidal Asencio, I.; Hernández Perez, J.G.; Ramírez Morales, E. Analysis of Thermomechanical Stresses of a Photovoltaic Panel Using a Passive System of Cooling. *Appl. Sci.* **2021**, *11*, 9806. [CrossRef]
43. Available online: https://ae-solar.com/wp-content/uploads/2018/10/AE_Eclipse-Ultra-Black_HM6-60_310W-320W.pdf (accessed on 15 November 2021).
44. Nizetic, S.; Papadopoulos, A.M.; Giama, E. Comprehensive analysis and general economic-environmental evaluation of cooling techniques for photovoltaic panels, Part I: Passive cooling techniques. *Energy Convers. Manag.* **2017**, *149*, 334–354. [CrossRef]
45. Ansys Fluent Documentation, 2021-R1. Available online: https://www.ansys.com/products/fluids/ansys-fluent (accessed on 15 November 2021).
46. El Fouas, C.; Hajji, B.; Gagliano, A.; Tina, G.M.; Aneli, S. Numerical model and experimental validation of the electrical and thermal performances of photovoltaic/thermal plant. *Energy Convers. Manag.* **2020**, *220*, 112939. [CrossRef]
47. Nguyen, D.P.N.; Neyts, K.; Lauwaert, J. Proposed Models to Improve Predicting the Operating Temperature of Different Photovoltaic Module Technologies under Various Climatic Conditions. *Appl. Sci.* **2021**, *11*, 7064. [CrossRef]
48. Almuwailhi, A.; Zeitoun, O. Investigating the cooling of solar photovoltaic modules under the conditions of Riyadh. *J. King Saud Univ.-Eng. Sci.* **2021**, *186*, 116522. [CrossRef]
49. Mattar, S.J.; Kavian Nezhad, M.R.; Versteege, M.; Lange, C.F.; Fleck, B.A. Validation Process for Rooftop Wind Regime CFD Model in Complex Urban Environment Using an Experimental Measurement Campaign. *Energies* **2021**, *14*, 2497. [CrossRef]
50. Alizadeh, H.; Nazari, M.A.; Ghasempour, R.; Shafii, M.B.; Akbarzadeh, A. Numerical analysis of photovoltaic solar panel cooling by a flat plate closed-loop pulsating heat pipe. *Sol. Energy* **2020**, *206*, 455–463. [CrossRef]